RICE UNIVERSITY

Numerical Methods and Applications for Reduced Models of Blood Flow

by

Charles Puelz

A Thesis Submitted
in Partial Fulfillment of the
Requirements for the Degree

Doctor of Philosophy

Approved, Thesis Committee:

Béatrice Rivière, Director and Co–Chair
Noah G. Harding Chair and Professor of
Computational and Applied Mathematics,
Rice University

Craig G. Rusin, Co–Chair
Assistant Professor of Pediatrics–
Cardiology, Baylor College of Medicine

Matthias Heinkenschloss
Noah G. Harding Chair and Professor of
Computational and Applied Mathematics,
Rice University

Jane Grande–Allen
Isabel C. Cameron Professor of
Bioengineering, Rice University

Sunčica Čanić
Cullen Distinguished Professor of
Mathematics, University of Houston

Houston, Texas
April, 2017

ABSTRACT

Numerical Methods and Applications
for Reduced Models of Blood Flow

by

Charles Puelz

The human cardiovascular system is a vastly complex collection of interacting components, including vessels, organ systems, valves, regulatory mechanisms, microcirculations, remodeling tissue, and electrophysiological signals. Experimental, mathematical, and computational research efforts have explored various hemodynamic questions; the scope of this literature is a testament to the intricate nature of cardiovascular physiology. In this work, we focus on computational modeling of blood flow in the major vessels of the human body. We consider theoretical questions related to the numerical approximation of reduced models for blood flow, posed as nonlinear hyperbolic systems in one space dimension. Further, we apply this modeling framework to abnormal physiologies resulting from surgical intervention in patients with congenital heart defects. This thesis contains three main parts: (*i*) a discussion of the implementation and analysis for numerical discretizations of reduced models for blood flow, (*ii*) an investigation of solutions to different classes of models in the realm of smooth and discontinuous solutions, and (*iii*) an application of these models within a multiscale framework for simulating flow in patients with hypoplastic left heart syndrome. The two numerical discretizations studied in this thesis are a characteristics–based method for approximating the Riemann–invariants of reduced

blood flow models, and a discontinuous Galerkin scheme for approximating solutions to the reduced models directly. A priori error estimates are derived in particular cases for both methods. Further, two classes of hyperbolic systems for blood flow, namely the mass–momentum and the mass–velocity formulations, are systematically compared with each numerical method and physiologically relevant networks of vessels and boundary conditions. Lastly, closed loop vessel network models of various Fontan physiologies are constructed. Arterial and venous trees are built from networks of one–dimensional vessels while the heart, valves, vessel junctions, and organ beds are modeled by systems of algebraic and ordinary differential equations.

Acknowledgments

I am very grateful for my advisors, Béatrice and Craig. They agreed to mentor me following my masters, and their patience and expertise facilitated my transition into a new research area. Béatrice focused me on the task at hand, and Craig motivated me by inquiring about results. They both set incredible examples for excellence in research and mentorship.

Sebastián Acosta has been an important friend and collaborator. Several parts of this work came out of our discussions, and I am thankful for these interactions. I would also like to acknowledge Sunčica Čanić; her mathematical hemodynamics class was my first formal introduction to this material.

My family in the CAAM department at Rice has been a wonderful part of the journey through graduate school. I am continually blessed by the support of my parents, my brother, and Emily.

Contents

Illustrations

Tables

Chapter 1

Introduction and review

The human cardiovascular system consists of many complex components including organ systems, laminar and turbulent blood, regulatory mechanisms, and interfaces between fluid and structure. Each piece governs phenomena occurring at different time and length scales. These intricacies, along with our desire to understand cardiovascular disease, have promoted a thrust of experimental and computational research devoted to broadening our comprehension of hemodynamic systems. This thesis focuses on computational models for blood flow within the major vessels of the human body. In particular, approximate descriptions for blood flow, known as *reduced models*, are employed. This approach enables us to efficiently characterize global hemodynamics in complex physiologies, with an emphasis on post–surgical circulations of patients with congenital heart defects. Three main parts comprise this work:

1. Implementation and analysis of numerical methods for discretizing reduced models of blood flow (Chapters 2, 3, 4, and 5).

2. An extensive numerical comparison of numerical methods and reduced models of blood flow (Chapter 6)

3. Application of these numerical methods for understanding complex physiological systems arising from hypoplastic left heart syndrome (Chapter 7).

The main contributions of this thesis are in the numerical analysis for methods approximating solutions to conservation laws, as well as novel applications of reduced

blood flow models. In Chapter 2, we comment on some theoretical aspects of reduced models for blood flow, namely their symmetrizability, which may aid researchers in analyzing numerical methods. Part of this investigation reveals conditions under which different models are symmetrizable. The results in Chapter 3 establish a priori error estimates for discontinuous Galerkin approximations of smooth solutions to scalar conservation laws, where the time discretization is a popular choice in the blood flow modeling community. These results are a first step toward analyzing fully discrete numerical schemes for one–dimensional blood flow models. In Chapter 4, we present an approach for efficiently approximating the Riemann invariants of reduced blood flow models, along with stability and convergence results. It is shown in Chapter 6 that this algorithm agrees well with standard discontinuous Galerkin approximations on complex vessel networks. Further, in Chapter 6, a novel comparison of various blood flow models is given, in the realm of both smooth and discontinuous solutions. Lastly, in Chapter 7, we describe mathematical models for several versions of the Fontan physiology, a circulation typically present in patients with a congenital heart defect called hypoplastic left heart syndrome (HLHS). We consider the standard extracardiac Fontan, the fenestrated Fontan, and the Fontan with hepatic vein exclusion. To our knowledge, these Fontan circulations have not been studied in the same modeling framework, and more broadly, mutliscale one–dimensional/zero–dimensional models have yet to be extensively applied to HLHS physiologies.

Reduced blood flow models in the context of this thesis are systems of nonlinear conservation laws in one space dimension that describe axi–symmetric blood flow in vessels with elastic walls. We will use the terms *reduced* and *one–dimensional* to mean the same thing. These models attract researchers from a variety of fields, and have generated interesting and applicable research in the mathematics, bioengineering, and

physiological modeling communities. Mathematical work has addressed questions related to shock formation and coupling techniques for multiscale modeling (e.g. [7, 8, 9, 10]). For applications, researchers use these equations as building blocks for developing complex models of the arterial tree [4, 11], closed loop models of the neonatal and adult circulations, (i.e. arterial tree and venous tree models [12, 13]), and multiscale models of the cardiovascular system [9, 14, 15].

This review is organized as follows. First, we present relevant literature on one–dimensional models. Some of these papers describe multiscale models which incorporate one–dimensional modeling as a particular component (e.g. three–dimensional simulations of local hemodynamics with the Navier–Stokes equations with zero– and one–dimensional models providing outflow conditions). Other papers focus on model development at the PDE level (i.e. specifying either a *flat* or *no–slip* axial velocity profile) and develop theoretical results for one–dimensional models. When relevant, we mention different numerical methods used to discretize and approximate the models.

The second section of this review discusses important developments regarding numerical methods for hyperbolic conservation laws, with a focus on numerical techniques commonly used by the community of researchers studying reduced blood flow models. We also discuss related work for discontinuous Galerkin discretizations (DG), with a focus on numerical analysis of DG methods for nonlinear hyperbolic equations which are either scalar or vector valued.

The final section of this review focuses on mathematical modeling for hypoplastic left heart syndrome, a congenital heart defect which induces complex physiological dynamics. Most of the current work in this area involves three–dimensional computational fluid dynamics and multiscale modeling with the goal of characterizing local hemodynamics in post–surgical physiologies. We apply the approaches discussed in

this thesis to construct global hemodynamic models, with some relatively high local anatomical detail, that allow us to address other questions beyond the reach of some current modeling approaches.

1.1 One–dimensional and multiscale models

One–dimensional models of blood flow have existed in the literature for quite a while. According to Hughes, the origins of one–dimensional models can be traced back to the 1956 work of Lambert [16, 7]. In his own thesis, Hughes derived one–dimensional equations of fluid flow from a vector calculus identity and a version of the Navier–Stokes equations in the axial direction. Following the derivation, he provided analysis for two versions of a reduced model differentiated by the choice of axial velocity profile: (1) a *flat profile* and (2) a profile satisfying the *no–slip* boundary condition. He concluded his thesis with numerical simulations of these models with Lax–Wendroff type methods.

Čanić and Kim's more recent work also addressed theory for one–dimensional fluid flow [8]. In their paper, the authors provided a derivation for a reduced model of blood flow of a different flavor from Hughes' work. Their argument began with the expression of three dimensional, incompressible, and axially–symmetric Navier–Stokes equations in non–dimensional form, assumed the vessel radius to be much smaller than the vessel length, and applied an asymptotic reduction argument. A summary of the derivation is given at the beginning of Chapter 2. Their choice for the axial velocity profile in numerical simulations, performed with the two–step Lax–Wendroff method, corresponds to the no–slip theory of Hughes' thesis and takes the form:

$$u_x(x,r,t) = \frac{\zeta+2}{\zeta} U(x,t)\left[1-\left(\frac{r}{R}\right)^{\zeta}\right] \tag{1.1}$$

for some parameter $\zeta > 0$ governing the profile shape. This formula is typically called the *ad hoc closure* in the literature. Notice this choice for the axial profile satisfies the no–slip boundary condition at the vessel wall (i.e. $u_x|_{r=R} = 0$) and the average of u_x over a cross–section equals the average axial velocity over a cross–section denoted by $U(x,t)$.

In the next part of their paper, Čanić and Kim presented their main theoretical contribution: the derivation of conditions on initial and boundary data which lead to a smooth solution locally in time for a general, strictly hyperbolic system of two conservation laws [8].

Blood flow under normal conditions is typically smooth, but abnormalities in the hemodynamic system (e.g. aortic regurgitation) can lead to shock formation [8]. In this light, Čanić and Kim applied this theory to the reduced equations for blood flow to understand shock formation in physiologically relevant vessel models [8]. Despite the fact that their presentation of the reduced model assumed a no–slip profile, in the application of their theory, they assumed a simplifying flat profile:

$$u_x(x,r,t) = U(x,t). \tag{1.2}$$

As will be shown later, the Riemann invariants may be computed explicitly in the flat–profile case, and the authors needed this fact in their application. Furthermore, a flat profile describes an absence of a boundary layer effect from the vessel wall; this property is typically seen in non–viscous fluids. Thus, the authors also assumed the fluid was inviscid, i.e. kinematic viscosity equal to zero. Regardless of these simplifying assumptions, numerical studies with versions of the equations arising from the ad hoc closure, i.e. the no–slip theory, aligned with the theoretical estimate for shock formation (from flat–profile, inviscid flow).

The flat–profile and no–slip theories are mentioned in the context of the work

of Čanić and Kim and Hughes since distinctions between these models are generally overlooked by the current engineering community. Further, several simplifying properties of the flat–profile choice appear to make the system of conservation laws more amenable for analysis [8]. These ideas are presented in mathematical detail in Chapter 2. Hughes, in his thesis, presents some related numerical results comparing the flat–profile and no–slip theories with a canine aorta model [7]. A portion of this thesis focuses on an extension of Hughes' computational work to a careful numerical comparison of the different reduced models presented here, in the context of physiological vessel networks and in the realm of shock formation (Chapter 6).

Formaggia, Quarteroni, and collaborators have contributed significant theoretical and numerical results for reduced blood flow models [10, 9, 17, 18]. Several works focused on the application of the reduced models for numerically studying branching networks of vessels and arterial stents [17, 18]. In these papers, the authors used the equations corresponding to a flat velocity profile, carefully presented techniques for modeling vessel networks, and performed some numerical simulations using a finite element method called the Taylor–Galerkin scheme.

A notable theoretical paper by Formaggia et al. described techniques for coupling reduced models with three–dimensional descretizations of the Navier–Stokes equations [9]. In particular, the authors derived the total energy of the reduced models with the assumption of a flat axial velocity profile; this result led the authors to an entropy function which may be employed to symmetrize reduced models, as will be discussed in Chapter 2.

Related theoretical work by Fernández et al. and Quarteroni et al. explored existence and uniqueness of solutions to coupled multiscale hemodynamic models, i.e. three–dimensional Navier–Stokes equations coupled with zero–dimensional (ODE)

models, or reduced models coupled with zero–dimensional models [19, 10]. In most of the mathematical analysis (including [10]) for reduced models, a flat–profile theory is assumed. Although not presented in this thesis, it would be interesting to see if and where these results can be extended to the no–slip theory, and whether one may use these results to comment on numerical discretizations of multiscale models.

Research from the last decade or so may be characterized by the application of reduced models to vessel networks in an effort to model clinically relevant physiologies. This endeavor has been driven primarily by engineers and mathematicians collaborating with clinicians.

An important work by Olufsen et al. described a multi–vessel model of the arterial tree with carefully derived outflow conditions at terminal vessels [11]. The authors provided a brief derivation of a reduced model and specified an axial velocity that was flat, except in a small neighborhood of the vessel wall; in this region it was defined as the linear interpolant from the average axial velocity to zero, and hence satisfied the no–slip condition. Following this choice, they argued the boundary layer effect was negligible, and the resulting equations aligned with the flat–profile model. Their work incorporated boundary conditions at vessel junctions and novel, "structured–tree" outflow conditions.

For vessel junctions, as is typical throughout the literature, they imposed conservation of momentum (inflow into junction is equal to outflow) and continuity of total pressure. From the terminal vessels, blood flows into progressively smaller arteries, arterioles, and then into capillaries in vascular beds. The high resistivity of the beds induce reflected waves flowing backwards toward the heart. Thus, the authors incorporated models of the beds into the vessel network by assuming a structured–tree geometry for the capillaries, and derived boundary conditions for the terminal vessels

based on analytical solutions to a linearized one–dimensional model [11].

For numerical simulations of the vessel network, a two–step Lax–Wendroff scheme was used. Experimental data collected from magnetic resonance imaging provided inlet boundary data for the flow, and their computed results agreed well with measured data [11].

Sherwin et al. published a highly cited work in 2003 describing simulations of vessels with discontinuous material properties (like stents) and vessel networks, with two finite–element–type methods: the Taylor–Galerkin method and a discontinuous Galerkin method [4]. Although the reduced model was given in a general form, they considered equations arising from the flat profile assumption. The mathematical simplifications resulting from this assumption are evident in their presentation, since the design of discontinous Galerkin schemes required analytical expressions for the Riemann invariants. The invariants can be calculated in the flat–profile case. At this point, it is unclear if the invariants for the no–slip case may be analytically computed.

In their paper, the Taylor–Galerkin and discontinous Galerkin (DG) schemes were presented, but most of the numerical simulations utilized the DG discretization coupled with a second order Adams-Bashforth (multistep) method for the temporal discretization [4]. The authors employed Riemann invariants of the reduced model in the design of an "upwinding" numerical flux: at an interface between elements, the left–to–right moving invariant was computed on the left element, the right–to–left moving invariant was computed on the right element, and the upwinded values for the physical variables were computed for evaluation of the original flux function. Mathematical details about this method are provided in Chapter 3. We remark their numerical flux relies on the system being strictly hyperbolic *and* the invariants propagating in opposite directions. Further, the fully–discrete scheme presented by Sherwin et al. is a

departure from the classical works of Cockburn and Shu in their choice of numerical flux and their selection of a multistep time discretization instead of a Runge–Kutta scheme (e.g. [20]). This particular multistep time discretization scheme is quite popular in the blood flow literature. In Chapter 3, we present convergence results for a DG scheme coupled to this time discretization for approximating solutions to scalar nonlinear hyperbolic conservation laws.

Numerical experiments by Sherwin et al. included models of single vessels with an inserted stent, mathematically described as a discontinuous material property of the vessel wall (incorporated into the parameters of the state equation relating fluid pressure to vessel cross–sectional area) [4]. The authors also presented results for a fifty–five vessel network model of the arterial tree, and other researchers tend to use this arterial tree model as a test case in their own numerical experiments. The outflow boundary conditions at the terminal arteries were reflective, but different from the work of Olufsen et al. [11]. Sherwin et al. derived outflow conditions by reflecting the outgoing Riemann invariant by a particular fraction, as described in Chapter 5.

Mynard and his collaborators have contributed notable work in simulating networks of vessels [12, 3, 13]. The work of Mynard and Nithiarasu described a 61 vessel model of the arterial tree with additional features, including models for the coronary vessels, the aortic valve, and vessel tapering [12]. The authors employed reduced equations derived from flat–profile theory, and their discretization scheme, called "locally conservative Galerkin," is essentially a discontinuous Galerkin method. Boundary conditions at vessel junctions and reflective conditions at the terminal vessels were handled in the same manner as in the work of Sherwin et al. and others [4]. Their numerical results included a comparison of the reduced model to three–dimensional simulations.

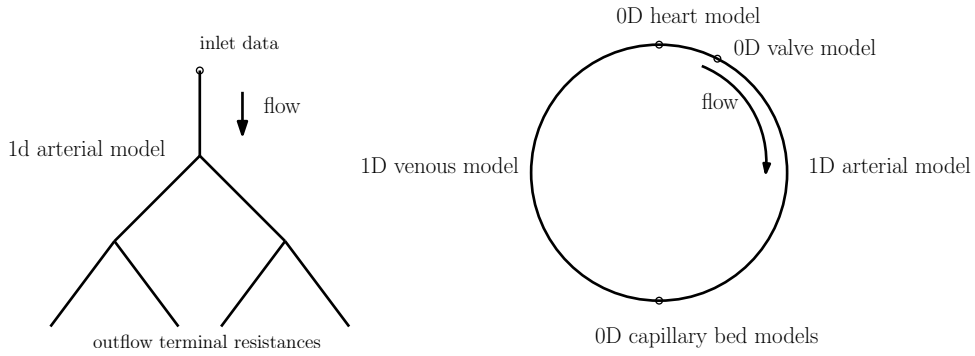

Figure 1.1 : Schematics of open–loop (left) and close–loop (right) reduced models incorporating one–dimensional equations for flow in vessels with zero–dimensional equations for capillary beds, etc..

Most research in applying reduced equations to model networks of vessels focused on open–loop models of the arterial tree, often with resistance or RC circuit models at the terminal vessels. Recently, closed loop models constructed from reduced equations have gained popularity. Figure 1.1 shows simple depictions of open–loop and closed–loop models employing one–dimensional equations for the vessel trees and zero–dimensional equations for the capillary beds, valves, and heart. In particular, work by Mynard and Smolich described an extension of the arterial tree model to a closed–loop model linking the arterial and venous trees [3, 13]. The arterial and venous circulations were modeled as networks of vessels and zero–dimensional organ bed models provided interface conditions. Organ beds were modeled with RC circuits since they hold blood (capacitance) and establish pressure gradients between different vessel networks (resistance).

Blanco et al. constructed a more complex closed–loop configuration containing three–dimensional, one–dimensional, and zero–dimensional components [21]. In contrast to Mynard's work, the authors used one–dimensional models only for the arterial

tree; zero–dimensional equations were used for the venous circulation and capillary beds. The three–dimensional Navier–Stokes equations were employed to resolve flow in a small portion of the arterial tree, and this work considered cerebral aneurism dynamics.

Closed–loop models require a mathematical description of the heart at the outlet of the venous tree and inlet into the arterial tree (as opposed to a prescribed Dirichlet inlet boundary condition at the ascending aorta in an open–loop model). Mynard et al. and Blanco et al. used a zero–dimensional model of the heart to drive flow in a closed loop model [3, 13, 21]. In the heart model, the pressure $p(t)$ in a heart chamber was related to a specified function called the elastance $E(t)$ and chamber volume $V(t)$ via

$$p(t) = E(t)V(t). \tag{1.3}$$

The building blocks for a closed–loop model of HLHS physiologies presented in this thesis were taken from Mynard's work and others, and are shown in more detail in Chapter 5.

1.2 Numerical discretizations for hyperbolic conservation laws

Reduced models of blood flow presented in this thesis belong to a class of differential equations called *hyperbolic conservation laws*. This section is devoted to a summary of previous work on numerical approximations for this class of equations. The literature is quite large, so particular emphasis is placed on discontinuous Galerkin (DG) discretizations and on other numerical methods typically used by researchers employing reduced blood flow models. Further, we recapitulate some theoretical developments for DG schemes.

A finite–difference scheme for hyperbolic conservation laws is the Lax–Wendroff

method [22]. Although simple to implement, it requires the law to be expressed in conservative form. It has been employed by mutiple authors in the context of one–dimensional blood flow, including by Hughes and Čanić and Kim. [7, 8]. Hughes focused on shock formation in his thesis from both theoretical and numerical perspectives and had some success using Lax–Wendroff schemes to investigate discontinous solutions. Čanić and Kim also performed numerical studies of to shock formation and obtained results aligning with their theoretical predicitions.

Reymond et al. validated an arterial tree model with in vivo data [23]. The model was a version of the setup used by Westerhof et al., Stergiopulos et al., and Sherwin et al. [24, 25, 4]. The equations were discretized with a finite–difference method, presumably a Lax–Wendroff type method, although there is no mention of specifics of their scheme in the paper.

Recent work containing numerical simulations of reduced blood flow models utilize finite–element type discretizations. Variants include the so–called Taylor–Galerkin scheme, noted to be the finite–element extension of the Lax–Wendroff scheme [17, 18, 4]. Mynard and his collaborators used a similar scheme termed the "locally–conservative Galerkin method," designed by Thomas and Nithiasaru [12, 26]. This approach effectively decouples the computation on each element.

Sherwin et al. wrote one of the more prominent papers in blood flow modeling which described a discontinuous Galerkin discretization of a one–dimensional model [4]. The authors designed a numerical flux termed the "upwinding flux" depending on the traces of the Riemann invariants at an elemental interface and used a second order Adams–Bashforth discretization to time step the scheme.

Recent papers summarized several numerical schemes for hyperbolic conservation laws used in the context of one–dimensional blood flow modeling and presented

careful comparisons of these methods. Wang et al. focused on the MacCormack, Taylor–Galerkin, monotonic upwind, and discontinuous Galerkin schemes [27]. In addition to comparing numerical solutions with shocks and physiological vessel networks (including the fifty–five vessel network from Sherwin et al. [4]), the authors analyzed computational tractability of each method. Their one–dimensional model differs slightly from the one we use in the sense that it captures the viscoelastic nature of the vessel wall; this modification to the model manifests itself as a second order spatial derivative term in the momentum equation. A similar paper by Boileau et al. studied six different numerical schemes with a reduced model analogous to the equations presented in this thesis (without a viscoelastic vessel wall) [28]. Novelty in their work stems from carefully designed test cases, including one that allows for a comparison of the reduced model with results from a three–dimensional model. Both papers serve as reference texts for popular numerical methods used to approximate one–dimensional blood flow models.

A classical series of papers by Shu, Cocburn, and their collaborators invented and analyzed discontinuous Galerkin discretizations for hyperbolic conservations laws coupled with special Runge–Kutta time integration schemes, called Runge–Kutta discontinuous Galerkin (RKDG) methods [29, 20, 30, 31]. The series began with scalar equations in one space dimension and incrementally generalized the methods to systems of conservation laws in multiple space dimensions.

Numerical fluxes employed by the authors, including the local Lax–Friedrichs (LLF) flux, are more standard than the one appearing in the work of Sherwin et al. [4]. The LLF flux is implemented for a portion of the numerical experiments in this thesis because of its simplicity and associated theoretical development. In particular, the LLF flux belongs to a class of fluxes termed *E–fluxes*, and Zhang, Shu, and their

collaborators analyzed RKDG methods using these numerical fluxes [32, 33, 34].

Several important themes are common throughout the analysis of the RKDG methods by Zhang et al. [32, 33, 34]. First, for systems of conservation laws, a vital assumption is that the system is *symmetrizable*; this requirement boils down to the existence of a transformation converting the system into a form more amenable for numerical analysis. Second, theoretical arguments appear to be specialized to particular time discretizations; see for example the work for second and third order Runge–Kutta schemes [33, 34].

1.3 Modeling for hypoplastic left heart syndrome

Hypoplastic left heart syndrome is a fairly rare congenital heart defect; according to Marshall et al., it occurs in about .02% of live births [1]. The defining characteristic of this defect is a small and ineffective left ventricle, the part of the heart responsible for pumping oxygenated blood into the body. The seriousness of this defect becomes apparent in the following statistic: "Despite its low incidence relative to other congenital cardiac disorders, HLHS, if left untreated, is responsible for 25 to 40 percent of all neonatal cardiac deaths [1]."

Current treatment for hypoplastic left heart syndrome typically follows a sequence of three surgeries: the Norwood (Stage I), the Glenn (Stage II), and the Fontan (Stage III). Each procedure is an incremental step towards preparing the patient's cardiovascular system to function effectively with a single right ventricle pump.

Figure 1.2 depicts a version of the final Fontan physiology. A notable aspect of this physiology is the linking of the pulmonary artery and the vena cavas (called the *total cavopulmonary connection*). Further, the connection of the right ventricle to the ascending aorta (from the prior surgical stages) allows the right side of the heart

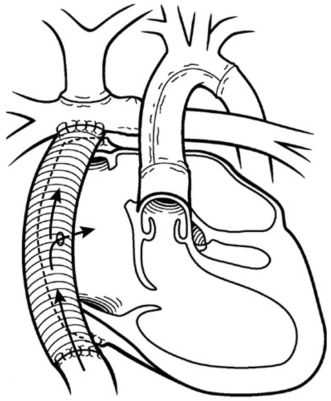

Figure 1.2 : The Fontan physiology. Adapted from [1].

to drive systemic circulation. Deviations from a normal physiology not only include local modifications to the heart (resection of the atrial septum from the Norwood procedure) but also global changes to the hemodynamics (passive bloodflow into the lungs, bypassing the heart) [1].

A variety of mathematical efforts ranging from simple algebraic models to complex three–dimensional fluid dynamics simulations have focused on characterizing the intricate hemodynamics of HLHS patients. An early set of papers by Barnea et al. studied oxygen delivery in single ventricle neonatal patients prior to any surgical procedure [35, 36]. The neonatal physiology contains several artifacts from the fetus including the foramen ovale* and the ductus arteriosus†. The foramen ovale allows for the passage of oxygenated blood to the right side of the heart, and the ductus arteriosus provides the pulmonary artery with oxygenated blood [35]. This combination effectively creates a parallel circuit for oxygen transport in the systemic and

*a small hole between the left and right atria.

†a vessel connecting the aorta and pulmonary arteries.

venous systems; Barnea et al. developed an algebraic model for this transport and studied configurations for optimal oxygen delivery.

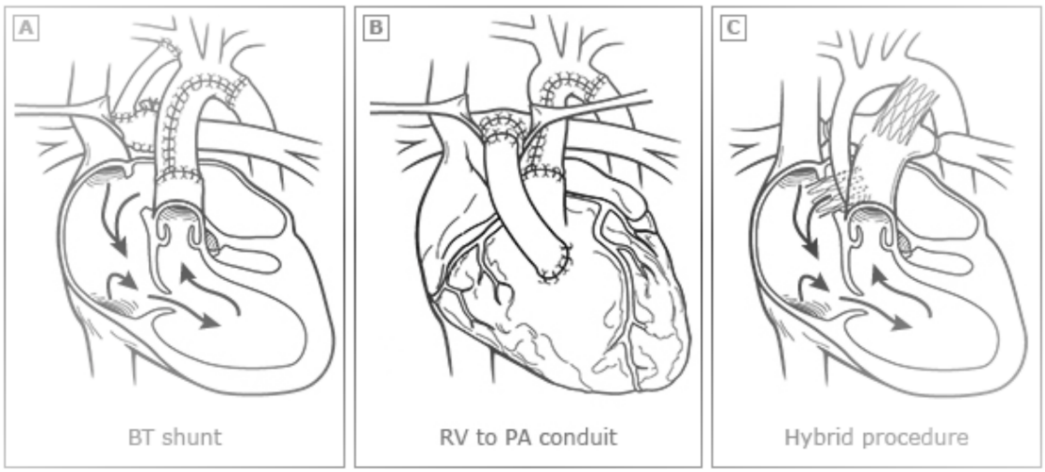

Figure 1.3 : Physiology after variants of the Stage I procedure. Adapted from [1].

Early experimental work by Sievers et al. suggested the importance fluid flow and its relation to energy loss in shunt geometries; in turn, more complex three–dimensional numerical studies attempted to quantify the impact of shunt geometries on the fluid dynamics [37]. For example, the work of Migliavacca et al. provided a numerical comparison of three shunts of varying sizes for the Stage I procedure: (1) the Blalock–Taussig shunt linking the innominate artery[‡] to the right pulmonary artery, the (2) central shunt connecting the aorta to the right pulmonary artery, and (3) the Sano shunt providing direct pathway from the right ventricle to the pulmonary artery. The three–dimensional Navier–Stokes equations, discretized with a finite volume method, provided the mathematical model for vessels in the neighborhood of the shunt. Three–dimensional geometries were determined from patient measurements;

[‡]provides blood from the aortic arch to the head.

it is unclear how the authors combined this information into one geometry. Zero–dimensional circuit models[§] determined outflow conditions for the three–dimensional geometry. The authors characterized shunt performance by analyzing flow/velocity within the shunts and pressure in the pulmonary artery [38].

A related work by Qian et al. on the Stage I surgery considered the anatomy of a single patient and investigated whether numerical simulations could be used to assess the post–operation functionality of the hemodynamic system [39]. The techniques used by the authors include a discretization of the three–dimensional Navier–Stokes equations with outflow boundary conditions provided by clinical data. CT data provided a means for constructing the patient–specific geometry, and outputs from the model of interest included velocity profiles and energy losses.

Recent papers on the Norwood Stage I procedure utilized the same mathematical technology (i.e. three-dimensional fluid flow coupled with zero–dimensional equations for boundary conditions) and considered similar model outputs. Researchers recognized the power of computational fluid dynamics in enabling the exploration of new surgical techniques without harming the patient. In this light, some recent work has analyzed new variants of the Stage I surgery like the *hybrid* Norwood operation [40, 41, 42].

Other research on Stage I operations include formalizing the notion of an *optimal* shunt geometry. Moghadam et al. emphasized the importance of sufficient oxygen delivery to the body [43]. They incorporated three–dimensional fluid dynamics models coupled to lumped parameter outflow models into an optimization algorithm for maximizing the amount of available oxygen. The parameter space for the optimization characterized the geometry of the shunt, including attachment loca-

[§]These models incorporated resistance, compliance, and inductance.

tion and shunt diameter. Despite challenges introduced by the differential equation constraints, the authors computed optimal geometries by implementing a *surrogate management framework* for solving the optimization problem.

Extensive work has focused on hemodynamics following the final operation for hypoplastic left heart syndrome patients, the Fontan procedure. Topics of interest include the quantification of energy loss due to different physiological configurations, and the characterization of hemodynamics in an "exercise" state [44, 14]. An understanding of the latter topic is particularly important because the Fontan physiology is intended to be the final configuration in which patients must survive. The complexity of the physiology necessitates careful investigation, including computational simulation, to quantify its limits.

In particular, the effects of the total cavopulmonary connection (TCPC), including impact on the energy of the fluid, has been a topic of great interest to researchers and clinicians [44, 14, 45]. Recall from Figure 1.2 that the TCPC is the connection of the inferior vena cava to the pulmonary artery [1]. Below, we discuss in more detail some of research on this topic.

Whitehead et al. developed a computational study of the TCPC for "baseline" and "exercise" conditions [44]. MRI data provided geometries for the TCPC and baseline fluid flow data for three–dimensional simulations, and scaled flow data were used to simulate excerise conditions. Their results included visualization of fluid flow, analysis of the fraction of flow to the left and right pulmonary arteries, and relation of cardiac output to power loss; they concluded power loss increases with cardiac output. Further, they defined a "normalized power loss" called the "effective resistance index" and demonstrated the resistance, as quantified by this index, increases with exercise [44].

Marsden and her collaborators performed similar computational experiments, incorporating a model for respiration, to study the impact of exercise on the TCPC junction [14]. The authors argued that vena caval flow is affected by respiration; hence, a high fidelity Fontan model should include this process. Data from two patients provided the geometries for three–dimensional flow simulations. Further, at the outlets of the pulmonary arteries, physiologically derived resistance boundary conditions were employed. The authors emphasized the importance of these conditions in producing meaningful numerical solutions. Computational results from their model agreed with clinical data obtained in a catheter lab, and as in the work of Whitehead et al., fluid flow during exercise differed substantially from at rest: during exercise and with an incoporated respiration model, the flow dissipated more energy [14].

A recent paper by Kung et al., including coauthors Migliavacca and Marsden, describes a closed–loop, zero–dimensional model for the Fontan [46]. The authors emphasized the utility of three–dimensional open–loop simulations (the modeling approach for all the papers summarized above), but acknowleDGed the challenges and inaccuracies produced by specifying artificial outlet boundary conditions. They argued that a closed loop model can better resolve the "physiological response" of the systemic circulation interacting with the Fontan physiology [46]. Another goal of their work was to create a model that can be more easily constructed with and validated by clinical data. This paper serves as a proof–of–concept of the relevance of closed–loop mathematical models linked with clinical data in describing hypoplastic left heart syndrome physiologies.

1.4 Summary of thesis

The summary of this thesis is as follows.

Chapter 2 presents a derivation of the reduced models used in this thesis following the work of Čanić and Kim. [8]. We summarize some of the mathematical properties of these models that are particularly important for numerical schemes.

Chapters 3 and 4 elaborate on two numerical methods for the reduced models: (1) a numerical method of characteristics (NMC) and (2) a discontinuous Galerkin (DG) scheme. The NMC method is collaborative work with B. Rivière, C.G. Rusin, S. Acosta, and D. Penny; the content of this section appears in the following paper [47]. The discontinous Galerkin scheme follows from the work of Sherwin et al. [4]. We first implemented their scheme directly from the paper and then modified it by using a different numerical flux and different time-stepping scheme.

In Chapter 5, we discuss different boundary conditions used in building multiscale one–dimensional/zero–dimensional hemodynamic models. These include models for the heart, organ beds, vessel junctions (also referred to as "interior nodes" in this work), as well as terminal boundary conditions and Dirichlet data for open loop vessel networks.

Chapter 6 details numerical results comparing different DG schemes (different numerical fluxes) and reduced models. The content of this section is taken from our paper [48]. Some of this work is an extension of the results presented in Hughes thesis [7]. In particular, we were interested in the effect of the axial velocity profile on the waveforms for physiological networks of vessels. Other numerical results validate software developed in MATLAB for these numerical simulations.

Chapter 7 presents an application of the modeling framework to study several Fontan physiologies. Software for approximating the equations was developed in C/C^{++} with C.G. Rusin and S. Acosta.

The content of this thesis closely follows several papers:

- S. Acosta, C. Puelz, B. Rivière, D. J. Penny, and C.G. Rusin, "Cardiovascular mechanics in the early stages of pulmonary hypertension: a computational study," *submitted* 2017.

- C. Puelz and B. Rivière, "A priori error estimates of Adams-Bashforth discontinuous Galerkin methods for scalar nonlinear conservation laws," *submitted* 2017.

- C. Puelz, B. Riviere, S. Canic, and C.G. Rusin, "Comparison of reduced models for blood flow using Runge-Kutta discontinuous Galerkin methods," *Applied Numerical Mathematics*, 115, pp. 114–141, 2017.

- S. Acosta, C. Puelz, B. Rivière, D.J. Penny, and C.G. Rusin, "Numerical method of characteristics for one-dimensional blood flow," *Journal of Computational Physics*, vol. 294, pp. 96–109, 2015.

We clearly indicate where content from these papers appears in the following chapters.

Chapter 2

Derivation of PDE models

Parts of this chapter closely follow our paper [48], especially the results in Section 2.4 on symmetrizability.

2.1 Summary of the model derivation

This section follows the derivation from Čanić and Kim for the reduced models of blood flow [8]. Let (x, r, θ) denote the cylindrical variables, i.e. the axial direction x, the radius r, and angle θ. The flow is assumed to be axisymmetric.

Assumption 2.1. *The fluid flow is axisymmetric, i.e. the angular component of the velocity is zero.*

The fluid velocity $\mathbf{u}$ is expressed in component form as $(u_x, u_r, u_\theta = 0)$, ρ is the fluid density, and ν is the kinematic viscosity. To derive a one–dimensional model of blood flow, one begins with the incompressible axisymmetric Navier–Stokes equations in cylindrical coordinates (the dependence on θ is removed):

$$
\begin{aligned}
&\frac{\partial u_x}{\partial t} + u_r \frac{\partial u_x}{\partial r} + u_x \frac{\partial u_x}{\partial x} + \frac{1}{\rho}\frac{\partial p}{\partial x} = \nu\left(\frac{\partial^2 u_x}{\partial r^2} + \frac{1}{r}\frac{\partial u_x}{\partial r} + \frac{\partial^2 u_x}{\partial x^2}\right),\\
&\frac{\partial u_r}{\partial t} + u_r \frac{\partial u_r}{\partial r} + u_x \frac{\partial u_r}{\partial x} + \frac{1}{\rho}\frac{\partial p}{\partial r} = \nu\left(\frac{\partial^2 u_r}{\partial r^2} + \frac{1}{r}\frac{\partial u_r}{\partial r} - \frac{u_r}{r^2} + \frac{\partial^2 u_r}{\partial x^2}\right),\\
&\frac{\partial u_x}{\partial x} + \frac{1}{r}\frac{\partial (r u_r)}{\partial r} = 0.
\end{aligned}
$$

The argument follows from an expression of the equations in non–dimensional form. Let the characteristic radius, length, and time be denoted R_0, L_0, and T_0 respectively. The characteristic axial velocity is $U_x := L_0/T_0$ and characteristic radial velocity is U_r. The non–dimensional radius, length, and time are $\tilde{r}$, $\tilde{x}$, and $\tilde{t}$. We use analagous notation for the non–dimensional axial velocity $\tilde{u}_x$, radial velocity $\tilde{u}_r$, and pressure $\tilde{p}$. The original variables are the characteristic values multiplied by the non–dimensional variables. An assumption on the vessel geometry that will lead to asymptotic reduction of the equations is the following:

Assumption 2.2. *The vessel is much longer than it is wide, i.e. there is a small* $\varepsilon > 0$ *so that*

$$\frac{L_0}{R_0} = \varepsilon << 1. \tag{2.1}$$

In asymptotic reduction of the equations, terms of order ε^2 in the non–dimensional form are ignored. The algebraic details are omitted; see the paper by Čanić and Kim for a complete derivation [8]. Following from the original equations, the non–dimensional equations without terms of ε^2 are:

$$\begin{aligned}
&\frac{\partial}{\partial\tilde{t}}(\tilde{r}\tilde{u}_x) + \frac{\partial}{\partial\tilde{r}}(\tilde{r}\tilde{u}_r\tilde{u}_x) + \frac{\partial}{\partial\tilde{x}}(\tilde{r}\tilde{u}_x^2) + \frac{\partial}{\partial\tilde{x}}(\tilde{r}\tilde{p}) = \frac{\nu L_0}{U_x R_0^2}\left\{\frac{\partial}{\partial\tilde{r}}\left(\tilde{r}\frac{\partial\tilde{u}_x}{\partial\tilde{r}}\right)\right\},\\
&\frac{\partial\tilde{p}}{\partial\tilde{r}} = 0,\\
&\frac{\partial}{\partial\tilde{r}}(\tilde{r}\tilde{u}_r) + \frac{\partial}{\partial\tilde{x}}(\tilde{r}\tilde{u}_x) = 0.
\end{aligned}$$

Some definitions and another assumption follow below. See Figure 2.1 for a reference.

Definition 2.1. *Let the non–dimensional distance and the original distance from the vessel center to the wall be* $\tilde{R}$ *and* R *respectively. Then, the* **average non–dimensional velocity** *and the* **average velocity** *are:*

$$\tilde{U} := \frac{1}{\tilde{R}}\int_0^{\tilde{R}} 2\tilde{u}_x\tilde{r}d\tilde{r} \quad \textit{and} \quad U := \frac{1}{R}\int_0^{R} 2u_x r dr.$$

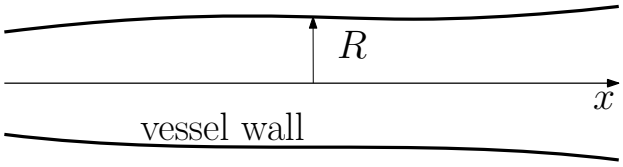

Figure 2.1 : Schematic of the vessel.

Definition 2.2. *The* **Coriolis coefficient** *is defined as:*

$$\alpha := \frac{1}{\tilde{R}^2\tilde{U}^2}\int_0^{\tilde{R}} 2\tilde{u}_x^2\tilde{r}d\tilde{r} = \frac{1}{R^2U^2}\int_0^{R} 2u_x^2 r dr.$$

The second equality in the definition holds true for the dimensional variables by algebraic manipulation. We have the following expression for the behavior of the fluid velocity at the vessel wall.

Assumption 2.3. *The boundary condition for the velocity at the vessel wall ($\tilde{r} = \tilde{R}$) is called the* **streamline condition** *and is given:*

$$(\tilde{u}_r)\,|_{\tilde{r}=\tilde{R}} = \frac{\partial\tilde{R}}{\partial\tilde{x}}\,(\tilde{u}_x)\,|_{\tilde{r}=\tilde{R}} + \frac{\partial\tilde{R}}{\partial\tilde{t}}. \tag{2.2}$$

By integrating the non–dimensional equations from 0 to $\tilde{R}$, using the above definitions, and applying the streamline condition, one obtains the non–dimensional reduced model:

$$\frac{\partial\tilde{R}^2}{\partial\tilde{t}} + \frac{\partial}{\partial\tilde{x}}(\tilde{R}^2\tilde{U}) = 0,$$
$$\frac{\partial}{\partial\tilde{t}}(\tilde{R}^2\tilde{U}) + \frac{\partial}{\partial\tilde{x}}(\alpha\tilde{R}^2\tilde{U}^2) + \tilde{R}^2\frac{\partial\tilde{p}}{\partial\tilde{x}} = \left(\frac{2\nu L_0\tilde{R}}{U_x R_0^2}\right)\frac{\partial\tilde{u}_x}{\partial\tilde{r}}|_{\tilde{r}=\tilde{R}}.$$

Definition 2.3. *Define the following dimensional variables:*

$$A := \pi R^2 \quad \textit{vessel cross–sectional area}$$

$$Q := AU \quad \textit{average fluid momentum}$$

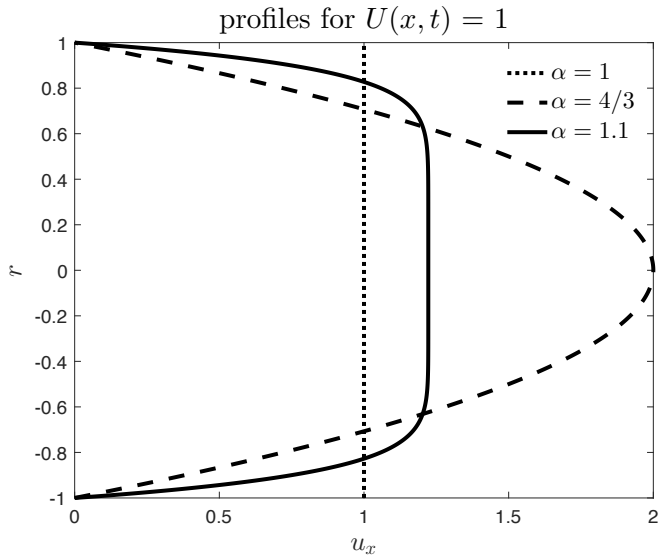

Figure 2.2 : Different choices for the axial velocity profile, including no–slip ($\alpha = 4/3, 1.1$) and flat ($\alpha = 1$).

The model transformed to these variables takes the form:

$$\frac{\partial A}{\partial t} + \frac{\partial Q}{\partial x} = 0, \tag{2.3}$$

$$\frac{\partial Q}{\partial t} + \frac{\partial}{\partial x}\left(\alpha \frac{Q^2}{A}\right) + \frac{A}{\rho}\frac{\partial p}{\partial x} = 2\pi\nu R \frac{\partial u_x}{\partial r}|_{r=R}. \tag{2.4}$$

The axial velocity profile in the source term needs to be specified. We can select several different types, as depicted in Figure 2.2. If the no–slip condition at the vessel wall is satisfied, the so–called *ad hoc* closure may be used (see e.g. [7, 8]).

Definition 2.4. *The* **ad hoc closure** *corresponding to the no–slip theory is defined as follows:*

$$u_x(x, r, t) = \frac{\zeta + 2}{\zeta} U \left[1 - \left(\frac{r}{R}\right)^{\zeta}\right].$$

An equation relating the parameter ζ and the Coriolis coefficient α is given by combining the definition of α and the ad hoc closure:

$$\zeta = \frac{2 - \alpha}{\alpha - 1}.$$

This profile choice results in the following reduced model:

$$\boxed{(A,Q)\text{–system}}$$

$$\frac{\partial A}{\partial t}+\frac{\partial Q}{\partial x}=0, \tag{2.5}$$

$$\frac{\partial Q}{\partial t}+\frac{\partial}{\partial x}\left(\alpha\frac{Q^2}{A}\right)+\frac{A}{\rho}\frac{\partial p}{\partial x}=-2\pi\nu\frac{\alpha}{\alpha-1}\frac{Q}{A}. \tag{2.6}$$

In contrast to the no–slip theory, one may select a simple flat velocity profile.

Definition 2.5. *The flat velocity profile is defined:*

$$u_x(x,r,t)=U(x,t).$$

The selection of a flat profile corresponds to inviscid flow (i.e. the kinematic viscosity of the fluid is equal to zero) since the vessel wall is not affecting the axial velocity of the fluid [8]. In this case, $\alpha=1$ and the system takes the form:

$$\boxed{\text{inviscid } (A,Q)\text{–system}}$$

$$\frac{\partial A}{\partial t}+\frac{\partial Q}{\partial x}=0, \tag{2.7}$$

$$\frac{\partial Q}{\partial t}+\frac{\partial}{\partial x}\left(\frac{Q^2}{A}\right)+\frac{A}{\rho}\frac{\partial p}{\partial x}=0. \tag{2.8}$$

The (A,U)–system follows from combining the inviscid (A,Q) model and the viscous term from no–slip (A,Q) model, using $Q=AU$, and performing some algebraic manipulations. We remark that this derivation is mathematically inconsistent since it utilizes models derived from two different axial velocity profiles and requires smoothness on the exact solution. Further, the choice for α only affects the viscous term. Regardless, this model appears quite frequently in the literature, perhaps because it may be expressed in conservative form (as we will see below) [12, 4].

$\boxed{(A,U)\text{–system}}$

$$\frac{\partial A}{\partial t} + \frac{\partial (AU)}{\partial x} = 0, \tag{2.9}$$

$$\frac{\partial U}{\partial t} + \frac{1}{2}\frac{\partial U^2}{\partial x} + \frac{1}{\rho}\frac{\partial p}{\partial x} = -2\pi\nu\frac{\alpha}{\alpha - 1}\frac{U}{A}. \tag{2.10}$$

The inviscid version of this system is:

$\boxed{\text{inviscid } (A,U)\text{–system}}$

$$\frac{\partial A}{\partial t} + \frac{\partial (AU)}{\partial x} = 0 \tag{2.11}$$

$$\frac{\partial U}{\partial t} + \frac{1}{2}\frac{\partial U^2}{\partial x} + \frac{1}{\rho}\frac{\partial p}{\partial x} = 0. \tag{2.12}$$

This section is devoted to the documentation of the mathematical features of these reduced models of blood flow. More specifically, under reasonable assumptions, one can show strict hyperbolicity of both systems, i.e. the eigenvalues of the Jacobian of the flux function are real and distinct. Furthermore, one may explicitly compute the Riemann invariants of these systems in a particular case: these functions will be used in designing numerical discretizations.

2.2 Conservative and quasilinear forms

Before continuing further in the derivations, one must close the hyperbolic systems with a *state equation*, relating the pressure and the cross-sectional area, of the form

$$p(A) = p_0 + \psi(A; A_0, \beta), \tag{2.13}$$

where p_0 is the pressure of blood at rest in the vessel. We assume p_0 to be constant. The function ψ contains two parameters; β depends on the material properties of the vessels and A_0 is the cross–sectional area when the fluid pressure is equal to p_0. Both

β and A_0 may be functions of space, but for simplicity of presentation in this section, we assume they are constant. Further, the function ψ satisfies the following (see e.g. [49], p. 353):

$$\psi' = \frac{d\psi}{dA} > 0 \text{ for } A > 0 \quad \text{and} \quad \psi(A_0; A_0, \beta) = 0. \tag{2.14}$$

Lastly, as in [9], define:

$$\Psi(A) = \int_{A_0}^{A} \psi(\xi; A_0, \beta) d\xi. \tag{2.15}$$

For some arbitrary scalar–valued function $f = f(\mathbf{U})$ and vector–valued function $\mathbf{F} = \mathbf{F}(\mathbf{U})$, define

$$\mathbf{F}_{\mathbf{U}} = \text{ the Jacobian of } \mathbf{F} \text{ with respect to the variables } \mathbf{U}, \tag{2.16}$$

$$f_{\mathbf{U}} = \text{ the gradient of } f \text{ (as a row vector) with respect to the variables } \mathbf{U}. \tag{2.17}$$

With this notation, the (A, Q)–system is expressed in conservative form as:

$$\underbrace{\frac{\partial}{\partial t}\begin{bmatrix} A \\ Q \end{bmatrix}}_{:=\partial\hat{\mathbf{U}}/\partial t} + \underbrace{\frac{\partial}{\partial x}\begin{bmatrix} Q \\ \alpha\frac{Q^2}{A} + \frac{1}{\rho}(A\psi - \Psi) \end{bmatrix}}_{:=\partial\hat{\mathbf{F}}/\partial x} = \underbrace{\begin{bmatrix} 0 \\ -2\pi\nu\frac{\alpha}{\alpha-1}\frac{Q}{A} \end{bmatrix}}_{:=\hat{\mathbf{S}}}. \tag{2.18}$$

For these manipulations, we use applications of Leibniz's rule, i.e. $\frac{\partial}{\partial x}\Psi = \psi(A; A_0, \beta)\frac{\partial A}{\partial x}$ and $\frac{\partial}{\partial A}\Psi = \psi(A; A_0, \beta)$. The quasilinear form is:

$$\frac{\partial}{\partial t}\begin{bmatrix} A \\ Q \end{bmatrix} + \underbrace{\begin{bmatrix} 0 & 1 \\ A\frac{\psi'}{\rho} - \alpha\frac{Q^2}{A^2} & 2\alpha\frac{Q}{A} \end{bmatrix}}_{:=\hat{\mathbf{F}}_{\hat{\mathbf{U}}}} \underbrace{\frac{\partial}{\partial x}\begin{bmatrix} A \\ Q \end{bmatrix}}_{:=\partial\hat{\mathbf{U}}/\partial x} = \begin{bmatrix} 0 \\ -2\pi\nu\frac{\alpha}{\alpha-1}\frac{Q}{A} \end{bmatrix}. \tag{2.19}$$

One can similarly express the (A, U)–system in conservative and quasilinear form with flux $\tilde{\mathbf{F}}$ and source $\tilde{\mathbf{S}}$. The resulting conservative form is

$$\underbrace{\frac{\partial}{\partial t}\begin{bmatrix} A \\ U \end{bmatrix}}_{:=\partial\tilde{\mathbf{U}}/\partial t} + \underbrace{\frac{\partial}{\partial x}\begin{bmatrix} AU \\ \frac{U^2}{2} + \frac{\psi}{\rho} \end{bmatrix}}_{:=\tilde{\mathbf{F}}} = \underbrace{\begin{bmatrix} 0 \\ -2\pi\nu\frac{\alpha}{\alpha-1}\frac{U}{A} \end{bmatrix}}_{:=\tilde{\mathbf{S}}}, \tag{2.20}$$

and quasilinear form is

$$\frac{\partial}{\partial t}\begin{bmatrix} A \\ U \end{bmatrix} + \underbrace{\begin{bmatrix} U & A \\ \frac{\psi'}{\rho} & U \end{bmatrix}}_{:=\tilde{\mathbf{F}}_{\tilde{\mathbf{U}}}} \underbrace{\frac{\partial}{\partial x}\begin{bmatrix} A \\ U \end{bmatrix}}_{:=\partial\tilde{\mathbf{U}}/\partial x} = \begin{bmatrix} 0 \\ -2\pi\nu\frac{\alpha}{\alpha-1}\frac{U}{A} \end{bmatrix}. \tag{2.21}$$

2.3 Eigenvalues and Riemann invariants

The eigenvalues of the Jacobian $\hat{\mathbf{F}}_{\hat{\mathbf{U}}}$ for (A, Q)–system are

$$\hat{\lambda}_1 = \alpha\frac{Q}{A} + \sqrt{(\alpha^2-\alpha)\frac{Q^2}{A^2} + A\frac{\psi'}{\rho}}, \quad \hat{\lambda}_2 = \alpha\frac{Q}{A} - \sqrt{(\alpha^2-\alpha)\frac{Q^2}{A^2} + A\frac{\psi'}{\rho}}.$$

Similarly, the eigenvalues for the Jacobian $\tilde{\mathbf{F}}_{\tilde{\mathbf{U}}}$ of the (A, U)–system are

$$\tilde{\lambda}_1 = U + \sqrt{A\frac{\psi'}{\rho}} := U + c, \quad \tilde{\lambda}_2 = U - \sqrt{A\frac{\psi'}{\rho}} := U - c,$$

where the function c is

$$c(A) := \sqrt{A\frac{\psi'}{\rho}}. \tag{2.22}$$

The physical meaning of the function $c(A)$ becomes more clear if one considers a linearized version of the inviscid (A, Q)–system, where we assume A does not deviate far from A_0 and the inertial part of the momentum equation, $\frac{\partial}{\partial x}\left(\frac{Q^2}{A}\right)$, is negligible:

$$\frac{\partial A}{\partial t} + \frac{\partial Q}{\partial x} = 0, \tag{2.23}$$

$$\frac{\partial Q}{\partial t} + \frac{A_0}{\rho}\frac{\partial p}{\partial x} = 0. \tag{2.24}$$

Differentiating the state equation $p = p_0 + \psi(A)$, for $A \approx A_0$, one obtains:

$$\frac{\partial p}{\partial t} = \psi'(A)\frac{\partial A}{\partial t} \approx \psi'(A_0)\frac{\partial A}{\partial t}. \tag{2.25}$$

Substituting (2.25) into the mass conservation equation (2.23) results in a system for the pressure p and momentum Q:

$$\frac{\partial p}{\partial t} + \psi'(A_0)\frac{\partial Q}{\partial x} = 0, \tag{2.26}$$

$$\frac{\partial Q}{\partial t} + \frac{A_0}{\rho}\frac{\partial p}{\partial x} = 0. \tag{2.27}$$

Differentiating (2.26) with respect to time and substituting in (2.27) yields a wave equation for the pressure p:

$$\frac{\partial^2 p}{\partial t^2} = c(A_0)^2 \frac{\partial^2 p}{\partial x^2}. \tag{2.28}$$

These manipulations demonstrate the pressure waves propagate with a speed close to $c(A_0)$, when A is close to A_0.

In the case of blood flow models, with physiological parameters, one has

$$U << c.$$

This implies the (A, U)–system is strictly hyperbolic and $\tilde{\lambda}_1 > 0$, $\tilde{\lambda}_2 < 0$. In practice, the term $c(A)$ is dominant, so for α close to 1, the (A, Q)–system is also strictly hyperbolic with a positive and a negative eigenvalue.

Below we derive and discuss the Riemann invariants. For a general, two–equation hyperbolic system given as

$$\frac{\partial \mathbf{U}}{\partial t} + \frac{\partial}{\partial x}\mathbf{F}(\mathbf{U}) = \mathbf{S}(\mathbf{U}), \tag{2.29}$$

one has the following definition.

Definition 2.6. *The* **Riemann invariants** W_i $(i = 1, 2)$ *are functions with gradients parallel to the left eigenvectors of* $\mathbf{F}_\mathbf{U}$.

More explicitly, consider functions W_i^* and W_i $(i = 1, 2)$ whose gradients $(W_i^*)_{\mathbf{U}}$ and $(W_i)_{\mathbf{U}}$ are parallel to the left eigenvectors of $\mathbf{F}_{\mathbf{U}}$. These functions are Riemann invariants by definition, and further, one can choose constants k_i satisfying $(k_i)_{\mathbf{U}} = 0$ $(k = 1, 2)$ so that:

$$W_1(\mathbf{U}(x,t)) = W_1^*(\mathbf{U}(x,t)) + k_1(x,t),$$
$$W_2(\mathbf{U}(x,t)) = W_2^*(\mathbf{U}(x,t)) + k_2(x,t).$$

If λ_i, $i = 1, 2$ are the eigenvalues of $\mathbf{F}_{\mathbf{U}}$, the one may compute the following, using $(W_i^*)_{\mathbf{U}} = (W_i)_{\mathbf{U}}$:

$$\frac{\partial W_i}{\partial t} = (W_i^*)_{\mathbf{U}}^T \frac{\partial \mathbf{U}}{\partial t} + \frac{\partial k_i}{\partial t} = (W_i)_{\mathbf{U}}^T \frac{\partial \mathbf{U}}{\partial t} + \frac{\partial k_i}{\partial t},$$

and

$$\begin{aligned}\lambda_i \frac{\partial W_i}{\partial x} &= \lambda_i (W_i^*)_{\mathbf{U}}^T \frac{\partial \mathbf{U}}{\partial x} + \lambda_i \frac{\partial k_i}{\partial x} \\ &= \lambda_i (W_i)_{\mathbf{U}}^T \frac{\partial \mathbf{U}}{\partial x} + \lambda_i \frac{\partial k_i}{\partial x} \\ &= (W_i)_{\mathbf{U}}^T \mathbf{F}_{\mathbf{U}} \frac{\partial \mathbf{U}}{\partial x} + \lambda_i \frac{\partial k_i}{\partial x},\end{aligned}$$

where the second equality follows from the definition of the Riemann invariants. Summing these equations and using the quasilinear form of (2.29), one can see that the invariants satisfy the diagonal (but still nonlinear) system:

$$\frac{\partial W_1}{\partial t} + \lambda_1 \frac{\partial W_1}{\partial x} = (W_1)_{\mathbf{U}}^T \mathbf{S}(\mathbf{U}) + \frac{\partial k_1}{\partial t} + \lambda_1 \frac{\partial k_1}{\partial x}, \tag{2.30}$$
$$\frac{\partial W_2}{\partial t} + \lambda_2 \frac{\partial W_2}{\partial x} = (W_2)_{\mathbf{U}}^T \mathbf{S}(\mathbf{U}) + \frac{\partial k_2}{\partial t} + \lambda_2 \frac{\partial k_2}{\partial x}. \tag{2.31}$$

For the inviscid (A, Q)–system, we consider the following form for the function ψ the state equation (which we use for the rest of the thesis):

$$\psi(A; A_0, \beta) := \beta(A^{1/2} - A_0^{1/2}).$$

The Riemann invariants may be computed analytically:

$$\hat{W}_1 = \frac{Q}{A} + 4c + k_1, \quad \hat{W}_2 = \frac{Q}{A} - 4c + k_2.$$

Similarly for the (A, U)–system, the invariants are:

$$\hat{W}_1 = U + 4c + k_1, \quad \hat{W}_2 = U - 4c + k_2.$$

Typically the functions of integration k_i $(i = 1, 2)$ are set to zero, but for particular reflecting boundary conditions or for characteristics–based approximations of the Riemann invariants, one would like the invariants to vanish when the physical variables satisfy $(A, Q) = (A_0, 0)$ or $(A, U) = (A_0, 0)$. These ideas are made more clear by context, later in the thesis. In this case, set

$$c_0 = c(A_0), \quad k_1 = -4c_0, \quad k_2 = 4c_0.$$

2.4 Symmetrizability

Consider an invertible transformation $\mathbf{V} : S \subset \mathbb{R}^2 \to \mathbf{V}(S)$ expressed in the notation

$$\mathbf{U} \to \mathbf{V}(\mathbf{U}) \quad \text{for each } \mathbf{U} \in S.$$

Let the transformation $\mathbf{U} : \mathbf{V}(S) \subset \mathbb{R}^2 \to S$ be in the inverse of $\mathbf{V}$, i.e.

$$\mathbf{V} \to \mathbf{U}(\mathbf{V}) \quad \text{for each } \mathbf{V} \in \mathbf{V}(S).$$

Since the composition

$$(\mathbf{U} \circ \mathbf{V}) : S \to S$$

defines the identity map on S, differentiating the composition provides the relation between the Jacobians of $\mathbf{U}$ and $\mathbf{V}$:

$$\mathbf{U}_\mathbf{V} \mathbf{V}_\mathbf{U} = \mathbf{I},$$

where $\mathbf{I}$ is the 2×2 identity matrix. With the notation $\mathbf{U}_{\mathbf{V}}^{-1}$ denoting the matrix inverse of $\mathbf{U}_{\mathbf{V}}$, one arrives at the fact:

$$\mathbf{U}_{\mathbf{V}}^{-1} = \mathbf{V}_{\mathbf{U}}.$$

Definition 2.7. *Consider the hyperbolic system (2.29) with zero source term. The system is* ***symmetrizable*** *provided there exists a map* $\mathbf{U} = \mathbf{U}(\mathbf{V})$ *satisfying*

1. *The matrix* $\mathbf{U}_{\mathbf{V}}$*, the Jacobian of the transformation* $\mathbf{V} \to \mathbf{U}(\mathbf{V})$*, is symmetric positive definite (SPD).*

2. *The matrix* $\mathbf{F}_{\mathbf{U}}\mathbf{U}_{\mathbf{V}}$ *is symmetric.*

The variables $\mathbf{V}$ *are called the* ***entropy variables****. If the such a map exists then the above system takes the form:*

$$\mathbf{U}_{\mathbf{V}}\frac{\partial \mathbf{V}}{\partial t} + \mathbf{F}_{\mathbf{U}}\mathbf{U}_{\mathbf{V}}\frac{\partial \mathbf{V}}{\partial x} = \mathbf{0}.$$

In analyzing Euler's equations for gas dynamics, Harten constructively demonstrated a general result that symmetrizability is equivalent to the existence of an *entropy function*, defined below [50].

Definition 2.8. *A scalar–valued function* $E = E(\mathbf{U})$ *is called an* **entropy function** *for (2.29) provided*

1. *There exists some scalar–valued function* $f = f(\mathbf{U})$ *so that* E *satifies:*

$$E_{\mathbf{U}}\mathbf{F}_{\mathbf{U}} = f_{\mathbf{U}}. \tag{2.32}$$

Recall

$$E_{\mathbf{U}} = \begin{bmatrix} \frac{\partial E}{\partial U_1} & \frac{\partial E}{\partial U_2} \end{bmatrix} \quad \textit{and} \quad f_{\mathbf{U}} = \begin{bmatrix} \frac{\partial f}{\partial U_1} & \frac{\partial f}{\partial U_2} \end{bmatrix} \tag{2.33}$$

are the gradients of the functions E *and* f *respectively.*

2. *The function E is a strictly convex function of $\mathbf{U}$. Supposing E is smooth enough this is true if and only if its Hessian matrix is positive definite.*

The function f is called the *entropy flux* since it corresponds to a flux function for a nonlinear, *scalar* conservation law. To see this, premultiply (2.29) in quasilinear form by $E_{\mathbf{U}}$ to obtain

$$\frac{\partial E}{\partial t} + \frac{\partial}{\partial x} f(E) = 0. \tag{2.34}$$

The following section is taken from our paper [48]. The notion of *symmetrizability* for systems of conservation laws is used to simplify the numerical analysis; see e.g. [33, 34] for an application of this idea to study Runge–Kutta discontinuous Galerkin approximations. Further, it is a reasonable assumption for systems modeling physical phenomena. One can show under reasonable assumptions that an entropy function derived from the energy of the system symmetrizes the equations for reduced blood flow. The entropy for the inviscid models was derived by Formaggia et al. [9]:

$$\boxed{\text{inviscid } (A,Q)\text{–system}} \quad \hat{\mathcal{E}}(x,t) = \frac{1}{2}\rho\frac{Q^2}{A} + \int_{A_0}^{A} \psi(\xi; A_0, \beta) d\xi, \tag{2.35}$$

$$\boxed{\text{inviscid } (A,U)\text{–system}} \quad \tilde{\mathcal{E}}(x,t) = \frac{1}{2}\rho A U^2 + \int_{A_0}^{A} \psi(\xi; A_0, \beta) d\xi. \tag{2.36}$$

Lemma 2.1. *If $A(x,t) > \delta > 0$ for $(x,t) \in [0,L] \times [0,T]$, the inviscid (A,Q) system is symmetrizable.*

Proof. With the physical variables $\mathbf{U} = [A,Q]^T$, following Harten's work [50], the entropy variables $\mathbf{V} = [V_1, V_2]^T$ are:

$$V_1(\mathbf{U}) = \frac{\partial \hat{\mathcal{E}}}{\partial A} = -\frac{\rho}{2}\frac{Q^2}{A^2} + \psi(A), \tag{2.37}$$

$$V_2(\mathbf{U}) = \frac{\partial \hat{\mathcal{E}}}{\partial Q} = \rho\frac{Q}{A}. \tag{2.38}$$

The definition of the entropy variables defines a transformation $\mathbf{U} \to \mathbf{V}(\mathbf{U})$. The inverse of this transformation, denoted $\mathbf{U}(\mathbf{V})$, will symmetrize the equations. Recall the notation and assumption on ψ:

$$\psi' := \frac{d\psi}{dA} > 0 \text{ for } A > 0. \tag{2.39}$$

So the function ψ' is positive since $A > \delta > 0$. Here is the Jacobian of $\mathbf{V}(\mathbf{U})$:

$$\mathbf{U}_{\mathbf{V}}^{-1} = \mathbf{V}_{\mathbf{U}} = \begin{bmatrix} \rho\frac{Q^2}{A^3} + \psi' & -\rho\frac{Q}{A^2} \\ -\rho\frac{Q}{A^2} & \frac{\rho}{A} \end{bmatrix}. \tag{2.40}$$

Its determinant and trace are:

$$\det \mathbf{V}_{\mathbf{U}} = \frac{\rho}{A}\psi', \tag{2.41}$$

$$\text{tr } \mathbf{V}_{\mathbf{U}} = \rho\frac{Q^2}{A^3} + \psi' + \frac{\rho}{A}. \tag{2.42}$$

It is clear that the determinant and trace are both positive, proving that $\mathbf{V}_{\mathbf{U}}$ is SPD. Thus, the inverse $\mathbf{U}_{\mathbf{V}}$ is also SPD. Lastly, using the form of $\mathbf{F}_{\mathbf{U}}$ given in (2.19) with $\alpha = 1$, one sees that

$$\mathbf{F}_{\mathbf{U}}\mathbf{U}_{\mathbf{V}} = \frac{A}{\rho\psi'} \begin{bmatrix} 0 & 1 \\ \frac{A}{\rho}\psi' - \frac{Q^2}{A^2} & 2\frac{Q}{A} \end{bmatrix} \begin{bmatrix} \frac{\rho}{A} & \rho\frac{Q}{A^2} \\ \rho\frac{Q}{A^2} & \rho\frac{Q^2}{A^3} + \psi' \end{bmatrix} \tag{2.43}$$

$$= \frac{A}{\rho\psi'} \begin{bmatrix} \rho\frac{Q}{A^2} & \rho\frac{Q^2}{A^3} + \psi' \\ \rho\frac{Q^2}{A^3} + \psi' & 3\frac{Q}{A}\psi' + \rho\frac{Q^3}{A^4} \end{bmatrix}, \tag{2.44}$$

verifying the matrix is symmetric. □

Lemma 2.2. *If $A(x,t) > \delta > 0$ and $|U(x,t)| < c(A(x,t))$ for $(x,t) \in [0,L] \times [0,T]$, the inviscid (A,U) system is symmetrizable.*

Proof. The proof follows closely the proof of the previous lemma. Let $\mathbf{U} = [A, U]^T$. From the entropy function given above, define the transformation as

$$V_1(\mathbf{U}) = \frac{\partial \tilde{\mathcal{E}}}{\partial A} = \frac{\rho}{2}U^2 + \psi(A), \tag{2.45}$$

$$V_2(\mathbf{U}) = \frac{\partial \tilde{\mathcal{E}}}{\partial U} = \rho A U. \tag{2.46}$$

The Jacobian is

$$\mathbf{V}_\mathbf{U} = \begin{bmatrix} \psi' & \rho U \\ \rho U & \rho A \end{bmatrix}. \tag{2.47}$$

Its determinant and trace are

$$\det \mathbf{V}_\mathbf{U} = \rho^2 \left(\frac{A}{\rho}\psi' - U^2 \right) = \rho^2(c^2 - U^2), \tag{2.48}$$

$$\text{tr } \mathbf{V}_\mathbf{U} = \psi' + \rho A, \tag{2.49}$$

where $c = c(A)$ is the speed appearing in the formula for the convective velocity of the Riemann invariants. The additional assumption that $|U| < c$ implies the determinant is positive. Since the trace is positive, $\mathbf{V}_\mathbf{U}$ is SPD, so its inverse $\mathbf{U}_\mathbf{V}$ is SPD. Lastly, symmetry is verified using $\mathbf{F}_\mathbf{U}$ from (2.21):

$$\mathbf{F}_\mathbf{U}\mathbf{U}_\mathbf{V} = \frac{1}{\rho^2(c^2 - U^2)} \begin{bmatrix} U & A \\ \frac{\psi'}{\rho} & U \end{bmatrix} \begin{bmatrix} \rho A & -\rho U \\ -\rho U & \psi' \end{bmatrix} \tag{2.50}$$

$$= \frac{1}{\rho^2(c^2 - U^2)} \begin{bmatrix} 0 & -\rho U^2 + A\psi' \\ -\rho U^2 + A\psi' & 0 \end{bmatrix} \tag{2.51}$$

□

Notice this perspective theoretically differentiates the (A, Q) and (A, U) models, i.e. verification of symmetrizability for the (A, U) model requires the additional assumption $|U| < c(A)$ rendering the (A, U) system strictly hyperbolic. To comment

briefly on numerical analysis with symmetrizability: the authors in [33, 34] estimate the error in a norm depending on $\mathbf{U_V}$; smoothness of the exact solutions and the SPD assumption allow one to conclude that this norm is equivalent to the L^2 norm used in the estimate. Further, the numerical flux must be in the class of *generalized E–fluxes*, and the local–Lax Friedrichs flux falls in this class.

Chapter 3

Discontinuous Galerkin methods

3.1 Formulation for scalar conservation laws

The content of this section is taken from our paper [51]. We consider approximating smooth solutions to the following nonlinear partial differential equation posed with initial conditions:

$$\frac{\partial u}{\partial t} + \frac{\partial}{\partial x} f(u) = s(u), \quad \text{in } \mathbb{R} \times (0, T], \tag{3.1}$$

$$u = u_0, \quad \text{in } \mathbb{R} \times \{0\}, \tag{3.2}$$

where $u : \mathbb{R} \times [0, T] \to \mathbb{R}$ and $f, s : \mathbb{R} \to \mathbb{R}$. The function s is assumed to be Lipschitz. As is typical for the numerical analysis of such problems [32, 52], we do not consider boundary conditions, and instead assume the solution has compact support in the interval $[0, 1]$.

We define notation relevant for the spatial discretization of (3.1)–(3.2) by the discontinuous Galerkin method. To do this, we make a similar technical modification to the flux function as in [32]. If the initial condition u_0 takes values within some open set Ω, then locally in time the solution to (3.1)–(3.2) also takes values in Ω [53]. We assume the flux function $f \in C^3(\mathbb{R})$ vanishes outside of Ω so derivatives up to third order are uniformly bounded, i.e. there exists some constant C depending only on f and its derivatives satisfying:

$$|f^{(\gamma)}(v)| \leq C, \quad \forall v \in \mathbb{R}, \quad \gamma = 1, 2, 3. \tag{3.3}$$

Let the collection of intervals $(I_j)_{j=0}^N$ be a uniform partition of the interval $[0,1]$, with $I_j = [x_j, x_{j+1}]$ of size h. Let $\mathbb{P}^k(I_j)$ denote the space of polynomials of degree k on the interval I_j. The approximation space is

$$\mathbb{V}_h = \{\phi_h : [0,1] \to \mathbb{R} \text{ s.t. } \phi_h|_{I_j} \in \mathbb{P}^k(I_j), \quad \forall j = 0, \ldots, N\}. \tag{3.4}$$

The space $L^2(0,1)$ is the standard L^2 space; let $(\cdot,\cdot)$ denote the L^2 inner-product over Ω, with associated norm $\|\cdot\|$. Let Π_h be the L^2 projection into $\mathbb{V}_h$:

$$(\Pi_h v, \phi_h) = (v, \phi_h), \quad \forall \phi_h \in \mathbb{V}_h, \quad \forall v \in L^2(0,1). \tag{3.5}$$

Define the notation for traces of a function $\phi : [0,1] \to \mathbb{R}$ to the boundaries of the intervals:

$$\phi^{\pm}|_{x_j} = \lim_{\varepsilon \to 0,\, \varepsilon > 0} \phi(x_j \pm \varepsilon), \quad 1 \le j \le N, \tag{3.6}$$

$$\phi^{+}|_{x_0} = \lim_{\varepsilon \to 0,\, \varepsilon > 0} \phi(x_0 + \varepsilon), \tag{3.7}$$

$$\phi^{-}|_{x_{N+1}} = \lim_{\varepsilon \to 0,\, \varepsilon > 0} \phi(x_{N+1} - \varepsilon). \tag{3.8}$$

The standard notation for jumps and averages is defined as follows:

$$[\phi]|_{x_j} = \phi^{-}|_{x_j} - \phi^{+}|_{x_j}, \quad 1 \le j \le N, \tag{3.9}$$

$$\{\phi\}|_{x_j} = \frac{1}{2}(\phi^{-}|_{x_j} + \phi^{+}|_{x_j}), \quad 1 \le j \le N. \tag{3.10}$$

Let $\hat{f}$ denote the numerical flux, that is assumed to be Lipschitz continuous and consistent.

Assumption 3.1. *There is a constant $C_L > 0$ such that for any p, q, u, $v \in \mathbb{R}$:*

$$|\hat{f}(p,q) - \hat{f}(u,v)| \le C_L \left(|p-u| + |q-v|\right), \tag{3.11}$$

and

$$\hat{f}(v, v) = f(v), \quad \forall v \in \mathbb{R}. \tag{3.12}$$

We also assume that $\hat{f}$ belongs to the class of E–fluxes [54].

Assumption 3.2. *The numerical flux $\hat{f}$ is an E–flux, which means it satisfies, for all w between v^- and v^+,*

$$\left(\hat{f}(v^-, v^+) - f(w)\right)[v] \geq 0. \tag{3.13}$$

An example of a numerical flux that satisfies Assumption 3.1 and Assumption 3.2 is the local Lax-Friedrichs flux, $\hat{f}_{LF}$, defined by:

$$\hat{f}_{LF}(v^-, v^+) = \{f(v)\} + \frac{1}{2} J(v^-, v^+)[v], \tag{3.14}$$

with

$$J(v^-, v^+) = \max_{\min(v^-, v^+) \leq w \leq \max(v^-, v^+)} |f'(w)|. \tag{3.15}$$

Finally, we define a discrete function α at each interior node and the boundary nodes x_0 and x_{N+1}. The fact that α is nonnegative and uniformly bounded is a key ingredient in the error analysis. For $1 \leq j \leq N$ we have the following definition

$$\alpha(v)|_{x_j} = \begin{cases} [v]|_{x_j}^{-1} \left(\hat{f}(v^-, v^+) - f(\{v\})\right)|_{x_j}, & \text{if } [v]|_{x_j} \neq 0, \\ \frac{1}{2} \left|f'(\{v\}|_{x_j})\right|, & \text{if } [v]|_{x_j} = 0. \end{cases} \tag{3.16}$$

At the boundary, α is defined analogously:

$$\alpha(v)|_{x_0} = \begin{cases} -(v^+|_{x_0})^{-1}\left(\hat{f}(0,v^+) - f(\frac{1}{2}v^+)\right)|_{x_0}, & \text{if } v^+|_{x_0} \neq 0, \\ \frac{1}{2}\left|f'(0)\right|, & \text{if } v^+|_{x_0} = 0. \end{cases} \tag{3.17}$$

$$\alpha(v)|_{x_{N+1}} = \begin{cases} (v^-|_{x_{N+1}})^{-1}\left(\hat{f}(v^-,0) - f(\frac{1}{2}v^-)\right)|_{x_{N+1}}, & \text{if } v^-|_{x_{N+1}} \neq 0, \\ \frac{1}{2}\left|f'(0)\right|, & \text{if } v^-|_{x_{N+1}} = 0. \end{cases} \tag{3.18}$$

We remark that the form of the term $f(\frac{1}{2}v^+)|_{x_0}$ in $\alpha(v)|_{x_0}$, and similarly at x_{N+1}, is important in the analysis on the boundary of the domain $[0,1]$.

Lemma 3.1. *There exist constants C_α, C_0 and C_1 such that*

$$0 \leq \alpha(v) \leq C_\alpha, \quad \forall (v^-, v^+) \in \mathbb{R}^2, \tag{3.19}$$

$$\frac{1}{2}\Big|f'(\{v\})\Big| \leq \alpha(v) + C_0\Big|[v]\Big|, \quad \forall (v^-, v^+) \in \mathbb{R}^2, \tag{3.20}$$

$$\frac{1}{8}f''(\{v\})[v] \leq \alpha(v) + C_1[v]^2, \quad \forall (v^-, v^+) \in \mathbb{R}^2. \tag{3.21}$$

The constants C_0 and C_1 depend on the derivatives of f.

The proof of Lemma 3.1 follows the one in [32]; the definition for α slightly differs from the one given in [32] so that it is suitable for the error analysis of the Adams–Bashforth scheme.

An additional assumption is made for the numerical flux.

Assumption 3.3. *There is a constant $C > 0$ such that for any $v_h \in \mathbb{V}_h$ and $v \in \mathcal{C}(0,1)$ with $v(0) = v(1) = 0$:*

$$|\alpha(v_h)|_{x_j} - \alpha(v)|_{x_j}| \leq C\|v_h - v\|_\infty, \quad \forall\, 0 \leq j \leq N+1. \tag{3.22}$$

Remark 3.1. *Assumption 3.3 is used in the error analysis for the Adams–Bashforth scheme. It is easy to check that the local Lax-Friedrichs flux defined by* (3.14) *satisfies* (3.22)*. We provide a sketch of the proof below.*

Proof. Assume $\hat{f}$ is the local Lax–Friedrichs flux. We first consider the case $[v_h]|_{x_j} \neq 0$ and $1 \leq j \leq N$. We omit x_j in most of the notation below for simplicity. By definition and Taylor expansions, for some ζ_1 and ζ_2 in between v_h^- and v_h^+, one has:

$$\begin{aligned}
\alpha(v_h) &= [v_h]^{-1}\left(\frac{1}{2}(f(v_h^-)+f(v_h^+)) + \frac{1}{2}J(v_h^-,v_h^+)[v_h] - f(\{v_h\})\right) \\
&= [v_h]^{-1}\left(\frac{1}{2}(f(v_h^-)-f(\{v_h\})) + \frac{1}{2}(f(v_h^+)-f(\{v_h\})) + \frac{1}{2}J(v_h^-,v_h^+)[v_h]\right) \\
&= [v_h]^{-1}\left(\frac{1}{4}f'(\zeta_1)[v_h] - \frac{1}{4}f'(\zeta_2)[v_h] + \frac{1}{2}J(v_h^-,v_h^+)[v_h]\right) \\
&= \frac{1}{4}f'(\zeta_1) - \frac{1}{4}f'(\zeta_2) + \frac{1}{2}J(v_h^-,v_h^+).
\end{aligned}$$

Note that by the extreme value theorem, there exists some ζ_3 between v_h^- and v_h^+ so that

$$J(v_h^-,v_h^+) = |f'(\zeta_3)|.$$

By definition, since $[v]|_{x_j} = 0$ one has $\alpha(v) = \frac{1}{2}|f'(v)|$ and:

$$\begin{aligned}
|\alpha(v_h)-\alpha(v)| &= \left|\frac{1}{4}f'(\zeta_1) - \frac{1}{4}f'(\zeta_2) + \frac{1}{2}|f'(\zeta_3)| - \frac{1}{2}|f'(v)|\right| \\
&= \left|\frac{1}{4}(f'(\zeta_1)-f'(v)) - \frac{1}{4}(f'(\zeta_2)-f'(v)) + \frac{1}{2}|f'(\zeta_3)| - \frac{1}{2}|f'(v)|\right| \\
&\leq \frac{1}{4}\Big|f'(\zeta_1)-f'(v)\Big| + \frac{1}{4}\Big|f'(\zeta_2)-f'(v)\Big| + \frac{1}{2}\Big||f'(\zeta_3)| - \frac{1}{2}|f'(v)|\Big| \\
&\leq C\|v_h - v\|_\infty.
\end{aligned}$$

If $[v_h]|_{x_j} = 0$, then by definition $\alpha(v_h) = \frac{1}{2}|f'(v_h)|$ and:

$$|\alpha(v_h)-\alpha(v)| = \left|\frac{1}{2}|f'(v_h)| - \frac{1}{2}|f'(v)|\right| \leq C\|v_h - v\|_\infty.$$

Now we consider the left boundary x_0. First assume $-v_h^+|_{x_0} \neq 0$. As before, there exist ζ_4, ζ_5 in between 0 and $v_h^+|_{x_0}$ so that:

$$\begin{aligned}
\alpha(v_h)|_{x_0} &= -(v_h^+|_{x_0})^{-1}\left(\frac{1}{2}(f(0)+f(v_h^+|_{x_0}))+\frac{1}{2}J(0,v_h^+)(-v_h^+|_{x_0})-f(\frac{1}{2}v_h^+)|_{x_0}\right)\\
&= -(v_h^+|_{x_0})^{-1}\left(\frac{1}{2}(f(0)-f(\frac{1}{2}v_h^+|_{x_0}))+\frac{1}{2}(f(v_h^+)-f(\frac{1}{2}v_h^+|_{x_0}))+\frac{1}{2}J(0,v_h^+)(-v_h^+|_{x_0})\right)\\
&= -(v_h^+|_{x_0})^{-1}\left(\frac{1}{4}f'(\zeta_4)(-v_h^+|_{x_0})-\frac{1}{4}f'(\zeta_5)(-v_h^+|_{x_0})+\frac{1}{2}J(0,v_h^+)(-v_h^+|_{x_0})\right)\\
&= \frac{1}{4}f'(\zeta_4)-\frac{1}{4}f'(\zeta_5)+\frac{1}{2}J(0,v_h^+).
\end{aligned}$$

By the extreme value theorem, there exists ζ_6 in between 0 and $v_h^+|_{x_0}$ so that

$$\alpha(v_h)|_{x_0} = \frac{1}{4}f'(\zeta_4)-\frac{1}{4}f'(\zeta_5)+\frac{1}{2}|f'(\zeta_6)|.$$

Since $v(x_0=0)=0$, $\alpha(v)|_{x_0}=\frac{1}{2}|f'(0)|$. We can again easily conclude using Taylor expansions

$$|\alpha(v_h)|_{x_0}-\alpha(v)|_{x_0}| \leq C\|v_h-v\|_\infty. \tag{3.23}$$

If $v^+|_{x_0}=0$, $\alpha(v_h)|_{x_0}=\frac{1}{2}|f'(0)|$ and

$$|\alpha(v_h)|_{x_0}-\alpha(v)|_{x_0}| = 0. \tag{3.24}$$

The bound for the other boundary x_{N+1} is similar. □

We now introduce the discontinuous Galerkin discretization on each interval

$$\begin{aligned}
\mathcal{H}_j(v,\phi_h) &= \int_{I_j} f(v)\frac{d\phi_h}{dx}+\int_{I_j} s(v)\phi_h\\
&\quad -\hat{f}(v^-,v^+)|_{x_{j+1}}\phi_h^-|_{x_{j+1}}+\hat{f}(v^-,v^+)|_{x_j}\phi_h^+|_{x_j} \quad \forall\, 1\leq j\leq N-1, \qquad (3.25)\\
\mathcal{H}_0(v,\phi_h) &= \int_{I_0} f(v)\frac{d\phi_h}{dx}+\int_{I_0} s(v)\phi_h-\hat{f}(v^-,v^+)|_{x_1}\phi_h^-|_{x_1}+\hat{f}(0,v^+)|_{x_0}\phi_h^+|_{x_0}, \qquad (3.26)\\
\mathcal{H}_N(v,\phi_h) &= \int_{I_N} f(v)\frac{d\phi_h}{dx}+\int_{I_N} s(v)\phi_h+\hat{f}(v^-,v^+)|_{x_N}\phi_h^+|_{x_N}-\hat{f}(v^-,0)|_{x_{N+1}}\phi_h^-|_{x_{N+1}}. \qquad (3.27)
\end{aligned}$$

For some number $M > 0$, define $\Delta t = T/M$.

Remark 3.2. *Noticing the boundary terms at x_0 in (3.26) and at x_{N+1} in (3.27), the scheme is consistent since the exact solution vanishes at the boundary of the domain and by consistency of the numerical flux.*

The second order in time Adams–Bashforth scheme is: given $u_h^0 \in \mathbb{V}_h$ and $u_h^1 \in \mathbb{V}_h$, for $n = 1, \ldots, M-1$, seek $u_h^{n+1} \in \mathbb{V}_h$ satisfying

$$\int_{I_j} u_h^{n+1}\phi_h = \int_{I_j} u_h^n\phi_h + \Delta t\frac{3}{2}\mathcal{H}_j(u_h^n, \phi_h) - \Delta t\frac{1}{2}\mathcal{H}_j(u_h^{n-1}, \phi_h), \quad \forall \phi_h \in \mathbb{V}_h, \quad \forall\, 0 \le j \le N. \tag{3.28}$$

Since (3.28) is a multi-step method, two starting values are needed. We choose $u_h^0 = \Pi_h u_0$ for the initial value, and we choose $u_h^1 = \tilde{u}_h^1$ where $\tilde{u}_h^1$ satisfies the first-order in time forward Euler scheme defined below.

With the choice $\tilde{u}_h^0 = \Pi_h u_0$, for $n = 0, \ldots, M-1$, seek $\tilde{u}_h^{n+1} \in \mathbb{V}_h$ satisfying

$$\int_{I_j} \tilde{u}_h^{n+1}\phi_h = \int_{I_j} \tilde{u}_h^n\phi_h + \Delta t\, \mathcal{H}_j(\tilde{u}_h^n, \phi_h), \quad \forall \phi_h \in \mathbb{V}_h, \quad \forall\, 0 \le j \le N. \tag{3.29}$$

The initial value u_h^1 is computed using (3.29) with a time step that is small enough so that the following assumption holds:

$$\|u_h^1 - \Pi_h u^1\| \le h^{k+1/2}. \tag{3.30}$$

Theorem 3.2 below shows that (3.30) is a reasonable assumption if the time step used for the forward Euler method is small enough.

We finish this section by recalling inverse inequalities, trace inequalities and approximations results. Let $\|v\|_\infty = \max_{x\in[0,1]} |v(x)|$ denote the sup-norm. There exists a

constant C independent of h such that

$$\|\phi_h\|_\infty \leq Ch^{-1/2}\|\phi_h\|, \quad \forall \phi_h \in \mathbb{V}_h, \tag{3.31}$$

$$|\phi_h^{n,\pm}|_{x_j}| \leq Ch^{-1/2}\|\phi_h\|_{L^2(I_j)}, \quad \forall\, 1 \leq j \leq N, \quad \forall \phi_h \in \mathbb{V}_h, \tag{3.32}$$

$$\left(\sum_{j=0}^{N} \|\frac{d}{dx}\phi_h\|^2_{L^2(I_j)}\right)^{1/2} \leq Ch^{-1}\|\phi_h\|, \quad \forall \phi_h \in \mathbb{V}_h. \tag{3.33}$$

For simplicity we denote u^n the function u evaluated at the time $t^n = n\Delta t$. The approximation error is denoted

$$\eta^n = u^n - \Pi_h u^n,$$

and it satisfies the optimal a priori bounds

$$\|\eta^n\| \leq Ch^{k+1}, \tag{3.34}$$

$$|\eta^{n,\pm}|_{x_j}| \leq Ch^{k+1/2}, \quad \forall\, 1 \leq j \leq N, \tag{3.35}$$

$$\|\eta^n\|_\infty \leq Ch^{k+1/2}, \tag{3.36}$$

$$\|\eta^{n+1} - \eta^n\| \leq C\Delta t\, h^{k+1}. \tag{3.37}$$

The constant C is independent of $h, \Delta t$ but depends on the exact solution u and its derivatives.

3.2 E–fluxes and L^2 stability for scalar conservation laws

In this section, we recall some consequences of Assumption 3.2, which enforces a condition on the numerical flux. It is shown that the E–flux property implies stability for a semi–discrete DG scheme. We follow the arguments given in [54].

Let us assume the source function s is zero. Following the notation in the previous section, the semi–discrete DG scheme for equations (3.1)–(3.2) is the following: With

the choice $u_h(\cdot, t=0) = \Pi_h u_0$, for each $t \in (0,T)$, seek $u_h(t) \in \mathbb{V}_h$ so that

$$\int_{I_j} \frac{\partial}{\partial t} u_h \phi_h = \mathcal{H}_j\left(u_h, \phi_h\right), \quad \forall \phi_h \in \mathbb{V}_h, \quad \forall\, 0 \le j \le N. \tag{3.38}$$

One obtains the following stability result.

Lemma 3.2. *Consider the scheme (3.38). Assume the numerical flux $\hat{f}$ satisfies Assumption 3.2. For each $t \in (0,T)$ one has:*

$$\|u_h\| \le \|\Pi_h u_0\|.$$

Proof. Take $\phi_h = u_h$ in (3.38) and sum over the elements I_j to obtain:

$$\frac{1}{2}\frac{d}{dt}\|u_h\|^2 = \sum_{j=0}^{N} \mathcal{H}_j\left(u_h, u_h\right).$$

By definition one has:

$$\begin{aligned}\sum_{j=0}^{N} \mathcal{H}_j\left(u_h, u_h\right) = \sum_{j=0}^{N} \int_{I_j} f(u_h)\frac{du_h}{dx} - \sum_{j=1}^{N} \hat{f}(u_h^-, u_h^+)|_{x_j}[u_j]|_{x_j} \\ + \hat{f}(0, u_h^+)|_{x_0} u_h^+|_{x_0} - \hat{f}(u_h^-, 0)|_{x_{N+1}} u_h^-|_{x_{N+1}}.\end{aligned}$$

Define a function g so that $g' = f$, i.e. take $g(y) = \int_a^y f(s)ds$. Then, the first term in parentheses above may be written as follows:

$$\sum_{j=0}^{N} \int_{I_j} f(u_h)\frac{du_h}{dx} = \sum_{j=0}^{N} \int_{I_j} \frac{d}{dx} g(u_h) = \sum_{j=1}^{N} [g(u_h)]|_{x_j} - g(u_h^+|_{x_0}) + g(u_h^-|_{x_{N+1}}).$$

By the mean value theorem, for each $1 \le j \le N$ there exists numbers ζ_j satisfying $\min(u_h^-|_{x_j}, u_h^+|_{x_j}) \le \zeta_j \le \max(u_h^-|_{x_j}, u_h^+|_{x_j})$ so that

$$\sum_{j=1}^{N} [g(u_h)]|_{x_j} = \sum_{j=1}^{N} f(\zeta_j)[u_h]|_{x_j}.$$

Similarly there is ζ_0 satisfying $\min(0, u_h^+|_{x_0}) \leq \zeta_0 \leq \max(0, u_h^+|_{x_0})$ and there is ζ_{N+1} satisfying $\min(0, u_h^-|_{x_{N+1}}) \leq \zeta_{N+1} \leq \max(0, u_h^-|_{x_{N+1}})$ so that:

$$g(u_h^+|_{x_0}) = f(\zeta_0)u_h^+|_{x_0}$$
$$g(u_h^-|_{x_{N+1}}) = f(\zeta_{N+1})u_h^-|_{x_{N+1}}.$$

Employing the E–flux property, one has:

$$\frac{1}{2}\frac{d}{dt}\|u_h\|^2 \leq 0,$$

and integrating this equation finishes the proof.

□

3.3 Analysis for scalar nonlinear conservation laws with forward Euler and second order Adams–Bashforth time discretizations

The focus of this section is the analysis of the second order Adams–Bashforth method in time combined with the discontinuous Galerkin method in space. The main motivation for studying this discretization is its popularity in the hemodynamic modeling community for approximating a nonlinear hyperbolic system describing blood flow in an elastic vessel [8]. For a selection of work simulating this model with a discontinuous Galerkin spatial discretization coupled to the second order Adams–Bashforth scheme, see [4, 55, 56, 28, 27, 57, 58, 59, 60, 48]. To the best of our knowledge, there is little analysis for this fully discrete scheme. The results presented in this section for scalar hyperbolic equations provide a first step towards theoretically understanding the numerical approximation of the hyperbolic system modeling blood flow. In addi-

tion, we provide an error analysis for the first order forward Euler in time combined with discontinuous Galerkin in space.

Discontinuous Galerkin schemes for hyperbolic conservations laws have been extensively studied, especially when coupled with Runge–Kutta methods for the time discretization. This class of schemes was introduced in the series of papers by Cockburn, Shu, and co-authors [61, 29, 20, 30, 31]. We recall the work from Zhang, Shu, and others analyzing Runge–Kutta discontinuous Galerkin methods applied to scalar conservation laws and symmetrizable systems [32, 33, 62, 34]. These papers establish error estimates for smooth solutions for both second and third order Runge–Kutta schemes. Their analysis requires the CFL condition $\Delta t = O(h^{4/3})$ for the second order Runge–Kutta scheme and piecewise polynomials of degree two and higher. The CFL condition $\Delta t = O(h)$ may be used for the third order Runge-Kutta scheme for piecewise polynomials of degree one and higher and for the second order Runge–Kutta scheme with piecewise linear polynomials.

Recent stability and convergence results have been obtained for IMEX (implicit–explicit) multistep schemes applied to a nonlinear convection diffusion equation, i.e. (3.1)–(3.2) augmented with a nonzero diffusion term [63]. These schemes implicitly discretize the diffusion term and explicitly discretize the hyperbolic term. It is not immediately clear how to adapt the analysis to the case of zero diffusion since the estimates depend on the reciprocal of the diffusion parameter.

The main result of this section is the convergence result for the Adams–Bashforth scheme (3.28).

Theorem 3.1. *Assume the exact solution u belongs to $\mathcal{C}^2([0,T];H^{k+1}(\Omega))$. Let u_h^1 satisfy* (3.30)*. Under Assumptions 3.1, 3.2, 3.3 and the CFL condition $\Delta t = O(h^2)$, there is a constant C independent of h and Δt such that, for h sufficiently small, and*

for $k \geq 2$:

$$\max_{n=0,\ldots,M} \|u^n - u_h^n\| \leq C(\Delta t^2 + h^{k+1/2}). \tag{3.39}$$

The proof of Theorem 3.1 is given in Section 3.3.1. An easy modification of the proof yields the following convergence result for the forward Euler scheme (3.29). Its proof is outlined in Section 3.3.4.

Theorem 3.2. *Assume the exact solution u belongs to $\mathcal{C}^2([0,T]; H^{k+1}(\Omega))$. Let $(\tilde{u}_h^n)_n$ satisfy* (3.29)*. Under Assumptions 3.1, 3.2 and the CFL condition $\Delta t = O(h^2)$, for h sufficiently small, and for $k \geq 1$, there is a constant C independent of h and Δt such that:*

$$\max_{n=0,\ldots,M} \|u^n - \tilde{u}_h^n\| \leq C(\Delta t + h^{k+1/2}). \tag{3.40}$$

Remark 3.3. *We remark that von Neumann stability analysis conducted in [64] suggests a less restrictive CFL condition $\Delta t = O(h^{4/3})$ for the second order Adams–Bashforth scheme. Our theoretical estimates require $\Delta t = O(h^2)$; at the moment we are unable to relax this condition.*

3.3.1 Proof of Theorem 3.1

For the error analysis, we denote

$$\chi^n = u_h^n - \Pi_h u^n.$$

The proof of Theorem 3.1 is based on an induction hypothesis:

$$\|\chi^\ell\| \leq h^{3/2}, \quad \forall 0 \leq \ell \leq M. \tag{3.41}$$

Since $\chi^0 = 0$, the hypothesis (3.41) is trivially satisfied for $\ell = 0$. With the assumption (3.30), it is also true for $\ell = 1$. Fix $\ell \in \{2, \ldots, M\}$ and assume that

$$\|\chi^n\| \leq h^{3/2}, \quad \forall 0 \leq n \leq \ell - 1. \tag{3.42}$$

We will show that (3.42) is valid for $n = \ell$. We begin by deriving an error inequality. We fix an interval I_j for $0 \leq j \leq N$. It is easy to see that the scheme is consistent in space and the exact solution satisfies

$$\frac{3}{2}\int_{I_j} u_t^n \phi_h - \frac{1}{2}\int_{I_j} u_t^{n-1}\phi_h = \frac{3}{2}\mathcal{H}_j(u^n, \phi_h) - \frac{1}{2}\mathcal{H}_j(u^{n-1}, \phi_h), \quad \forall 1 \leq n \leq M-1. \tag{3.43}$$

In the above, the notation u_t^n is used for the time derivative of u evaluated at t^n. Subtracting (3.43) from (3.28) and rearranging terms, one obtains:

$$\begin{aligned}\int_{I_j} \left(u_h^{n+1} - u_h^n - \Delta t\frac{3}{2}u_t^n + \Delta t\frac{1}{2}u_t^{n-1}\right)\phi_h \\ = \Delta t\frac{3}{2}(\mathcal{H}_j(u_h^n, \phi_h) - \mathcal{H}_j(u^n, \phi_h)) - \Delta t\frac{1}{2}(\mathcal{H}_j(u_h^{n-1}, \phi_h) - \mathcal{H}_j(u^{n-1}, \phi_h)), \quad \forall\, 1 \leq n \leq M-1.\end{aligned}$$

Summing over the elements $j = 0, \ldots, N$ and adding and subtracting the L^2 projection of u at t^n and t^{n+1} yields the equality:

$$\int_0^L (\chi^{n+1} - \chi^n)\phi_h = \int_0^L \left(u^n - u^{n+1} + \Delta t\frac{3}{2}u_t^n - \Delta t\frac{1}{2}u_t^{n-1}\right)\phi_h + \int_0^L (\eta^{n+1} - \eta^n)\phi_h + b^n(\phi_h), \tag{3.44}$$

with the following definition for $n \geq 1$

$$b^n(\phi_h) = \Delta t\frac{3}{2}\sum_{j=0}^{N}\left(\mathcal{H}_j(u_h^n, \phi_h) - \mathcal{H}_j(u^n, \phi_h)\right) - \Delta t\frac{1}{2}\sum_{j=0}^{N}\left(\mathcal{H}_j(u_h^{n-1}, \phi_h) - \mathcal{H}_j(u^{n-1}, \phi_h)\right).$$

The second term on the right hand side of (3.44) vanishes due to the property (3.5) of the local L^2 projection. To handle the first term, we obtain from the following

Taylor expansions for some $\tilde{\zeta} \in [t^{n-1}, t^n]$ and some $\zeta \in [t^n, t^{n+1}]$:

$$u^{n+1} - u^n = \Delta t u_t^n + \frac{1}{2}\Delta t^2 u_{tt}^n + \frac{1}{6}\Delta t^3 u_{ttt}|_\zeta,$$
$$u_t^{n-1} - u_t^n = -\Delta t u_{tt}^n + \frac{1}{2}\Delta t^2 u_{ttt}|_{\tilde{\zeta}}.$$

Thus we have

$$u^n - u^{n+1} + \Delta t\frac{3}{2}u_t^n - \Delta t\frac{1}{2}u_t^{n-1} = -\Delta t^3(\frac{1}{6}u_{ttt}|_\zeta + \frac{1}{4}u_{ttt}|_{\tilde{\zeta}}).$$

Hence (3.44) becomes:

$$\int_0^L \left(\chi^{n+1} - \chi^n\right)\phi_h \leq C\Delta t^3 \int_0^L |\phi_h| + b^n(\phi_h). \tag{3.45}$$

Cauchy Schwarz's inequality and Young's inequalities imply:

$$\int_0^L \left(\chi^{n+1} - \chi^n\right)\phi_h \leq C\Delta t^5 + \Delta t\|\phi_h\|^2 + b^n(\phi_h). \tag{3.46}$$

We choose $\phi_h = \chi^n$ in inequality (3.46) to obtain:

$$\int_0^L \left(\chi^{n+1} - \chi^n\right)\chi^n \leq C\Delta t^5 + \Delta t\|\chi^n\|^2 + b^n(\chi^n).$$

So, the following error inequality holds for $n \geq 1$:

$$\frac{1}{2}\|\chi^{n+1}\|^2 - \frac{1}{2}\|\chi^n\|^2 \leq C\Delta t^5 + \Delta t\|\chi^n\|^2 + \frac{1}{2}\|\chi^{n+1} - \chi^n\|^2 + b^n(\chi^n). \tag{3.47}$$

It remains to handle the last two terms in (3.47). The proofs of the following two lemma are given in the next section.

Lemma 3.3. *Assume that $\Delta t = O(h^2)$. The following holds for $n \geq 1$:*

$$\|\chi^{n+1} - \chi^n\|^2 \leq C\Delta t^6 + C\Delta t\left(\|\chi^n\|^2 + \|\chi^{n-1}\|^2\right) + C\Delta t\, h^{2k+2}. \tag{3.48}$$

Lemma 3.4. *Let $n \geq 2$ and assume $\|\chi^n\| \leq h^{3/2}$, $\|\chi^{n-1}\| \leq h^{3/2}$, and $\Delta t = O(h^2)$. The following holds $\forall \varepsilon > 0$:*

$$b^n(\chi^n) \leq C\Delta t(\|\chi^n\|^2 + \|\chi^{n-1}\|^2) + C\Delta t^6 + C\Delta t\,(1+2\varepsilon^{-1})h^{2k+1}$$
$$-(\frac{1}{2}-2\varepsilon)\Delta t\left(\alpha(u_h^n)|_{x_0}(\chi^{n,+}|_{x_0})^2 + \alpha(u_h^n)|_{x_{N+1}}(\chi^{n,-}|_{x_{N+1}})^2 + \sum_{j=1}^{N}\alpha(u_h^n)|_{x_j}[\chi^n]|_{x_j}^2\right) \tag{3.49}$$
$$-(\frac{1}{2}-2\varepsilon)\Delta t\left(\alpha(u_h^{n-1})|_{x_0}(\chi^{n-1,+}|_{x_0})^2 + \alpha(u_h^{n-1})|_{x_{N+1}}(\chi^{n-1,-}|_{x_{N+1}})^2 + \sum_{j=1}^{N}\alpha(u_h^{n-1})|_{x_j}[\chi^{n-1}]|_{x_j}^2\right). \tag{3.50}$$

For $n = 1$ one has the following $\forall \varepsilon > 0$:

$$b^1(\chi^1) \leq C\Delta t\|\chi^1\|^2 + C\Delta t\,(1+2\varepsilon^{-1})h^{2k+1} + 7\|\chi^1\|^2$$
$$-(\frac{1}{2}-2\varepsilon)\Delta t\left(\alpha(u_h^1)|_{x_0}(\chi^{1,+}|_{x_0})^2 + \alpha(u_h^1)|_{x_{N+1}}(\chi^{1,-}|_{x_{N+1}})^2 + \sum_{j=1}^{N}\alpha(u_h^1)|_{x_j}[\chi^1]|_{x_j}^2\right). \tag{3.51}$$

Substituting the bounds from (3.48), (3.49), (3.51) (with $\varepsilon = 1/4$), and using the fact that $\alpha(u_h^n)$ and $\alpha(u_h^{n-1})$ are nonnegative, the error inequality (3.47) simplifies to:

$$\|\chi^{n+1}\|^2 - \|\chi^n\|^2 \leq C\Delta t^5 + C\Delta t\,(\|\chi^n\|^2 + \|\chi^{n-1}\|^2 + \|\chi^{n-2}\|^2) + C\Delta t\,h^{2k+1}, \quad n \geq 2, \tag{3.52}$$

and

$$\|\chi^{n+1}\|^2 - \|\chi^n\|^2 \leq C\Delta t^5 + C\Delta t\,\|\chi^n\|^2 + C\Delta t\,h^{2k+1} + C\|\chi^n\|^2, \quad n = 1. \tag{3.53}$$

Summing (3.52) from $n = 2, \ldots, \ell - 1$ and adding to (3.53) one obtains:

$$\|\chi^\ell\|^2 \leq C\Delta t^4 + Ch^{2k+1} + C\|\chi^1\|^2 + C\Delta t\sum_{n=0}^{\ell-1}\|\chi^n\|^2.$$

Gronwall's inequality and assumption (3.30) immediately gives

$$\|\chi^{\ell}\|^2 \leq C_2 T \mathrm{e}^T \left(\Delta t^4 + h^{2k+1}\right),$$

where C_2 is independent of ℓ, h and Δt. Employing the CFL condition $\Delta t = O(h^2)$, one has:

$$\|\chi^{\ell}\| \leq \left(C_2 T \mathrm{e}^T\right)^{1/2} \left(h^4 + h^{k+1/2}\right).$$

The induction proof is complete if h is small enough so that

$$C_2 T \mathrm{e}^T h < 1,$$

implying that for $k \geq 2$:

$$\|\chi^{\ell}\| \leq \left(C_2 T \mathrm{e}^T\right)^{1/2} h \left(h^3 + h^{k-1/2}\right) \leq h^{3/2}.$$

Since $\|\eta^n\| \leq C h^{k+1}$ and $\|u^n - u_h^n\| \leq \|\eta^n\| + \|\chi^n\|$ we can conclude:

$$\|u^n - u_h^n\| \leq C \left(\Delta t^2 + h^{k+1/2}\right).$$

3.3.2 Proof of Lemma 3.3

Choose $\phi_h = \chi^{n+1} - \chi^n$ in (3.45) and use Cauchy-Schwarz's and Young's inequalities to obtain:

$$\|\chi^{n+1} - \chi^n\|^2 \leq C \Delta t^6 + 2\, b^n(\chi^{n+1} - \chi^n). \tag{3.54}$$

We will now obtain a bound for $b^n(\phi_h)$ for any $\phi_h \in \mathbb{V}_h$. By definition, we write

$$b^n(\phi_h) = \theta_1 + \theta_2 + \theta_3,$$

where

$$\theta_1 = \frac{3}{2}\Delta t \sum_{j=0}^{N} \int_{I_j} (f(u_h^n) - f(u^n)) \frac{d\phi_h}{dx} - \frac{1}{2}\Delta t \sum_{j=0}^{N} \int_{I_j} (f(u_h^{n-1}) - f(u^{n-1})) \frac{d\phi_h}{dx}$$
$$- \frac{3}{2}\Delta t \sum_{j=1}^{N} (f(\{u_h^n\}) - f(u^n))|_{x_j}[\phi_h]|_{x_j} + \frac{1}{2}\Delta t \sum_{j=1}^{N} (f(\{u_h^{n-1}\}) - f(u^{n-1}))|_{x_j}[\phi_h]|_{x_j}$$
$$+ \frac{3}{2}\Delta t (f(\frac{1}{2}u_h^{n,+}) - f(u^n))|_{x_0}\phi_h^+|_{x_0} - \frac{1}{2}\Delta t (f(\frac{1}{2}u_h^{n-1,+}) - f(u^{n-1}))|_{x_0}\phi_h^+|_{x_0}$$
$$- \frac{3}{2}\Delta t (f(\frac{1}{2}u_h^{n,-}) - f(u^n))|_{x_{N+1}}\phi_h^-|_{x_{N+1}} + \frac{1}{2}\Delta t (f(\frac{1}{2}u_h^{n-1,-}) - f(u^{n-1}))|_{x_{N+1}}\phi_h^-|_{x_{N+1}}, \tag{3.55}$$

$$\theta_2 = \Delta t \sum_{j=0}^{N} \int_{I_j} \left(\frac{3}{2}(s(u_h^n) - s(u^n)) - \frac{1}{2}(s(u_h^{n-1}) - s(u^{n-1})) \right) \phi_h, \tag{3.56}$$

$$\theta_3 = -\frac{3}{2}\Delta t \sum_{j=1}^{N} (\hat{f}(u_h^{n,-}, u_h^{n,+}) - f(\{u_h^n\}))|_{x_j}[\phi_h]|_{x_j}$$
$$+ \frac{1}{2}\Delta t \sum_{j=1}^{N} (\hat{f}(u_h^{n-1,-}, u_h^{n-1,+}) - f(\{u_h^{n-1}\}))|_{x_j}[\phi_h]|_{x_j}$$
$$+ \frac{3}{2}\Delta t (\hat{f}(0, u_h^{n,+}) - f(\frac{1}{2}u_h^{n,+}))|_{x_0}\phi_h^+|_{x_0} - \frac{1}{2}\Delta t (\hat{f}(0, u_h^{n-1,+}) - f(\frac{1}{2}u_h^{n-1,+}))|_{x_0}\phi_h^+|_{x_0}$$
$$- \frac{3}{2}\Delta t (\hat{f}(u_h^{n,-}, 0) - f(\frac{1}{2}u_h^{n,-}))|_{x_{N+1}}\phi_h^-|_{x_{N+1}} + \frac{1}{2}\Delta t (\hat{f}(u_h^{n-1,-}, 0) - f(\frac{1}{2}u_h^{n-1,-}))|_{x_{N+1}}\phi_h^-|_{x_{N+1}} \tag{3.57}$$

Using Taylor expansions and the fact that the exact solution u vanishes at x_0 and x_{N+1}, we write for some ζ_i^n, ζ_i^{n-1}, $i = 1, \ldots, 4$:

$$
\begin{aligned}
f(u_h^n) - f(u^n) &= f'(\zeta_1^n)(u_h^n - u^n) = f'(\zeta_1^n)(\chi^n - \eta^n),\\
f(\{u_h^n\}) - f(u^n) &= f'(\zeta_2^n)(\{u_h^n\} - \{u^n\}) = f'(\zeta_2^n)(\{\chi^n\} - \{\eta^n\}),\\
f(\frac{1}{2}u_h^{n,+}|_{x_0}) - f(u^n|_{x_0}) &= f'(\zeta_3^n)(\frac{1}{2}u_h^{n,+} - \frac{1}{2}u^n)|_{x_0} = f'(\zeta_3^n)(\frac{1}{2}\chi^{n,+} - \frac{1}{2}\eta^{n,+})|_{x_0},\\
f(\frac{1}{2}u_h^{n,-}|_{x_{N+1}}) - f(u^n|_{x_{N+1}}) &= f'(\zeta_4^n)(\frac{1}{2}u_h^{n,-} - \frac{1}{2}u^n)|_{x_{N+1}} = f'(\zeta_4^n)(\frac{1}{2}\chi^{n,-} - \frac{1}{2}\eta^{n,-})|_{x_{N+1}},\\
f(u_h^{n-1}) - f(u^{n-1}) &= f'(\zeta_1^{n-1})(u_h^{n-1} - u^{n-1}) = f'(\zeta_1^{n-1})(\chi^{n-1} - \eta^{n-1}),\\
f(\{u_h^{n-1}\}) - f(u^{n-1}) &= f'(\zeta_2^n)(\{u_h^{n-1}\} - \{u^{n-1}\}) = f'(\zeta_2^{n-1})(\{\chi^{n-1}\} - \{\eta^{n-1}\})\\
f(\frac{1}{2}u_h^{n-1,+}|_{x_0}) - f(u^{n-1}|_{x_0}) &= f'(\zeta_3^{n-1})(\frac{1}{2}u_h^{n-1,+} - \frac{1}{2}u^{n-1})|_{x_0}\\
&= f'(\zeta_3^{n-1})(\frac{1}{2}\chi^{n-1,+} - \frac{1}{2}\eta^{n-1,+})|_{x_0},\\
f(\frac{1}{2}u_h^{n-1,-}|_{x_{N+1}}) - f(u^{n-1}|_{x_{N+1}}) &= f'(\zeta_4^{n-1})(\frac{1}{2}u_h^{n-1,-} - \frac{1}{2}u^{n-1})|_{x_{N+1}}\\
&= f'(\zeta_4^{n-1})(\frac{1}{2}\chi^{n-1,-} - \frac{1}{2}\eta^{n-1,-})|_{x_{N+1}}.
\end{aligned}
$$

Using the above expansions in the definition of θ_1, trace inequalities and the CFL condition $\Delta t = \mathcal{O}(h^2)$, we can obtain for any $\varepsilon > 0$

$$
|\theta_1| \leq \varepsilon \|\phi_h\|^2 + C\varepsilon^{-1}\Delta t(\|\chi^n\|^2 + \|\chi^{n-1}\|^2) + C\varepsilon^{-1}\,\Delta t\, h^{2k+2}. \tag{3.58}
$$

The term θ_2 is bounded using Lipschitz continuity of s, approximation results, Cauchy-Schwarz's and Young's inequalities. For any $\varepsilon > 0$, we have

$$
\theta_2 \leq C\varepsilon^{-1}\Delta t^2 h^{2k+2} + C\varepsilon^{-1}\Delta t^2(\|\chi^n\|^2 + \|\chi^{n-1}\|^2) + \varepsilon\|\phi_h\|^2.
$$

Lastly, the term θ_3 can be rewritten using the definitions (3.16), (3.19), (3.18).

$$\begin{aligned}
\theta_3 &= -\frac{3}{2}\Delta t\sum_{j=1}^{N}\alpha(u_h^n)|_{x_j}[u_h^n]|_{x_j}[\phi_h]|_{x_j} + \frac{1}{2}\Delta t\sum_{j=1}^{N}\alpha(u_h^{n-1})|_{x_j}[u_h^{n-1}]|_{x_j}[\phi_h]|_{x_j}\\
&- \frac{3}{2}\Delta t\alpha(u_h^n)|_{x_0}(u_h^{n,+}|_{x_0})(\phi_h^+|_{x_0}) + \frac{1}{2}\Delta t\alpha(u_h^{n-1})|_{x_0}(u_h^{n-1,+}|_{x_0})(\phi_h^+|_{x_0})\\
&- \frac{3}{2}\Delta t\alpha(u_h^n)|_{x_{N+1}}(u_h^{n,-}|_{x_{N+1}})(\phi_h^-|_{x_{N+1}}) + \frac{1}{2}\Delta t\alpha(u_h^{n-1})|_{x_{N+1}}(u_h^{n-1,-}|_{x_{N+1}})(\phi_h^-|_{x_{N+1}}),\\
&= -\frac{3}{2}\Delta t\sum_{j=1}^{N}\alpha(u_h^n)|_{x_j}[\chi^n-\eta^n]|_{x_j}[\phi_h]|_{x_j} + \frac{1}{2}\Delta t\sum_{j=1}^{N}\alpha(u_h^{n-1})|_{x_j}[\chi^{n-1}-\eta^{n-1}]|_{x_j}[\phi_h]|_{x_j}\\
&- \frac{3}{2}\Delta t\alpha(u_h^n)|_{x_0}(\chi^{n,+}-\eta^{n,+})|_{x_0})(\phi_h^+|_{x_0}) + \frac{1}{2}\Delta t\alpha(u_h^{n-1})|_{x_0}(\chi^{n-1,+}-\eta^{n-1,+})|_{x_0})(\phi_h^+|_{x_0})\\
&- \frac{3}{2}\Delta t\alpha(u_h^n)|_{x_{N+1}}(\chi^{n,-}-\eta^{n,-})|_{x_{N+1}})(\phi_h^-|_{x_{N+1}}) + \frac{1}{2}\Delta t\alpha(u_h^{n-1})|_{x_{N+1}}(\chi^{n-1,-}-\eta^{n-1,-})|_{x_{N+1}})(\phi_h^-|_{x_{N+1}}
\end{aligned}$$

Using Young's and Cauchy-Schwarz's inequalities, approximation results, trace inequalities, boundedness of α and the CFL condition, we have

$$|\theta_3| \le \varepsilon\|\phi_h\|^2 + C\varepsilon^{-1}\Delta t(\|\chi^n\|^2 + \|\chi^{n-1}\|^2) + C\varepsilon^{-1}\Delta t\, h^{2k+2}.$$

Combining the bounds above yields

$$b(\phi_h) \le \varepsilon\|\phi_h\|^2 + C\varepsilon^{-1}\Delta t(\|\chi^n\|^2 + \|\chi^{n-1}\|^2) + C\varepsilon^{-1}\Delta t\, h^{2k+2}, \quad \forall\varepsilon>0, \quad \forall\phi_h\in\mathbb{V}_h. \tag{3.59}$$

We choose $\varepsilon = 1/4$ and $\phi_h = \chi^n - \chi^{n-1}$ in (3.59) and substitute the bound in (3.54) to obtain (3.48).

$$\|\chi^{n+1}-\chi^n\|^2 \le C\Delta t^6 + C\Delta t(\|\chi^n\|^2 + \|\chi^{n-1}\|^2) + C\Delta t\, h^{2k+2}. \tag{3.60}$$

3.3.3 Proof of Lemma 3.4

As in the proof of Lemma 3.3, we write

$$b^n(\chi^n) = \theta_1 + \theta_2 + \theta_3,$$

where the definitions of $\theta_1, \theta_2, \theta_3$ are given in (3.55), (3.56) and (3.57) respectively for the particular choice $\phi_h = \chi^n$. Unfortunately we cannot make use of the bound (3.59) since the factor Δt is missing in front of $\varepsilon\|\phi_h\|^2$. A more careful analysis is needed, and we will take advantage of the CFL condition. Define

$$\mathcal{F}(n,\phi_h) = \Delta t \sum_{j=0}^{N} \int_{I_j} (f(u_h^n) - f(u^n)) \frac{d\phi_h}{dx} - \Delta t \sum_{j=1}^{N} (f(\{u_h^n\}) - f(u^n))|_{x_j}[\phi_h]|_{x_j}$$
$$+ \Delta t (f(\frac{1}{2}u_h^{n,+}) - f(u^n))|_{x_0}\phi_h^+|_{x_0} - \Delta t (f(\frac{1}{2}u_h^{n,-}) - f(u^n))|_{x_{N+1}}\phi_h^-|_{x_{N+1}}. \quad (3.61)$$

Using the function $\mathcal{F}$ which is linear in its second argument, we rewrite the term θ_1 as

$$\theta_1 = \frac{3}{2}\mathcal{F}(n,\chi^n) - \frac{1}{2}\mathcal{F}(n-1,\chi^{n-1}) + \frac{1}{2}\mathcal{F}(n-1,\chi^{n-1}-\chi^n).$$

We now state a bound for the term $\mathcal{F}(n,\chi^n)$.

$$\mathcal{F}(n,\chi^n) \le C\Delta t\|\chi^n\|^2 + C(1+\varepsilon^{-1})\Delta t\, h^{2k+1}$$
$$+ \varepsilon\Delta t \left(\alpha(u_h^n)|_{x_0}(\chi^{n,+}|_{x_0})^2 + \alpha(u_h^n)|_{x_{N+1}}(\chi^{n,-}|_{x_{N+1}})^2 + \sum_{j=1}^{N} \alpha(u_h^n)|_{x_j}[\chi^n]|_{x_j}^2 \right), \quad \forall \varepsilon > 0. \quad (3.62)$$

The proof of (3.62) is technical and can be found in Appendix 3.3.8. The bound for $\mathcal{F}(n-1,\chi^{n-1})$ is identical.

$$\mathcal{F}(n-1,\chi^{n-1}) \le C\Delta t\|\chi^{n-1}\|^2 + C(1+\varepsilon^{-1})\Delta t\, h^{2k+1}$$
$$+ \varepsilon\Delta t \left(\alpha(u_h^{n-1})|_{x_0}(\chi^{n-1,+}|_{x_0})^2 + \alpha(u_h^{n-1})|_{x_{N+1}}(\chi^{n-1,-}|_{x_{N+1}})^2 + \sum_{j=1}^{N} \alpha(u_h^{n-1})|_{x_j}[\chi^{n-1}]|_{x_j}^2 \right), \quad \forall \varepsilon > 0$$

(3.63)

We are left with bounding $\mathcal{F}(n-1,\chi^{n-1}-\chi^n)$. Following the technique used for bound (3.58), we can obtain

$$\mathcal{F}(n-1,\chi^{n-1}-\chi^n) \le \|\chi^{n-1}-\chi^n\|^2 + C\Delta t\|\chi^{n-1}\|^2 + C\Delta t\, h^{2k+2}. \quad (3.64)$$

Combining the above with (3.60), we have for $n \geq 2$

$$\theta_1 \leq C\Delta t(\|\chi^n\|^2 + \|\chi^{n-1}\|^2 + \|\chi^{n-2}\|^2) + C(1+2\varepsilon^{-1})\Delta t\, h^{2k+1} + C\Delta t^6$$
$$+ \varepsilon\Delta t\left(\alpha(u_h^n)|_{x_0}(\chi^{n,+}|_{x_0})^2 + \alpha(u_h^n)|_{x_{N+1}}(\chi^{n,-}|_{x_{N+1}})^2 + \sum_{j=1}^{N}\alpha(u_h^n)|_{x_j}[\chi^n]|_{x_j}^2\right)$$
$$+ \varepsilon\Delta t\left(\alpha(u_h^{n-1})|_{x_0}(\chi^{n-1,+}|_{x_0})^2 + \alpha(u_h^{n-1})|_{x_{N+1}}(\chi^{n-1,-}|_{x_{N+1}})^2 + \sum_{j=1}^{N}\alpha(u_h^{n-1})|_{x_j}[\chi^{n-1}]|_{x_j}^2\right), \quad \forall\epsilon > 0$$

For $n = 1$, since $\chi^0 = 0$, inequalities (3.62) and (3.64) imply

$$\theta_1 \leq C\Delta t\|\chi^1\|^2 + C(1+\varepsilon^{-1})\Delta t\, h^{2k+1}$$
$$+ \varepsilon\Delta t\left(\alpha(u_h^1)|_{x_0}(\chi^{1,+}|_{x_0})^2 + \alpha(u_h^1)|_{x_{N+1}}(\chi^{1,-}|_{x_{N+1}})^2 + \sum_{j=1}^{N}\alpha(u_h^1)|_{x_j}[\chi^1]|_{x_j}^2\right) + \|\chi^1\|^2, \quad \forall\epsilon > 0.$$

The term θ_2 is bounded using Lipschitz continuity of s, approximation results, Cauchy-Schwarz's inequality:

$$\theta_2 \leq C\Delta t(\|\chi^n\| + \|\eta^n\| + \|\chi^{n-1}\| + \|\eta^{n-1}\|)\|\chi^n\| \leq C\Delta t(\|\chi^n\|^2 + \|\chi^{n-1}\|^2) + C\Delta t\, h^{2k+2}.$$

For the term θ_3, we use the definition (3.16) and write

$$\theta_3 = -\frac{3}{2}\Delta t\sum_{j=1}^{N}\alpha(u_h^n)|_{x_j}[\chi^n - \eta^n]|_{x_j}[\chi^n]|_{x_j} + \frac{1}{2}\Delta t\sum_{j=1}^{N}\alpha(u_h^{n-1})|_{x_j}[\chi^{n-1} - \eta^{n-1}]|_{x_j}[\chi^n]|_{x_j}$$
$$- \frac{3}{2}\Delta t\alpha(u_h^n)|_{x_0}(\chi^{n,+} - \eta^{n,+})|_{x_0})(\chi^{n,+}|_{x_0}) + \frac{1}{2}\Delta t\alpha(u_h^{n-1})|_{x_0}(\chi^{n-1,+} - \eta^{n-1,+})|_{x_0})(\chi^{n,+}|_{x_0})$$
$$- \frac{3}{2}\Delta t\alpha(u_h^n)|_{x_{N+1}}(\chi^{n,-} - \eta^{n,-})|_{x_{N+1}})(\chi^{n,-}|_{x_{N+1}})$$
$$+ \frac{1}{2}\Delta t\alpha(u_h^{n-1})|_{x_{N+1}}(\chi^{n-1,-} - \eta^{n-1,-})|_{x_{N+1}})(\chi^{n,-}|_{x_{N+1}}).$$

After some manipulation we rewrite the first two terms in θ_3, i.e. the sums from

$j = 1, \cdots, N$, as:

$$
\begin{aligned}
-\frac{3}{2}\Delta t \sum_{j=1}^{N} \alpha(u_h^n)|_{x_j}[\chi^n - \eta^n]|_{x_j}[\chi^n]|_{x_j} + \frac{1}{2}\Delta t \sum_{j=1}^{N} \alpha(u_h^{n-1})|_{x_j}[\chi^{n-1} - \eta^{n-1}]|_{x_j}[\chi^n]|_{x_j} \\
= -\frac{1}{2}\Delta t \sum_{j=1}^{N} \alpha(u_h^n)|_{x_j}[\chi^n]^2|_{x_j} - \frac{1}{2}\Delta t \sum_{j=1}^{N} \alpha(u_h^{n-1})|_{x_j}[\chi^{n-1}]^2|_{x_j} \\
+ \Delta t \sum_{j=1}^{N} \left(\alpha(u_h^{n-1}) - \alpha(u_h^n)\right)|_{x_j}[\chi^{n-1} - \eta^{n-1}]|_{x_j}[\chi^{n-1}]|_{x_j} \\
- \frac{1}{2}\Delta t \sum_{j=1}^{N} \alpha(u_h^{n-1})|_{x_j}[\chi^{n-1} - \eta^{n-1}]|_{x_j}[\chi^{n-1} - \chi^n]|_{x_j} \\
+ \Delta t \sum_{j=1}^{N} \alpha(u_h^n)|_{x_j}[\chi^{n-1} - \eta^{n-1}]|_{x_j}[\chi^{n-1} - \chi^n]|_{x_j} \\
+ \Delta t \sum_{j=1}^{N} \alpha(u_h^n)|_{x_j}[(\chi^{n-1} - \chi^n) - (\eta^{n-1} - \eta^n)]|_{x_j}[\chi^n]|_{x_j} \\
+ \frac{1}{2}\Delta t \sum_{j=1}^{N} \alpha(u_h^n)|_{x_j}[\eta^n]|_{x_j}[\chi^n]|_{x_j} + \frac{1}{2}\Delta t \sum_{j=1}^{N} \alpha(u_h^{n-1})|_{x_j}[\eta^{n-1}]|_{x_j}[\chi^{n-1}]|_{x_j}.
\end{aligned}
\tag{3.65}
$$

We now bound the terms in the right-hand side of (3.65) except for the first two terms. We write

$$
\begin{aligned}
&\alpha(u_h^{n-1})|_{x_j} - \alpha(u_h^n)|_{x_j} \\
&= (\alpha(u_h^{n-1})|_{x_j} - \alpha(u^{n-1})|_{x_j}) + (\alpha(u^{n-1})|_{x_j} - \alpha(u^n)|_{x_j}) - (\alpha(u_h^n)|_{x_j} - \alpha(u^n)|_{x_j}).
\end{aligned}
$$

From (3.22) and (3.16), we have

$$
|\alpha(u_h^{n-1})|_{x_j} - \alpha(u_h^n)|_{x_j}| \le C\|u_h^{n-1} - u^{n-1}\|_\infty + C\|u_h^n - u^n\|_\infty + \frac{1}{2}\left|\, |f'(u^{n-1})|_{x_j}| - |f'(u^n)|_{x_j}|\,\right|.
$$

With a Taylor expansion, we obtain

$$
\left|\alpha(u_h^{n-1})|_{x_j} - \alpha(u_h^n)|_{x_j}\right| \le C\left(\|u^{n-1} - u_h^{n-1}\|_\infty + \|u^n - u_h^n\|_\infty + \Delta t\right), \quad \forall\, 1 \le j \le N.
$$

With the assumption $\|\chi^n\| \leq h^{3/2}$ and $\|\chi^{n-1}\| \leq h^{3/2}$, bound (3.31) and approximation results, we have

$$\left|\alpha(u_h^{n-1})|_{x_j} - \alpha(u_h^n)|_{x_j}\right| \leq C(h + \Delta t), \quad \forall\, 1 \leq j \leq N.$$

Using trace inequalities, we then have

$$\Delta t \sum_{j=1}^{N} \left(\alpha(u_h^{n-1})|_{x_j} - \alpha(u_h^n)|_{x_j}\right) [\chi^{n-1}]^2|_{x_j} \leq C\Delta t(1 + h^{-1}\Delta t)\|\chi^{n-1}\|^2.$$

With the CFL condition, we conclude a bound for part of the third term in (3.65):

$$\Delta t \sum_{j=1}^{N} \left(\alpha(u_h^{n-1})|_{x_j} - \alpha(u_h^n)|_{x_j}\right) [\chi^{n-1}]^2|_{x_j} \leq C\Delta t\|\chi^{n-1}\|^2.$$

Similarly, for the other part of the third term in (3.65), we have

$$-\Delta t \sum_{j=1}^{N} \left(\alpha(u_h^{n-1})|_{x_j} - \alpha(u_h^n)|_{x_j}\right) [\eta^{n-1}]|_{x_j}[\chi^{n-1}]|_{x_j} \leq C\Delta t\|\chi^{n-1}\|^2 + C\Delta t\, h^{2k+1}.$$

The fourth term in (3.65) is bounded by Cauchy-Schwarz's inequality, trace inequalities, approximation results, the CFL condition and (3.19):

$$\begin{aligned}\frac{1}{2}\Delta t \sum_{j=1}^{N} \alpha(u_h^{n-1})|_{x_j}[\chi^{n-1} - \eta^{n-1}]|_{x_j}[\chi^{n-1} - \chi^n]|_{x_j} &\leq \|\chi^{n-1} - \chi^n\|^2 + C\Delta t^2 h^{-2}\|\chi^{n-1}\|^2 + C\Delta t^2\, h^{2k} \\ &\leq \|\chi^{n-1} - \chi^n\|^2 + C\Delta t\|\chi^{n-1}\|^2 + C\Delta t h^{2k+2}.\end{aligned}$$

The fifth term in (3.65) is handled exactly like the fourth term. Similarly the first part in the sixth term has the following bound:

$$\Delta t \sum_{j=1}^{N} \alpha(u_h^n)|_{x_j}[\chi^{n-1} - \chi^n]|_{x_j}[\chi^n]|_{x_j} \leq \|\chi^{n-1} - \chi^n\|^2 + C\Delta t\|\chi^n\|^2.$$

For the second part, we use a Taylor expansion in time and the CFL condition:

$$\Delta t \sum_{j=1}^{N} \alpha(u_h^n)|_{x_j}[\eta^{n-1} - \eta^n]|_{x_j}[\chi^n]|_{x_j} \leq C\Delta t^2 h^k\|\chi^n\| \leq C\Delta t\|\chi^n\|^2 + C\Delta t\, h^{2k+2}.$$

The last two terms in (3.65) are treated almost identically, using approximation results, and the boundedness of α:

$$\begin{aligned}\frac{1}{2}\Delta t\sum_{j=1}^{N}\alpha(u_h^n)|_{x_j}[\eta^n]|_{x_j}[\chi^n]|_{x_j}+\frac{1}{2}\Delta t\sum_{j=1}^{N}\alpha(u_h^{n-1})|_{x_j}[\eta^{n-1}]|_{x_j}[\chi^{n-1}]|_{x_j}\\ \leq C\varepsilon^{-1}\Delta t\,h^{2k+1}+\varepsilon\Delta t\sum_{j=1}^{N}\alpha(u_h^n)|_{x_j}[\chi^n]^2|_{x_j}\\ +\varepsilon\Delta t\sum_{j=1}^{N}\alpha(u_h^{n-1})|_{x_j}[\chi^{n-1}]^2|_{x_j},\quad \forall\varepsilon>0.\end{aligned}$$

The boundary terms in θ_3 can be handled in the same fashion. To summarize, with (3.60), the term θ_3 is bounded as:

$$\begin{aligned}&\theta_3\leq C\Delta t(\|\chi^n\|^2+\|\chi^{n-1}\|^2)+C\Delta t^6+C\Delta t\,(1+\varepsilon^{-1})h^{2k+1}\\ &-(\frac{1}{2}-\varepsilon)\Delta t\left(\alpha(u_h^n)|_{x_0}(\chi^{n,+}|_{x_0})^2+\alpha(u_h^n)|_{x_{N+1}}(\chi^{n,-}|_{x_{N+1}})^2+\sum_{j=1}^{N}\alpha(u_h^n)|_{x_j}[\chi^n]|_{x_j}^2\right)\\ &-(\frac{1}{2}-\varepsilon)\Delta t\left(\alpha(u_h^{n-1})|_{x_0}(\chi^{n-1,+}|_{x_0})^2+\alpha(u_h^{n-1})|_{x_{N+1}}(\chi^{n-1,-}|_{x_{N+1}})^2+\sum_{j=1}^{N}\alpha(u_h^{n-1})|_{x_j}[\chi^{n-1}]|_{x_j}^2\right),\\ &\forall\varepsilon>0,\quad n\geq 2.\end{aligned}$$

For $n=1$, the term θ_3 is simply bounded as:

$$\begin{aligned}&\theta_3\leq C\Delta t\|\chi^1\|^2+C\Delta t\,(1+\varepsilon^{-1})h^{2k+1}\\ &-(\frac{1}{2}-\varepsilon)\Delta t\left(\alpha(u_h^1)|_{x_0}(\chi^{1,+}|_{x_0})^2+\alpha(u_h^1)|_{x_{N+1}}(\chi^{1,-}|_{x_{N+1}})^2+\sum_{j=1}^{N}\alpha(u_h^1)|_{x_j}[\chi^1]|_{x_j}^2\right)+6\|\chi^1\|^2,\\ &\forall\varepsilon>0.\end{aligned}$$

Combining the bounds above for θ_i, $1\leq i\leq 3$, we conclude the proof.

3.3.4 Proof of Theorem 3.2

The proof for the forward Euler scheme is also done by induction. It is a less technical proof than for the Adams–Bashforth scheme. We skip many details and give an outline

of the proof. Denote

$$\xi^n = \tilde{u}_h^n - \Pi_h u^n.$$

The induction hypothesis is less restrictive than for the Adams-Bashforth method, which yields a convergence result that is valid for polynomials of degree one and above.

$$\|\xi^\ell\| \leq h, \quad \forall 0 \leq \ell \leq M. \tag{3.66}$$

Since $\xi^0 = 0$, the hypothesis (3.66) is trivially satisfied for $\ell = 0$. Fix $\ell \in \{1, \ldots, M\}$ and assume that

$$\|\xi^n\| \leq h, \quad \forall 0 \leq n \leq \ell - 1. \tag{3.67}$$

We now have to show that (3.67) is valid for $n = \ell$. We begin by deriving an error inequality. We fix an interval I_j for $0 \leq j \leq N$. Using consistency in space of the scheme:

$$\int_{I_j} u_t^n \phi_h = \mathcal{H}_j(u^n, \phi_h), \quad 0 \leq n \leq M, \tag{3.68}$$

we obtain, after some manipulation, the error equation:

$$\begin{aligned} \int_{I_j} \left(\xi^{n+1} - \xi^n\right) \phi_h = \int_{I_j} \left(\Delta t\, u_t^n - u^{n+1} + u^n\right) \phi_h \\ + \int_{I_j} \left(\eta^{n+1} - \eta^n\right) \phi_h + \Delta t \left(\mathcal{H}_j(u_h^n, \phi_h) - \mathcal{H}_j(u^n, \phi_h)\right). \end{aligned} \tag{3.69}$$

The first term in the right-hand side of (3.69) is bounded using a Taylor expansion, whereas the second term vanishes due to (3.5). Summing over the elements from $j = 0, \ldots, N$ results in

$$\int_0^L \left(\xi^{n+1} - \xi^n\right) \phi_h \leq C\Delta t^2 \int_0^L |\phi_h| + \Delta t \sum_{j=0}^{N} \left(\mathcal{H}_j(u_h^n, \phi_h) - \Delta t \mathcal{H}_j(u^n, \phi_h)\right). \tag{3.70}$$

Define

$$\tilde{b}^n(\phi_h) = \Delta t \sum_{j=0}^{N} \left(\mathcal{H}_j(u_h^n, \phi_h) - \Delta t \mathcal{H}_j(u^n, \phi_h) \right). \tag{3.71}$$

Then equation (3.70) becomes

$$\int_0^L \left(\xi^{n+1} - \xi^n \right) \phi_h \leq C\Delta t^2 \int_0^L |\phi_h| + \tilde{b}^n(\phi_h), \tag{3.72}$$

and Cauchy Schwarz's and Young's inequalities imply

$$\int_0^L \left(\xi^{n+1} - \xi^n \right) \phi_h \leq C\Delta t^3 + C\Delta t \|\phi_h\|^2 + \tilde{b}^n(\phi_h). \tag{3.73}$$

We now choose $\phi_h = \xi^n$ to obtain:

$$\int_0^L \left(\xi^{n+1} - \xi^n \right) \xi^n \leq C\Delta t^3 + C\Delta t \|\xi^n\|^2 + \tilde{b}^n(\xi^n). \tag{3.74}$$

It then follows that

$$\frac{1}{2}\|\xi^{n+1}\|^2 - \frac{1}{2}\|\xi^n\|^2 \leq \frac{1}{2}\|\xi^{n+1} - \xi^n\|^2 + C\Delta t^3 + C\Delta t \|\xi^n\|^2 + \tilde{b}^n(\xi^n). \tag{3.75}$$

The terms $\|\xi^{n+1} - \xi^n\|$ and $\tilde{b}^n(\xi^n)$ are bounded by:

$$\|\xi^{n+1} - \xi^n\|^2 \leq C\Delta t^4 + C\Delta t \|\xi^n\|^2 + C\Delta t\, h^{2k+2}, \tag{3.76}$$

$$\tilde{b}^n(\xi^n) \leq C\Delta t \|\xi^n\|^2 + C\Delta t\, h^{2k+1}. \tag{3.77}$$

Proof of (3.76) follows closely the proof of Lemma 3.3 but is less technical. We skip it. Proof of (3.77) differs from the proof of Lemma 3.4 and details are given in Appendix 3.3.9. The error inequality simplifies to:

$$\|\xi^{n+1}\|^2 - \|\xi^n\|^2 \leq C\Delta t^3 + C\Delta t \|\xi^n\|^2 + C\Delta t\, h^{2k+1}.$$

Summing from $n = 0, \ldots, \ell - 1$, and using the fact that $\xi^0 = 0$, one obtains:

$$\|\xi^\ell\|^2 \leq C\Delta t^2 + Ch^{2k+1} + C\Delta t \sum_{n=0}^{\ell-1} \|\xi^n\|^2.$$

We now apply Gronwall's inequality:

$$\|\xi^\ell\|^2 \leq C_4 T \mathrm{e}^T (\Delta t^2 + h^{2k+1}),$$

where C_4 is independent of ℓ. Employing the CFL condition $\Delta t = O(h^2)$, one has:

$$\|\xi^\ell\| \leq \left(C_4 T \mathrm{e}^T\right)^{1/2} \left(\Delta t + h^{k+1/2}\right) = \left(C_4 T \mathrm{e}^T\right)^{1/2} \left(h^2 + h^{k+1/2}\right).$$

Hence the induction is complete if h is small enough so that

$$C_4 T \mathrm{e}^T h < 1.$$

Since $\|\eta^\ell\| \leq C h^{k+1}$ and $\|u^\ell - u_h^\ell\| \leq \|\eta^\ell\| + \|\xi^\ell\|$ one obtains:

$$\|u^\ell - u_h^\ell\| \leq C(\Delta t + h^{k+1/2}),$$

and we conclude the proof.

3.3.5 Numerical results: scalar case

3.3.6 Scalar case

In this section, we use the method of manufactured solutions to numerically verify convergence rates. Solutions to the inviscid Burger's equation,

$$\frac{\partial u}{\partial t} + \frac{\partial}{\partial x}\left(\frac{1}{2}u^2\right) = 0, \tag{3.78}$$

are approximated using the Adams–Bashforth scheme (3.28). We consider the following exact solution to (3.78) posed in the interval $[0, 1]$:

$$u(x,t) = \sin(2\pi x)\cos(t)\left(1 + \cos^2(2\pi x)\right).$$

Convergence rates in space, given in Table 3.1, are calculated for polynomial degrees $k = 1, 2, 3$ by fixing a small timestep $\Delta t = 10^{-4}$ so the temporal error is small

compared to the spatial error. The spatial discretization parameter $h = 1/2^m$ for $m = 1, \ldots, 5$, and we evolve the solution for ten timesteps. Our results yield a rate of $k + 1$ in space, verifying the fact that the convergence estimate in Theorem 3.1 is suboptimal.

Errors and rates in time are provided in Table 3.2. We fix $h = 1/4$, vary $\Delta t = 1/2^m$, $m = 9, \ldots, 12$, and consider high polynomial degrees $k = 10, 11$ so the spatial error is smaller than the temporal error. We evolve the solution to the final time $T = 1$ s. We recover the expected second order rate in time.

	$k=1$		$k=2$		$k=3$	
h	L^2 error	rate	L^2 error	rate	L^2 error	rate
5.000×10^{-1}	3.03340×10^{-1}	–	1.12946×10^{-1}	–	1.12951×10^{-1}	–
2.500×10^{-1}	1.77840×10^{-1}	7.7×10^{-1}	3.52657×10^{-2}	1.68	1.47901×10^{-2}	2.93
1.250×10^{-1}	3.93757×10^{-2}	2.18	6.97597×10^{-3}	2.34	1.03024×10^{-3}	3.84
6.250×10^{-2}	1.03568×10^{-2}	1.93	9.20564×10^{-4}	2.92	6.86900×10^{-5}	3.91
3.125×10^{-2}	2.66598×10^{-3}	1.96	1.18688×10^{-4}	2.96	4.60065×10^{-6}	3.90

Table 3.1 : Errors and rates in space for the manufactured solution to Burgers'equation.

	$k=10$		$k=11$	
Δt	L^2 error	rate	L^2 error	rate
1.953×10^{-3}	2.15378×10^{-5}	–	2.24857×10^{-5}	–
9.766×10^{-4}	5.85285×10^{-6}	1.88	6.26141×10^{-6}	1.84
4.883×10^{-4}	1.50158×10^{-6}	1.96	1.61103×10^{-6}	1.96
2.441×10^{-4}	3.84742×10^{-7}	1.96	4.06618×10^{-7}	1.99

Table 3.2 : Errors and rates in time for the manufactured solution to Burgers'equation.

3.3.7 Numerical results: system case

In this section we compute convergence rates for a hyperbolic system that is the motivation for this work: a model which describes one–dimensional blood flow in an elastic vessel:

$$\frac{\partial}{\partial t}\begin{bmatrix} A \\ Q \end{bmatrix} + \frac{\partial}{\partial x}\begin{bmatrix} Q \\ \alpha\frac{Q^2}{A} + \frac{1}{\rho}(A\psi - \Psi) \end{bmatrix} = \begin{bmatrix} 0 \\ -2\pi\nu\frac{\alpha}{\alpha-1}\frac{Q}{A} \end{bmatrix}, \tag{3.79}$$

$$p = p_0 + \psi(A; A_0), \quad \Psi = \int_{A_0}^{A} \psi(\xi; A_0)d\xi. \tag{3.80}$$

The variables are vessel cross sectional area A and fluid momentum Q. The parameters are the reference pressure $p_0 = 0$ dynes/cm^2, the reference cross sectional area $A_0 = 1$ cm^2, the non–dimensional Coriolis coefficient $\alpha = 1.1$, the fluid density $\rho = 1.06$ g/cm^3, and the kinematic viscosity $\nu = 3.302 \times 10^{-2}$ cm^2/s. For these computations we use a typical form for the function relating area to pressure [65]:

$$\psi = \beta(A^{1/2} - A_0^{1/2}),$$

with $\beta = 1$ dynes/cm^3. In defining the numerical flux for our computations, we use a version of the local Lax–Friedrichs flux suggested for nonlinear hyperbolic systems in [20]. With $\mathbf{U} = [A, Q]^T$ and $\lambda_1(\mathbf{U})$ and $\lambda_2(\mathbf{U})$ the eigenvalues of the Jacobian of the flux function in (2.18), the flux is defined with:

$$J(\mathbf{U}^-|_{x_j}, \mathbf{U}^+|_{x_j}) = \max\left(\left|\lambda_1(\mathbf{U}^-|_{x_j})\right|, \left|\lambda_1(\mathbf{U}^+|_{x_j})\right|, \left|\lambda_2(\mathbf{U}^-|_{x_j})\right|, \left|\lambda_2(\mathbf{U}^+|_{x_j})\right|\right).$$

To compute errors and rates, we solve (2.18) in the interval $[0, 1]$ with the following exact solution:

$$A(x,t) = \cos(2\pi x)\cos(t) + 2, \quad Q(x,t) = \sin(2\pi x)\cos(t).$$

The discretization for a hyperbolic system follows the same procedure as for a scalar hyperbolic equation. For these simulations, we employ the second–order Adams–Bashforth scheme (3.28) with the local Lax–Friedrichs numerical flux.

Errors and convergence rates in space, provided in Tables 6.1 and 6.2 , are determined by fixing a small time step $\Delta t = 2 \times 10^{-5}$ s and taking $h = 1/2^m$ for $m = 1, \ldots 5$. We consider $k = 1, 2, 3$ and evolve the solution for ten time steps.

	$k=1$		$k=2$		$k=3$	
h	L^2 error	rate	L^2 error	rate	L^2 error	rate
5.000×10^{-1}	8.50463×10^{-2}	–	8.50463×10^{-2}	–	2.77383×10^{-3}	–
2.500×10^{-1}	6.27702×10^{-2}	0.43	8.38200×10^{-3}	3.34	8.33345×10^{-4}	1.73
1.250×10^{-1}	1.61152×10^{-2}	1.96	1.07125×10^{-3}	2.96	5.31039×10^{-5}	3.97
6.250×10^{-2}	4.05695×10^{-3}	1.98	1.34722×10^{-4}	2.99	3.34118×10^{-6}	3.99
3.125×10^{-2}	1.01713×10^{-3}	1.99	1.69031×10^{-5}	2.99	2.10357×10^{-7}	3.98

Table 3.3 : Errors and rates in space for A.

	$k=1$		$k=2$		$k=3$	
h	L^2 error	rate	L^2 error	rate	L^2 error	rate
5.000×10^{-1}	3.07761×10^{-1}	–	1.72654×10^{-2}	–	1.72638×10^{-2}	–
2.500×10^{-1}	6.27688×10^{-2}	2.29	8.38233×10^{-3}	1.04	8.33176×10^{-4}	4.37
1.250×10^{-1}	1.61145×10^{-2}	1.96	1.07130×10^{-3}	2.96	5.30850×10^{-5}	3.97
6.250×10^{-2}	4.05679×10^{-3}	1.98	1.34717×10^{-4}	2.99	3.33998×10^{-6}	3.99
3.125×10^{-2}	1.01736×10^{-3}	1.99	1.68933×10^{-5}	2.99	2.10567×10^{-7}	3.98

Table 3.4 : Errors and rates in space for Q.

To calculate the rate in time, we make the error in space small by choosing high order polynomials $k = 8, 9$ on a mesh with size $h = 1/4$. By taking h to be constant, we avoid overly refining Δt due to the CFL condition. The time step $\Delta t = 1/2^m$ for

$m = 10, \ldots, 13$ and we evolve the solution to the final time $T = 1$ s. Results are displayed in Tables 6.3 and 6.4.

	$k = 8$		$k = 9$	
Δt	L^2 error	rate	L^2 error	rate
9.766×10^{-4}	2.90612×10^{-7}	–	2.98344×10^{-7}	–
4.883×10^{-4}	7.27141×10^{-8}	1.99	7.46399×10^{-8}	1.99
2.441×10^{-4}	1.82053×10^{-8}	1.99	1.86720×10^{-8}	1.99
1.221×10^{-4}	4.59094×10^{-9}	1.98	4.67588×10^{-9}	1.99

Table 3.5 : Errors and rates in time for A.

	$k = 8$		$k = 9$	
Δt	L^2 error	rate	L^2 error	rate
9.766×10^{-4}	1.88619×10^{-7}	–	1.91639×10^{-7}	–
4.883×10^{-4}	4.71556×10^{-8}	1.99	4.79006×10^{-8}	2.00
2.441×10^{-4}	1.18056×10^{-8}	1.99	1.19766×10^{-8}	1.99
1.221×10^{-4}	2.99433×10^{-9}	1.97	2.99764×10^{-9}	1.99

Table 3.6 : Errors and rates in time for Q.

The computed rates in space and time indicate that results analogous to Theorems 3.1 and 3.2 can be expected for such numerical discretizations of nonlinear hyperbolic systems. Numerical analysis for systems will be the subject of future work.

3.3.8 Proof of bound (3.62)

We use Taylor expansions up to third order. Note that below, we also use the fact that the exact solution u vanishes at x_0 and x_{N+1}:

$$
\begin{aligned}
&f(u_h^n) - f(u^n) = f'(u^n)(u_h^n - u^n) + \frac{1}{2}f''(u^n)(u_h^n - u^n)^2 + \frac{1}{6}f'''(\zeta_1^n)(u_h^n - u^n)^3 \\
&= f'(u^n)(\chi^n - \eta^n) + \frac{1}{2}f''(u^n)(\chi^n - \eta^n)^2 + \frac{1}{6}f'''(\zeta_1^n)(\chi^n - \eta^n)^3, \\
&= f'(u^n)\chi^n + \frac{1}{2}f''(u^n)(\chi^n)^2 - f'(u^n)\eta^n - f''(u^n)\chi^n\eta^n + \frac{1}{2}f''(u^n)(\eta^n)^2 + \frac{1}{6}f'''(\zeta_1^n)(\chi^n - \eta^n)^3 \\
&= \beta_1 + \cdots + \beta_6, \\
&f(\{u_h^n\}) - f(u^n) = f'(u^n)(\{u_h^n\} - \{u^n\}) + \frac{1}{2}f''(u^n)(\{u_h^n\} - u^n)^2 + \frac{1}{6}f'''(\zeta_2^n)(\{u_h^n\} - u^n)^3 \\
&= f'(u^n)(\{\chi^n\} - \{\eta^n\}) + \frac{1}{2}f''(u^n)(\{\chi^n\} - \{\eta^n\})^2 + \frac{1}{6}f'''(\zeta_2^n)(\{\chi^n\} - \{\eta^n\})^3, \\
&= f'(u^n)\{\chi^n\} + \frac{1}{2}f''(u^n)(\{\chi^n\})^2 - f'(u^n)\{\eta^n\} - f''(u^n)\{\chi^n\}\{\eta^n\} \\
&+ \frac{1}{2}f''(u^n)(\{\eta^n\})^2 + \frac{1}{6}f'''(\zeta_2^n)(\{\chi^n\} - \{\eta^n\})^3 \\
&= \gamma_1 + \cdots + \gamma_6,
\end{aligned}
$$

$$
\begin{aligned}
&f(\frac{1}{2}u_h^{n,+}|_{x_0}) - f(u^n|_{x_0}) \\
&= f'(u^n|_{x_0})(\frac{1}{2}u_h^{n,+} - u^n)|_{x_0} + \frac{1}{2}f''(u^n|_{x_0})(\frac{1}{2}u_h^{n,+} - u^n)^2|_{x_0} + \frac{1}{6}f'''(\zeta_3^n)(\frac{1}{2}u_h^{n,+} - u^n)^3|_{x_0} \\
&= f'(u^n|_{x_0})(\frac{1}{2}u_h^{n,+} - \frac{1}{2}u^n)|_{x_0} + \frac{1}{2}f''(u^n|_{x_0})(\frac{1}{2}u_h^{n,+} - \frac{1}{2}u^n)^2|_{x_0} + \frac{1}{6}f'''(\zeta_3^n)(\frac{1}{2}u_h^{n,+} - \frac{1}{2}u^n)^3|_{x_0} \\
&= f'(u^n|_{x_0})(\frac{1}{2}\chi^{n,+} - \frac{1}{2}\eta^{n,+})|_{x_0} + \frac{1}{2}f''(u^n|_{x_0})(\frac{1}{2}\chi^{n,+} - \frac{1}{2}\eta^{n,+})^2|_{x_0} + \frac{1}{6}f'''(\zeta_3^n)(\frac{1}{2}\chi^{n,+} - \frac{1}{2}\eta^{n,+})^3|_{x_0} \\
&= f'(u^n|_{x_0})\frac{1}{2}\chi^{n,+}|_{x_0} + \frac{1}{2}f''(u^n|_{x_0})(\frac{1}{2}\chi^{n,+}|_{x_0})^2 - f'(u^n|_{x_0})\frac{1}{2}\eta^{n,+}|_{x_0} \\
&- f''(u^n|_{x_0})(\frac{1}{2}\chi^{n,+}|_{x_0})(\frac{1}{2}\eta^{n,+}|_{x_0}) + \frac{1}{2}f''(u^n|_{x_0})(\frac{1}{2}\eta^{n,+}|_{x_0})^2 + \frac{1}{6}f'''(\zeta_3^n)(\frac{1}{2}\chi^{n,+} - \frac{1}{2}\eta^{n,+})^3|_{x_0} \\
&= \sigma_1 + \cdots + \sigma_6 \\
&f(\frac{1}{2}u_h^{n,-}|_{x_{N+1}}) - f(u^n|_{x_{N+1}}) \\
&= f'(u^n|_{x_{N+1}})\frac{1}{2}\chi^{n,-}|_{x_{N+1}} + \frac{1}{2}f''(u^n|_{x_{N+1}})(\frac{1}{2}\chi^{n,-}|_{x_{N+1}})^2 - f'(u^n|_{x_{N+1}})\frac{1}{2}\eta^{n,-}|_{x_{N+1}} \\
&- f''(u^n|_{x_{N+1}})(\frac{1}{2}\chi^{n,-}|_{x_{N+1}})(\frac{1}{2}\eta^{n,-}|_{x_{N+1}}) + \frac{1}{2}f''(u^n|_{x_{N+1}})(\frac{1}{2}\eta^{n,-}|_{x_{N+1}})^2 \\
&+ \frac{1}{6}f'''(\zeta_4^n)(\frac{1}{2}\chi^{n,-} - \frac{1}{2}\eta^{n,-})^3|_{x_{N+1}} \\
&= \psi_1 + \cdots + \psi_6
\end{aligned}
\tag{3.81}
$$

where ζ_1^n and ζ_2^n are some points between u_h^n and u^n, and $\{u_h^n\}$ and u^n respectively. We substitute these expansions in the terms $\mathcal{F}(n, \chi^n)$ and write:

$$
\mathcal{F}(n, \chi^n) = X_1 + \ldots + X_6, \tag{3.82}
$$

with

$$
X_i = \Delta t \sum_{j=0}^{N} \int_{I_j} \beta_i \frac{d\chi^n}{dx} - \Delta t \sum_{j=1}^{N} \gamma_i|_{x_j}[\chi^n]|_{x_j} + \Delta t \sigma_i \chi^{n,+}|_{x_0} - \Delta t \psi_i \chi^{n,-}|_{x_{N+1}}, \quad 1 \le i \le 6. \tag{3.83}
$$

We have X_1 equal to:

$$X_1 = \Delta t \sum_{j=0}^{N} \int_{I_j} f'(u^n)\chi^n \frac{d\chi^n}{dx} - \Delta t \sum_{j=1}^{N} f'(u^n)|_{x_j}\{\chi^n\}|_{x_j}[\chi^n]|_{x_j}$$
$$+ \Delta t f'(u^n|_{x_0})\frac{1}{2}(\chi^{n,+}|_{x_0})^2 - \Delta t f'(u^n|_{x_{N+1}})\frac{1}{2}(\chi^{n,-}|_{x_{N+1}})^2.$$

Integrate by parts the first term in the definition of X_1. The term X_1 then simplifies to

$$X_1 = -\frac{1}{2}\Delta t \sum_{j=0}^{N} \int_{I_j} (\frac{\partial}{\partial x} f'(u^n))(\chi^n)^2 \leq C\Delta t \|\chi^n\|^2.$$

Using the assumption $\|\chi^n\| \leq h^{3/2}$ and trace inequalities, we have

$$\begin{aligned} X_2 &= \frac{1}{2}\Delta t \sum_{j=0}^{N} \int_{I_j} f''(u^n)(\chi^n)^2 \frac{d\chi^n}{dx} - \frac{1}{2}\Delta t \sum_{j=1}^{N} f''(u^n)|_{x_j}(\{\chi^n\})^2|_{x_j}[\chi^n]|_{x_j} \\ &+ \Delta t \frac{1}{2} f''(u^n|_{x_0})(\frac{1}{2}\chi^{n,+}|_{x_0})^2 \chi^{n,+}|_{x_0} - \Delta t \frac{1}{2} f''(u^n|_{x_{N+1}})(\frac{1}{2}\chi^{n,-}|_{x_{N+1}})^2 \chi^{n,-}|_{x_{N+1}} \\ &\leq C\Delta t \|\chi^n\|_\infty h^{-1} \|\chi^n\|^2 \leq C\Delta t \|\chi^n\|^2. \end{aligned} \tag{3.84}$$

To bound the term X_3 we define the following piecewise constant function u_c^n elementwise as:

$$u_c^n|_{I_j}(x) = u^n|_{x_j}, \quad \forall x \in I_j, \quad \forall 0 \leq j \leq N. \tag{3.85}$$

We note that

$$\|f'(u^n) - f'(u_c^n)\|_\infty \leq Ch. \tag{3.86}$$

We then rewrite the term X_3

$$
\begin{aligned}
X_3 &= -\Delta t \sum_{j=0}^{N} \int_{I_j} f'(u^n)\eta^n \frac{d\chi^n}{dx} + \Delta t \sum_{j=1}^{N} f'(u^n)\{\eta^n\}|_{x_j}[\chi^n]|_{x_j} \\
&- \Delta t f'(u^n|_{x_0})\frac{1}{2}\eta^{n,+}|_{x_0}\chi^{n,+}|_{x_0} + \Delta t f'(u^n|_{x_{N+1}})\frac{1}{2}\eta^{n,-}|_{x_{N+1}}\chi^{n,-}|_{x_{N+1}} \\
&= -\Delta t \sum_{j=0}^{N} \int_{I_j} (f'(u^n) - f'(u_c^n))\eta^n \frac{d\chi^n}{dx} - \Delta t \sum_{j=0}^{N} f'(u_c^n) \int_{I_j} \eta^n \frac{d\chi^n}{dx} \\
&+ \Delta t \sum_{j=1}^{N} (f'(u^n) - f'(\{u_h^n\}))|_{x_j}\{\eta^n\}|_{x_j}[\chi^n]|_{x_j} + \Delta t \sum_{j=1}^{N} f'(\{u_h^n\})|_{x_j}\{\eta^n\}|_{x_j}[\chi^n]|_{x_j} \\
&- \Delta t (f'(u^n|_{x_0}) - f'(\frac{1}{2}u_h^{n,+}|_{x_0}))\frac{1}{2}\eta^{n,+}|_{x_0}\chi^{n,+}|_{x_0} \\
&- \Delta t f'(\frac{1}{2}u_h^{n,+}|_{x_0})\eta^{n,+}|_{x_0}\chi^{n,+}|_{x_0} \\
&+ \Delta t (f'(u^n|_{x_{N+1}}) - f'(\frac{1}{2}u_h^{n,-}|_{x_{N+1}}))\frac{1}{2}\eta^{n,-}|_{x_{N+1}}\chi^{n,-}|_{x_{N+1}} \\
&+ \Delta t f'(\frac{1}{2}u_h^{n,-}|_{x_{N+1}})\frac{1}{2}\eta^{n,-}|_{x_{N+1}}\chi^{n,-}|_{x_{N+1}}. \qquad (3.87)
\end{aligned}
$$

The second term above vanishes because of (3.5). The first term is bounded using approximation properties and (3.86).

$$
\Delta t \sum_{j=0}^{N} \int_{I_j} (f'(u^n) - f'(u_c^n))\eta^n \frac{d\chi^n}{dx} \leq C\Delta t\, h^{2k+2} + C\Delta t \|\chi^n\|^2.
$$

Using Taylor expansions, for some ζ_5^n, ζ_6^n, ζ_7^n we have

$$
\begin{aligned}
f'(u^n) - f'(\{u_h^n\}) &= f''(\zeta_5^n)\{u^n - u_h^n\} \leq C(\|\chi^n\|_\infty + \|\eta^n\|_\infty), \\
f'(u^n|_{x_0}) - f'(\frac{1}{2}u_h^{n,+}|_{x_0}) &= f'(\frac{1}{2}u^n|_{x_0}) - f'(\frac{1}{2}u_h^{n,+}|_{x_0}) = f''(\zeta_6^n)(\frac{1}{2}u^n - \frac{1}{2}u_h^{n,+})|_{x_0} \\
&\leq C(\|\chi^n\|_\infty + \|\eta^n\|_\infty), \\
f'(u^n|_{x_{N+1}}) - f'(\frac{1}{2}u_h^{n,-}|_{x_{N+1}}) &= f'(\frac{1}{2}u^n|_{x_{N+1}}) - f'(\frac{1}{2}u_h^{n,-}|_{x_{N+1}}) = f''(\zeta_7^n)(\frac{1}{2}u^n - \frac{1}{2}u_h^{n,-})|_{x_{N+1}} \\
&\leq C(\|\chi^n\|_\infty + \|\eta^n\|_\infty).
\end{aligned}
$$

Using the assumption $\|\chi^n\| \leq h^{3/2}$ one then obtains

$$\Delta t \sum_{j=1}^{N} (f'(u^n) - f'(\{u_h^n\}))\{\eta^n\}|_{x_j}[\chi^n]|_{x_j} \leq C\Delta t\|\chi^n\|^2 + C\Delta t\, h^{2k+2},$$

$$-\Delta t(f'(u^n|_{x_0}) - f'(\frac{1}{2}u_h^{n,+}|_{x_0}))\frac{1}{2}\eta^{n,+}|_{x_0}\chi^{n,+}|_{x_0} \leq C\Delta t\|\chi^n\|^2 + C\Delta t\, h^{2k+2},$$

$$\Delta t(f'(u^n|_{x_{N+1}}) - f'(\frac{1}{2}u_h^{n,-}|_{x_{N+1}}))\frac{1}{2}\eta^{n,-}|_{x_{N+1}}\chi^{n,-}|_{x_{N+1}} \leq C\Delta t\|\chi^n\|^2 + C\Delta t\, h^{2k+2}.$$

For the remaining terms in (3.87) we employ (3.20) to obtain:

$$\Delta t \sum_{j=1}^{N} f'(\{u_h^n\})|_{x_j}\{\eta^n\}|_{x_j}[\chi^n]|_{x_j} \leq C\Delta t \sum_{j=1}^{N} \left(\alpha(u_h^n)|_{x_j} + C|[u_h^n]|_{x_j}|\right)\left|\{\eta^n\}|_{x_j}\right|\left|[\chi^n]|_{x_j}\right|$$

$$= C\Delta t \sum_{j=1}^{N} \alpha(u_h^n)|_{x_j}\left|\{\eta^n\}|_{x_j}\right|\left|[\chi^n]|_{x_j}\right| + C\Delta t \sum_{j=1}^{N} |[u_h^n]|\left|\{\eta^n\}|_{x_j}\right|\left|[\chi^n]|_{x_j}\right|, .$$

$$-\Delta t f'(\frac{1}{2}u_h^{n,+}|_{x_0})\eta^{n,+}|_{x_0}\chi^{n,+}|_{x_0} \leq C\Delta t\left(\alpha(u_h^n)|_{x_0} + |u_h^{n,+}|_{x_0}|\right)\left|\eta^{n,+}|_{x_0}\right|\left|\chi^{n,+}|_{x_0}\right|,$$

$$\Delta t f'(\frac{1}{2}u_h^{n,-}|_{x_{N+1}})\frac{1}{2}\eta^{n,-}|_{x_{N+1}}\chi^{n,-}|_{x_{N+1}} \leq C\Delta t\left(\alpha(u_h^n)|_{x_{N+1}} + |u_h^{n,-}|_{x_{N+1}}|\right)\left|\eta^{n,-}|_{x_{N+1}}\right|\left|\chi^{n,-}|_{x_{N+1}}\right|,$$

Using Cauchy-Schwarz's and Young's inequalities, approximation results and the assumption $\|\chi^n\| \leq h^{3/2}$, we obtain

$$\Delta t \sum_{j=1}^{N} f'(\{u_h^n\})|_{x_j}\{\eta^n\}|_{x_j}[\chi^n]|_{x_j} \leq \varepsilon\Delta t \sum_{j=1}^{N} \alpha(u_h^n)|_{x_j}[\chi^n]|_{x_j}^2 + C\varepsilon^{-1}\Delta t\, h^{2k+1} + C\Delta t\|\chi^n\|^2,$$

$$-\Delta t f'(\frac{1}{2}u_h^{n,+}|_{x_0})\eta^{n,+}|_{x_0}\chi^{n,+}|_{x_0} \leq \varepsilon\Delta t\alpha(u_h^n)|_{x_0}(\chi^{n,+}|_{x_0})^2 + C\varepsilon^{-1}\Delta t\, h^{2k+1} + C\Delta t\|\chi^n\|^2,$$

$$-\Delta t f'(\frac{1}{2}u_h^{n,-}|_{x_{N+1}})\eta^{n,-}|_{x_{N+1}}\chi^{n,-}|_{x_{N+1}} \leq \varepsilon\Delta t\alpha(u_h^n)|_{x_{N+1}}(\chi^{n,-}|_{x_{N+1}})^2 + C\varepsilon^{-1}\Delta t\, h^{2k+1} + C\Delta t\|\chi^n\|^2$$

In summary we have

$$X_3 \leq \varepsilon\Delta t\left(\alpha(u_h^n)|_{x_0}(\chi^{n,+}|_{x_0})^2 + \alpha(u_h^n)|_{x_{N+1}}(\chi^{n,-}|_{x_{N+1}})^2 + \sum_{j=1}^{N} \alpha(u_h^n)|_{x_j}[\chi^n]|_{x_j}^2\right)$$

$$+ C\varepsilon^{-1}\Delta t\, h^{2k+1} + C\Delta t\|\chi^n\|^2 + C\Delta t\, h^{2k+1}.$$

The bounds for X_4, X_5, and X_6 are standard applications of Cauchy Schwarz's inequality, Young's inequality, the induction hypothesis, assumption (3.3), and inequalities (3.32), (3.33), and (3.34)–(3.36):

$$\begin{aligned}
X_4 &= -\Delta t \sum_{j=0}^{N} \int_{I_j} f''(u_n)\chi^n \eta^n \frac{d\chi^n}{dx} + \Delta t \sum_{j=1}^{N} f''(u_n)|_{x_j}\{\chi^n\}|_{x_j}\{\eta^n\}|_{x_j}[\chi^n]|_{x_j} \\
&\quad - \Delta t f''(u^n|_{x_0})(\frac{1}{2}\chi^{n,+}|_{x_0})(\frac{1}{2}\eta^{n,+}|_{x_0})\chi^{n,+}|_{x_0} + \Delta t f''(u^n|_{x_{N+1}})(\frac{1}{2}\chi^{n,-}|_{x_{N+1}})(\frac{1}{2}\eta^{n,-}|_{x_{N+1}})\chi^{n,-}|_{x_{N+1}} \\
&\quad \leq C\Delta t \|\chi^n\|^2 + \Delta t\, h^{2k+1}, \qquad (3.88) \\
X_5 &= \frac{1}{2}\Delta t \sum_{j=0}^{N} \int_{I_j} f''(u_n)|_{x_j}(\eta^n)^2 \frac{d\chi^n}{dx} - \frac{1}{2}\Delta t \sum_{j=1}^{N} f''(u_n)\{\eta^n\}^2|_{x_j}[\chi^n]|_{x_j} \\
&\quad + \Delta t \frac{1}{2} f''(u^n|_{x_0})(\frac{1}{2}\eta^{n,+}|_{x_0})^2\chi^{n,+}|_{x_0} - \Delta t \frac{1}{2} f''(u^n|_{x_{N+1}})(\frac{1}{2}\eta^{n,-}|_{x_{N+1}})^2\chi^{n,-}|_{x_{N+1}} \\
&\quad \leq C\Delta t\, h^{2k+2} + C\Delta t \|\chi^n\|^2, \qquad (3.89) \\
X_6 &= \frac{1}{6}\Delta t \sum_{j=0}^{N} \int_{I_j} f'''(\zeta_1^n)(\chi^n - \eta^n)^3 \frac{d\chi^n}{dx} - \frac{1}{6}\Delta t \sum_{j=1}^{N} f'''(\zeta_2^n)(\{\chi^n\} - \{\eta^n\})^3|_{x_j}[\chi^n]|_{x_j} \\
&\quad + \Delta t \frac{1}{6} f'''(\zeta_3^n)(\frac{1}{2}\chi^{n,+} - \frac{1}{2}\eta^{n,+})^3|_{x_0}\chi^{n,+}|_{x_0} - \Delta t \frac{1}{6} f'''(\zeta_4^n)(\frac{1}{2}\chi^{n,-} - \frac{1}{2}\eta^{n,-})^3|_{x_{N+1}}\chi^{n,-}|_{x_{N+1}} \\
&\quad \leq C\Delta t \|\chi^n\|^2 + C\Delta t\, h^{2k+1}. \qquad (3.90)
\end{aligned}$$

We can then conclude by combining all the bounds above.

3.3.9 Proof of bound (3.77)

We rewrite, using the definition of α

$$\tilde{b}^n(\xi^n) = \theta_1 + \theta_2 + \theta_3,$$

with

$$\theta_1 = \Delta t \sum_{j=0}^{N} \int_{I_j} (f(\tilde{u}_h^n) - f(u^n))\frac{d\xi^n}{dx} - \Delta t \sum_{j=1}^{N} (f(\{\tilde{u}_h^n\}) - f(u^n))|_{x_j}[\xi^n]|_{x_j},$$

$$\theta_2 = \Delta t \sum_{j=1}^{N} \int_{I_j} (s(\tilde{u}_h^n) - s(u^n))\xi^n,$$

$$\theta_3 = -\Delta t \sum_{j=1}^{N} \alpha(\tilde{u}_h^n)|_{x_j}[\tilde{u}_h^n]|_{x_j}[\xi^n]|_{x_j}.$$

We note that the bound for θ_1 follows the argument of the proof of (3.62), where we substitute χ^n by ξ^n. As in the previous section, we use Taylor expansions up to third order and write the term $\tilde{b}^n(\xi^n)$ as a sum of six terms, X_i, $1 \le i \le 6$. Bounds for X_i are obtained in a similar fashion, except for the term X_2 which is bounded differently because the the induction hypothesis for the forward Euler scheme is weaker than the hypothesis for the Adams–Bashforth scheme. We have

$$X_2 = \Delta t \frac{1}{2} \sum_{j=0}^{N} \int_{I_j} f''(u^n)(\xi^n)^2 \frac{d\xi^n}{dx} - \Delta t \frac{1}{2} \sum_{j=1}^{N} f''(u^n)(\{\xi^n\})^2|_{x_j}[\xi^n]|_{x_j} \tag{3.91}$$

$$+ \Delta t \frac{1}{2} f''(u^n|_{x_0})(\frac{1}{2}\xi^{n,+}|_{x_0})^2 \xi^{n,+}|_{x_0} - \Delta t \frac{1}{2} f''(u^n|_{x_{N+1}})(\frac{1}{2}\xi^{n,-}|_{x_{N+1}})^2 \xi^{n,-}|_{x_{N+1}}. \tag{3.92}$$

We rewrite the first term above. Integrating the first term by parts gives:

$$\begin{aligned}
\Delta t \frac{1}{2} \sum_{j=0}^{N} \int_{I_j} f''(u^n)(\xi^n)^2 \frac{d\xi^n}{dx} &= \Delta t \frac{1}{6} \sum_{j=0}^{N} \int_{I_j} f''(u^n) \frac{d(\xi^n)^3}{dx} \\
&= \Delta t \frac{1}{6} \sum_{j=1}^{N} f''(u^n)|_{x_j}[(\xi^n)^3]|_{x_j} - \Delta t \frac{1}{6} \sum_{j=0}^{N} \int_{I_j} \frac{\partial f''(u^n)}{\partial x} (\xi^n)^3 \\
&\quad - \Delta t \frac{1}{6} f''(u^n)|_{x_0}(\xi^{n,+}|_{x_0})^3 + \Delta t \frac{1}{6} f''(u^n)|_{x_{N+1}}(\xi^{n,-}|_{x_{N+1}})^3.
\end{aligned} \tag{3.93}$$

Now, we use the identity $[\xi^3] = 2\{\xi\}^2[\xi] + \{\xi^2\}[\xi]$ to rewrite the first term and the boundary terms on the right-hand side of (3.93):

$$X_2 = \Delta t \frac{1}{6} \sum_{j=1}^{N} f''(u^n)|_{x_j} \left(\{(\xi^n)^2\} - \{\xi^n\}^2 \right) [\xi^n]|_{x_j} - \Delta t \frac{1}{6} \sum_{j=0}^{N} \int_{I_j} \frac{\partial f''(u^n)}{\partial x} (\xi^n)^3 \tag{3.94}$$

$$- \Delta t \frac{1}{24} f''(u^n)|_{x_0}(\xi^{n,+}|_{x_0})^3 + \Delta t \frac{1}{24} f''(u^n)|_{x_{N+1}}(\xi^{n,-}|_{x_{N+1}})^3. \tag{3.95}$$

Employing the identity $\{\xi^2\}-\{\xi\}^2=\frac{1}{4}[\xi]^2$ for the first term and inductive hypothesis $\|\xi^n\|_\infty \le h^{1/2}$ on the second term gives:

$$\begin{aligned}
X_2 &\le \Delta t\frac{1}{24}\sum_{j=1}^{N} f''(u^n)|_{x_j}[\xi^n]^3|_{x_j} + C\Delta t\|\xi\|_\infty\|\xi\|^2 \\
&\quad - \Delta t\frac{1}{24}f''(u^n)|_{x_0}(\xi^{n,+}|_{x_0})^3 + \Delta t\frac{1}{24}f''(u^n)|_{x_{N+1}}(\xi^{n,-}|_{x_{N+1}})^3 \\
&\le \Delta t\frac{1}{24}\sum_{j=1}^{N} f''(u^n)|_{x_j}[\xi^n]^3|_{x_j} + C\Delta t\|\xi\|^2 \\
&\quad - \Delta t\frac{1}{24}f''(u^n)|_{x_0}(\xi^{n,+}|_{x_0})^3 + \Delta t\frac{1}{24}f''(u^n)|_{x_{N+1}}(\xi^{n,-}|_{x_{N+1}})^3. \qquad (3.96)
\end{aligned}$$

The first, third and fourth terms in (3.96) are broken into two parts:

$$\begin{aligned}
\Delta t\frac{1}{24}\sum_{j=1}^{N} f''(u^n)|_{x_j}[\xi^n]^3|_{x_j} &= \Delta t\frac{1}{24}\sum_{j=1}^{N}\left(f''(u^n)|_{x_j} - f''(\{\tilde{u}_h^n\})|_{x_j}\right)[\xi^n]^3|_{x_j} \\
&\quad + \Delta t\frac{1}{24}\sum_{j=1}^{N} f''(\{\tilde{u}_h^n\})|_{x_j}[\xi^n]^3|_{x_j} \qquad (3.97) \\
-\Delta t\frac{1}{24}f''(u^n)|_{x_0}(\xi^{n,+}|_{x_0})^3 &= -\Delta t\frac{1}{24}(f''(u^n)|_{x_0} - f''(\frac{1}{2}\tilde{u}_h^{n,+})|_{x_0})(\xi^{n,+}|_{x_0})^3 \\
&\quad - \Delta t\frac{1}{24}f''(\frac{1}{2}\tilde{u}_h^{n,+})|_{x_0})(\xi^{n,+}|_{x_0})^3 \qquad (3.98) \\
\Delta t\frac{1}{24}f''(u^n)|_{x_{N+1}}(\xi^{n,-}|_{x_{N+1}})^3 &= \Delta t\frac{1}{24}(f''(u^n)|_{x_{N+1}} - f''(\frac{1}{2}\tilde{u}_h^{n,-})|_{x_{N+1}})(\xi^{n,-}|_{x_{N+1}})^3 \\
&\quad + \Delta t\frac{1}{24}f''(\frac{1}{2}\tilde{u}_h^{n,-})|_{x_{N+1}}(\xi^{n,-}|_{x_{N+1}})^3. \qquad (3.99)
\end{aligned}$$

We use for the first term in (3.97) a Taylor expansion $f''(u^n)-f''(\{\tilde{u}_h^n\}) = f'''(\zeta^n)\{\eta^n-\xi^n\}$ with the inductive hypothesis to obtain the following bound:

$$\Delta t\frac{1}{24}\sum_{j=1}^{N}(f''(u^n)|_{x_j} - f''(\{\tilde{u}_h^n\})|_{x_j})[\xi^n]^3|_{x_j} \le C\Delta t\|\xi^n\|^2. \qquad (3.100)$$

For the last term in (3.97), since $[u^n] = 0$, we rewrite it using the identity $[\xi^n] = [\eta^n] + [\tilde{u}_h^n]$:

$$\Delta t \frac{1}{24} \sum_{j=1}^{N} f''(\{\tilde{u}_h^n\})|_{x_j} [\xi^n]^3|_{x_j} = \Delta t \frac{1}{24} \sum_{j=1}^{N} f''(\{\tilde{u}_h^n\})|_{x_j} [\eta^n]|_{x_j} [\xi^n]^2|_{x_j} + \Delta t \frac{1}{24} \sum_{j=1}^{N} f''(\{\tilde{u}_h^n\})|_{x_j} [\tilde{u}_h^n]|_{x_j} [\xi^n]^2|_{x_j}. \tag{3.101}$$

The first term in (3.101) can be estimated with trace inequalities and approximation results. The second term in (3.101) is bounded using inequality (3.21) and the induction hypothesis:

$$\begin{aligned}
\Delta t \frac{1}{24} \sum_{j=1}^{N} f''(\{\tilde{u}_h^n\})|_{x_j} [\xi^n]^3|_{x_j} &\leq C\Delta t h^{-1} \|\eta^n\|_\infty \|\xi^n\|^2 + \Delta t \frac{1}{3} \sum_{j=1}^{N} \left(\alpha(\tilde{u}_h^n)|_{x_j} + C|[\tilde{u}_h^n]|^2|_{x_j} \right) [\xi^n]^2|_{x_j} \\
&\leq C\Delta t \|\xi^n\|^2 + \Delta t \frac{1}{3} \sum_{j=1}^{N} \alpha(\tilde{u}_h^n)|_{x_j} [\xi^n]^2|_{x_j} + C\Delta t\, h^{-1} \|\tilde{u}_h^n\|_\infty^2 \|\xi^n\|^2 \\
&\leq C\Delta t \|\xi^n\|^2 + \Delta t \frac{1}{3} \sum_{j=1}^{N} \alpha(\tilde{u}_h^n)|_{x_j} [\xi^n]^2|_{x_j}.
\end{aligned} \tag{3.102}$$

The boundary terms evaluated at x_0 and x_{N+1} in (3.98) and (3.99) are estimated in the same way. Combining all the estimates gives:

$$X_2 \leq \Delta t \frac{1}{3} \left(\alpha(\tilde{u}_h^n)|_{x_0} (\xi^{n,+}|_{x_0})^2 + \alpha(\tilde{u}_h^n)|_{x_{N+1}} (\xi^{n,-}|_{x_{N+1}})^2 + \sum_{j=1}^{N} \alpha(\tilde{u}_h^n)|_{x_j} [\xi^n]^2|_{x_j} \right) + C\Delta t \|\xi^n\|^2. \tag{3.103}$$

This bound is added to the bounds for the other terms X_i's to obtain:

$$\begin{aligned}
\theta_1 &\leq C\Delta t \, \|\xi^n\|^2 + C\Delta t (1 + \varepsilon^{-1}) h^{2k+1} \\
&\quad + (\frac{1}{3} + \varepsilon) \left(\alpha(\tilde{u}_h^n)|_{x_0} (\xi^{n,+}|_{x_0})^2 + \alpha(\tilde{u}_h^n)|_{x_{N+1}} (\xi^{n,-}|_{x_{N+1}})^2 + \sum_{j=1}^{N} \alpha(\tilde{u}_h^n)|_{x_j} [\xi^n]^2|_{x_j} \right).
\end{aligned}$$

The term θ_2 is bounded using Lipschitz continuity of s:

$$\theta_2 \leq C\Delta t \|\xi^n\|^2 + C\Delta t \, h^{2k+2}.$$

The term θ_3 is rewritten as

$$\begin{aligned}\theta_3 = &-\Delta t \sum_{j=1}^{N} \alpha(\tilde{u}_h^n)|_{x_j}[\xi^n]^2|_{x_j} + \Delta t \sum_{j=1}^{N} \alpha(\tilde{u}_h^n)|_{x_j}[\eta^n]|_{x_j}[\xi^n]|_{x_j} \\ &- \Delta t \alpha(\tilde{u}_h^n)|_{x_0} \left(\xi^{n,+}|_{x_0}\right)^2 + \Delta t \alpha(\tilde{u}_h^n)|_{x_0} \left(\xi^{n,+}|_{x_0}\right) \left(\eta^{n,+}|_{x_0}\right) \\ &- \Delta t \alpha(\tilde{u}_h^n)|_{x_{N+1}} \left(\xi^{n,+}|_{x_{N+1}}\right)^2 + \Delta t \alpha(\tilde{u}_h^n)|_{x_{N+1}} \left(\xi^{n,+}|_{x_{N+1}}\right) \left(\eta^{n,+}|_{x_{N+1}}\right).\end{aligned}$$

Using Young's inequality and approximation results we obtain

$$\theta_3 \leq (-1+\varepsilon) \left(\alpha(\tilde{u}_h^n)|_{x_0}(\xi^{n,+}|_{x_0})^2 + \alpha(\tilde{u}_h^n)|_{x_{N+1}}(\xi^{n,-}|_{x_{N+1}})^2 + \Delta t \sum_{j=1}^{N} \alpha(\tilde{u}_h^n)|_{x_j}[\xi^n]^2|_{x_j} \right)$$
$$+ C\Delta t\, h^{2k+1}, \quad \forall \varepsilon > 0.$$

This means that by choosing $\varepsilon = 1/3$ in the above, we conclude

$$\tilde{b}^n(\xi^n) \leq C\Delta t \|\xi^n\|^2 + C\Delta t\, h^{2k+1}.$$

3.4 Formulation for hyperbolic systems

In this section we describe discontinuous Galerkin discretizations for a nonlinear strictly hyperbolic system of two equations in one space dimension:

$$\frac{\partial \mathbf{U}}{\partial t} + \frac{\partial}{\partial x}\mathbf{F}(\mathbf{U}) = \mathbf{S}(\mathbf{U}), \quad \text{in } [a,b] \times (0,T] \tag{3.104}$$

$$\mathbf{U}(x,0) = \mathbf{U}_0(x) \quad \text{in } [a,b]. \tag{3.105}$$

This discretization scheme is used to approximate solutions of reduced models for blood flow. Boundary conditions will be specified in Chapter 5, and the notation for the spatial discretization is the same as in the scalar case. As before, define the left

and right traces of a vector valued function $\mathbf{\Phi} : [a, b] \to \mathbb{R}^2$ as

$$\mathbf{\Phi}^{\pm}|_{x_j} := \lim_{\varepsilon \to 0 \text{ and } \varepsilon > 0} \mathbf{\Phi}(x_j \pm \varepsilon), \quad 1 \leq j \leq N \tag{3.106}$$

$$\mathbf{\Phi}^{+}|_{x_0} := \lim_{\varepsilon \to 0 \text{ and } \varepsilon > 0} \mathbf{\Phi}(x_0 + \varepsilon) \tag{3.107}$$

$$\mathbf{\Phi}^{-}|_{x_{N+1}} := \lim_{\varepsilon \to 0 \text{ and } \varepsilon > 0} \mathbf{\Phi}(x_{N+1} - \varepsilon). \tag{3.108}$$

The average and jump of f at x_j are then given:

$$[\mathbf{\Phi}]|_{x_j} := \mathbf{\Phi}^{-}|_{x_j} - \mathbf{\Phi}^{+}|_{x_j}, \quad 1 \leq j \leq N \tag{3.109}$$

$$\{\mathbf{\Phi}\}|_{x_j} := \frac{1}{2}(\mathbf{\Phi}^{+}|_{x_j} + \mathbf{\Phi}^{-}|_{x_j}), \quad 1 \leq j \leq N \tag{3.110}$$

Define the following forms for the spatial discretization:

$$\mathcal{H}_j(\mathbf{U}, \mathbf{\Phi}) := \int_{I_j} \mathbf{F}(\mathbf{U}) \cdot \frac{d\mathbf{\Phi}}{dx} - \hat{\mathbf{F}}(\mathbf{U}) \cdot \mathbf{\Phi}|_{x_j}^{x_{j+1}} + \int_{I_j} \mathbf{S}(\mathbf{U}) \cdot \mathbf{\Phi}, \quad 0 \leq j \leq N. \tag{3.111}$$

A semi–discrete discontinuous Galerkin discretization of the equations is formulated as follows: with the choice $\mathbf{U}_h(0) = \Pi_h \mathbf{U}_0$, for each $t \in (0, T)$, seek $\mathbf{U}_h(t) \in \mathbb{V}_h^k \times \mathbb{V}_h^k$ satisfying

$$\int_{I_j} \frac{\partial \mathbf{U}_h}{\partial t} \cdot \mathbf{\Phi}_h = \mathcal{H}_j(\mathbf{U}_h, \mathbf{\Phi}_h), \quad \forall \mathbf{\Phi}_h \in \mathbb{V}_h^k \times \mathbb{V}_h^k, \text{ and } j = 0, \ldots, N. \tag{3.112}$$

As before, the function $\hat{\mathbf{F}}$ is called the numerical flux. For approximating the hyperbolic systems for blood flow, we work with two different numerical fluxes: the *local Lax–Friedrichs flux* and a *Riemann invariant upwinding flux*. Before providing these definitions, we introduce notation for boundary conditions. Since the equations of interest model flow through a vessel, denote the point x_0 the *inlet* and x_{N+1} the *outlet*.

$$\mathbf{U}_{\text{inlet}} := \text{ boundary conditions at } x_0 \tag{3.113}$$

$$\mathbf{U}_{\text{outlet}} := \text{ boundary conditions at } x_{N+1}. \tag{3.114}$$

Lastly, let $\lambda_i(\mathbf{U})$ $(i = 1, 2)$ be the distinct real eigenvalues of the Jacobian of $\mathbf{F}$ as provided by our assumption of strict hyperbolicity.

Definition 3.1. *The following terms incorporate boundary conditions into the numerical scheme through the local Lax–Friedrichs numerical flux:*

$$\{\mathbf{F}\}|_{x_0} = \frac{1}{2}\left(\mathbf{F}(\mathbf{U}^+|_{x_0}) + \mathbf{F}(\mathbf{U}_{\text{inlet}})\right), \quad [\mathbf{U}]|_{x_0} = \mathbf{U}_{\text{inlet}} - \mathbf{U}^+|_{x_0}$$
$$\{\mathbf{F}\}|_{x_{N+1}} = \frac{1}{2}\left(\mathbf{F}(\mathbf{U}_{\text{outlet}}) + \mathbf{F}(\mathbf{U}^-|_{x_{N+1}})\right), \quad [\mathbf{U}]|_{x_{N+1}} = \mathbf{U}^-|_{x_{N+1}} - \mathbf{U}_{\text{outlet}}.$$

The **local Lax–Friedrichs flux** *evaluated at a point x_j is*

$$\mathbf{F}^{LF}(\mathbf{U})|_{x_j} = \{\mathbf{F}\}|_{x_j} + \frac{1}{2}\max_{i=1,2}\left(|\lambda_i(\mathbf{U}^+|_{x_j})|, |\lambda_i(\mathbf{U}^-|_{x_j})|\right)[\mathbf{U}]|_{x_j}, \quad 1 \le j \le N,$$
$$\mathbf{F}^{LF}(\mathbf{U})|_{x_0} = \{\mathbf{F}\}|_{x_0} + \frac{1}{2}\max_{i=1,2}\left(|\lambda_i(\mathbf{U}^+|_{x_0})|, |\lambda_i(\mathbf{U}_{\text{inlet}})|\right)[\mathbf{U}]|_{x_0},$$
$$\mathbf{F}^{LF}(\mathbf{U})|_{x_{N+1}} = \{\mathbf{F}\}|_{x_{N+1}} + \frac{1}{2}\max_{i=1,2}\left(|\lambda_i(\mathbf{U}_{\text{outlet}})|, |\lambda_i(\mathbf{U}^-|_{x_{N+1}})\right)[\mathbf{U}]|_{x_{N+1}}.$$

Now we define the Riemann invariant upwinding flux, as given in the paper by Sherwin et al. [4]. Let us assume that the eigenvalues of Jacobian of the flux function are of opposite sign, i.e. $\lambda_1 > 0$ and $\lambda_2 < 0$, and the corresponding Riemann invariants $W_1 = W_1(\mathbf{U})$ and $W_2 = W_2(\mathbf{U})$ may be explicitly computed at functions of the physical variables $\mathbf{U}$. In this way, the traces of the Riemann invariants on x_j may be used to specify the flux.

The left trace of W_1 is used since this invariant propagates from left to right, and similarly, the right trace of W_2 is used since this invariant propagates from right to

left. Explicitly, these are defined at a point x_j as

$$W_{1,j}^{-} = W_1(\mathbf{U}^{-}|_{x_j}), \quad 1 \leq j \leq N+1, \tag{3.115}$$

$$W_{2,j}^{+} = W_2(\mathbf{U}^{+}|_{x_j}), \quad 0 \leq j \leq N, \tag{3.116}$$

$$W_{1,\text{inlet}} = W_1(\mathbf{U}_{\text{inlet}}), \tag{3.117}$$

$$W_{2,\text{outlet}} = W_2(\mathbf{U}_{\text{outlet}}). \tag{3.118}$$

Note the values $W_{1,\text{inlet}}$ and $W_{2,\text{outlet}}$ can be specified directly instead of providing data $\mathbf{U}_{\text{inlet}}$ and $\mathbf{U}_{\text{outlet}}$. With these traces, an "upwinded" value for $\mathbf{U}$ at each point x_j, denoted $\mathbf{U}_j^{\uparrow}$, is defined by evaluating the physical variables $\mathbf{U} = \mathbf{U}(W_1, W_2)$ at the appropriate traces of each invariant:

$$\mathbf{U}_j^{\uparrow} := \mathbf{U}(W_{1,j}^{-}, W_{2,j}^{+}), \quad 1 \leq j \leq N \tag{3.119}$$

$$\mathbf{U}_0^{\uparrow} := \mathbf{U}(W_{1,\text{inlet}}, W_{2,0}^{+}) \tag{3.120}$$

$$\mathbf{U}_{N+1}^{\uparrow} := \mathbf{U}(W_{1,N+1}^{-}, W_{2,\text{outlet}}). \tag{3.121}$$

Then, the numerical flux is computed by evaluating $\mathbf{F}$ at the upwinded values, as given below:

Definition 3.2. *The* **Riemann invariant upwinding flux** *evaluated at a point x_j is*

$$\mathbf{F}^{UP}(\mathbf{U})|_{x_j} := \mathbf{F}(\mathbf{U}_j^{\uparrow}), \quad 0 \leq j \leq N+1. \tag{3.122}$$

We employ the same notation for time discretization as in the scalar case, i.e. let the timestep be denoted $\Delta t > 0$, and for some final time T, define:

$$M = \frac{T}{\Delta t} \tag{3.123}$$

Discontinuous Galerkin discretizations for hyperbolic conservation laws have been extensively studied. For example, the seminal sequence of papers by Cockburn, Shu,

and others discuss these schemes paired with special Runge–Kutta (RK) time discretizations [29, 20, 30, 31]. One particular RK discretization employed in this thesis is a second–order scheme given as follows (see e.g. [33]):

For $n = 0, \ldots, M-1$, given $\mathbf{U}_h^n$, compute $\mathbf{V}_h^n$ and $\mathbf{U}_h^{n+1}$ in $\mathbb{V}_h^k \times \mathbb{V}_h^k$ satisfying

$$\int_{I_j} \mathbf{V}_h^n \cdot \mathbf{\Phi}_h = \int_{I_j} \mathbf{U}_h^n \cdot \mathbf{\Phi}_h + \Delta t \mathcal{H}_j(\mathbf{U}_h^n, \mathbf{\Phi}_h) \tag{3.124}$$

$$\int_{I_j} \mathbf{U}_h^{n+1} \cdot \mathbf{\Phi}_h = \frac{1}{2}\int_{I_j} \mathbf{V}_h^n \cdot \mathbf{\Phi}_h + \frac{1}{2}\int_{I_j} \mathbf{U}_h^n \cdot \mathbf{\Phi}_h + \frac{\Delta t}{2}\mathcal{H}_j(\mathbf{V}_h^n, \mathbf{\Phi}_h). \tag{3.125}$$

for all $\mathbf{\Phi}_h \in \mathbb{V}_h^k \times \mathbb{V}_h^k$ and $j = 0, \ldots, N$. We have also employed a second–order Adams–Bashforth multistep (AB) scheme, as appearing in the papers of Sherwin et. al. and Wang et. al. [4, 27]. Wang et al. notes that this scheme may be preferable when simulating large vessel networks since the boundary conditions, incorporated into $\mathcal{H}_0$ (inlet) and $\mathcal{H}_N$ (outlet), are computed as solutions to particular nonlinear systems. The AB scheme requires that the boundary values be computed only at the nth step since the values at the $(n-1)$th step may be stored. In contrast, the RK scheme requires that the boundary values be computed at the current step *and* the intermediate stage; this extra step may be detrimental to performance if parallel computing techniques are used.

Chapter 4

Numerical method of characteristics

This chapter describes a numerical scheme developed in collaboration with B. Rivière, C. Rusin, S. Acosta, and D. Penny. The content of this section is taken from sections 2–4 of our paper [47], with some slight modifications. The scheme is presented for a nonlinear hyperbolic conservation law of two equations, taking the form:

$$\frac{\partial \mathbf{U}}{\partial t} + \frac{\partial}{\partial x}\mathbf{F}(\mathbf{U}) = \mathbf{S}(\mathbf{U}) \tag{4.1}$$

We assume the system is strictly hyperbolic and the eigenvalues of the Jacobian of the flux function $\mathbf{F}$ satisfy $\lambda_1 > 0$ and $\lambda_2 < 0$. When applying this method in practice, we approximate the Riemann invariants of the (A, U) system from equation (2.20). The following section has some overlap with Chapter 2 to reiterate some relevant ideas for this method.

4.1 Characteristics for one-dimensional blood flow

In this section, we recapitulate some useful mathematical properties of (2.20). First, let us consider a general system of the form:

$$\frac{\partial \mathbf{U}}{\partial t} + \frac{\partial \mathbf{F}(\mathbf{U})}{\partial x} = \mathbf{S}(\mathbf{U}) \tag{4.2}$$

where $\mathbf{U} \in \mathbb{R}^2$ $\left(\mathbf{U} = (u_1, u_2)^T\right)$. This system may be written in a quasilinear form, namely

$$\frac{\partial \mathbf{U}}{\partial t} + \nabla_{\mathbf{U}}\mathbf{F}\frac{\partial \mathbf{U}}{\partial x} = \mathbf{S}(\mathbf{U}) \tag{4.3}$$

where $\nabla_{\mathbf{U}}\mathbf{F}$ is the 2×2 Jacobian matrix of $\mathbf{F}$ and the source function may change to include some terms from differentiating $\mathbf{F}$. As we shall see, (2.20) may be expressed in this form. Let the left eigenvectors of $\nabla_{\mathbf{U}}\mathbf{F}$ be given as $\{\mathbf{l}_1(\mathbf{U}), \mathbf{l}_2(\mathbf{U})\}$ with eigenvalues $\{\lambda_1(\mathbf{U}), \lambda_2(\mathbf{U})\}$ (we will henceforth drop the notation indicating their dependence on $\mathbf{U}$). The system (4.2) is *strictly hyperbolic* provided the Jacobian matrix has real distinct eigenvalues.

The general idea for the method of characteristics is to transform system (4.2) by diagonalizing the principal part of the differential equation in the hope that one finds functions remaining constant along particular curves. With this in mind, consider $Z_i : \mathbb{R}^2 \to \mathbb{R}$ whose gradient $\nabla_{\mathbf{U}} Z_i$ is parallel to $\mathbf{l}_i$; these are called *Riemann–invariants* (see e.g. [66, p. 637]). Now, define functions V_1 and V_2 from Z_1 and Z_2 like

$$V_1(x,t) = Z_1(\mathbf{U}(x,t)) + k_1(x,t), \tag{4.4}$$

$$V_2(x,t) = Z_2(\mathbf{U}(x,t)) + k_2(x,t), \tag{4.5}$$

where k_i are arbitrary constants of integration, that is, $\nabla_{\mathbf{U}} k_i = 0$. We refer to V_1 and V_2 as the *characteristics variables* of system (4.2). From the chain rule combined with (4.3), V_1 and V_2 satisfy

$$\frac{\partial V_1}{\partial t} + \lambda_1 \frac{\partial V_1}{\partial x} = R_1 := \nabla_{\mathbf{U}} Z_1^T \mathbf{S}(\mathbf{U}) + \frac{\partial k_1}{\partial t} + \lambda_1 \frac{\partial k_1}{\partial x} \tag{4.6}$$

$$\frac{\partial V_2}{\partial t} + \lambda_2 \frac{\partial V_2}{\partial x} = R_2 := \nabla_{\mathbf{U}} Z_2^T \mathbf{S}(\mathbf{U}) + \frac{\partial k_2}{\partial t} + \lambda_2 \frac{\partial k_2}{\partial x}. \tag{4.7}$$

The next statement is important for our method. It is easy to see that the following holds.

Proposition 4.1. *The function $V_i(x,t) - \int_0^t R_i(x,s)ds$ is constant along the curve $(\gamma_i(s), s)$ satisfying*

$$\frac{d\gamma_i}{ds} = \lambda_i(\gamma_i(s), s).$$

We derive the characteristic variables for system (2.20) by following equations (4.4) – (4.7) with Proposition 4.1. Assuming constant β, we rewrite the system with the Jacobian of $\mathbf{F}$ as follows,

$$\underbrace{\frac{\partial}{\partial t}\begin{bmatrix} A \\ U \end{bmatrix}}_{\partial \mathbf{U}/\partial t} + \underbrace{\begin{bmatrix} U & A \\ c^2/A & U \end{bmatrix}}_{\nabla_{\mathbf{U}}\mathbf{F}} \underbrace{\frac{\partial}{\partial x}\begin{bmatrix} A \\ U \end{bmatrix}}_{\partial \mathbf{U}/\partial x} = \underbrace{\begin{bmatrix} 0 \\ -8\pi\nu\frac{U}{A} + 4c_0\frac{dc_0}{dx} \end{bmatrix}}_{\mathbf{S}(\mathbf{U})},$$

where the perturbed and unperturbed wave speeds are given by

$$c = c(A) = \left(\frac{\beta\sqrt{A}}{2\rho}\right)^{1/2} \quad \text{and} \quad c_0 = c(A_0). \tag{4.8}$$

The left eigenvectors and eigenvalues for $\nabla_{\mathbf{U}}\mathbf{F}$ are

$$\lambda_1 = U + c, \qquad \mathbf{l}_1 = \begin{bmatrix} c/A \\ 1 \end{bmatrix}, \tag{4.9}$$

$$\lambda_2 = U - c, \qquad \mathbf{l}_2 = \begin{bmatrix} -c/A \\ 1 \end{bmatrix}. \tag{4.10}$$

If we set $\nabla_{\mathbf{U}} Z_1 = \mathbf{l}_1$ and $\nabla_{\mathbf{U}} Z_2 = \mathbf{l}_2$, then with $\mathbf{U} = (A, U)^T$ we have

$$\begin{aligned} \frac{\partial Z_1}{\partial A} &= \frac{c}{A}, \qquad \frac{\partial Z_1}{\partial u} = 1, \\ \frac{\partial Z_2}{\partial A} &= -\frac{c}{A}, \qquad \frac{\partial Z_2}{\partial u} = 1. \end{aligned}$$

For convenience we choose $k_1 = -4c_0$ and $k_2 = 4c_0$. Integrating, we obtain:

$$V_1(x,t) = U(x,t) + 4\left(c(A(x,t)) - c_0(x)\right), \tag{4.11}$$

$$V_2(x,t) = U(x,t) - 4\left(c(A(x,t)) - c_0(x)\right), \tag{4.12}$$

where these variables satisfy the system

$$\begin{aligned} \frac{\partial V_1}{\partial t} + (U+c)\frac{\partial V_1}{\partial x} &= R_1 = -8\pi\nu\frac{U}{A} - 4(U + c - c_0)\frac{dc_0}{dx}, \\ \frac{\partial V_2}{\partial t} + (U-c)\frac{\partial V_2}{\partial x} &= R_2 = -8\pi\nu\frac{U}{A} + 4(U - c + c_0)\frac{dc_0}{dx}. \end{aligned} \tag{4.13}$$

One may recover the cross-sectional area (and hence the pressure or wave speed) and velocity from the characteristic variables, and vice versa. Specifically,

$$U = \frac{V_1 + V_2}{2} \quad \text{and} \quad c - c_0 = \frac{V_1 - V_2}{8}. \tag{4.14}$$

The above derivation reveals that the characteristic variables propagate at speeds $U \pm c$, where U is the velocity of blood. For physiologically relevant parameter values, $c \gg |U|$. In particular, this relationship between U and c implies that $\lambda_1 > 0$ and $\lambda_2 < 0$, that is, the characteristic variables propagate in opposite directions.

Most explicit time discretizations require a CFL–type restriction on the timestep determined by c despite the fact that the speed of blood U is much smaller. To avoid this strong restriction, we propose a method that is stable regardless of the chosen timestep.

4.2 Description of scheme

For the presentation of the algorithm, let us focus on the following initial value problem,

$$\begin{aligned}
\frac{\partial V_1}{\partial t} + \lambda_1(V_1, V_2, x, t)\frac{\partial V_1}{\partial x} &= R_1(V_1, V_2, x, t) && (4.15)\\
\frac{\partial V_2}{\partial t} + \lambda_2(V_1, V_2, x, t)\frac{\partial V_2}{\partial x} &= R_2(V_1, V_2, x, t) && (4.16)\\
V_1(x, 0) &= V_1^0(x) && (4.17)\\
V_2(x, 0) &= V_2^0(x) && (4.18)
\end{aligned}$$

defined on intervals $x \in [a, b]$ and $t \in [0, T]$, and augmented by periodic boundary conditions of the form

$$V_i(a, t) = V_i(b, t) \quad i = 1, 2.$$

Now we introduce some notation. We use the following supremum norms in our analysis:

$$\|q\| := \sup_{x\in[a,b]} |q(x)| \quad \text{and} \quad \|p\|_T := \sup_{x\in[a,b],\ t\in[0,T]} |p(x,t)|. \tag{4.19}$$

Let dashes denote derivatives in space and dots denote derivatives in time, i.e. $p' := \partial p/\partial x$ and $\dot{p} := \partial p/\partial t$. For the spatial discretization, let $G_h := \Big\{ x_j = a + j(b-a)/M,\ j = 0, \dots M \Big\}$, i.e. the collection of uniformly spaced points between a and b with spacing $h := (b-a)/M$. Define $\mathcal{C}[a,b]$ to be the space of continuous functions on $[a,b]$, and $\mathcal{C}_h[a,b]$ to be the subset of continuous functions that are linear when restricted to each interval $[x_j, x_{j+1}]$ for $j = 0, \dots M-1$. For the temporal discretization, given a positive integer N, define the timestep $\Delta t := T/N$ and $t_n := n\Delta t$.

In what follows, V_i refers to the exact solution whereas W_i refers to the approximate solution. The numerical method of characteristics for solving (4.15) – (4.18) is based on the following idea: to obtain an approximation W_i to V_i given information on the grid G_h, follow the movement of the points in G_h along the characteristic curves *back* in time, and then assign values at the *current* time via spatial interpolation of the solution. More explicitly, from Proposition 4.1 with $\gamma_i(t+\Delta t) = x \in G_h$ one has

$$V_i(x, t+\Delta t) = V_i(\gamma_i(t), t) + \int_t^{t+\Delta t} R_i(\gamma_i(s), s) ds. \tag{4.20}$$

With this in mind, we have the following set of definitions. For each $x \in [a,b]$ define the characteristic curve $\gamma_i(x, t_{n+1}; t) : [t_n, t_{n+1}] \to \mathbb{R}$ passing through point x at time t_{n+1} as the solution to the following *final* value problem:

$$\begin{aligned} &\frac{d\gamma_i(x, t_{n+1}; t)}{dt} = \lambda_i\big(\gamma_i(x, t_{n+1}; t), t\big) \\ &\gamma_i(x, t_{n+1}; t_{n+1}) = x. \end{aligned} \tag{4.21}$$

Definition 4.1. *Let $n = 1, 2, ..., N$. For $x \in [a, b]$, let $\tilde{g}_i^n(x)$ $(i = 1, 2)$ be an approximation to the quantity*

$$g_i^n(x) = x - \mathcal{I}_i^n(x) := x - \int_{t_n}^{t_{n+1}} \lambda_i\big(\gamma_i(x, t_{n+1}; t), t\big)dt \tag{4.22}$$

in the sense that

$$\tilde{g}_i^n(x) := x - \tilde{\mathcal{Q}}_i^n(x) \tag{4.23}$$

where $\tilde{\mathcal{Q}}_i^n$ is a "pseudo–quadrature rule" for the integral $\mathcal{I}_i^n$ computed with the approximate solution W_i. Define $\mathcal{Q}_i^n$ to be this same pseudo–quadrature rule computed with the exact solution V_i. As we will see below, the rule we define is equivalent to a linearization of the characteristic curve. An illustration of the definition of $g^n(x)$ and and $\tilde{g}^n(x)$ is displayed in Figure 4.1. Note that $g_i^n(x)$ and $\tilde{g}_i^n(x)$ may not lie in the interval $[a, b]$, but its definition can be easily adjusted to handle the periodic boundary condition.

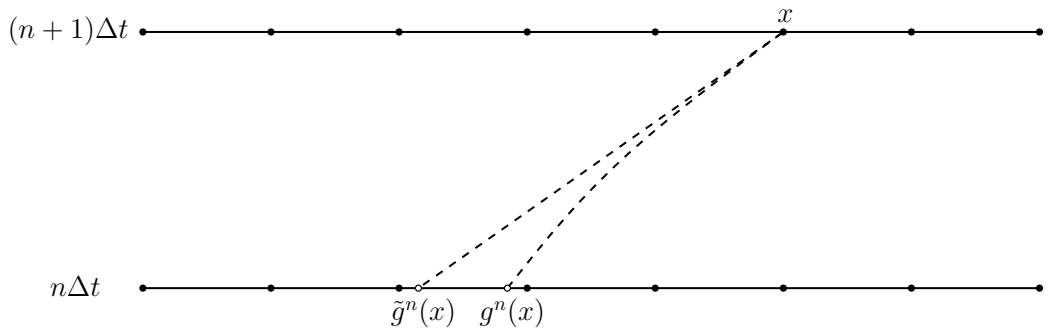

Figure 4.1 : The characteristic curve and its approximation. The *head* of the characteristic curve is the grid point x, and its *foot* is denoted by $g^n(x)$. The approximate *foot*, denoted by $\tilde{g}^n(x)$, is obtained by a linearization of the characteristic curve given in Definition 4.1.

Take $x \in [a, b]$ and consider the characteristic curve within the time interval $[t_n, t_{n+1}]$ on which x lies at time t_{n+1}, i.e. $\gamma_i(x, t_{n+1}, t)$. To declutter notation, define $V_i^n(x) =$

$V_i(x,t_n)$ for all n. By Definition 4.1 and (4.21) we have $g_i^n(x) = \gamma_i(x,t_{n+1};t_n)$. In turn, for the solution V_i one has

$$V_i^{n+1}(x) = V_i(\gamma_i(x,t_{n+1};t_n),t_n) + \mathcal{J}_i^n(x) := V_i^n(g_i^n(x)) + \int_{t_n}^{t_{n+1}} R_i(\gamma_i(x,t_{n+1};t),t)dt.$$

We have shown the following lemma which is nothing more than rewriting (4.20) in more compact notation.

Lemma 4.1. *The solutions V_i to (4.15) – (4.18) satisfy*

$$V_i^{n+1}(x) = V_i^n(g^n(x)) + \mathcal{J}_i^n(x) \quad \text{for all } x \in [a,b] \text{ and } n = 1 \dots N. \tag{4.24}$$

To define the quadrature rule $\mathcal{Q}_i^n$ (and hence $\tilde{\mathcal{Q}}_i^n$), we recall that λ_i is a function of the characteristic variables V_1 and V_2. For example, for the (A,U) system (2.20), combining (4.9)–(4.10) and (4.11)–(4.12), one has,

$$\lambda_1(x,t) = \frac{5}{8}V_1(x,t) + \frac{3}{8}V_2(x,t) + c_0(x) \quad \text{and} \quad \lambda_2(x,t) = \frac{3}{8}V_1(x,t) + \frac{5}{8}V_2(x,t) - c_0(x), \tag{4.25}$$

so in accordance with our previous notation, we can write $\lambda_i(x,t_n) = \lambda_i(V_1^n(x), V_2^n(x), x, t_n)$. In turn, we would like to approximate the integral by the simplest "rectangle rule", i.e.

$$\mathcal{I}_i^n(x) \approx \Delta t \lambda_i(\gamma_i(x,t_{n+1};t_n),t_n) = \Delta t \lambda_i(V_1^n(g_i^n(x)), V_2^n(g_i^n(x)), g_i^n(x), t_n). \tag{4.26}$$

Let us define $\mathcal{Q}_{i,R}$ and $\tilde{\mathcal{Q}}_{i,R}$ via the rectangle rule approximation:

$$\mathcal{Q}_{i,R}^n(x) := \Delta t \lambda_i(V_1^n(g_i^n(x)), V_2^n(g_i^n(x)), g_i^n(x), t_n) \tag{4.27}$$

$$\tilde{\mathcal{Q}}_{i,R}^n(x) := \Delta t \lambda_i(W_1^n(\tilde{g}_i^n(x)), W_2^n(\tilde{g}_i^n(x)), \tilde{g}_i^n(x), t_n), \tag{4.28}$$

where $\tilde{\mathcal{Q}}_{i,R}^n$ is computed with the approximate solution W_1^n, W_2^n.

Remark 4.1. *If we were to take our pseudo–quadrature rule to be* $\mathcal{Q}_i^n = \mathcal{Q}_{i,R}^n$ *and* $\tilde{\mathcal{Q}}_i^n = \tilde{\mathcal{Q}}_{i,R}^n$*, then the formula to determine* $\tilde{g}_i^n(x)$ *becomes nonlinear and hence implicit in time, i.e.*

$$\tilde{g}_i^n(x) = x - \Delta t \lambda_i(W_1^n(\tilde{g}_i^n(x)), W_2^n(\tilde{g}_i^n(x)), \tilde{g}_i^n(x), t_n) := \mathcal{K}_i^n(\tilde{g}_i^n(x)).$$

For small enough Δt*,* $\mathcal{K}^n$ *is a contraction. If the rectangle rule scheme is employed,* $\tilde{g}^n(x)$ *may be computed as the limit of the sequence* $y^{(k+1)} = \mathcal{K}^n(y^{(k)})$ *with initial condition* $y^{(0)} = x$*.*

To simplify the method and have an explicit time stepping procedure, we define the rule we implement from the rectangle rule by replacing both $g_i^n(x)$ and $\tilde{g}_i^n(x)$ with x in both $\mathcal{Q}_{i,R}^n$ and $\tilde{\mathcal{Q}}_{i,R}^n$ respectively.

Similarly, the source term R_i may be a function of the characteristic variables V_1 and V_2 so that $R_i(x,t) = R_i(V_1(x,t), V_2(x,t), x, t)$. We approximate the exact integral $\mathcal{J}_i^n$ using a similar explicit quadrature rule denoted by $\tilde{\mathcal{R}}_i^n$. More precisely, we have the following definition:

Definition 4.2. *The pseudo–quadrature rules applied to the exact and approximate solutions are defined as follows:*

$$\begin{aligned}
\mathcal{Q}_i^n(x) &:= \Delta t \lambda_i(V_1^n(x), V_2^n(x), x, t_n),\\
\mathcal{R}_i^n(x) &:= \Delta t R_i(V_1^n(\tilde{g}_i^n(x)), V_2^n(\tilde{g}_i^n(x)), \tilde{g}_i^n(x), t_n),\\
\tilde{\mathcal{Q}}_i^n(x) &:= \Delta t \lambda_i(W_1^n(x), W_2^n(x), x, t_n),\\
\tilde{\mathcal{R}}_i^n(x) &:= \Delta t R_i(W_1^n(\tilde{g}_i^n(x)), W_2^n(\tilde{g}_i^n(x)), \tilde{g}_i^n(x), t_n).
\end{aligned}$$

The last missing piece is the specification of the spatial interpolation procedure.

Definition 4.3. $\Pi_h : \mathcal{C}[a,b] \to \mathcal{C}_h[a,b]$ *projects a continuous function* f *into its piecewise linear interpolant* $\Pi_h f$ *at the points in* G_h*.*

The algorithm follows below.

Algorithm 1 NMC algorithm for system (4.15)-(4.18)

Input: $V_1^0, V_2^0 \in \mathcal{C}[a,b]$.

Initialize $W_1^0 = \Pi_h[V_1^0]$ and $W_2^0 = \Pi_h[V_2^0]$.

`for` $n = 1, 2, \ldots N$

$$\tilde{g}_i^{n-1}(x) = x - \tilde{\mathcal{Q}}_i^{n-1}(x) \qquad i = 1, 2$$

$$W_i^n(x) = \Pi_h[W_i^{n-1}(\tilde{g}_i^{n-1}(x)) + \tilde{\mathcal{R}}_i^{n-1}(x)] \qquad i = 1, 2$$

`end`

Remark 4.2. *Higher order interpolation and quadrature is possible. We work with piecewise linear interpolation for our analysis since the norm of* Π_h *is uniformly bounded by* 1 *for all* h *which leads to stability. Also, the rule defined in Definition 4.2 allows our method to remain explicit in time.*

Remark 4.3. *In practice, we compute the approximate solution* W_i *at the points in* G_h*, but in the presentation of the algorithm above, the approximate solution is viewed equivalently as a piecewise linear function in* $\mathcal{C}_h[a,b]$*. We use this presentation since we work with the continuous supremum norm for our analysis.*

4.3 Numerical analysis

Let $V_1(x,t^n)$, $V_2(x,t^n)$ and $W_1^n(x)$, $W_2^n(x)$ be the exact and approximate solutions to (4.15) – (4.18) respectively. We make the following assumptions:

Assumption 4.1. *The exact solutions satisfy* $V_i \in \mathcal{C}^2([0,T] \times [a,b])$.

Assumption 4.2. *The eigenvalues* $\lambda_i = \lambda_i(V_1, V_2, x, t)$ *are continuously differentiable. Also, there are positive constants* δ *and* $K = K(\delta)$ *so that in the domain*

$(|V_1| + |V_2|) < \delta$ the source functions $R_i = R_i(V_1, V_2, x, t)$ are continuously differentiable and satisfy $|R_i(V_1, V_2)| \leq K\,(|V_1| + |V_2|)$.

Note that Assumption 4.2 regarding λ_i holds for the (A, U) system (2.20) because the eigenvalues λ_i are affine functions of the characteristic variables, as verified in (4.25). Assumption 4.2 concerning R_i is satisfied if the cross-sectional area $A(x,t)$ is bounded away from zero uniformly in space and time, which is guaranteed when $\|V_1\| + \|V_2\|$ is sufficiently small. In turn, we need our numerical solution (W_1^n, W_2^n) to satisfy the same property up to some finite time T so that R_i remains sufficiently smooth along the trajectory of the numerical solution. This is ensured by the following proposition.

Proposition 4.2 (Stability)**.** *Under Assumption 4.2, if* $(\|W_1^0\| + \|W_2^0\|) < \delta e^{-2KT}$, *then*

$$\|W_1^n\| + \|W_2^n\| \leq e^{2KT}\left(\|W_1^0\| + \|W_2^0\|\right) < \delta, \quad n = 1, ..., N.$$

Proof. We rely on the fact that for piecewise linear interpolation we have $\|\Pi_h\| = 1$. We proceed by induction. Assume that

$$\|W_1^m\| + \|W_2^m\| < \delta, \quad \text{for all } m = 0, ..., n-1,$$

and consider the following inequality,

$$\begin{aligned}
\|W_1^n\| &\leq \|W_1^{n-1}(\tilde{g}_1^{n-1}) + \Delta t R_1(W_1^{n-1}(\tilde{g}_1^{n-1}), W_2^{n-1}(\tilde{g}_1^{n-1}))\| \\
&\leq \|W_1^{n-1}\| + \Delta t K\left(\|W_1^{n-1}\| + \|W_2^{n-1}\|\right), \\
\|W_2^n\| &\leq \|W_2^{n-1}(\tilde{g}_2^{n-1}) + \Delta t R_2(W_1^{n-1}(\tilde{g}_2^{n-1}), W_2^{n-1}(\tilde{g}_2^{n-1}))\| \\
&\leq \|W_2^{n-1}\| + \Delta t K\left(\|W_1^{n-1}\| + \|W_2^{n-1}\|\right).
\end{aligned}$$

Therefore,

$$\|W_1^n\| + \|W_2^n\| \leq (1 + 2K\Delta t)\left(\|W_1^{n-1}\| + \|W_2^{n-1}\|\right) \leq e^{2KT}\left(\|W_1^0\| + \|W_2^0\|\right) < \delta,$$

where the second inequality follows by recursion and the strong inductive hypothesis. The last inequality follows from the assumption on the initial condition. This concludes the proof. □

Remark 4.4. *We wish to comment on the physical meaning of Assumption 4.2. When the characteristics variables (V_1, V_2) are sufficiently small, the cross-sectional area A is positive and the velocity u remains bounded. This prevents the solution from going into the vacuum state corresponding to $A = 0$, i.e. vessel collapse. Further, a sufficiently small constant δ in Assumption 4.2 can be estimated from the unperturbed wave speed c_0 as $\delta < 8 \inf_x c_0(x)$.*

A convergence result for the algorithm follows below.

Theorem 4.1 (Convergence)**.** *Fix $T > 0$ and $\Delta t = T/N$ for $N \in \mathbb{N}$. Under Assumptions 4.1 and 4.2, and the hypothesis from Proposition 4.2 on the initial condition (W_1^0, W_2^0), the following convergence bound holds:*

$$\|W_1^n - V_1^n\| + \|W_2^n - V_2^n\| \leq T \exp(CT) \big[\mathcal{O}(h^2/\Delta t) + \mathcal{O}(\Delta t)\big] \qquad \text{for all } n = 1, 2, ..., N,$$

for some positive constant $C = C(V_1, V_2)$.

Proof. We first bound $\|W_1^n - V_1^n\|$. One has $\|W_1^n - V_1^n\| \leq \|W_1^n - \Pi_h V_1^n\| + \|\Pi_h V_1^n - V_1^n\|$. We apply Lemma 4.1 to plug in $V_1^n = V_1^{n-1}(g_1^{n-1}) + \mathcal{J}_1^{n-1}$, use $\|\Pi_h\| = 1$, and then bound the first term as follows.

$$\begin{aligned}
\|W_1^n - \Pi_h V_1^n\| &\leq \|W_1^{n-1}(\tilde{g}_1^{n-1}) - V_1^{n-1}(\tilde{g}_1^{n-1})\| + \|V_1^{n-1}(\tilde{g}_1^{n-1}) - V_1^{n-1}(g_1^{n-1})\| \\
&\quad + \|\tilde{\mathcal{R}}_1^{n-1} - \mathcal{R}_1^{n-1}\| + \|\mathcal{R}_1^{n-1} - \mathcal{J}_1^{n-1}\| \\
&\leq \|W_1^{n-1} - V_1^{n-1}\| + \|(V_1^{n-1})'\| \|\tilde{g}_1^{n-1} - g_1^{n-1}\| \\
&\quad + \|\tilde{\mathcal{R}}_1^{n-1} - \mathcal{R}_1^{n-1}\| + \|\mathcal{R}_1^{n-1} - \mathcal{J}_1^{n-1}\|
\end{aligned}$$

To bound $\|\tilde{g}_1^{n-1} - g_1^{n-1}\|$, note that for any x, we have

$$\begin{aligned}|\tilde{g}_1^{n-1}(x) - g_1^{n-1}(x)| &= |\mathcal{I}_1^{n-1}(x) - \tilde{\mathcal{Q}}_1^{n-1}(x)| \\ &\leq |\mathcal{I}_1^{n-1}(x) - \mathcal{Q}_{1,R}^{n-1}(x)| + |\mathcal{Q}_{1,R}^{n-1}(x) - \tilde{\mathcal{Q}}_1^{n-1}(x)|.\end{aligned}$$

The first term is the quadrature error due to the rectangle rule and the second term may be bounded in the following way:

$$\begin{aligned}&|\mathcal{Q}_{1,R}^{n-1}(x) - \tilde{\mathcal{Q}}_1^{n-1}(x)| \leq |\mathcal{Q}_{1,R}^{n-1}(x) - \mathcal{Q}_1^{n-1}(x)| + |\mathcal{Q}_1^{n-1}(x) - \tilde{\mathcal{Q}}_1^{n-1}(x)| \\ &= \Delta t\,|\lambda_1\big(V_1^{n-1}(g_1^{n-1}(x)), V_2^{n-1}(g_1^{n-1}(x))\big) - \lambda_1\big(V_1^{n-1}(x), V_2^{n-1}(x)\big)| \\ &\quad + \Delta t\,|\lambda_1(V_1^{n-1}(x), V_2^{n-1}(x)) - \lambda_1(W_1^{n-1}(x), W_2^{n-1}(x))| \\ &\leq \Delta t C_\lambda\Big\{|V_1^n(g_1^{n-1}(x)) - V_1^{n-1}(x)| + |V_2^n(g_1^{n-1}(x)) - V_2^{n-1}(x)| \\ &\quad + |W_1^{n-1}(x) - V_1^{n-1}(x)| + |W_2^{n-1}(x) - V_2^{n-1}(x)|\Big\} \\ &\leq \Delta t C_\lambda\Big\{\|(V_1^{n-1})'\||g_1^{n-1}(x) - x| + \|(V_2^{n-1})'\||g_1^{n-1}(x) - x| \\ &\quad + |W_1^{n-1}(x) - V_1^{n-1}(x)| + |W_2^{n-1}(x) - V_2^{n-1}(x)|\Big\} \\ &\leq \Delta t^2\|\lambda_1\|_T C_\lambda\Big\{\|(V_1^{n-1})'\| + \|(V_2^{n-1})'\|\Big\} \\ &\quad + \Delta t C_\lambda\Big\{|W_1^{n-1}(x) - V_1^{n-1}(x)| + |W_2^{n-1}(x) - V_2^{n-1}(x)|\Big\}.\end{aligned}$$

With this bound, one has

$$\begin{aligned}\|\tilde{g}_1^{n-1} - g_1^{n-1}\| \leq \|\mathcal{I}_1^{n-1} - \mathcal{Q}_{1,R}^{n-1}\| &+ \Delta t C_\lambda\Big\{\|W_1^{n-1} - V_1^{n-1}\| + \|W_2^{n-1} - V_2^{n-1}\|\Big\} \\ &+ \Delta t^2\|\lambda_1\|_T C_\lambda\Big\{\|(V_1^{n-1})'\| + \|(V_2^{n-1})'\|\Big\}.\end{aligned}$$

Now we proceed to bound the term $\|\tilde{\mathcal{R}}_1^{n-1} - \mathcal{R}_1^{n-1}\|$ as follows. From Assumption 4.2, we get

$$\|\tilde{\mathcal{R}}_1^{n-1} - \mathcal{R}_1^{n-1}\| \leq \Delta t\, C_R\big\{\|W_1^{n-1} - V_1^{n-1}\| + \|W_2^{n-1} - V_2^{n-1}\|\big\}$$

where C_R is a Lipschitz constant working for both R_1 and R_2. Similarly,

$$\begin{aligned}\|\mathcal{R}_1^{n-1} - \mathcal{J}_1^{n-1}\| &\leq \Delta t C_R\big\{\|V_1^{n-1}(\tilde{g}_1^{n-1}) - V_1^{n-1}(g_1^{n-1})\| \\ &\qquad + \|V_2^{n-1}(\tilde{g}_1^{n-1}) - V_2^{n-1}(g_1^{n-1})\|\big\}) + \hat{C}\Delta t^2 \\ &\leq \Delta t C_R\big\{\|(V_1^{n-1})'\| + \|(V_2^{n-1})'\|\big\}\|\tilde{g}_1^{n-1} - g_1^{n-1}\| + \hat{C}\Delta t^2,\end{aligned}$$

where the last term is obtained by approximating the integral $\mathcal{J}_1^{n-1}$ by the rectangle rule and employing the differentiability of R_1 and of the exact solution V_i.

With Assumption 4.1, we choose a constant $\tilde{C}$ that simultaneously bounds the terms involving C_R, C_λ, $\|\lambda_i\|_T$ and the norm of the first derivative of V_i^n for $i = 1, 2$ and $n = 1 \ldots N$. Then we have,

$$\begin{aligned}\|W_1^n - V_1^n\| \leq (1 + \Delta t\tilde{C})\|W_1^{n-1} - V_1^{n-1}\| + \Delta t\tilde{C}\|W_2^{n-1} - V_2^{n-1}\| + \|\Pi_h V_1^n - V_1^n\| \\ + \tilde{C}(1 + \tilde{C}\Delta t)\|\mathcal{I}_1^{n-1} - \mathcal{Q}_{1,R}^{n-1}\| + \tilde{C}\Delta t^2.\end{aligned}$$

The same argument as above provides the bound for the error in the second characteristic variable:

$$\begin{aligned}\|W_2^n - V_2^n\| \leq (1 + \Delta t\tilde{C})\|W_2^{n-1} - V_2^{n-1}\| + \Delta t\tilde{C}\|W_1^{n-1} - V_1^{n-1}\| + \|\Pi_h V_2^n - V_2^n\| \\ + \tilde{C}(1 + \tilde{C}\Delta t)\|\mathcal{I}_2^{n-1} - \mathcal{Q}_{2,R}^{n-1}\| + \tilde{C}\Delta t^2.\end{aligned}$$

Summing the two above inequalities, and possibly increasing $\tilde{C}$, one obtains:

$$\begin{aligned}\|W_1^n - V_1^n\| + \|W_2^n - V_2^n\| &\leq (1 + \tilde{C}\Delta t)\Big\{\|W_1^{n-1} - V_1^{n-1}\| + \|W_2^{n-1} - V_2^{n-1}\|\Big\} \\ &\quad + \|\Pi_h V_1^n - V_1^n\| + \|\Pi_h V_2^n - V_2^n\| \\ &\quad + \tilde{C}(1 + \tilde{C}\Delta t)\Big\{\|\mathcal{I}_1^{n-1} - \mathcal{Q}_{1,R}^{n-1}\| + \|\mathcal{I}_2^{n-1} - \mathcal{Q}_{2,R}^{n-1}\|\Big\} \\ &\quad + \tilde{C}\Delta t^2.\end{aligned}$$

We apply the same argument to successively bound the terms $\|W_1^j - V_1^j\| + \|W_2^j - V_2^j\|$ and conclude:

$$\begin{aligned}\|W_1^n - V_1^n\| + \|W_2^n - V_2^n\| &\leq \sum_{j=0}^{n} \exp(\tilde{C}\Delta t)^{n-j} \Big\{ \|\Pi_h V_1^j - V_1^j\| + \|\Pi_h V_2^j - V_2^j\| \Big\} \\ &+ \sum_{j=0}^{n-1} \exp(\tilde{C}\Delta t)^{n-j} \tilde{C} \Big\{ \|\mathcal{I}_1^j - \mathcal{Q}_{1,R}^j\| + \|\mathcal{I}_2^j - \mathcal{Q}_{2,R}^j\| \Big\} + \sum_{j=0}^{n-1} \tilde{C} \exp(\tilde{C}\Delta t)^j \Delta t^2 \\ &\leq \frac{T}{\Delta t} \exp(CT) \Big[\max_{i,j} \|\Pi_h V_i^j - V_i^j\| + \max_{i,j} \|\mathcal{I}_i^j - \mathcal{Q}_{i,R}^j\| + O(\Delta t^2) \Big],\end{aligned}$$

where $C > 0$ is a new constant, large enough such that we can take all the prefactors outside the parentheses. The maximum is taken over $i = 1, 2$ and $j = 1, \ldots, n$. For the rectangle rule, one can show:

$$\max_j \|\mathcal{I}_i^j - \mathcal{Q}_{i,R}^j\| \leq C_V \frac{\Delta t^2}{2} \tag{4.29}$$

where $C_V = C_V(V_1, V_2)$. For piecewise linear interpolation, we have:

$$\max_j \|\Pi_h V_i^j - V_i^j\| \leq \frac{h^2}{8} \|V_i''\|_T. \tag{4.30}$$

With these bounds we obtain the result. □

Remark 4.5. *Practically we take h proportional to Δt, so the error decreases linearly in both Δt and h. Notice that neither the Stability Proposition 4.2 nor the Convergence Theorem 4.1 are dependent on the choice for the constant of proportionality. In fact, in order to obtain convergence at a linear rate, it is only needed that $h/\Delta t$ is bounded above. In other words, our proposed method is unconditionally stable with no need to satisfy a CFL–type condition.*

Chapter 5

Boundary conditions and zero–dimensional models for vessels and vessel networks

The content of this chapter is taken from our papers with small modifications to adapt the text to this thesis; sections 5.1–5.4 are from [48], and sections 5.5–5.6 are from [67]. We employ standard approaches for boundary conditions in the form of Dirichlet data, at vessel junctions in a network, and at the terminal vessels of a network. Models for the heart and organ beds have been adapted from the work of Mynard et al. [3, 13]. These conditions are summarized below.

5.1 Dirichlet data

We describe the process for imposing Dirichlet boundary data $\mathbf{U}_{\text{inlet}}$ at the inlet x_0 for the (A, Q) class of systems. An analogous approach may be used for outlet data and for the (A, U) class of systems.

This process relies on the Riemann invariants W_i $(i = 1, 2)$ derived in Section 2.3. At time $n\Delta t$ corresponding to time step n, suppose we prescribe the area A^n_{inlet}. The corresponding value for the fluid momentum at the inlet Q^n_{inlet} is determined by first extrapolating the right–to–left moving Riemann invariant to the boundary using the solution at the previous time step W_2^{n-1}:

$$W^n_{2,\text{approx}} := W_2^{n-1}(x_0 - \Delta t \lambda^{n-1}_{2,\text{approx}}), \tag{5.1}$$

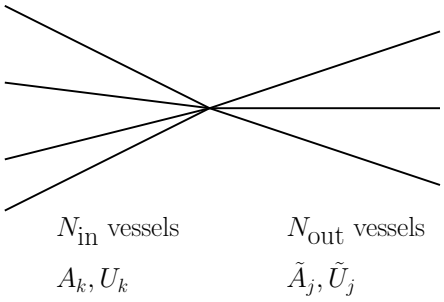

Figure 5.1 : A schematic of a vessel junction.

with the approximation to the eigenvalue given as follows:

$$\lambda_{2,\text{approx}}^{n-1} := \lambda_2^{n-1}(A^{+,n-1}|_{x_0}, Q^{+,n-1}|_{x_0}). \tag{5.2}$$

We use the value of the approximated Riemann invariant at the boundary and rearrange the formula to solve for the fluid momentum.

$$Q_{\text{inlet}}^n := A_{\text{inlet}}^n \left(W_{2,\text{approx}}^n + 4c(A_{\text{inlet}}^n) \right). \tag{5.3}$$

This process determines the Dirichlet boundary conditions at the inlet, $\mathbf{U}_{\text{inlet}}$, that are then built into the numerical flux function as described above. A similar approach may be used for prescribing the fluid momentum Q_{inlet}^n or the left–to–right moving invariant $W_{1,\text{inlet}}^n$ at the inlet of the vessel.

5.2 Vessel junctions

Boundary conditions at vessel junctions are determined by holding constant the values of the Riemann invariants and enforcing continuity of total pressure and conservation of fluid momentum. More precisely, suppose at a junction there are N_{in} incoming vessels and N_{out} outgoing vessels. We need to determine the values of the physical

variables at the incoming vessels $A_{\text{in}}^{(k)}, Q_{\text{in}}^{(k)}$ $(k = 1, \ldots, N_{\text{in}})$ and at the outgoing vessels $A_{\text{out}}^{(\ell)}, Q_{\text{out}}^{(\ell)}$ $(\ell = 1, \ldots, N_{\text{out}})$ as denoted in Figure 5.1. For simplicitly of presentation, we diverge from our previous notation and let $W_{1,\text{in}}^{(k)}$ and $W_{2,\text{out}}^{(\ell)}$ denote the traces of the Riemann invariants at the incoming and outgoing vessels respectively. The requirements at the vessel junction may be specified mathematically in the following nonlinear system of algebraic equations [18]:

$$W_{1,\text{in}}^{(k)} = \frac{Q_{\text{in}}^{(k)}}{A_{\text{in}}^{(k)}} + 4c\left(A_{\text{in}}^{(k)}\right) \quad \text{for } k = 1, \ldots, N_{\text{in}}, \tag{5.4}$$

$$W_{2,\text{out}}^{(\ell)} = \frac{Q_{\text{out}}^{(\ell)}}{A_{\text{out}}^{(\ell)}} - 4c\left(A_{\text{out}}^{(\ell)}\right) \quad \text{for } \ell = 1, \ldots, N_{\text{out}}, \tag{5.5}$$

$$Q_{\text{add}} + \sum_{k=1}^{N_{\text{in}}} Q_{\text{in}}^{(k)} = \sum_{\ell=1}^{N_{\text{out}}} Q_{\text{out}}^{(\ell)}, \tag{5.6}$$

$$\frac{\rho}{2}\left(\frac{Q_{\text{in}}^{(1)}}{A_{\text{in}}^{(1)}}\right)^2 + p\left(A_{\text{in}}^{(1)}\right) = \frac{\rho}{2}\left(\frac{Q_{\text{in}}^{(k)}}{A_{\text{in}}^{(k)}}\right)^2 + p\left(A_{\text{in}}^{(k)}\right) \quad \text{for } k = 2, \ldots, N_{\text{in}}, \tag{5.7}$$

$$\frac{\rho}{2}\left(\frac{Q_{\text{in}}^{(1)}}{A_{\text{in}}^{(1)}}\right)^2 + p\left(A_{\text{in}}^{(1)}\right) = \frac{\rho}{2}\left(\frac{Q_{\text{out}}^{(\ell)}}{A_{\text{out}}^{(\ell)}}\right)^2 + p\left(A_{\text{out}}^{(\ell)}\right) \quad \text{for } \ell = 1, \ldots, N_{\text{out}}. \tag{5.8}$$

The term Q_{add} is *additional flow*, which is specified in the case where we wish to add volume to a closed loop model. This may be done to help in model calibration. These equations are solved with Newton's method.

5.3 Reflection boundary conditions for terminal vessels

For code validation with the fifty–vessel network given in [4], we employ reflection boundary conditions used by these authors at terminal vessels in the network. More specifically, at the outlets of the terminal vessels in a given network, we expect reflections due to the resistive nature of organ beds. Described below is a simple approach for resistance boundary conditions using the Riemann invariants of the inviscid systems [4]. The Riemann invariants for the inviscid (A, Q) system satisfy the following

system:

$$\frac{\partial \hat{W}_1}{\partial t} + \hat{\lambda}_1 \frac{\partial \hat{W}_1}{\partial x} = 0, \tag{5.9}$$

$$\frac{\partial \hat{W}_2}{\partial t} + \hat{\lambda}_2 \frac{\partial \hat{W}_2}{\partial x} = 0. \tag{5.10}$$

Assuming that λ_1 remains positive and λ_2 remains negative, this system is well-defined when $\hat{W}_1$ is specified at the inlet of the vessel ($x = 0$) and $\hat{W}_2$ is specified at the outlet ($x = L$) of the vessel. Prescribing $\hat{W}_2(x = L, t) = 0$ on the outlet yields no effect on the characteristic variables in the interior of the domain. Alternatively, one may specify an outlet boundary condition depending on the outgoing characteristic W_1, i.e. for some $0 \leq R \leq 1$, let

$$\hat{W}_2(L, t) = -R\hat{W}_1(L, t), \tag{5.11}$$

$$A^+|_L = A^-|_L. \tag{5.12}$$

The parameter R can be thought of as a resistance. By equation (5.11), the incoming characteristic W_2 at the outlet will be a nonzero fraction of W_1 when R is greater than zero. The system (5.11)–(5.12) specifies the values of the physical variables to the right of the outlet, $A^+|_L$, $Q^+|_L$, given the known values to the left of the outlet, $A^-|_L$, $Q^-|_L$. Consider the following definition of the Riemann invariants now shifted by the constant $c_0 = c(A_0)$.

$$\hat{W}_1 = \frac{Q}{A} + 4(c - c_0) \quad \text{and} \quad \hat{W}_2 = \frac{Q}{A} - 4(c - c_0). \tag{5.13}$$

With this definition, (5.11) and (5.12) become the following:

$$A^+|_L = A^-|_L, \tag{5.14}$$

$$Q^+|_L = (1 - R)A^-|_L \left[\frac{Q^-|_L}{A^-|_L} + 4\left(c(A^-|_L) - c_0|_L\right) \right] - Q^-|_L. \tag{5.15}$$

The numerical flux at $x = L$ is then evaluated at these values. Similarly for the (A, U) system, one has

$$A^+|_L = A^-|_L, \tag{5.16}$$

$$U^+|_L = (1 - R)\left[U^-|_L + 4\left(c(A^-|_L) - c_0|_L\right)\right] - U^-|_L. \tag{5.17}$$

5.4 Three element windkessel boundary conditions for terminal vessels

For a physiologically meaningful comparison of the (A, Q) and (A, U) systems, we employ a three element windkessel boundary condition at the end of each terminal vessel. This terminal model, mathematically described by an RC circuit with two resistors (with resistances R_1 and R_2) and one capacitor (with capacitance C), accounts for both the pressure gradient across an organ bed and its compliance. For a review of these types of models, see e.g. [68]. A schematic, adapted from [28], is given in Figure 5.2.

As argued in [68], the resistance of the organ bed itself is mainly encoded in R_2, yielding a gradient between the pressure at the capacitor P_C and the pressure in the veins P_{out}. The resistance R_1 may be chosen as the *characteristic impedance* of the incoming one–dimensional vessel. This will be made more precise in the next section on closed loop organ bed models. We remark that in our simulations in Chapter 6 with this windkessel model, we do not use this approach and instead fix the parameter R_1 independently from the one–dimensional vessel parameters.

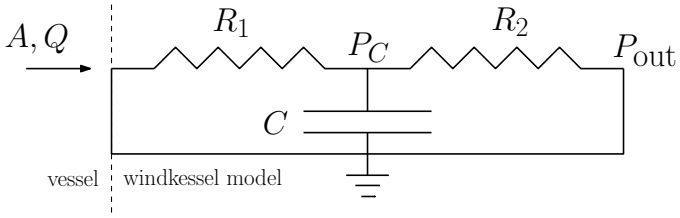

Figure 5.2 : A schematic of the three element windkessel model used for boundary conditions at the outlets of the terminal vessels in the network.

Ohm's and Kirhchoff's laws for this model are given respectively:

$$Q = \frac{p(A) - P_C}{R_1} \tag{5.18}$$

$$C\frac{dP_C}{dt} = Q - \frac{P_C - P_{\text{out}}}{R_2}. \tag{5.19}$$

At the nth timestep, given P_C^n and A^n, Q^n evaluated at the outlet of the terminal vessel, $P_C^{n+1}, A^{n+1}, Q^{n+1}$ are computed as the solution to the following system:

$$Q^{n+1} = \frac{p(A^{n+1}) - P_C^{n+1}}{R_1} \tag{5.20}$$

$$P_C^{n+1} = P_C^n + \frac{\Delta t}{C}\left(Q^{n+1} - \frac{P_C^{n+1} - P_{\text{out}}}{R_2}\right) \tag{5.21}$$

$$W_1^n = \frac{Q^{n+1}}{A^{n+1}} + 4c(A^{n+1}). \tag{5.22}$$

This approximation is the same as the process described in [69] except we use backward Euler to discretize the differential equation for P_C. The numerical flux at $x = L$ is evaluated at A^{n+1}, Q^{n+1}.

5.5 Closed loop organ bed models

Organ beds are modeled using an electric circuit analogy with resistor and capacitor elements. We employ the model used in [3] and [13] but allow the compliance and resistance to depend nonlinearly on the blood pressure, as described in [70]. We

provide a brief description as follows. We are given reference values for the resistance $R_{\text{cap,ref}}$, arteriole compliance $C_{\text{art,ref}}$, venule compliance $C_{\text{ven,ref}}$ and total volume of blood contained in the organ V_{ref}. Then we define the reference volume of blood contained in the arteriole and venule compartments as

$$V_{\text{art,ref}} = C_{\text{art,ref}}/(C_{\text{art,ref}} + C_{\text{ven,ref}})V_{\text{ref}}, \tag{5.23}$$

$$V_{\text{ven,ref}} = C_{\text{ven,ref}}/(C_{\text{art,ref}} + C_{\text{ven,ref}})V_{\text{ref}}, \tag{5.24}$$

so the following holds: $V_{\text{art,ref}} + V_{\text{ven,ref}} = V_{\text{ref}}$.

From the approach in [70], we can derive a state equation for the volume of blood contained in the arteriole and venule compartments of the organ bed,

$$V_{\text{art}} = V_{\text{art,ref}} \frac{(1 + \Gamma_{\text{art}}(p_{\text{art}} - p_{\text{ext}}))^2}{(1 + \Gamma_{\text{art}}(p_{\text{art,ref}} - p_{\text{ext}}))^2}, \tag{5.25}$$

$$V_{\text{ven}} = V_{\text{ven,ref}} \frac{(1 + \Gamma_{\text{ven}}(p_{\text{ven}} - p_{\text{ext}}))^2}{(1 + \Gamma_{\text{ven}}(p_{\text{ven,ref}} - p_{\text{ext}}))^2}, \tag{5.26}$$

where $p_{\text{art,ref}}$ and $p_{\text{ven,ref}}$ are reference values for the arteriole and venule blood pressure, and the effective arteriole and venule wall compliances are given by

$$\Gamma_{\text{art}} = \frac{C_{\text{art,ref}}}{2V_{\text{art,ref}} - C_{\text{art,ref}}(p_{\text{art,ref}} - p_{\text{ext}})}, \tag{5.27}$$

$$\Gamma_{\text{ven}} = \frac{C_{\text{ven,ref}}}{2V_{\text{ven,ref}} - C_{\text{ven,ref}}(p_{\text{ven,ref}} - p_{\text{ext}})}. \tag{5.28}$$

These are inversely proportional to the stiffness (Young's modulus) of the respective vascular tissue. Hence, they are parameters useful for representing the vascular stiffening exhibited in the progression of pulmonary hypertension and other vascular diseases.

From (5.25)–(5.26), we obtain the effective compliances associated with the organ

bed and their nonlinear dependence on the blood pressure,

$$C_{\text{art}} = \frac{dV_{\text{art}}}{dp_{\text{art}}} = 2\Gamma_{\text{art}} V_{\text{art,ref}} \frac{(1 + \Gamma_{\text{art}}(p_{\text{art}} - p_{\text{ext}}))}{(1 + \Gamma_{\text{art}}(p_{\text{art,ref}} - p_{\text{ext}}))^2}, \tag{5.29}$$

$$C_{\text{ven}} = \frac{dV_{\text{ven}}}{dp_{\text{ven}}} = 2\Gamma_{\text{ven}} V_{\text{ven,ref}} \frac{(1 + \Gamma_{\text{ven}}(p_{\text{ven}} - p_{\text{ext}}))}{(1 + \Gamma_{\text{ven}}(p_{\text{ven,ref}} - p_{\text{ext}}))^2}. \tag{5.30}$$

The dependence of the organ resistance R_{cap} on the blood pressure was derived in [70]. For the configuration depicted in Figure 5.3, we have that

$$R_{\text{cap}} = R_{\text{cap,ref}} \left(\left(\frac{V_{\text{art,ref}}}{V_{\text{art}}} \right)^2 + \left(\frac{V_{\text{ven,ref}}}{V_{\text{ven}}} \right)^2 \right), \tag{5.31}$$

where the volumes V_{art} and V_{ven} depend on the blood pressure as described by (5.25)–(5.26).

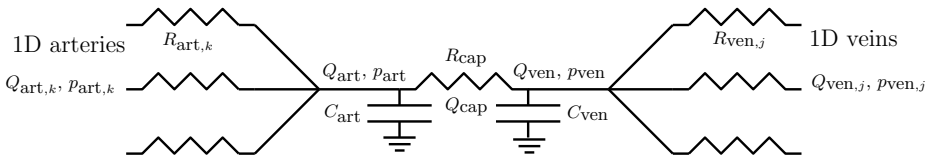

Figure 5.3 : A schematic of the organ bed model.

Lastly, the resistances $R_{\text{art},i}$ and $R_{\text{ven},j}$ are defined in terms of the parameters of the corresponding incoming or outgoing one–dimensional vessels as $\frac{\rho}{A_0} c\,(A_0)$ [3, 68]. This quantity is known as the characteristic impedance of the vessel, i.e. the ratio of pressure p to flow Q for waves traveling in one direction:

$$R_{\text{art}} = \frac{p}{Q}. \tag{5.32}$$

To make this more precise, consider an infinitely long vessel modeled by the linearized inviscid (A, Q)–system (2.26)–(2.27). Recall the pressure p satisfies a wave

equation from (2.28) with wave speed $c(A_0)$. A pressure wave traveling from left to right satisfies the following equation:

$$\frac{\partial p}{\partial t} + c(A_0)\frac{\partial p}{\partial x} = 0. \tag{5.33}$$

Using (5.32) in (5.33), we obtain:

$$\frac{1}{R_{\text{art}}}\frac{\partial Q}{\partial t} + c(A_0)\frac{\partial p}{\partial x} = 0.$$

Comparing with (2.27) yields the following formula for the resistance:

$$R_{\text{art}} = \frac{\rho}{A_0}c(A_0).$$

The equations governing the organ bed model are given below. Equations (5.34)–(5.36) formulate the analog of Ohm's law while equations (5.37) and (5.38) couple flow into the capacitors with conservation of mass. The last two equations (5.39) and (5.40) describe mass conservation at the incoming and outgoing vessels. We remark that the model for the liver takes a slightly different form from the circuit given in Figure 5.3, since it incorporates a high pressure hepatic artery and a low pressure portal vein. We use the same liver model as that given [3], as shown in Figure 5.4, and omit details for brevity.

$$p_{\text{art},k} - p_{\text{art}} = Q_{\text{art},k} R_{\text{art},k}, \quad k = 1, \ldots, N_{\text{in}}, \tag{5.34}$$

$$p_{\text{ven}} - p_{\text{ven},j} = Q_{\text{ven},j} R_{\text{ven},j}, \quad j = 1, \ldots, N_{\text{out}}, \tag{5.35}$$

$$p_{\text{art}} - p_{\text{ven}} = Q_{\text{cap}} R_{\text{cap}}, \tag{5.36}$$

$$C_{\text{art}} \frac{dp_{\text{art}}}{dt} = Q_{\text{art}} - Q_{\text{cap}}, \tag{5.37}$$

$$C_{\text{ven}} \frac{dp_{\text{ven}}}{dt} = Q_{\text{cap}} - Q_{ven}, \tag{5.38}$$

$$Q_{\text{art}} = \sum_{k=1}^{N_{\text{in}}} Q_{\text{art},k}, \tag{5.39}$$

$$Q_{\text{ven}} = \sum_{j=1}^{N_{\text{out}}} Q_{\text{ven},j}. \tag{5.40}$$

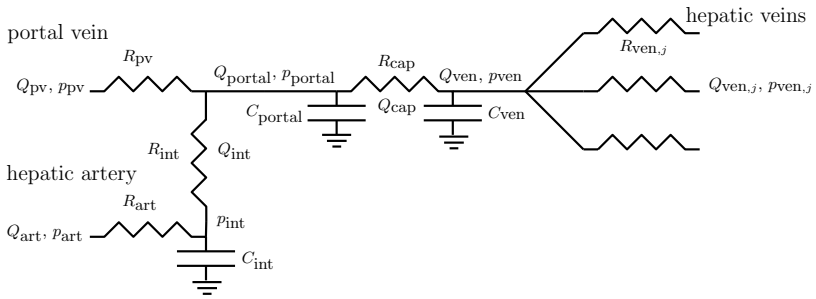

Figure 5.4 : A schematic of the liver model.

5.6 Heart model for a closed loop circulation

A sketch of the model for a single side of the heart is depicted in Figure 5.5.

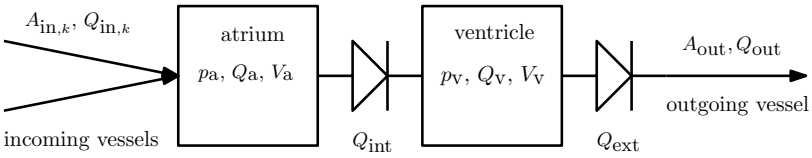

Figure 5.5 : A schematic of the heart model.

Each chamber contains three variables: pressure p, volume V, and flow rate Q, with subscripts "a" and "v" corresponding to the atrium and the ventricle respectively. The residual chamber volume is given as V^0. Our model also incorporates a viscoelastic term with parameter K similar to the work of Blanco et al. [21]. The variable Q_{int} is flow through the interior valve and Q_{ext} is flow through the exterior valve. The variable Q_{out} is flow imposed at the inlet of the 1D vessel connected to the heart, which is equal to the flow through the exterior valve Q_{ext}. The governing equations are given below:

$$p_{\mathrm{a}} = E_{\mathrm{a}}(t)\frac{(V_{\mathrm{a}} - V_{\mathrm{a}}^0)}{V_{\mathrm{a}}^0} + K_{\mathrm{a}}p_{\mathrm{a}}\frac{dV_{\mathrm{a}}}{dt}, \tag{5.41}$$

$$p_{\mathrm{v}} = E_{\mathrm{v}}(t)\frac{(V_{\mathrm{v}} - V_{\mathrm{v}}^0)}{V_{\mathrm{v}}^0} + K_{\mathrm{v}}p_{\mathrm{v}}\frac{dV_{\mathrm{v}}}{dt}, \tag{5.42}$$

$$L_{\mathrm{int}}\frac{dQ_{\mathrm{int}}}{dt} + \left(B_{\mathrm{int}}|Q_{\mathrm{int}}| + R_{\mathrm{int}}\right)Q_{\mathrm{int}} = H(p_{\mathrm{a}}, p_{\mathrm{v}}; \gamma_{\mathrm{int}})\left(p_{\mathrm{a}} - p_{\mathrm{v}}\right), \tag{5.43}$$

$$L_{\mathrm{ext}}\frac{dQ_{\mathrm{ext}}}{dt} + \left(B_{\mathrm{ext}}|Q_{\mathrm{ext}}| + R_{\mathrm{ext}}\right)Q_{\mathrm{ext}} = H(p_{\mathrm{v}}, p(A_{\mathrm{out}}); \gamma_{\mathrm{ext}})\left(p_{\mathrm{v}} - p(A_{\mathrm{out}})\right), \tag{5.44}$$

$$\frac{dV_{\mathrm{a}}}{dt} = -Q_{\mathrm{a}}, \tag{5.45}$$

$$\frac{dV_{\mathrm{v}}}{dt} = -Q_{\mathrm{v}}, \tag{5.46}$$

$$Q_{\mathrm{a}} = Q_{\mathrm{int}} - \sum_{k=1}^{N_{\mathrm{in}}} Q_{\mathrm{in},k}, \tag{5.47}$$

$$Q_{\mathrm{v}} = Q_{\mathrm{ext}} - Q_{\mathrm{int}}, \tag{5.48}$$

$$Q_{\mathrm{out}} = Q_{\mathrm{ext}}. \tag{5.49}$$

The first two equations (5.41) and (5.42) (for the atrium and ventricle respectively) use a specified time–periodic elastance function $E(t)$ to relate chamber volume and chamber pressure. We use a simplified form for the elastance function from [13]. The time–dependent profile for each chamber's elastance is defined as

$$E(t) = \frac{(E_{\max} - E_{\min})}{k}\left(\frac{g_1(t)}{1 + g_1(t)}\frac{1}{1 + g_2(t)}\right) + E_{\min}, \tag{5.50}$$

where

$$g_i(t) = \left(\frac{t - t_{\mathrm{onset}}}{\tau_i T_{\mathrm{heart}}}\right)^{m_i}, \quad i = 1, 2, \quad \text{and} \quad k = \max_{t\in[0,T_{\mathrm{heart}}]}\left(\frac{g_1}{1 + g_1}\frac{1}{1 + g_2}\right). \tag{5.51}$$

and where

$$T_{\text{heart}} = \text{ heart period,} \tag{5.52}$$

$$m_1, \tau_1 = \text{ parameters governing shape of contraction,} \tag{5.53}$$

$$m_2, \tau_2 = \text{ parameters governing shape of relaxation,} \tag{5.54}$$

$$t_{\text{onset}} = \text{ time at which contraction begins,} \tag{5.55}$$

$$E_{\min}, E_{\max} = \text{minimum and maximum elastances.} \tag{5.56}$$

The heart rate is defined as $\text{HR} = 1/T_{\text{heart}}$. We remark that this model neglects chamber interactions. Similar to [21] and [3], the heart valves are modeled as non-ideal diodes with flow governed by a modified version of Bernoulli's equation in (5.43) and (5.44). The variables and parameters for the interior valve, between the chambers, and the exterior valve, between the ventricle and outgoing vessel, are denoted with the subscript "int" and "ext" respectively. We choose to multiply the pressure gradient by a smoothed version of the heaviside function depending on a parameter $\gamma > 0$:

$$H(p_1, p_2; \gamma) := \left(1 + e^{-\gamma(p_1 - p_2)}\right)^{-1}. \tag{5.57}$$

This parameter γ controls the contribution of the pressure gradient term in Bernoulli's equation and in turn governs the shape of the dicrotic notch in the pressure waveforms. Lastly, L describes the valve inductance, R determines the linear resistance through the valve and B scales the nonlinear resistance term depending on the magnitude of the flow. Equations (5.45) and (5.46) relate the time derivative of chamber volume to the fluid momentum exiting the chamber, and the last three equations (5.47)–(5.49) enforce conservation of mass.

Finally, our heart model contains multiple incoming vessels but only one outgoing vessel. The incoming vessels allow us to retain the systemic and pulmonary venous circulations and close the loop of the model.

5.7 Implementation of boundary conditions for NMC and DG

For NMC, each model or boundary condition type determines values for the Riemann invariants at each timestep. The NMC solution is represented on a discrete grid including nodes at the inlet and outlet of each vessel; boundary conditions are numerically prescribed by setting the value of W_1 at the inlet node and the value of W_2 at the outlet node.

To incorporate conditions for vessel junctions into the DG scheme, for all models except vessel junctions, we employ the approach described in section 3.4. For vessel junctions, the definition of the numerical flux at the inlet and outlet nodes is redefined as follows: at the outlet of the incoming vessels one has

$$\mathbf{F}^{nf}(\mathbf{U})|_{x_{N+1}} := \mathbf{F}(A_{\text{in}}^{(k)}, Q_{\text{in}}^{(k)}).$$

Similarly, at the inlet of the outgoing vessels we have:

$$\mathbf{F}^{nf}(\mathbf{U})|_{x_0} := \mathbf{F}(A_{\text{out}}^{(\ell)}, Q_{\text{out}}^{(\ell)}).$$

Chapter 6

Numerical comparisons of models and methods

This chapter is devoted to a comparison of the numerical methods described in Chapters 3 and 4 and different reduced models presented in Chapter 2.

6.1 Comparison of NMC and DG

6.1.1 Model construction and numerical parameters

In this section, we compare results from the NMC and DG methods by simulating blood flow in two closed loop networks of vessels. We first consider a simple network consisting of two (half) heart models, two organ bed models, and four vessels, which has been adapted from the work of Mynard et al. [2]. Next, we perform experiments with a large network adapted from Mynard's thesis [3], which contains 158 vessels. Physical parameters for both simulations are provided in Appendices A.1 and A.2. We remark that results from an extensive sensitivity analysis for the parameters of the large vessel network are available in the appendix of [3].

A schematic for the four vessel network is given in Figure 6.1. The large vessel network has the same structure, except each of the systemic arteries, systemic veins, pulmonary arteries, and pulmonary veins are themselves networks of vessels.

For the four vessel network of vessels, the parameters β for

$$p = p_0 + \beta \left(A^{1/2} - A_0^{1/2} \right),$$

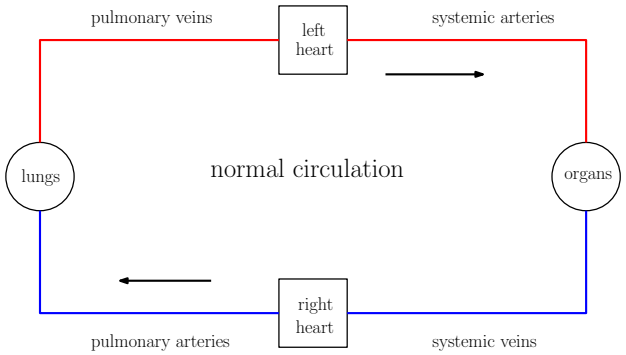

Figure 6.1 : A schematic of a four vessel closed loop model for a normal circulation, adapted from [2].

are explicitly set. For the large network of vessels, β is determined as follows. Let $D_0 = (4/\pi)^{1/2} A_0^{1/2}$ be the resting diameter for an arbitrary vessel, D_{ref} be the resting diameter of the ascending aorta, and consider parameters $k_1 > 0$, $k_2 < 0$, and $k_3 > 0$. For the systemic arteries we define

$$\beta(A_0) = \frac{16}{3}\frac{1}{D_0\sqrt{\pi}}\left(k_1\left[\exp\left(k_2\frac{D_0 - D_{\text{ref}}}{D_{\text{ref}}}\right) - 1\right] + k_3\right),$$

and for all other vessel networks we have:

$$\beta(A_0) = \frac{16}{3}\frac{1}{D_0\sqrt{\pi}}\left(k_1\exp\left(k_2\frac{D_0}{D_{\text{ref}}}\right) + k_3\right).$$

A scaling law of this form is used by several authors [13, 71]. We evaluate β at the average of A_0 at the vessel inlet and outlet for vessels that linearly taper (i.e. A_0 depends linearly on the distance from the vessel inlet).

Also, for the large vessel network, we add an additional 100 mL of blood over the first ten cardiac cycles. This addition of blood provides a way to calibrate the waveforms in the model, i.e. the mean pressures are quite sensitive to blood volume. With the period for a cardiac cycle given by T_{heart}, we use the following form for Q_{add}

at node 54 (refer to the table in Appendix A.2) in equation 5.6.

$$Q_{\text{add}}(t) = \begin{cases} 10/T_{\text{heart}} & \text{if } t \leq 10T_{\text{heart}}, \\ 0 & \text{otherwise.} \end{cases}$$

For the four vessel network, $T_{\text{heart}} = 1$ s. For the large vessel network, $T_{\text{heart}} = 6/7$ s.

The DG scheme defined in equations (3.124)–(3.125) with the local Lax–Friedrichs flux is used to approximate the conservative form of the (A, Q) system, as defined in equations (2.18). The NMC scheme approximates the Riemann invariants of (A, U) system given in equation (2.20). The parameters $\alpha = 1.1$ and $\nu = 3.019 \times 10^{-2}$ cm^2/s in both cases.

We employ the same numerical parameters for both the four vessel and large vessel networks. For the NMC simulations, we take $h = 5 \times 10^{-2}$ cm, and $\Delta t = 5 \times 10^{-5}$ s for the four vessel network and $\Delta t = 4.285714 \times 10^{-5}$ s for the large vessel network. For the DG simulations, we consider piecewise linear polynomials, $k = 1$, with $h = 1$ cm and $\Delta t = 1 \times 10^{-4}$ s. The simulations are run for fifteen seconds.

6.1.2 Four vessel closed loop network

Figures 6.2 and 6.3 display pressure and flow waveforms from the second–to–last full cardiac cycle, produced by NMC and DG. They also depict the relative difference in the waveforms from each method, measured pointwise in time and normalized by the maximum of waveform produced by DG.

Both methods produce flow and pressure waveforms with pointwise relative differences around 1%. The greatest discrepancies in the methods appear around parts of the waveform with rapid changes in time.

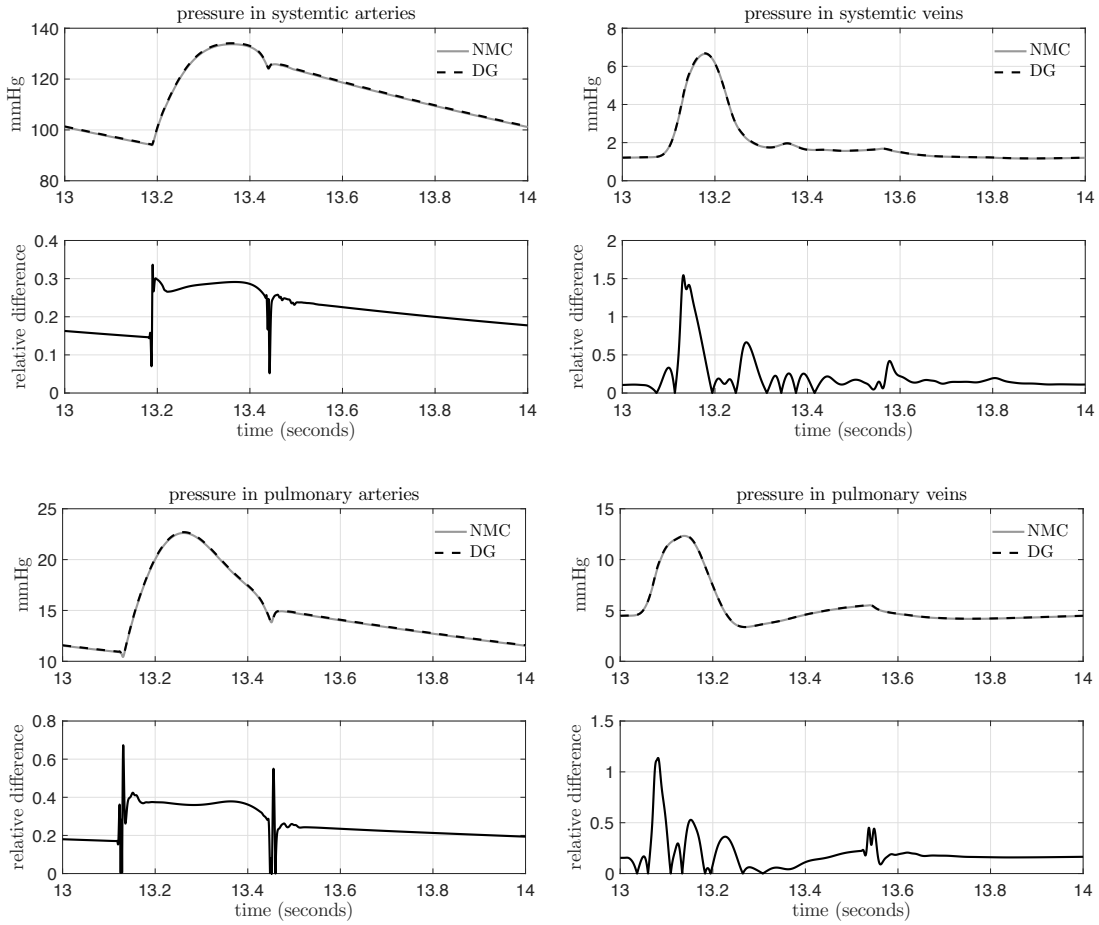

Figure 6.2 : Pressure waveforms from NMC and DG for the four vessel network, and their relative differences.

6.1.3 Large vessel network models of a normal circulation

In this section, we examine waveforms produced by NMC and DG in a larger network containing 158 vessels, adapted from Mynard's thesis [3]. The overall structure of the network is the same as in Figure 6.1, but now each of the systemic arteries, systemic veins, pulmonary arteries, and pulmonary veins is itself a network of vessels. This model also includes the portal circulation, i.e. a collection of vessels between the gastrointestinal organs and the liver. See Figure 6.4 for a schematic of this part of

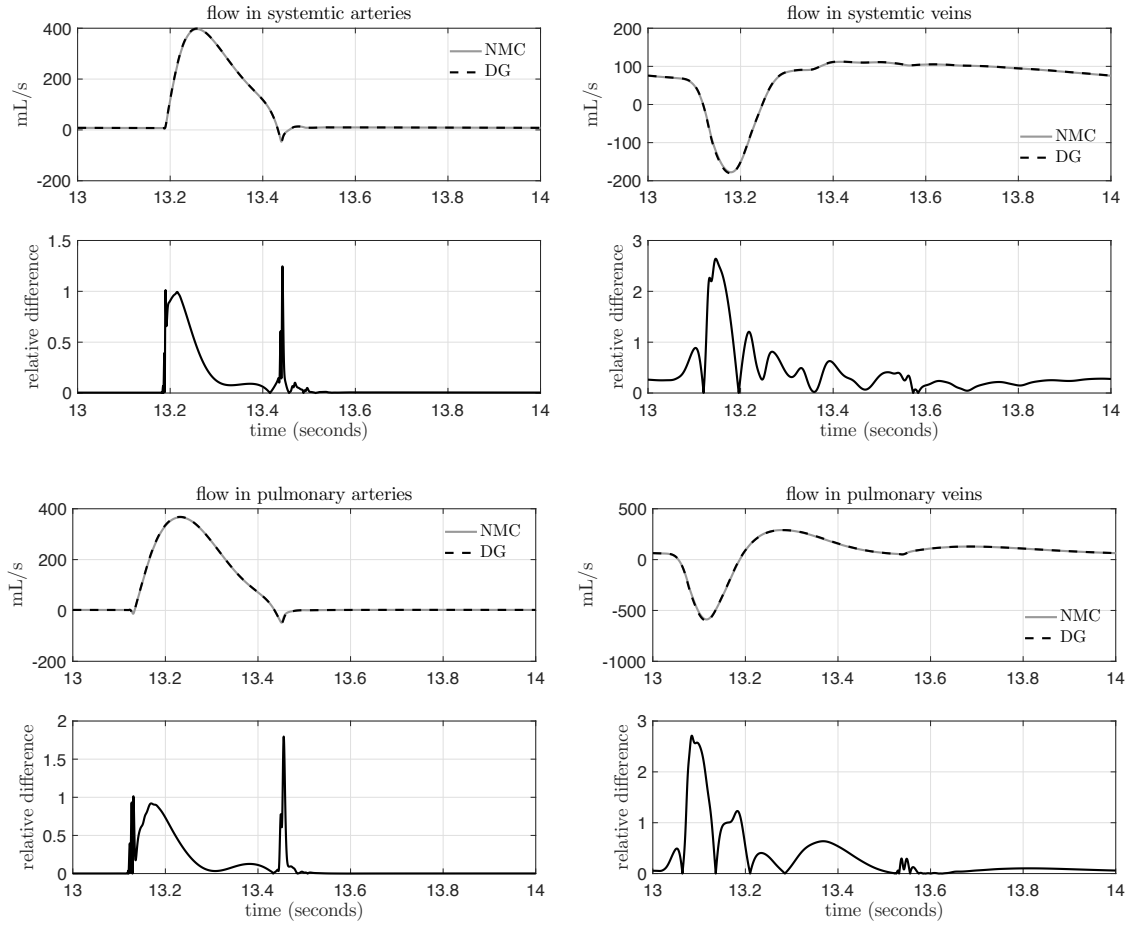

Figure 6.3 : Flow waveforms from NMC and DG for the four vessel network, and their relative differences.

the circulation.

Figures 6.5 and 6.6 compare waveforms during the second–to–last full cardiac cycle, produced by each method, along with their pointwise relative differences. Differences between waveforms from each method are larger that in the four vessel model due the higher complexity of this model.

Since we expect the numerical error for each method to grow time, the relative difference between waveforms will also grow. This effect is explored in 6.7, where we

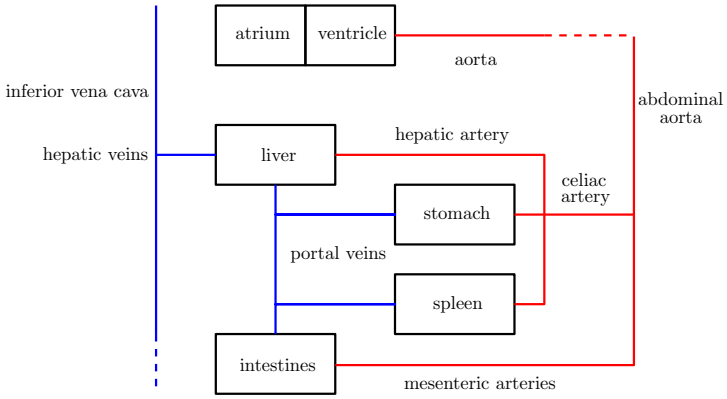

Figure 6.4 : A schematic of the portal circulation and surrounding vessels and organ beds in the larger 158 vessel network model adapted from [3].

compare the NMC and DG waveforms in the femoral artery for the full simulation time of fifteen seconds. Notice the relative difference between NMC and DG is small at the beginning of the simulation, but grows in time. Our experience in practice is that NMC suffers from some numerical diffusion, leading to a loss of blood volume and hence a decrease in the mean pressure.

6.1.4 Conclusions

We compared the numerical method of characteristics (NMC) and a discontinuous Galerkin scheme (DG) for approximating solutions to reduced models of blood flow. These methods were compared using a small four vessel network and a larger 158 vessel network, both for a normal circulation, adapted from the work of Mynard et al. [3, 2]. Both methods produced very similar results in each network, with larger discrepancies seen in the more complex 158 vessel network. The relative error between the methods grows in time, but remains small for simulations lasting about 15 cardiac cycles.

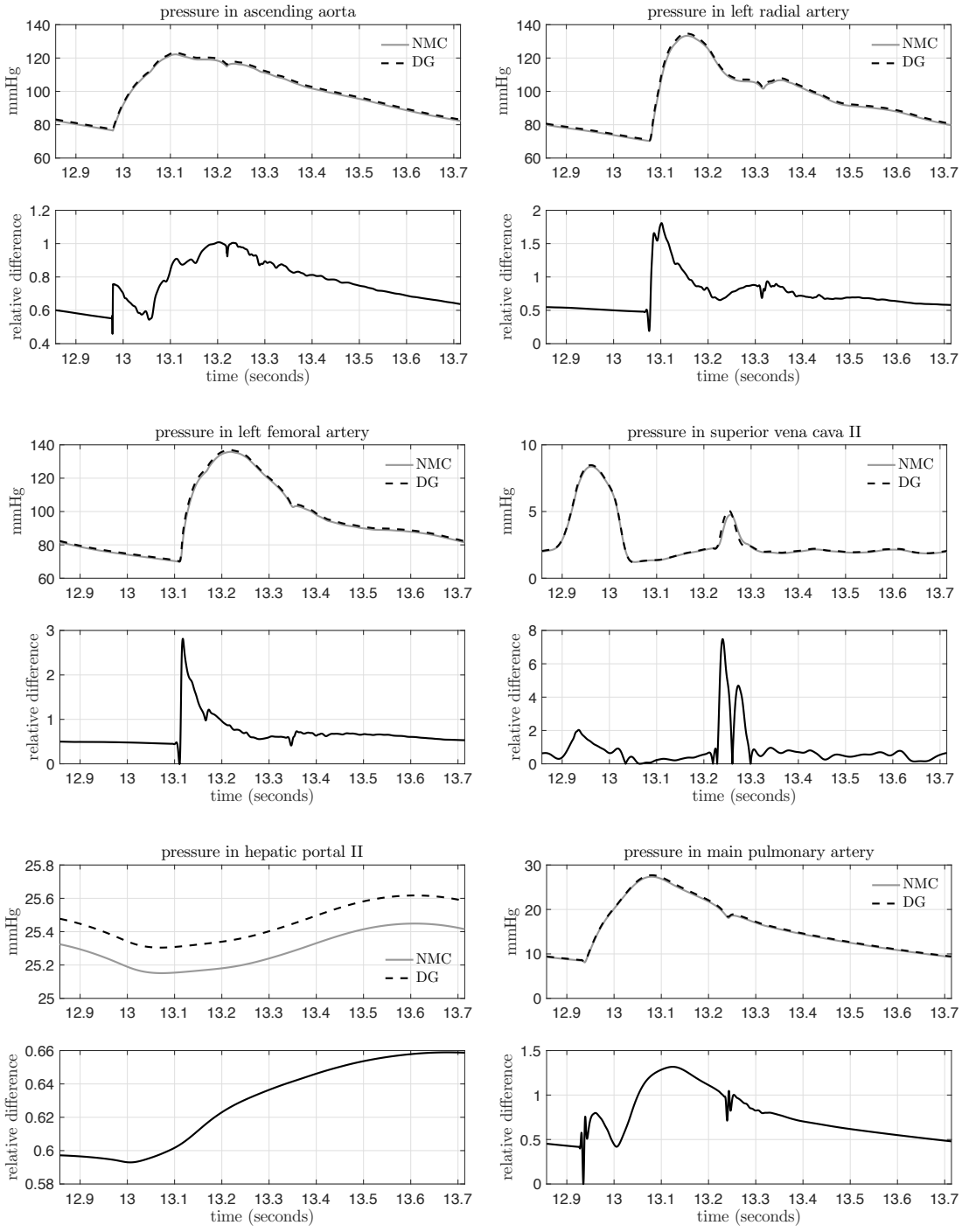

Figure 6.5 : Pressure waveforms from NMC and DG for the large vessel network, and their relative differences.

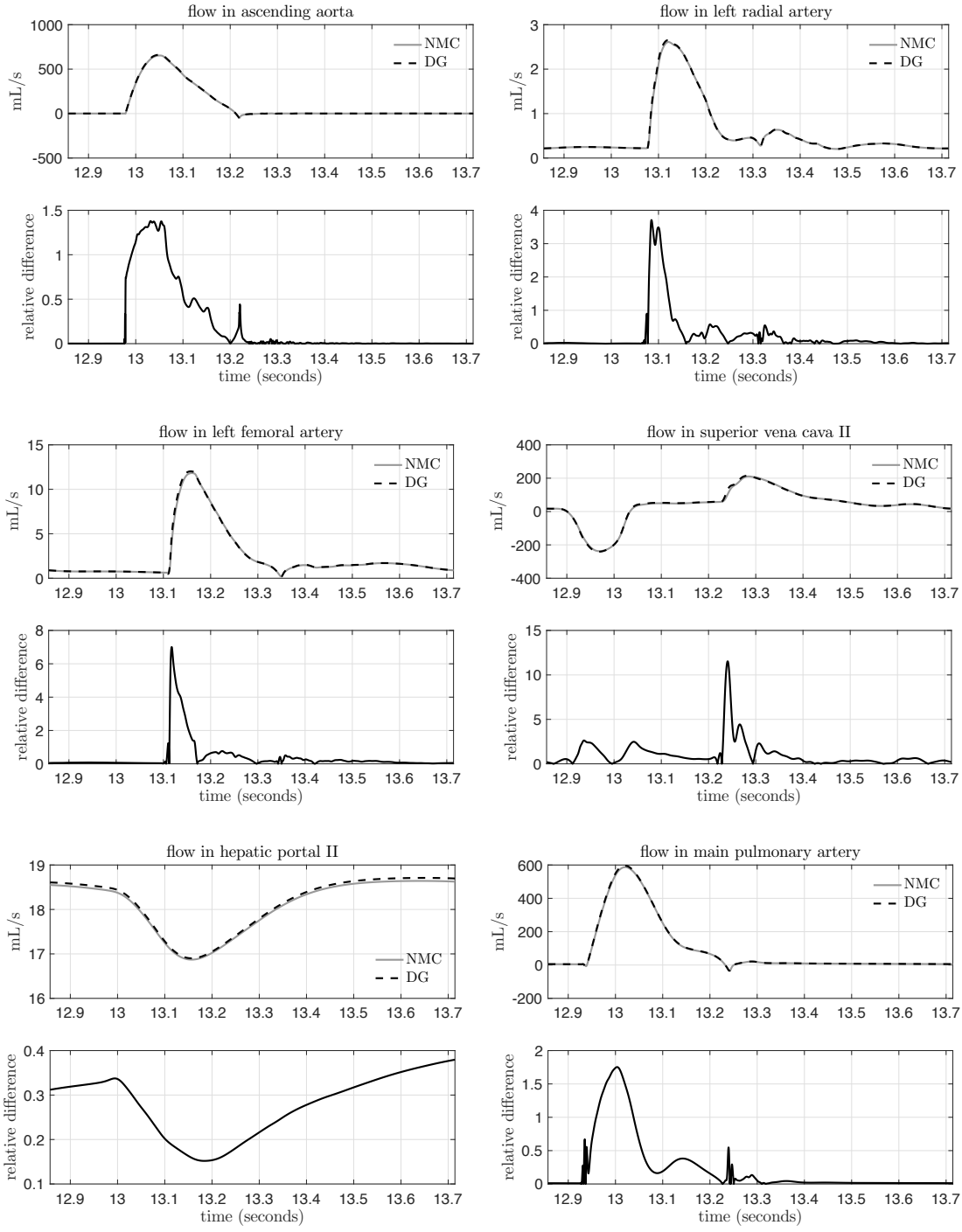

Figure 6.6 : Flow waveforms from NMC and DG for the large vessel network, and their relative differences.

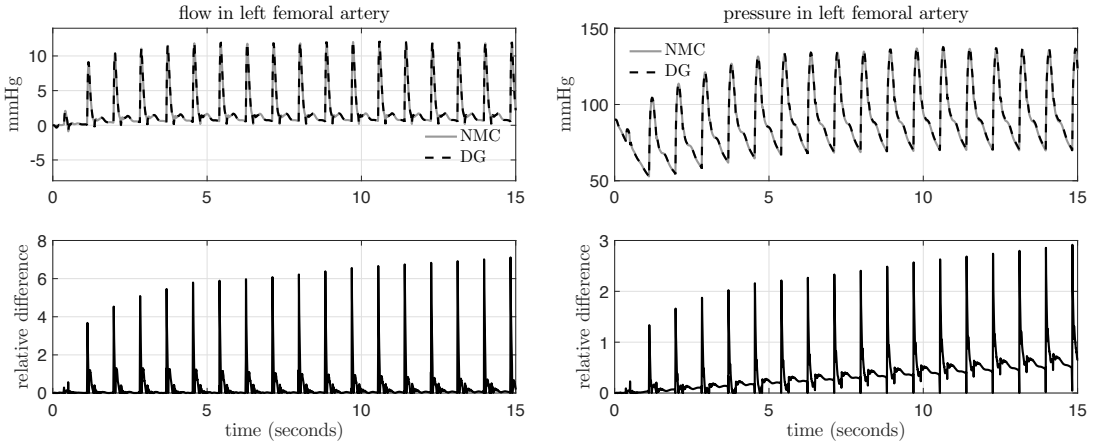

Figure 6.7 : Pressure and flow waveforms from NMC and DG in the femoral artery for multiple cardiac cycles. Notice the relative difference between these methods grows in time.

6.2 Comparison of various reduced models

This section is devoted to a numerical comparison of the the different reduced models of blood flow presented in Chapter 2. The content of this section is taken from our paper [48], with small modifications in the text to adapt it to this thesis. The numerical scheme is discontinuous Galerkin in space with second order Runge–Kutta in time, given in (3.124)–(3.125).

6.2.1 Introduction

In the following sections we compare several variants of reduced blood flow models expressed as nonlinear hyperbolic systems of conservation laws in one space dimension (the axial dimension of the blood vessel). We organize the models into two classes: (1) the (A, Q) system and (2) the (A, U) system modeling vessel cross–sectional area A and average fluid momentum Q or average axial velocity U, respectively. We remark that the (A, Q) system models the physically conserved variables of mass and

momentum. The velocity, however, is never conserved in physical problems, and this is why the (A, U) system does not follow that physical principle. Each class requires the specification of the axial velocity profile as a closure to the averaging process to completely determine the governing equations. Following the terminology of Hughes, we consider problems where either a *flat* profile (axial velocity equal to its average) or a *no–slip* profile (axial velocity at the vessel wall is zero) is chosen [7]. Models and terminology will be made more precise in the next section.

Despite popularity of reduced models for blood flow in a variety of research contexts (see e.g. [72, 9, 12, 4]), there is little work presenting a systematic comparison of different models using state–of–the–art numerical techniques. Further, to the best of our knowledge, many papers studying these models, for both theoretical investigation and clinical applications, use a simplifying flat velocity profile in the convective part of the equations; we call these *flat–profile models*.

The literature on reduced blood flow models is vast, due to the fact that simulations are much cheaper than full three–dimensional models of the circulatory system and that they perform relatively well in models of vessel networks when compared to physiological data [73, 11]. In particular, reduced models serve as an important component of "geometric multi–scale models," in which three–dimensional equations describe local phenomena while one– and zero–dimensional equations capture dynamics in the rest of the hemodynamic system [74, 75, 76].

We give a brief review of literature on models for the axial velocity profile and usage of the (A, Q) and (A, U) systems. Several authors have investigated different models for the axial velocity profile. Early work of Hughes and Lubliner provided a presentation of now popular classes of reduced blood flow models [77, 7]. In particular, Hughes derived jump conditions for various models arising from flat and no–slip

profiles and exhibited numerical experiments comparing different models in a single vessel using Lax–Wendroff–type discretizations [7]. Later work by Bessems et. al., using a variant of the (A, Q) system, extended the work of Hughes and Lubliner by describing a novel velocity profile with time dependent core and outer layer. [77, 78]. In certain limiting cases, their profile aligns with the model from Hughes and Lubliner. These authors performed numerical experiments in a single vessel, comparing their model with a profile derived from Poiseuille flow [78]. Lastly, Azer and Peskin constructed a profile from Womersley flow and presented numerical results in a single vessel and vessel network [79]. Using the Lax–Wendroff scheme to approximate a version of the (A, U) system, they compared their profile with different models for viscosity and with either "pure–resistance" or "structured–tree" outflow conditions at the terminal vessels [79].

For work utilizing the (A, U) class of systems, see e.g. [80, 47, 81, 4, 12, 82, 28]. Some examples of research using the (A, Q) system with a flat–profile closure include [83, 84, 72, 25, 11, 17, 85, 27]. A portion of these papers, including work from Formaggia et al., Sherwin et al. and Delestre and Lagrée are focused on careful descriptions of discontinuous Galerkin, Taylor Galerkin, and finite–volume schemes for these models; the flat–profile assumption is appealing in this context since these discretizations rely on the expression of the equations in conservative form [17, 4, 85]. Other works employing flat–profile models attempt to answer clinical questions, perform physiologically relevant experiments, and validate the models with measured data [11, 12, 82]. Lastly, there has been recent interest in performing systematic comparisons of different numerical schemes applied to flat–profile models [27, 28].

We remark that systems with a flat profile closure contain mathematical simplifications that lend to their appeal. In particular, the Riemann invariants can

be analytically computed and the (A, U) system can be expressed in conservative form. Important theoretical work regarding these models include existence of smooth solutions, estimates for shock formation, and analysis of coupling with the three–dimensional Navier–Stokes equations or ordinary differential equation models of the heart and organ beds [8, 9, 10].

The novel contribution of this section is to present thorough numerical experiments for the comparison reduced blood flow models derived from flat profile *and* no–slip profiles, in which the shape of the axial velocity profile is allowed to vary. In particular, we investigate the effect of profile shape on flow and pressure waveforms by considering both the (A, Q) and (A, U) systems; to the best of our knowledge, a comparison of these systems has not been done before. We use a discontinuous Galerkin scheme with Runge–Kutta method in time in a large vessel network and compare simple reflection terminal boundary conditions and more physiological three element windkessel terminal boundary conditions. In our simulations we compare two different numerical fluxes: (1) an upwinding flux in the Riemann invariants and (2) the classical local Lax–Friedrichs flux. Further, we run experiments in long vessels to study the formation of shocks in both the (A, Q) and (A, U) systems; this phenomena is of interest in modeling physiological conditions where sharp transitions may occur, like aortic regurgitation [86, 5, 87].

The outline of the remainder of the section is as follows. We begin by verifying the numerical scheme in Subsection 6.2.2 using the method of manufactured solutions to compute error rates. Then, in Subsection 6.2.3 we check the consistency of our results with those from Sherwin et al. [4]. Next, in Subsection 6.2.4, using nonphysiological input data from [4], we compare reflection conditions for the terminal vessels with more physiological three element windkessel conditions which incorporate a capacitor

to model the compliance of the distal vessels and organ beds. In Subsection 6.2.5, we then employ the vessel network from [4] with three element windkessel boundary conditions and physiological boundary data, to compare smooth solutions obtained from the (A, Q) and (A, U) systems for different choices of the velocity profile and different numerical fluxes. Finally, in in Subsection 6.2.6, we study the (A, Q) and (A, U) systems in the realm of discontinuous solutions using aortic regurgitation data. Versions of the systems used in these simulations appear throughout the literature, and have yet to be systematically compared.

6.2.2 Convergence rates for numerical scheme

We use the method of manufactured solutions to obtain numerical convergence rates for the spatial discretization of the scheme. The results presented here are only for the (A, Q) system, but we observe similar results for the (A, U) system. The domain is the unit interval and the exact solution is chosen as:

$$A(x,t) = \cos(2\pi x)\cos(t) + 2, \quad \forall x, t, \tag{6.1}$$

$$Q(x,t) = \sin(2\pi x)\cos(t), \quad \forall x, t. \tag{6.2}$$

The errors in the L^2 norm between the approximate and exact solution are computed on a sequence of uniformly refined meshes (from $h = 1/2$ to $h = 1/32$). Numerical convergence rates are derived from the numerical errors. We also study the effect of the approximation order by varying the polynomial degree ($k = 1, 2, 3$). For these computations, $\Delta t = 2 \times 10^{-5}$, small enough for the temporal error to be negligible, and the scheme is evolved for ten timesteps.

Table 6.1 and Table 6.2 show the errors and rates for the inviscid (A, Q) system for the DG method with the upwinding flux. We observe that we recover the convergence

	$k=1$		$k=2$		$k=3$	
h	L^2 error	rate	L^2 error	rate	L^2 error	rate
5.000×10^{-1}	8.50463×10^{-2}	–	8.50463×10^{-2}	–	2.77384×10^{-3}	–
2.500×10^{-1}	6.27686×10^{-2}	4.38206×10^{-1}	8.38200×10^{-3}	3.34288	8.33208×10^{-4}	1.73514
1.250×10^{-1}	1.61145×10^{-2}	1.96168	1.07115×10^{-3}	2.96813	5.30888×10^{-5}	3.97220
6.250×10^{-2}	4.05661×10^{-3}	1.99001	1.34655×10^{-4}	2.99183	3.33955×10^{-6}	3.99068
3.125×10^{-2}	1.01698×10^{-3}	1.99598	1.68662×10^{-5}	2.99706	2.10222×10^{-7}	3.98967

Table 6.1 : Errors and rates for A from the inviscid (A, Q) system with the upwinding flux.

	$k=1$		$k=2$		$k=3$	
h	L^2 error	rate	L^2 error	rate	L^2 error	rate
5.000×10^{-1}	3.07759×10^{-1}	–	1.72654×10^{-2}	–	1.72637×10^{-2}	–
2.500×10^{-1}	6.27688×10^{-2}	2.29368	8.38219×10^{-3}	1.04248	8.33190×10^{-4}	4.37296
1.250×10^{-1}	1.61144×10^{-2}	1.96170	1.07124×10^{-3}	2.96805	5.30835×10^{-5}	3.97231
6.250×10^{-2}	4.05662×10^{-3}	1.99000	1.34692×10^{-4}	2.99154	3.33921×10^{-6}	3.99068
3.125×10^{-2}	1.01714×10^{-3}	1.99576	1.68827×10^{-5}	2.99604	2.10339×10^{-7}	3.98872

Table 6.2 : Errors and rates for Q from the inviscid (A, Q) system with the upwinding flux.

rate $k+1$ for polynomial degree k, which is the optimal convergence rate for a scalar hyperbolic conservation law in one dimension, as noted in [33]. For general systems of conservation laws, the theoretical rates are suboptimal, as described in [33]. For comparison, in Table 6.3 and Table 6.4, we repeat the experiments for the DG method with the local Lax-Friedrichs flux. Similar conclusions can be made. The choice of the numerical flux does not have any effect on the errors or rates.

According to [33] and the symmetrizability results in this paper, the theoretical rates apply only to the DG approximation of inviscid reduced blood flow models with

	$k=1$		$k=2$		$k=3$	
h	L^2 error	rate	L^2 error	rate	L^2 error	rate
5.000×10^{-1}	8.50464×10^{-2}	–	8.50463×10^{-2}	–	2.77383×10^{-3}	–
2.500×10^{-1}	6.27701×10^{-2}	4.38172×10^{-1}	8.38198×10^{-3}	3.34289	8.33333×10^{-4}	1.73492
1.250×10^{-1}	1.61152×10^{-2}	1.96166	1.07124×10^{-3}	2.96802	5.31025×10^{-5}	3.97204
6.250×10^{-2}	4.05692×10^{-3}	1.98996	1.34713×10^{-4}	2.99132	3.34105×10^{-6}	3.99041
3.125×10^{-2}	1.01712×10^{-3}	1.99590	1.68984×10^{-5}	2.99493	2.10352×10^{-7}	3.98942

Table 6.3 : Errors and rates for A from the inviscid (A, Q) system with the local Lax–Friedrichs flux.

	$k=1$		$k=2$		$k=3$	
h	L^2 error	rate	L^2 error	rate	L^2 error	rate
5.000×10^{-1}	3.07761×10^{-1}	–	1.72654×10^{-2}	–	1.72637×10^{-2}	–
2.500×10^{-1}	6.27686×10^{-2}	2.29369	8.38229×10^{-3}	1.04247	8.33163×10^{-4}	4.37300
1.250×10^{-1}	1.61142×10^{-2}	1.96171	1.07129×10^{-3}	2.96800	5.30794×10^{-5}	3.97237
6.250×10^{-2}	4.05650×10^{-3}	1.99002	1.34712×10^{-4}	2.99140	3.33866×10^{-6}	3.99081
3.125×10^{-2}	1.01708×10^{-3}	1.99580	1.68910×10^{-5}	2.99555	2.10277×10^{-7}	3.98891

Table 6.4 : Errors and rates for Q from the inviscid (A, Q) system with the local Lax–Friedrichs flux.

the local Lax–Friedrichs flux. We next investigate the numerical rates for the general (A, Q) system with $\alpha = 1.1$. Similar results are obtained when we choose $\alpha = 4/3$, and we omit them for brevity. Table 6.5 and Table 6.6 show the errors and rates, with the same set-up as the previous experiments. The upwinding flux is used. The numerical rates are optimal. Theoretical error estimates remain an open question. Table 6.7 and Table 6.8 show optimal rates for the case of the local Lax-Friedrichs flux. Results are comparable to those obtained with the upwinding flux.

	$k=1$		$k=2$		$k=3$	
h	L^2 error	rate	L^2 error	rate	L^2 error	rate
5.000×10^{-1}	8.50463×10^{-2}	–	8.50463×10^{-2}	–	2.77384×10^{-3}	–
2.500×10^{-1}	6.27686×10^{-2}	4.38206×10^{-1}	8.38200×10^{-3}	3.34288	8.33208×10^{-4}	1.73514
1.250×10^{-1}	1.61145×10^{-2}	1.96168	1.07115×10^{-3}	2.96813	5.30887×10^{-5}	3.97220
6.250×10^{-2}	4.05661×10^{-3}	1.99001	1.34654×10^{-4}	2.99183	3.33952×10^{-6}	3.99069
3.125×10^{-2}	1.01698×10^{-3}	1.99599	1.68662×10^{-5}	2.99706	2.10208×10^{-7}	3.98975

Table 6.5 : Errors and rates for A from the (A, Q) system, $\alpha = 1.1$, with the upwinding flux.

	$k=1$		$k=2$		$k=3$	
h	L^2 error	rate	L^2 error	rate	L^2 error	rate
5.000×10^{-1}	3.07759×10^{-1}	–	1.72654×10^{-2}	–	1.72637×10^{-2}	–
2.500×10^{-1}	6.27691×10^{-2}	2.29368	8.38220×10^{-3}	1.04248	8.33214×10^{-4}	4.37292
1.250×10^{-1}	1.61148×10^{-2}	1.96167	1.07124×10^{-3}	2.96805	5.30905×10^{-5}	3.97216
6.250×10^{-2}	4.05694×10^{-3}	1.98992	1.34694×10^{-4}	2.99152	3.34070×10^{-6}	3.99023
3.125×10^{-2}	1.01743×10^{-3}	1.99546	1.68844×10^{-5}	2.99592	2.10646×10^{-7}	3.98726

Table 6.6 : Errors and rates for Q from the (A, Q) system, $\alpha = 1.1$, with the upwinding flux.

6.2.3 Verfication of numerical scheme

In this section, we verify our numerical scheme by simulating blood flow in a fifty–five vessel network and comparing with results from [4]. We provide results for both the inviscid (A, Q) and inviscid (A, U) systems in this section. The incoming Riemann invariant W_1 is prescribed at the inlet of the ascending aorta, and the reflection boundary conditons (5.11) and (5.12) are used at the outlets of the terminal vessels. Figure 6.8 displays the vessel network and the inlet boundary condition. Vessel parameters are taken from [4]. The numerical parameters are $\Delta t = 10^{-4}$ s, $h = 1$ cm,

	$k=1$		$k=2$		$k=3$	
h	L^2 error	rate	L^2 error	rate	L^2 error	rate
5.000×10^{-1}	8.50463×10^{-2}	–	8.50463×10^{-2}	–	2.77383×10^{-3}	–
2.500×10^{-1}	6.27702×10^{-2}	4.38168×10^{-1}	8.38200×10^{-3}	3.34288	8.33345×10^{-4}	1.73489
1.250×10^{-1}	1.61152×10^{-2}	1.96166	1.07125×10^{-3}	2.96800	5.31039×10^{-5}	3.97203
6.250×10^{-2}	4.05695×10^{-3}	1.98996	1.34722×10^{-4}	2.99124	3.34118×10^{-6}	3.99039
3.125×10^{-2}	1.01713×10^{-3}	1.99590	1.69031×10^{-5}	2.99463	2.10355×10^{-7}	3.98946

Table 6.7 : Errors and rates for A from the (A, Q) system, $\alpha = 1.1$, with the local Lax–Friedrichs flux.

	$k=1$		$k=2$		$k=3$	
h	L^2 error	rate	L^2 error	rate	L^2 error	rate
5.000×10^{-1}	3.07761×10^{-1}	–	1.72654×10^{-2}	–	1.72638×10^{-2}	–
2.500×10^{-1}	6.27688×10^{-2}	2.29369	8.38233×10^{-3}	1.04246	8.33176×10^{-4}	4.37298
1.250×10^{-1}	1.61145×10^{-2}	1.96169	1.07130×10^{-3}	2.96799	5.30850×10^{-5}	3.97225
6.250×10^{-2}	4.05679×10^{-3}	1.98995	1.34717×10^{-4}	2.99136	3.33997×10^{-6}	3.99039
3.125×10^{-2}	1.01736×10^{-3}	1.99551	1.68933×10^{-5}	2.99540	2.10566×10^{-7}	3.98750

Table 6.8 : Errors and rates for Q from the (A, Q) system, $\alpha = 1.1$, with the local Lax–Friedrichs flux.

$k = 1$, and the numerical flux is the upwinding flux. The physical parameters are $\nu = 0$ cm^2/s and $p_0 = 75$ mmHg.

The waveforms displayed are obtained during the tenth cardiac cycle at the inlet of the left femoral and left anterior tibial vessels. We plot results for the (A, U) system in Figures 6.9 and 6.10 and the (A, Q) system in Figures 6.11 and 6.12. Also plotted in circles are data taken from the waveforms in [4] obtained with different polynomial degree and timestep. We observe excellent agreement between our results and those from [4].

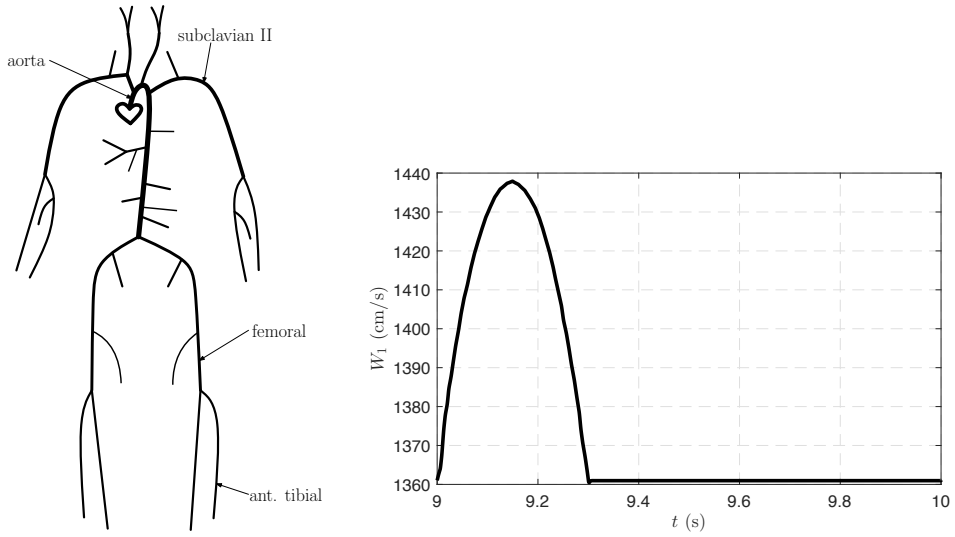

Figure 6.8 : The schematic on the left depicts the topology of the vessel network used throughout this paper, from Sherwin et al. [4]. The labels indicate the ascending aorta, where the inlet boundary condition is specified, and the femoral and anterior tibial arteries, where waveforms are measured. The figure on the right is the inlet boundary condition at the ascending aorta, also from [4].

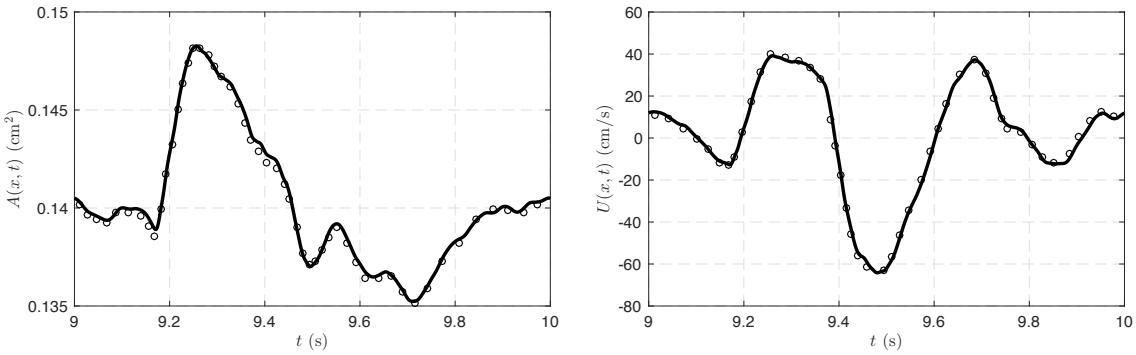

Figure 6.9 : Waveforms from the inviscid (A, U) system ($\alpha = 1$) obtained at the inlet of the left femoral artery. The upwinding numerical flux is used. Our numerical results are plotted with the solid line and the circles are data taken from Sherwin et al. [4].

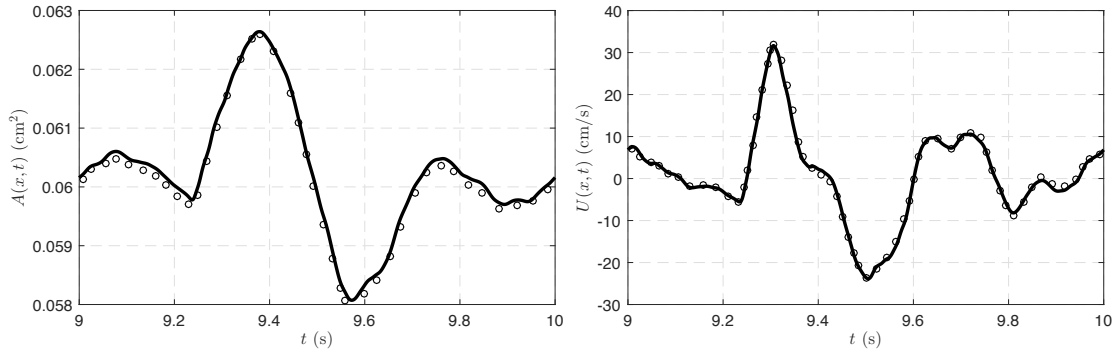

Figure 6.10 : Waveforms from the inviscid (A, U) system ($\alpha = 1$) obtained at the inlet of the left anterior tibial artery. The upwinding numerical flux is used. Our numerical results are plotted with the solid line and the circles are data taken from Sherwin et al. [4].

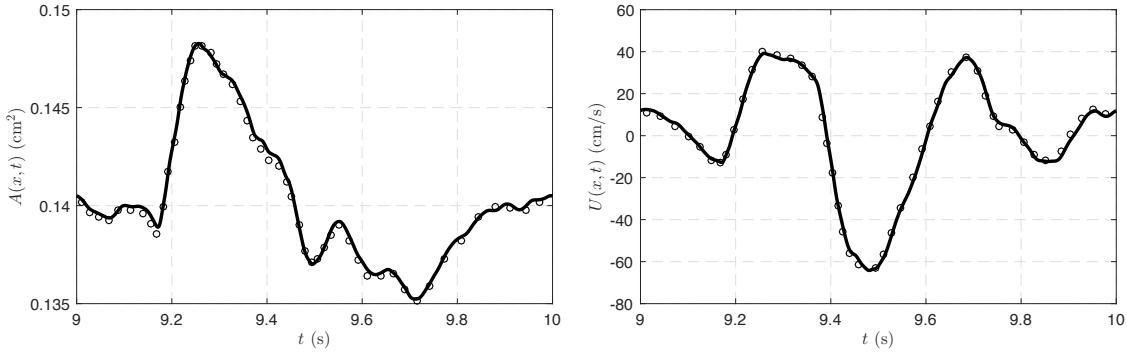

Figure 6.11 : Waveforms from the inviscid (A, Q) system ($\alpha = 1$) obtained at the inlet of the left femoral artery. The upwinding numerical flux is used. Our numerical results are plotted with the solid line and the circles are data taken from Sherwin et al. [4].

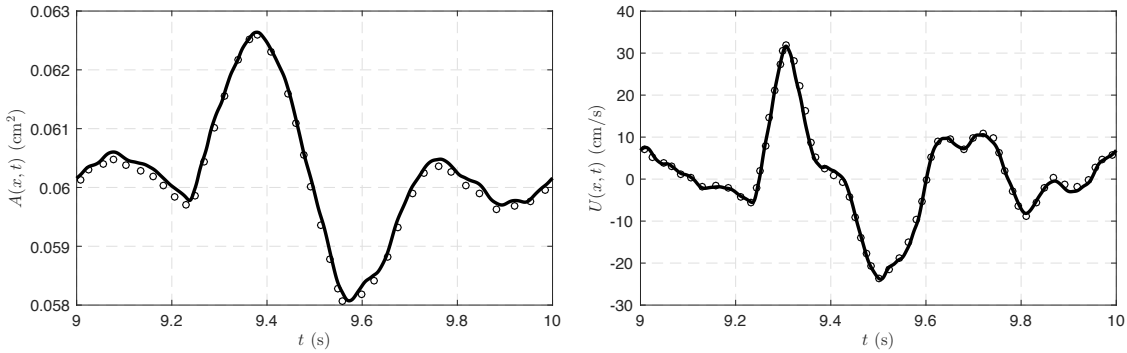

Figure 6.12 : Waveforms from the inviscid (A, Q) obtained $(\alpha = 1)$ at the inlet of the left anterior tibial artery. The upwinding numerical flux is used. Our numerical results are plotted with the solid line and the circles are data taken from Sherwin et al. [4].

6.2.4 Comparison of waveforms obtained with windkessel and reflection boundary conditions

In this section, we study the effect of different terminal boundary conditions on the waveforms. We compare the reflection boundary conditions given in equations (5.11) and (5.12), with three element windkessel boundary conditions specified by equations (5.18) and (5.19). The parameters for the windkessel boundary conditions are taken from [28] and for the reflection boundary condition from [4]. The vessel network and inlet boundary data are the same as in the previous section. The numerical parameters are $\Delta t = 10^{-4}$ s, $h = 1$ cm, $k = 1$, and the numerical flux is the upwinding flux. The physical parameters are $\nu = 0$ cm^2/s, $p_0 = 75$ mmHg, and $P_{\text{out}} = 0$ mmHg.

In Figures 6.13–6.16, the solid line waveforms are produced with the reflection boundary condition and the dashed line waveforms are produced with the three element windkessel model. Figures 6.13 and 6.14 are from the (A, U) system and Figures 6.15 and 6.16 are from the (A, Q) system. First, we note that the waveforms from either (A, Q) or (A, U) are similar for a given choice of boundary conditions. Second, we observe that both terminal boundary conditions produce different waveforms with relative similar shape and magnitude. The reflection conditions create higher frequency oscillations while the windkessel model yields distinctly smoother features. Since the oscillations from the reflection conditions are arguably less physiological, we use the windkessel conditions in the remainder of the paper.

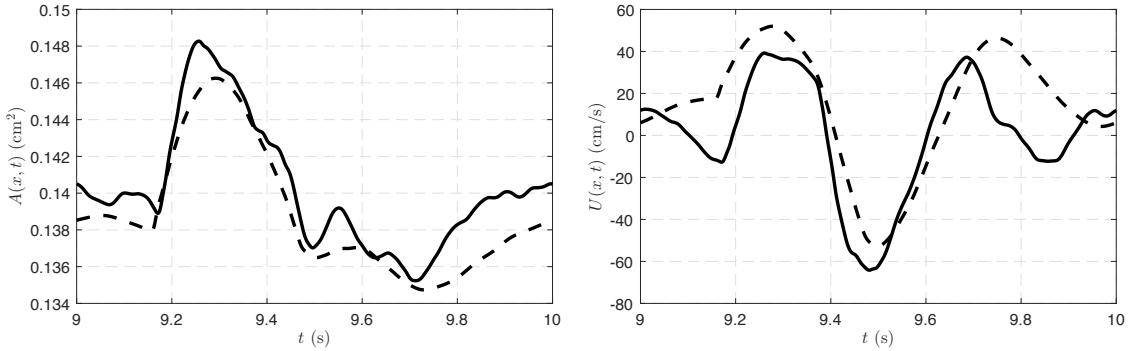

Figure 6.13 : Waveforms from the inviscid (A, U) system ($\alpha = 1$) obtained at the inlet of the left femoral artery. The upwinding numerical flux is used. Solid line corresponds to results with reflection boundary conditions and dashed line corresponds to results with windkessel boundary conditions.

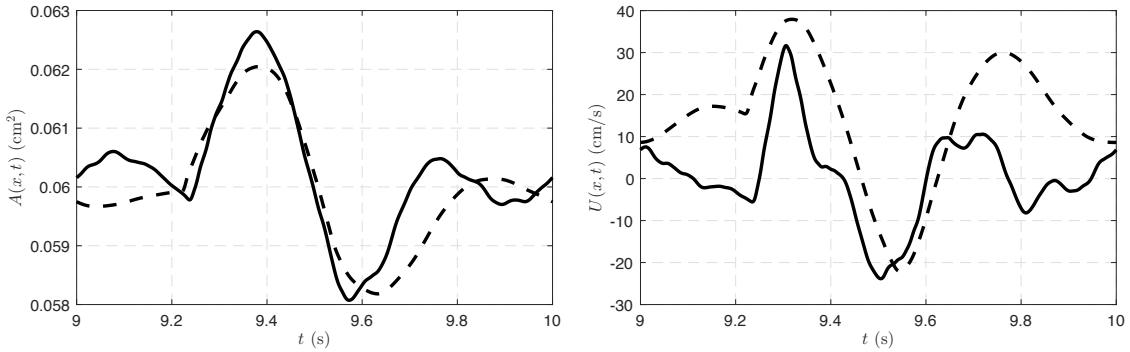

Figure 6.14 : Waveforms from the inviscid (A, U) system ($\alpha = 1$) obtained at the inlet of the left anterior tibial artery. The upwinding numerical flux is used. Solid line corresponds to results with reflection boundary conditions and dashed line corresponds to results with windkessel boundary conditions.

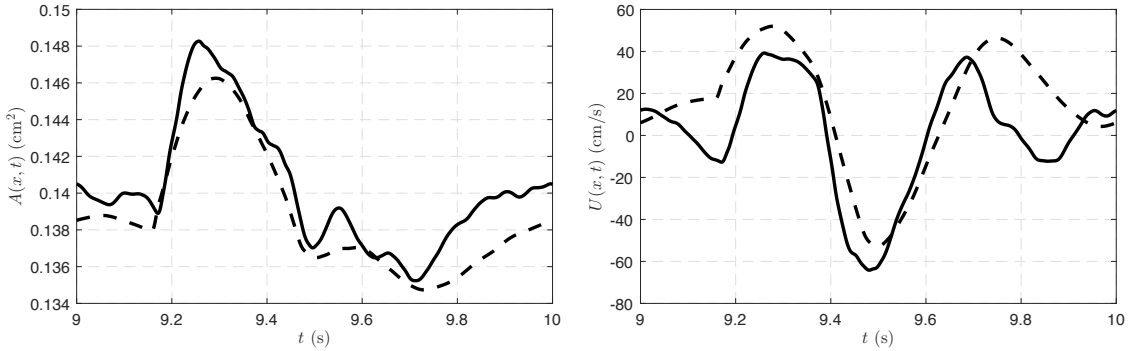

Figure 6.15 : Waveforms from the inviscid (A, Q) system ($\alpha = 1$) obtained at the inlet of the left femoral artery. The upwinding numerical flux is used. Solid line corresponds to results with reflection boundary conditions and dashed line corresponds to results with windkessel boundary conditions.

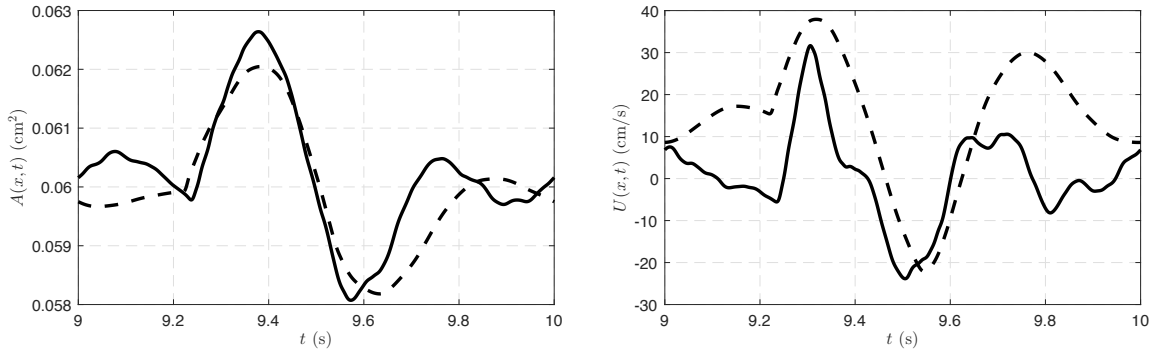

Figure 6.16 : Waveforms from the inviscid (A, Q) system ($\alpha = 1$) obtained at the inlet of the left anterior tibial artery. The upwinding numerical flux is used. Solid line corresponds to results with reflection boundary conditions and dashed line corresponds to results with windkessel boundary conditions.

6.2.5 Fifty–five vessel network with physiological inlet data

In this section, we study the effect of changing the shape of the velocity profile (changing α) on waveforms produced by the (A, Q) and (A, U) systems with physiological inlet data. For this simulation, we use the fifty–five vessel network and windkessel boundary conditions described in the previous section. The inlet condition at the ascending aorta is the momentum Q given in Figure 6.17 and is obtained from experimental data [28, 88]. The numerical parameters are $\Delta t = 10^{-4}$ s, $h = 1$ cm, and $k = 1$. The physical parameters are $\nu = 3.302 \times 10^{-2}$ cm^2/s, $p_0 = 75$ mmHg, and $P_{\text{out}} = 0$ mmHg.

Figures 6.18 and 6.19 compare flow and pressure waveforms obtained throughout the network with the (A, Q) system for α values 1, 4/3, and 1.1. In Figures 6.20 and 6.21, we show the same comparison for the (A, U) system. Figures 6.22 and 6.23 compare waveforms between the (A, Q) and (A, U) systems for $\alpha = 4/3$, and Figures 6.24 and 6.25 show the same comparison but for $\alpha = 1.1$.

We observe similar discrepancies in the waveforms for both the (A, Q) and (A, U) systems for different values of α. For the Poiseuille profile corresponding to $\alpha = 4/3$, the viscous term is smaller than for the flatter profile corresponding to $\alpha = 1.1$. This difference yields waveforms with higher magnitude pressure gradients and oscillations for $\alpha = 4/3$; see for example the radial and subclavian arteries. Further, note that most of the waveforms corresponding to $\alpha = 4/3$ exhibit a lower mean pressure, especially for the larger arteries. This difference could be explained by the fact that a fluid with lower viscosity ($\alpha = 4/3$) moves more easily through a compliant cylinder and therefore renders a lower mean pressure.

The case $\alpha = 1$ in Figures 6.18–6.21 refers to inviscid versions of the (A, Q) and (A, U) systems defined in equations (2.7)–(2.8) and (2.11)–(2.12) respectively. In this

case the profile is flat and the kinematic viscosity is equal to zero. Pressure gradients and oscillations in the waveforms are even more pronounced in this case.

For a fixed value of α, the (A, Q) and (A, U) systems generally produce waveforms with similar features and magnitudes. As expected, the results agree relatively well for $\alpha = 1.1$, since the (A, Q) and (A, U) systems are equivalent for smooth solutions when α is set equal to one in the convective part of the (A, Q) system. However, when $\alpha = 4/3$, there are some discrepancies between these systems since they differ more in the convective term.

Lastly, we compare results obtained with the local Lax–Friedrichs (LLF) and upwinding (UP) numerical fluxes in Figures 6.26 and 6.27. The (A, Q) system with $\alpha = 1.1$ is used; results are similar for the (A, U) system and other values of α. The upper subfigure displays the waveforms from each numerical flux, and the lower subfigure displays the pointwise relative difference between the waveforms. This difference is computed by normalizing by the maximum norm of the waveform produced by the LLF flux and is quite small ($\sim 10^{-5}$).

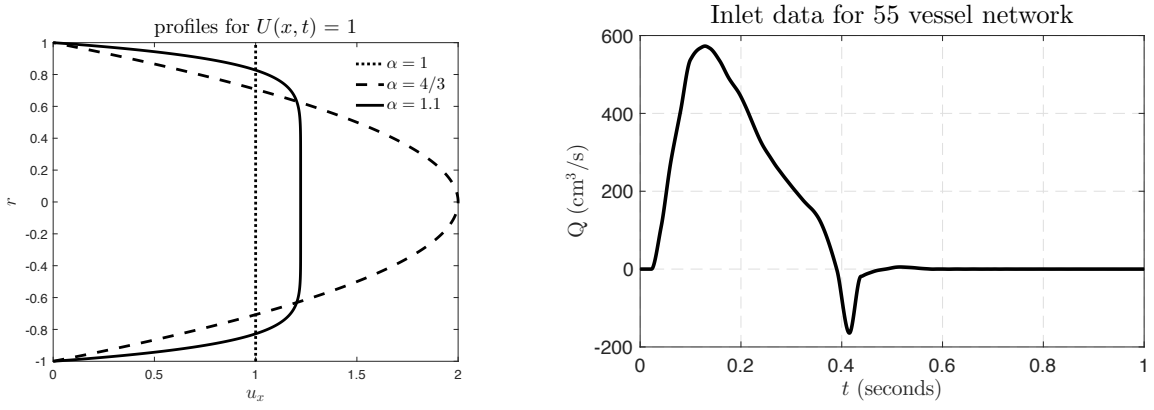

Figure 6.17 : The plot on the left shows the different velocity profiles compared in this section (with $U = 1$), along with the flat profile corresponding to $\alpha = 1$. The plot on the right depicts boundary data for Q at the inlet of the ascending aorta.

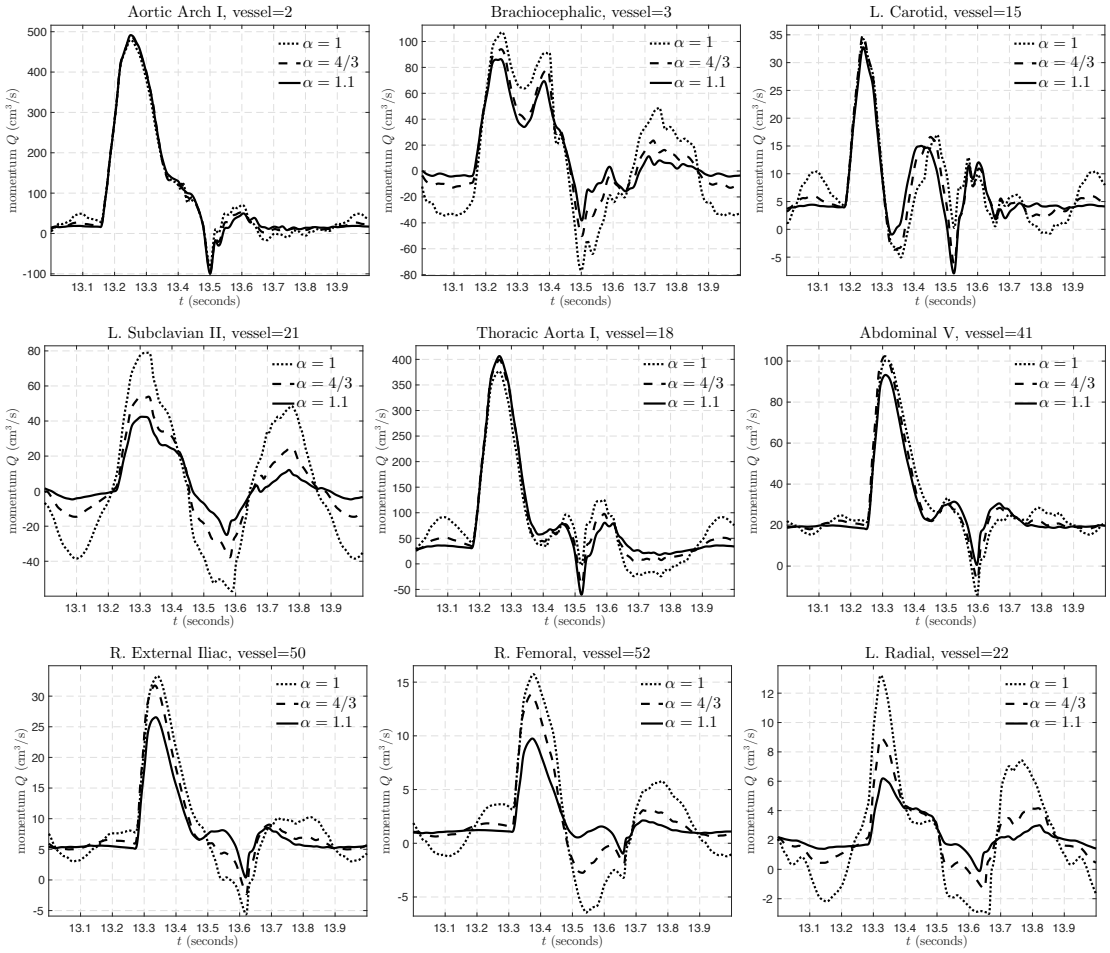

Figure 6.18 : A comparison of the momentum waveforms from the (A, Q) system with $\alpha = 1$, 1.1 and 4/3.

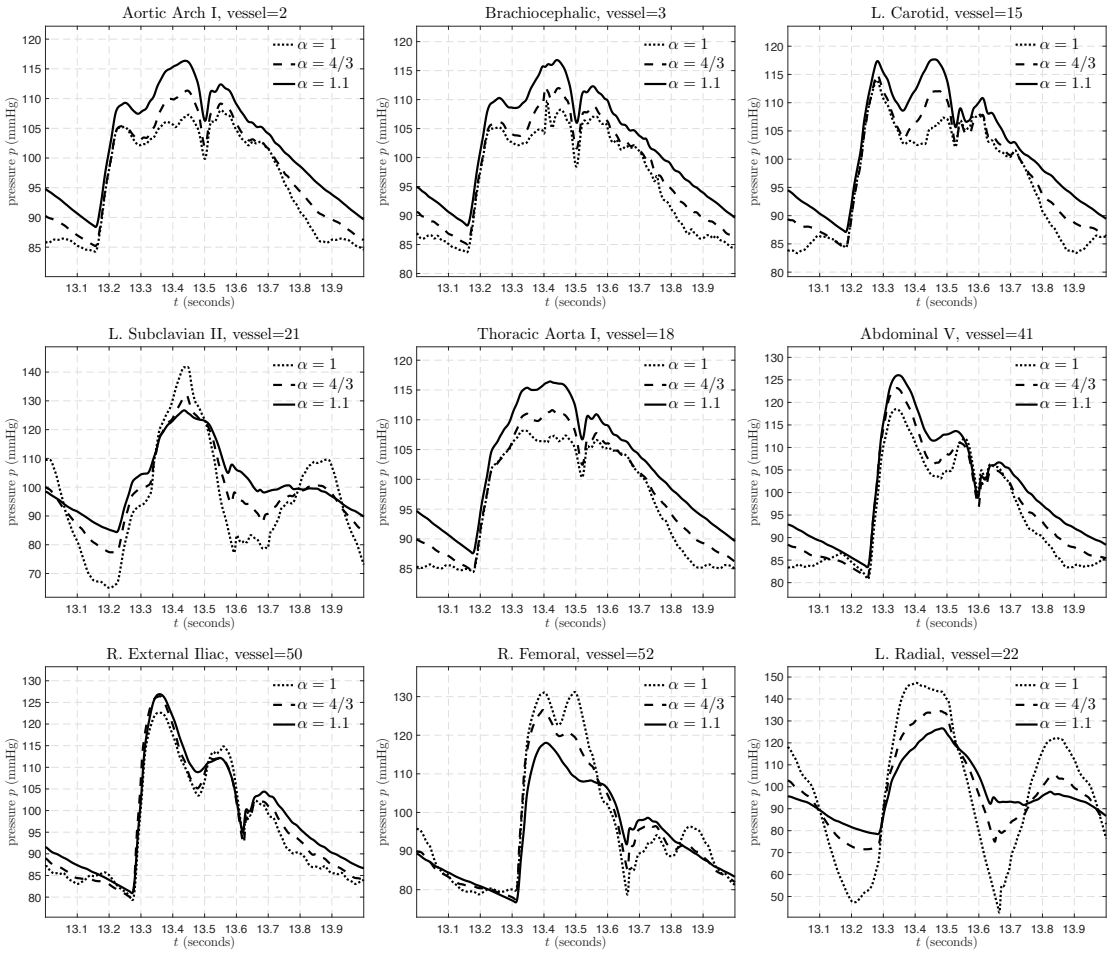

Figure 6.19 : A comparison of the pressure waveforms from the (A, Q) system with $\alpha = 1$, 1.1 and 4/3.

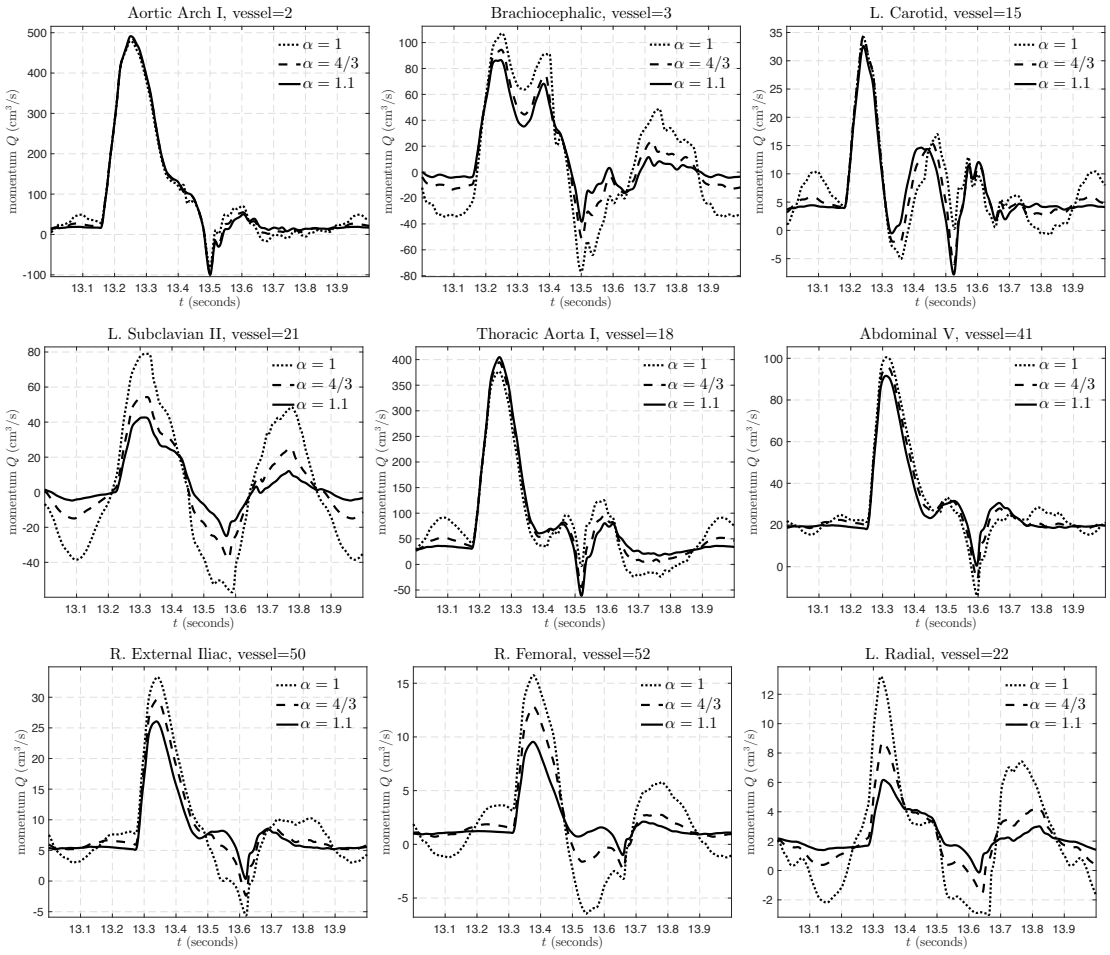

Figure 6.20 : A comparison of the momentum waveforms from the (A, U) system with $\alpha = 1$, 1.1 and 4/3.

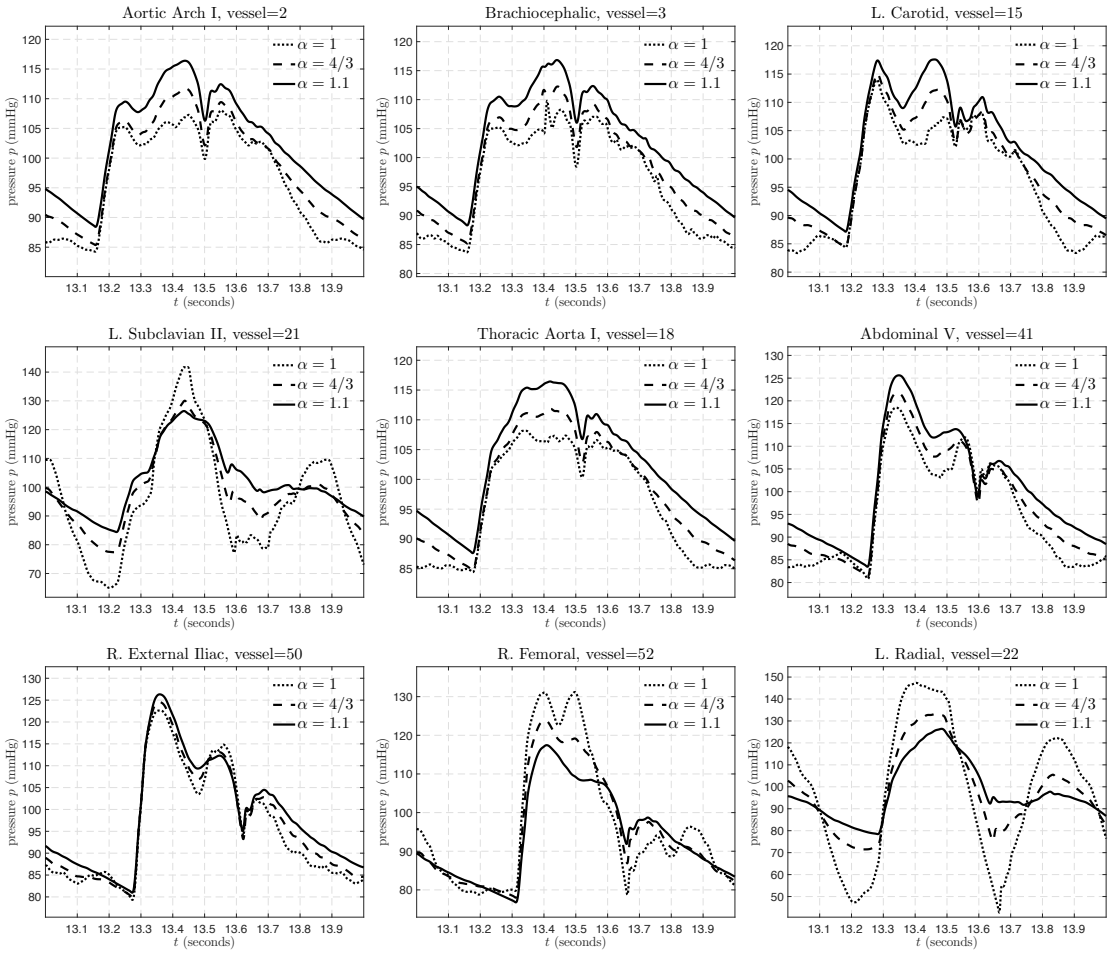

Figure 6.21 : A comparison of the pressure waveforms from the (A, U) system with $\alpha = 1$, 1.1 and 4/3.

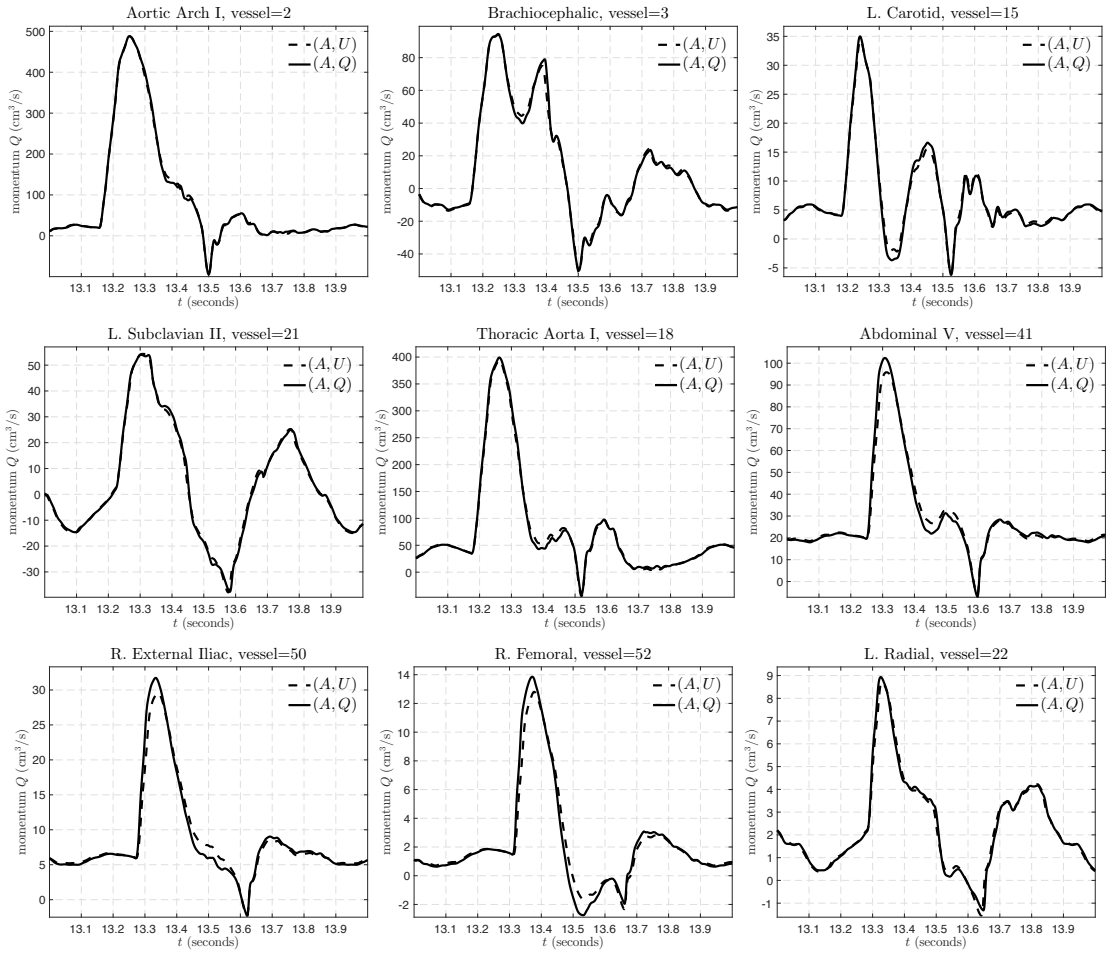

Figure 6.22 : A comparison of the momentum waveforms from the (A, Q) and (A, U) systems with $\alpha = 4/3$.

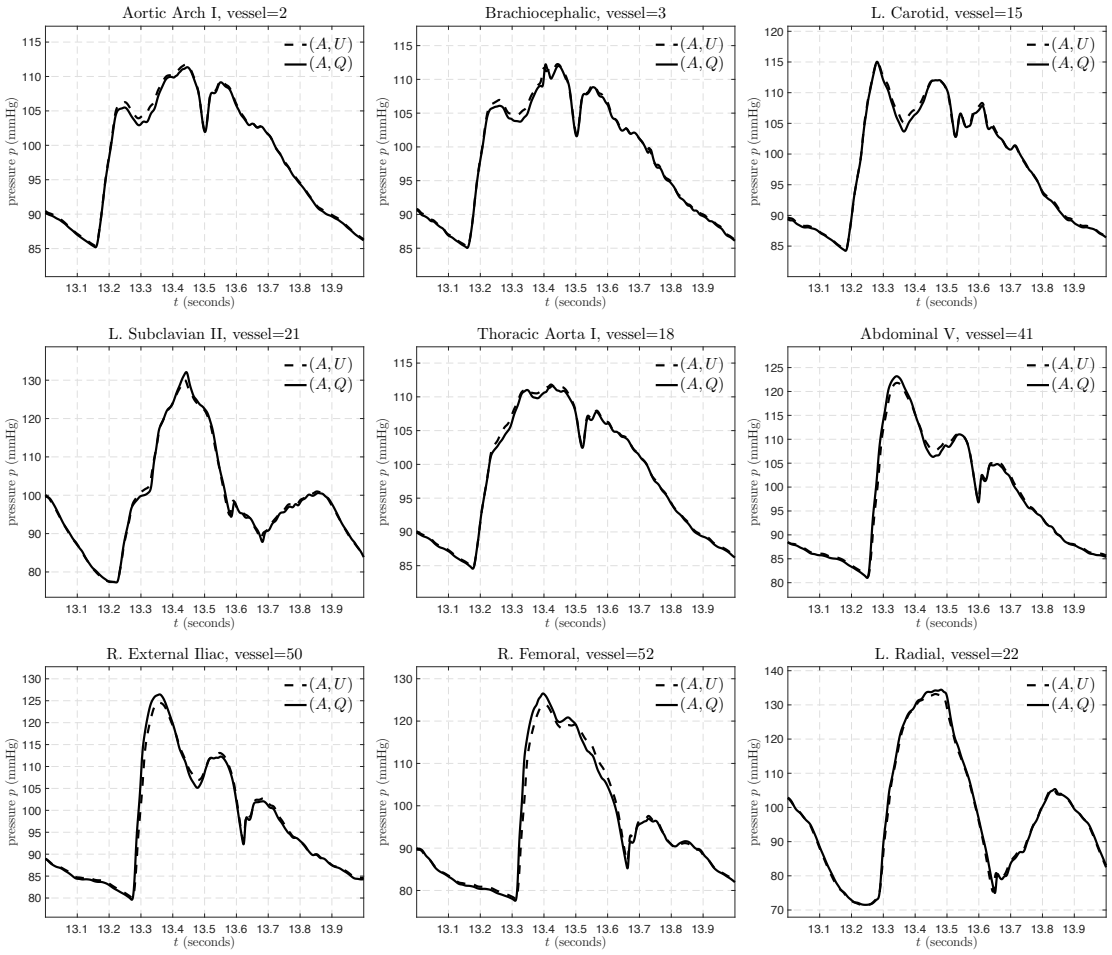

Figure 6.23 : A comparison of the pressure waveforms from the (A, Q) and (A, U) systems with $\alpha = 4/3$.

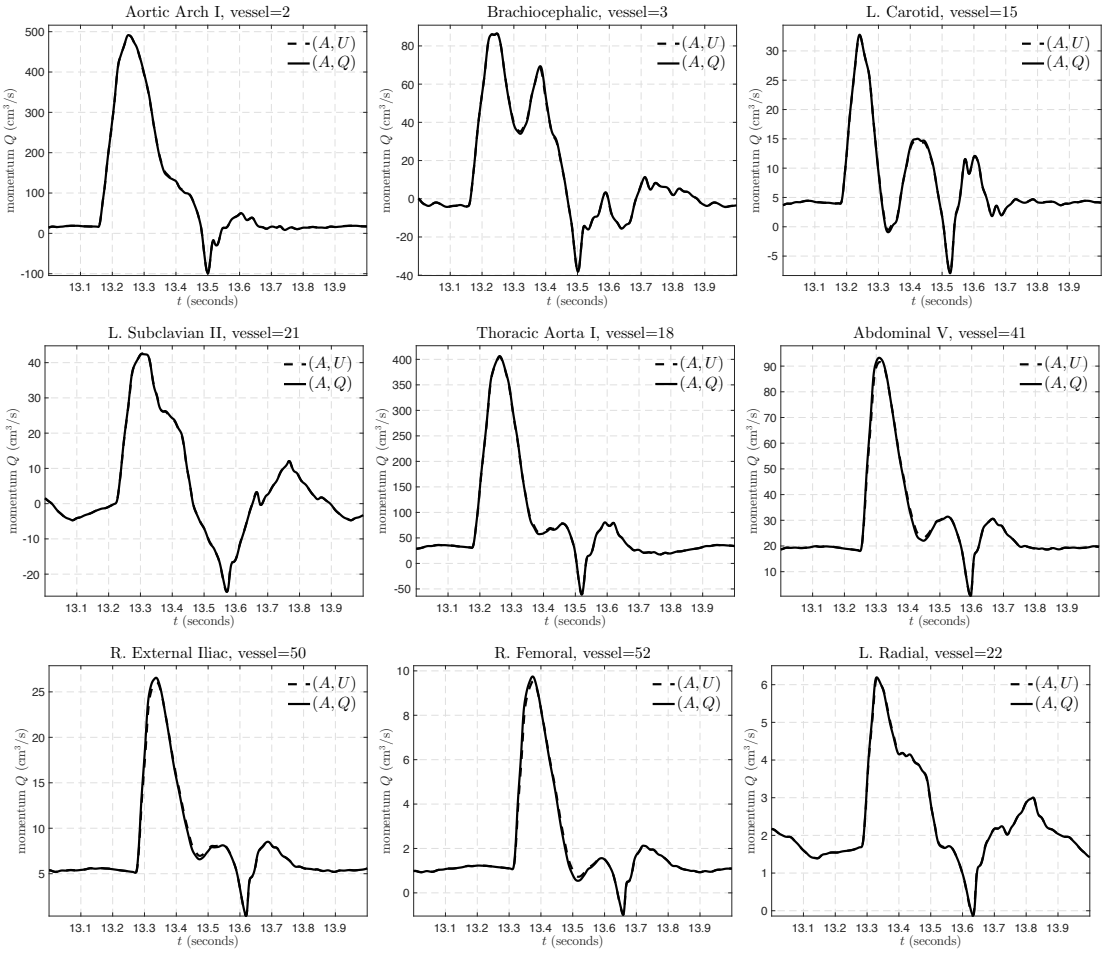

Figure 6.24 : A comparison of the momentum waveforms from the (A, Q) and (A, U) systems with $\alpha = 1.1$.

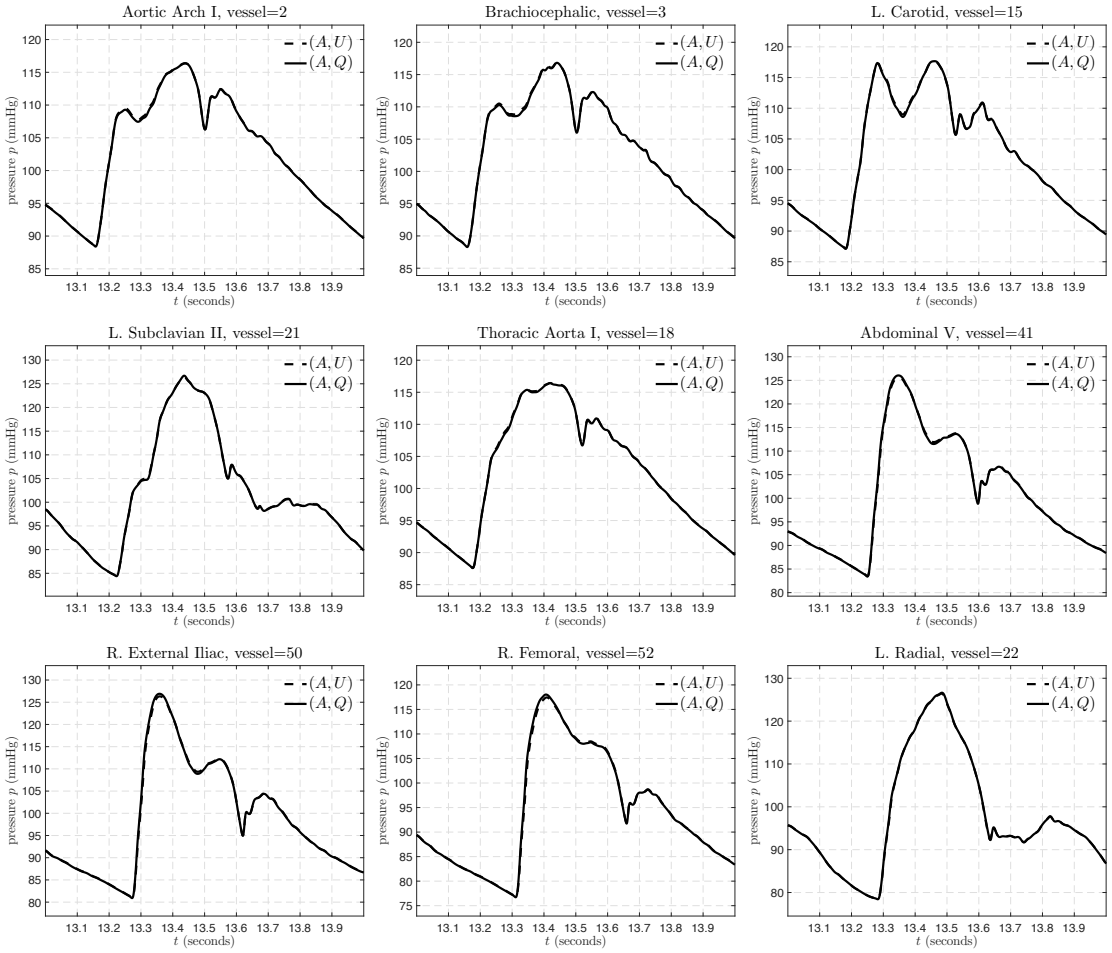

Figure 6.25 : A comparison of the pressure waveforms from the (A, Q) and (A, U) systems with $\alpha = 1.1$.

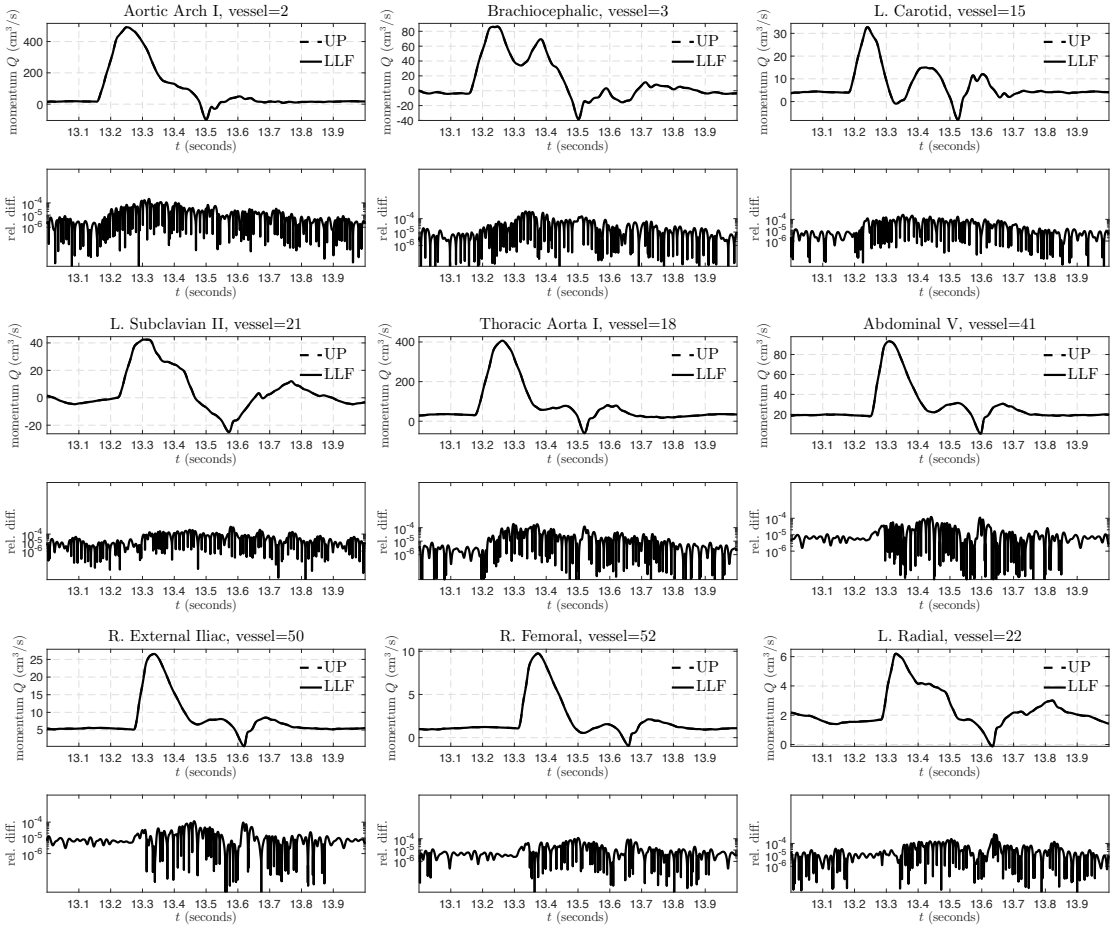

Figure 6.26 : A comparison of the momentum waveforms from the (A, Q) system with $\alpha = 1.1$ for different choices of the numerical flux.

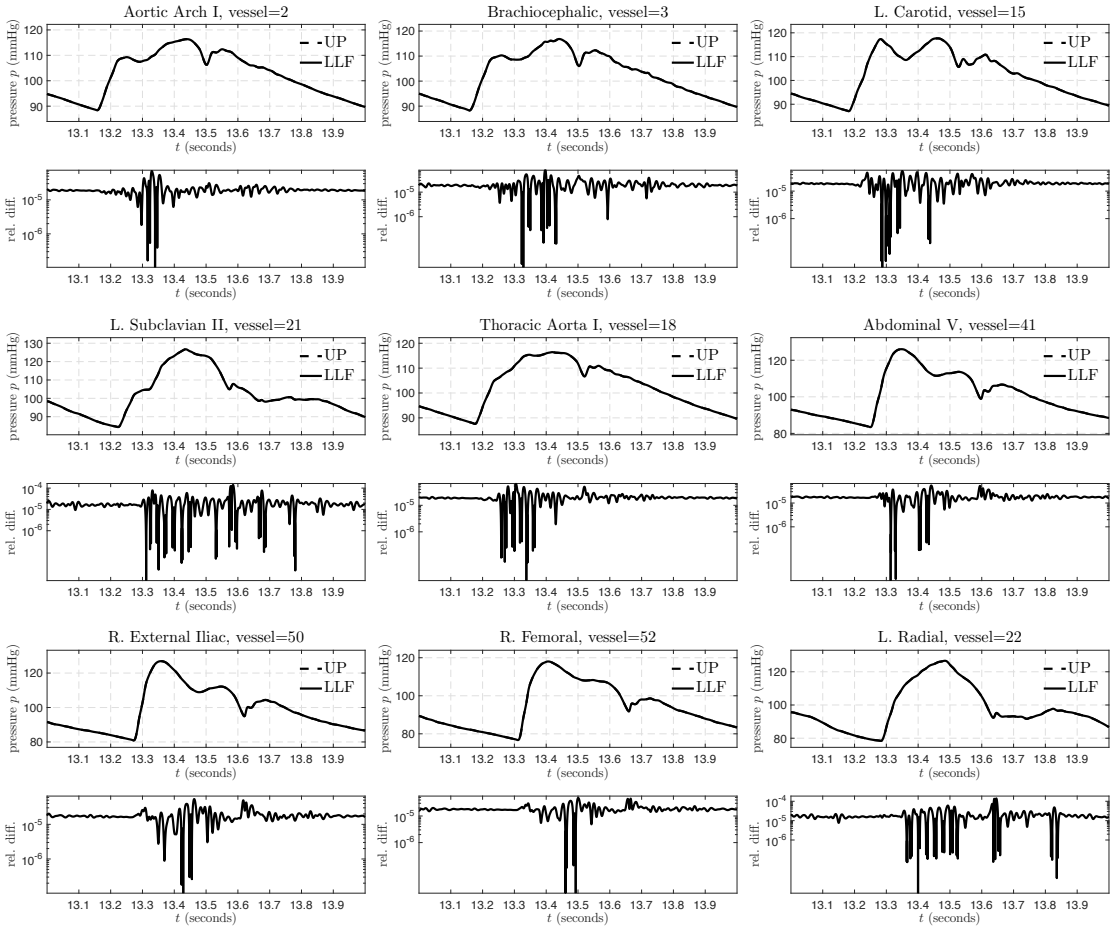

Figure 6.27 : A comparison of the pressure waveforms from the (A, Q) system with $\alpha = 1.1$ for different choices of the numerical flux.

6.2.6 Shock formation in the subclavian artery

In this section, we are interested in the effect of changing the Coriolis coefficient α among different models in the realm of solutions with possible shocks, i.e. a discontinuity in the pressure. Bloodflow waveforms are typically smooth in healthy individuals, but doctors speculate that a faulty heart produces flows that have the capacity to form sharp transitions within the body. An important problem potentially leading to nonsmooth waveforms is aortic regurgitation, characterized by an aortic valve which leaks blood back into the left ventricle. To compensate for the backflow of blood into the ventricle, the heart works harder and the pulse pressure (the difference between the maximum and minimum pressure) increases. Interestingly, this pathological problem was important for early work on bloodflow modeling: experimental and clinical evidence, including "pistol-shot" sounds in the arteries of patients with aortic regurgitation, indicated the importance of nonlinear effects in reduced bloodflow equations (see e.g. [89, 86]).

Figure 6.28 displays a pressure waveform measured in the subclavian artery (denoted "subclavian II" in Figure 6.8) of a patient with aortic regurgitation, taken from [5]. Notice the pulse pressure is greater than 100 mmHg, while a typical healthy pulse pressure is 40 mmHg. The large pulse pressure seen in aortic regurgitation leads to a rapid increase in the blood velocity at the beginning of the cardiac cycle, i.e. $\partial U/\partial t$ evaluated at the vessel inlet is larger than usual. In turn, Canic and Kim derived an estimate on the distance at which a shock develops (from the vessel inlet) that depends inversely on $\partial U/\partial t$; hence, we expect a shock to form more quickly (closer to the vessel inlet) in this pathological case [8].

We use the waveform in Figure 6.28 as the inlet boundary condition for the second subclavian vessel ("subclavian II") from the fifty–vessel network given above (mechan-

ical parameters for the vessel given in [4]). As with the fifty–five vessel network above, we set $p_0 = 75$ mmHg for these simulations. The vessel parameters are $\beta = 466000$ g cm^{-2} s^{-2} and $A_0 = 0.51$ cm^2. The numerical parameters are $\Delta t = 2 \times 10^{-5}$ s, $h = 0.25$ cm, $k = 1$, and the local Lax–Friedrichs flux is used. Further, since we expect the solution to develop sharp transitions and possibly shocks, we supplement the discontinuous Galerkin method with the minmod slope limiter [20].

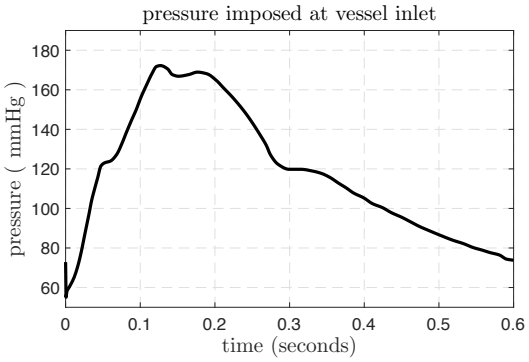

Figure 6.28 : Pressure imposed at the vessel inlet, taken from reference [5].

In Figure 6.29, we display the pressure waveforms measured at various distances from the vessel inlet for both the inviscid (A, Q) and inviscid (A, U) systems. The results for both systems are similar. Note the sharp transition from the minimum to maximum pressure at the beginning of each waveform; this transition increases in sharpness farther from the vessel inlet. This feature indicates shock formation and also appears in clinical data [5]. Similar results are seen in the waveforms for $\alpha = 1.1$ and $\alpha = 4/3$.

In Figure 6.30, we explore the formation of the shock. The panels on the left correspond to the (A, Q) system and the panels on the right correspond to the (A, U) system. Each panel displays six snapshots in time of pressure as a function of space,

where the horizontal axis displays distance from the vessel inlet. First, we make the general comment that in all models, a sharp transition forms within the length of a typical arm; it is interesting that the nonlinearity in the model is able to capture the shock within this distance. This modeling supports speculation that "pistol–shot" sounds in the body may indeed result from shock formation [5, 89, 86].

Next, we see that for the (A, Q) system, the pressure to the left of the shock on the curve VI is greater than 120 mmHg for $\alpha = 1$, is equal to 120 mmHg for $\alpha = 4/3$ and is smaller than 120 mmHg for $\alpha = 1.1$. This behavior can be explained by an increase in the viscosity term as α varies from from 1 to 4/3 to 1.1. The pressure to the left of the shock on the curve VI for the (A, U) system varies in the same way. We also comment on the formation of the shock as seen in how curves I through V vary in shape. Observe that the shock development for the (A, Q) system is similar for the cases $\alpha = 1$ and $\alpha = 1.1$ but is different for the case $\alpha = 4/3$. For this value, the shock develops the fastest and appears fully developed in snapshot IV. For the (A, U) system, the shock formation is very similar for all values of α.

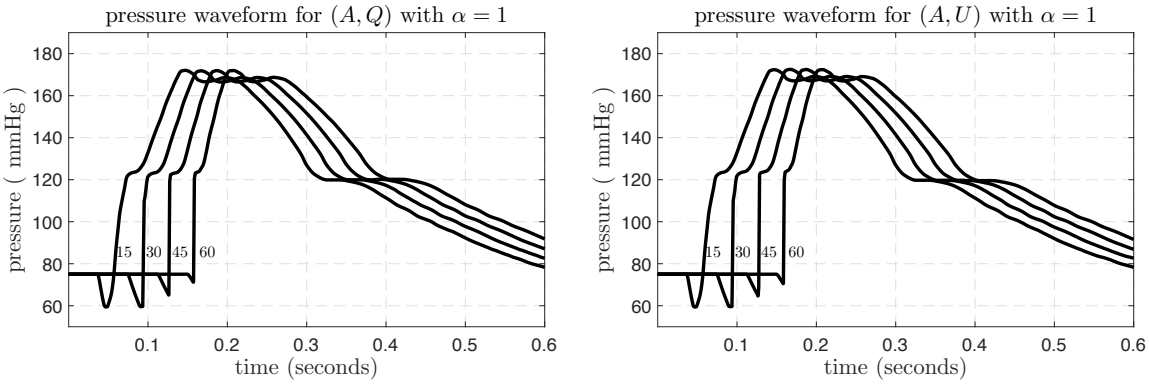

Figure 6.29 : Pressure waveforms measured at various distances from the vessel inlet. The distance from the inlet is given in centimeters to the right of each waveform.

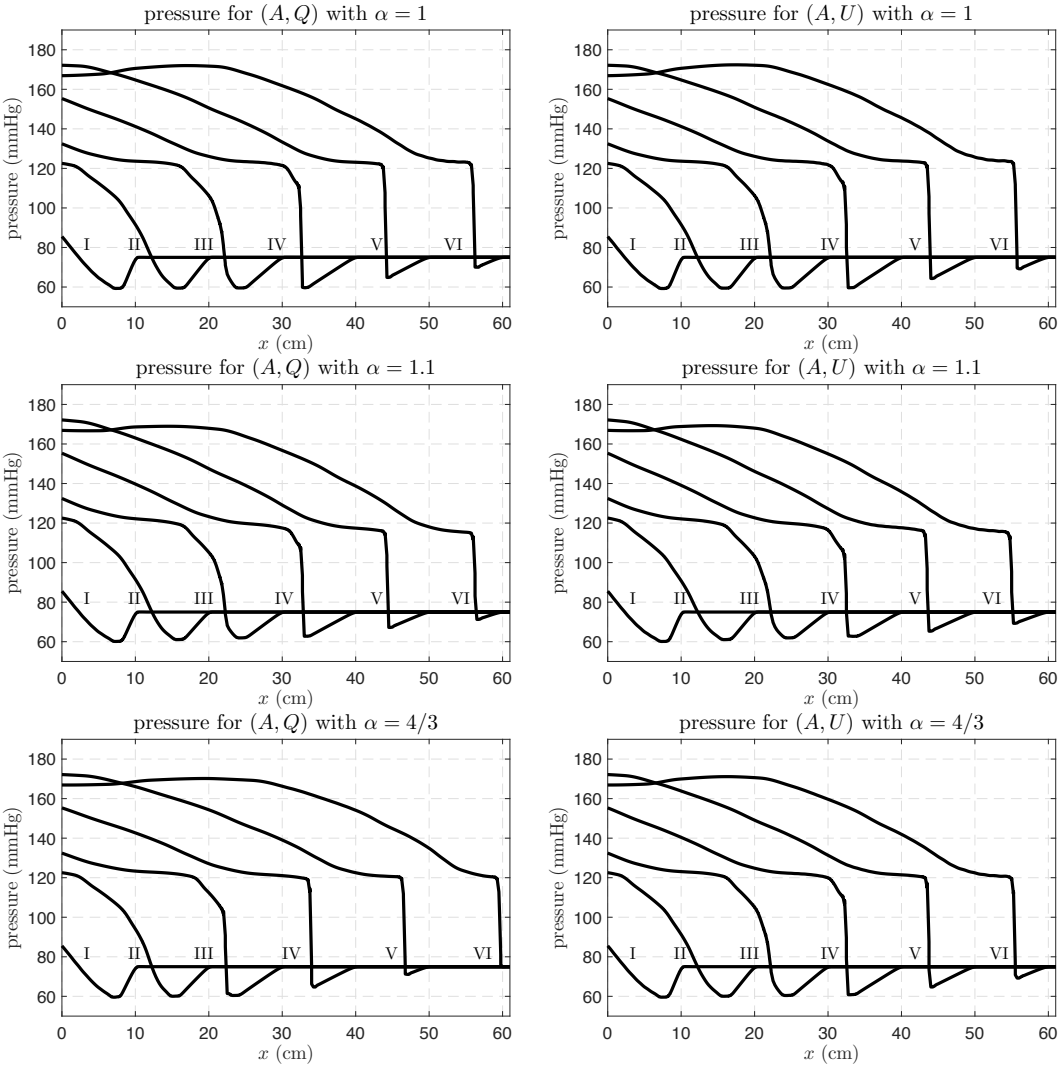

Figure 6.30 : The figures on the left are snapshots of pressure at uniformly spaced times: I(0.025 s), II(0.05 s), III(0.075 s), IV(0.1 s), V(0.125 s), and VI(0.15 s). Results for the (A, Q) system are on the left and for the (A, U) system are on the right. Each row corresponds to a different value of α.

6.2.7 Conclusions

The results in this section provided a systematic comparison of two classes of reduced blood flow models, the (A, Q) and (A, U) systems. Models within each class were further characterized by the Coriolis coefficient α, which takes different values for different axial velocity profiles. Discontinuous Galerkin in space with Runge–Kutta methods in time were used to discretize the system of conservation laws. Our results first showed that the approximations of pressure, momentum and velocity did not depend on the particular choice of numerical flux.

In addition to validating our code with the results from [4] and verifying convergence rates, we considered two separate experiments with different boundary conditions: a fifty–five vessel network with flow imposed at the inlet of the ascending aorta and a single vessel with pressure from a patient with aortic regurgitation imposed at the inlet. In the former experiment, the solutions were smooth, and in the latter, solutions exhibited a shock. In both cases we considered the effect of varying α on the solutions of the (A, Q) and (A, U) systems, with inviscid flow corresponding to $\alpha = 1$ and viscous flow corresponding to a Poiseuille profile ($\alpha = 4/3$) or a flatter profile ($\alpha = 1.1$).

For the fifty–five vessel network, we compared simple reflection terminal boundary conditions with three element windkessel boundary conditions. As expected, the results with the windkessel boundary conditions did not exhibit high frequency oscillations like we saw with the reflection boundary conditions. Thus, we employed the windkessel boundary conditions when comparing the (A, Q) and (A, U) systems with different values of α.

Our simulations revealed the selection of the Coriolis coefficient α does impact the solution; this effect is demonstrated in both the fifty–five vessel network and in the

single vessel with shock formation. The choice $\alpha = 4/3$ provides a smaller viscosity term than $\alpha = 1.1$ and produces solutions with higher pressure gradients. In the case $\alpha = 1.1$, the (A, U) system derived from a flat profile assumption compares reasonably well to the (A, Q) system in all cases. In light of these observations, the (A, U) system with $\alpha = 1.1$ is a reasonable choice for modeling when the solutions are smooth, but generally we favor the use of the (A, Q) system with $\alpha = 1.1$ since it describes the physically conserved variables.

In the shock formation experiments, the inviscid (A, Q) and (A, U) systems yielded the same result. In contrast, the models with $\alpha > 1$ developed shocks in differing locations, although these differences were quite small for the (A, U) system since α only appears in the viscous term. Knowledge of these discrepancies among models is important for physiological applications involving shock formation, like aortic regurgitation.

Chapter 7

A model for the Fontan circulation

7.1 Introduction

The Fontan circulation is a standard palliative solution for patients with single ventricle hearts and other cardiac abnormalities [90]. For patients with hypoplastic left heart syndrome (HLHS), this circulation is typically the third and final physiology they receive in a sequence of surgeries which transition their cardiovascular system to function with a single right ventricle pump. It is characterized by the systemic organs and lungs in series, with passive blood flow into the lungs via a surgical modification. A schematic of the Fontan physiology can be found in Figure 7.1.

There are several types of surgical modifications which allow passive blood flow into the lungs. The *lateral tunnel* Fontan contains a connection built out of the atrium, where flow from the inferior vena cava is diverted into the pulmonary artery. In the *extracardiac* Fontan, the inferior vena cava is disconnected from the atrium and connected directly to the pulmonary arteries with a synthetic tube. This connection between the vena cavas and pulmonary arteries is sometimes called the *total cavopulmonary connection*, or simply the *Fontan connection*. In our modeling, we focus on the extracardiac Fontan physiology since our zero-dimensional heart models do not have enough anatomical detail to build a lateral tunnel Fontan.

As Fontan patients age, they can experience challenging complications like protein–losing enteropathy as well as liver problems [91, 92, 93]. These issues may arise in part

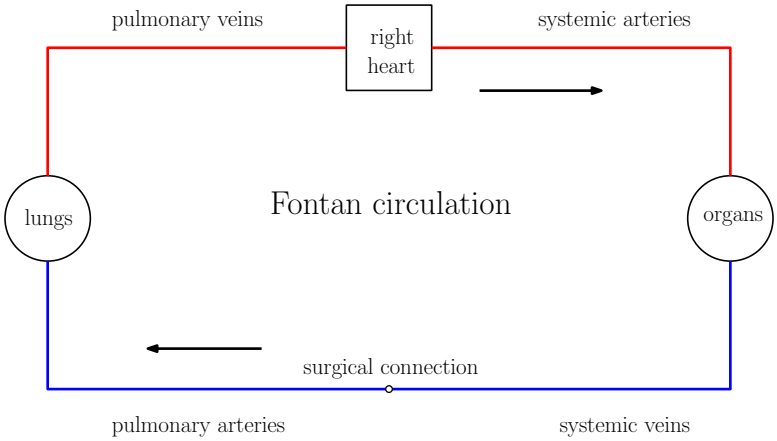

Figure 7.1 : A schematic of the Fontan physiology.

from an increase in systemic venous and portal venous pressures caused by the Fontan connection (see e.g. [94, 95]), but there is still uncertainty in both the mechanisms through which these complications develop and the best path for treatment.

Surgeons have had some success in managing complications through novel modifications of the original Fontan circulation. The purpose of this chapter is to employ multiscale one–dimensional/zero–dimensional hemodynamic models to study two modifications of the standard Fontan physiology which are used to treat issues like protein–losing enteropathy. We investigate (1) the fenestrated Fontan and (2) the Fontan with hepatic vein exclusion [96, 97, 98, 99].

The fenestrated Fontan includes a path near the Fontan connnection which diverts a small portion of blood directly to the heart. In the lateral tunnel Fontan, this path may be a small punched hole in the material which divides the atrium. In the extracardiac Fontan, a path may be established by creating by a small hole in both the continuation of the inferior vena cava and the atrium, and then surgically connecting them together. Some relevant references for each version of the Fontan along with

a comparison of these surgeries is provided in the work of Kumar et al. [100]. We remark that fenestrations may be given at the time of Fontan conversion, usually with the expectation that the small hole or conduit will close over time [101]. Our modeling is motivated more by understanding the effect of *late* fenestrations created after the Fontan surgery, often in response to complications.

The circulation established by the Fontan with hepatic vein exclusion diverts blood from the liver, through the hepatic veins, directly into the heart; this is achieved by connecting the hepatic veins directly to the atrium. The idea for this modification is the expectation that atrial pressure will be lower than the pressure in the pulmonary arteries and vena cavas. In turn, patients with elevated pressures around their intestines and liver may experience a decongestion of the splanchnic circulation after hepatic exclusion, along with the mitigation of intestinal and hepatic problems.

7.2 Previous computational modeling for HLHS

Before presenting our mathematical models for the Fontan physiology, we review approaches for several HLHS physiologies which appear in the literature.

Electrical circuit and computational fluid dynamic models have proved to be powerful tools for studying the inherently complex hemodynamics of each HLHS physiology: the stage I Norwood, stage II Glenn, and stage III Fontan procedures. We provide a brief review of some of the main highlights of these modeling techniques below.

Systems of algebraic and ordinary differential equations, so–called zero–dimensional or "lumped–parameter" models, provide simple mathematical descriptions for various physiologies. Early work by Barnea et al. employed a purely algebraic model of fluid flow to study oxygen transport in a single ventricle parallel circulation [35].

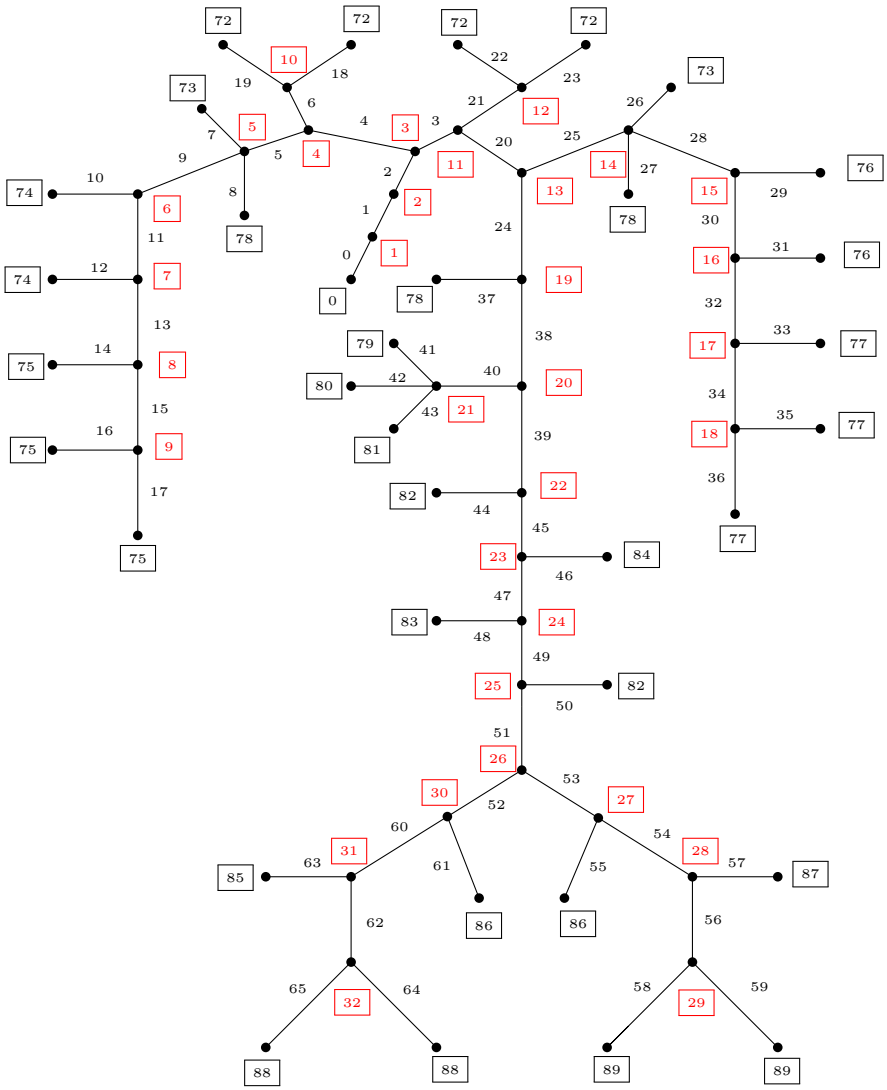

Figure 7.2 : Topology of the systemic arteries for the standard Fontan physiology, adapted from [3]. The non–squared numbers label the vessels and the squared numbers label the nodes. Red squared numbers correspond the interior nodes, or vessel junctions, and black squared numbers correspond to an organ bed or the heart.

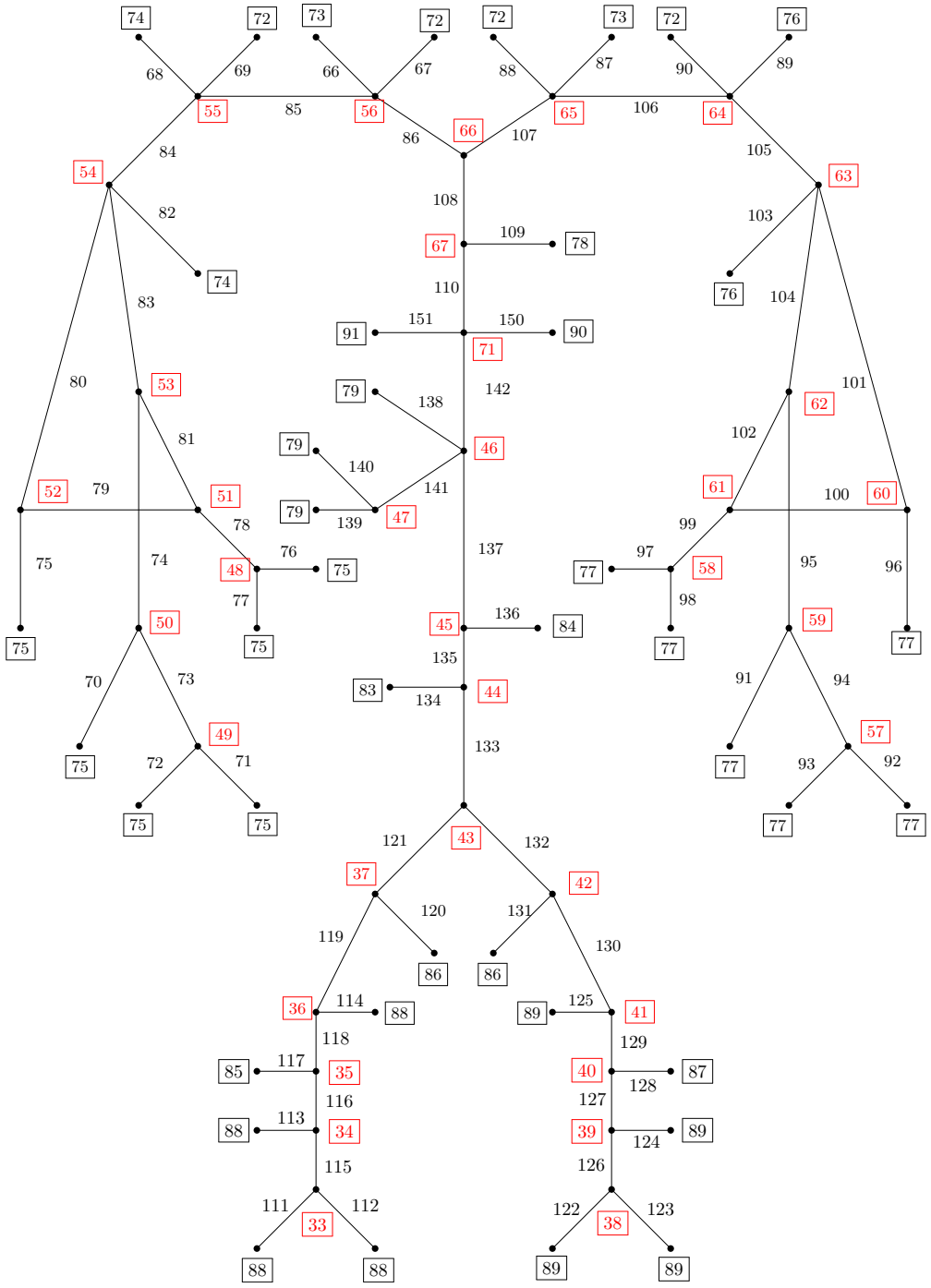

Figure 7.3 : Topology of the systemic veins and pulmonary arteries for the standard Fontan physiology, adapted from [3]. The non–squared numbers label the vessels and the squared numbers label the nodes. Red squared numbers correspond the interior nodes, or vessel junctions, and black squared numbers correspond to an organ bed or the heart.

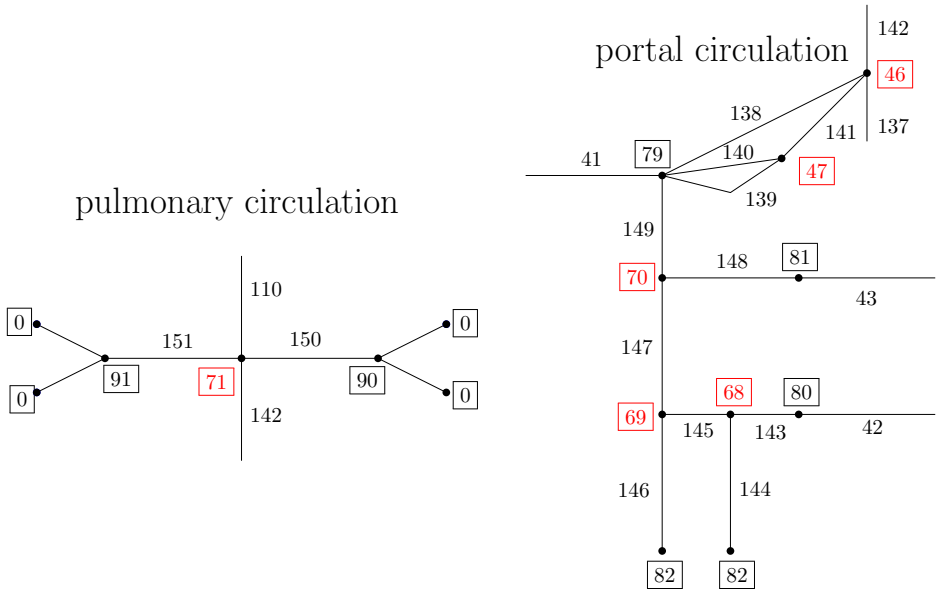

Figure 7.4 : Topology of the pulmonary and portal circulations for the standard Fontan physiology, adapted from [3]. The non–squared numbers label the vessels and the squared numbers label the nodes. Red squared numbers correspond the interior nodes, or vessel junctions, and black squared numbers correspond to an organ bed or the heart.

Migliavacca et al. developed a more complex pulsatile, closed–loop model of the Norwood circulation to explore the sensitivity of pulmonary and systemic flow to changes in different hemodynamic parameters, including heart rate and the geometry of the shunt which establishes the parallel circulation [102]. The works of Vallecilla et al. used zero–dimensional models of variations on the Glenn physiology to characterize oxygen transport and other hemodynamic variables; in particular, they modeled the effect of exercise and a high altitude environment on blood flow [103, 104]. Other researchers studied complications of HLHS by modeling pre– and post– surgerical conditions [105]. Lastly, several groups have considered mathematical descriptions of the Fontan physiology. The set of papers by Watrous et al. and Chin et al. present a general software framework, complete with a graphical user interface, for computational hemodynamics using zero–dimensional models, and consider examples of normal and Fontan circulations [106, 107]. Kung et al. created a Fontan model to investigate the effect of exercise, and carefully refined their approach with clinical data [46]. Finally, recent work by Di Molfetta et al. describes models for the Fontan circulation and other HLHS physiologies used to study the impact of ventricular assist devices on blood flow [108].

Recent computational work for HLHS physiologies has also relied on geometric multiscale models which use zero–dimensional equations in concert with the Navier–Stokes equations or reduced (one–dimensional) versions thereof, as described in Section 2. This approach enables the characterization of complex blood flow patterns in a region of interest while still accounting for peripheral hemodynamics using lumped–parameter models. For well–posedness and numerical considerations of these coupled models, see e.g. [109, 15, 19, 10].

Many computational studies for HLHS physiologies utilize geometric multiscale

models of the total cavopulmonary connection (TCPC), a surgically created junction in the Fontan circulation. This connection links the vena cavas directly to the pulmonary arteries, allowing passive flow of unoxygenated blood back to the lungs. In this light, it is clinically useful to characterize complex flow patterns in the TCPC and the corresponding impact on venous return.

Geometric multiscale models of the TCPC typically use finite element approximations of the Navier–Stokes equations for the connection itself and surrounding vessels, and zero–dimensional models for outflow boundary conditions. Early papers by Dubini et al., de Leval et al., and Miglavacca et al. constructed such models to investigate the effect of TCPC geometry on flow to each lung and fluid energy loss [110, 111, 112]. Later work from Hsia et al. and de Zélicourt et al. exhibited similar computational experiments, but with models generated from patient data [113, 114]. Recent research from Marsden and her collaborators considered, among many topics, the effect of exercise and novel surgical techniques on flow in the TCPC [14, 115].

The Norwood physiology has also been studied using geometric multiscale models; some representative research includes the work of Qian et al., Hsia et al., and Moghadam et al. [39, 113, 43].

7.3 Model construction

Our one–dimensional/zero–dimensional Fontan models are adapted from the normal circulation model presented in Mynard's thesis [3]. Diagrams for these vessel networks with node and vessel labeling can be found in Figures 7.2, 7.3, and 7.4. These networks are connected together through the organ beds and heart to create a closed–loop model. The vessel network topology is adjusted to align with the Fontan physiology, and we incorporate our heart model which includes valves (Section 5.6), and the novel

organ bed model developed by Acosta et al. (Section 5.5) [70].

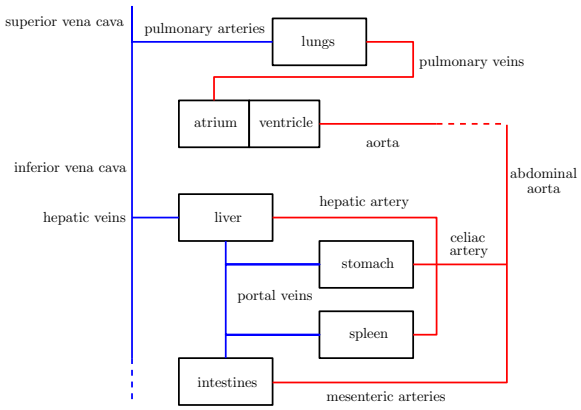

Figure 7.5 : A schematic of the standard Fontan connection.

The fenestration conduit is modeled as two small vessels on either side of an organ bed. This organ bed model is the same as that described in Section 5.5, but with constant resistance and compliance set to zero. We consider fenestration diameters of 6mm, 8mm, and 10mm. Schematics of the models for modified Fontan circulations, with the splanchnic circulation shown in more detail, are given in Figure 7.6. Parameters for the models can be found in Appendices A.3, A.4, and A.5. The parameter β for each vessel is set according to the scaling law with respect to A_0, as discussed in Section 6.1.1.

For this simulations in this chapter, NMC is used to approximate solutions to the (A, U)–system given in (2.20), with parameters $\alpha = 1.1$ and $\nu = 3.019 \times 10^{-2}$ cm^2/s. We take $h = 5 \times 10^{-2}$ cm, and $\Delta t = 8.57142 \times 10^{-5}$ s. In all simulations we add an additional 200 mL of blood into the model, over the first four cardiac cycles with period $T_{\text{heart}} = 6/7$ s, via the vessel junction corresponding to node 56. This is done

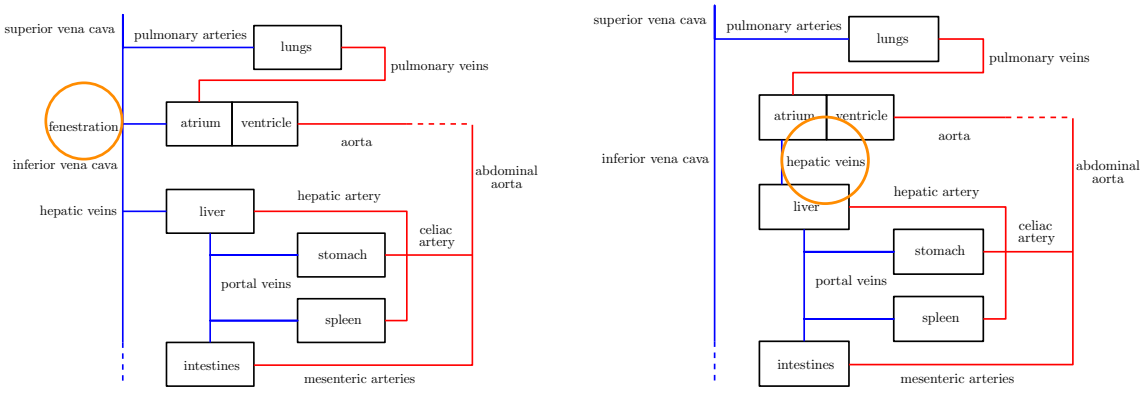

Figure 7.6 : Schematics of the Fontan with fenestration on the left and with the hepatic vein exclusion on the right. The circle on each figure highlights the modification.

by setting Q_{add} in equation (5.6) to:

$$Q_{\text{add}}(t) = \begin{cases} 50/T_{\text{heart}} & \text{if } t \leq 4T_{\text{heart}}, \\ 0 & \text{otherwise.} \end{cases}$$

The addition of blood volume allows for the the calibration of mean pressures within the models.

7.4 Scaling the mesenteric resistance

There is a lack of clinical insight regarding the development of intestinal and hepatic problems in Fontan patients, like protein losing enteropathy and liver cirrohsis. Several researchers hypothesize these issues arise in part due to vasoconstriction induced by low cardiac output. This compensatory process results in decreased flow to the mesenteric ciculation [6, 116]. Related work has uncovered unexpected features in the mesenteric waveform and increased mesenteric vascular resistance in patients with the Fontan circulation [117, 118]. We explore this hypothesis relating mesenteric vascular resistance to complications like protein losing enteropathy by allowing

the resistance in mesenteric circulation of our model to vary. In particular, we compare the hemodynamics in each of the three Fontan configurations as an index γ, to be called the *mensenteric resistance index*, scales the arterial vessel stiffness and reference resistance in the intestinal organ bed [70]. The organ bed parameters for the intestine are scaled as follows:

$$\Gamma_{\text{art}} \to \Gamma_{\text{art}}/\gamma,$$

$$R_{\text{ref,art}} \to \gamma R_{\text{ref,art}}.$$

7.5 Results for the standard Fontan model

In this section, we present some experimental results obtained from our computational models of the standard Fontan, fenestrated Fontan, and Fontan with hepatic vein exclusion. In all of our simulations, we run the model for fifteen cardiac cycles, at which point we observe a periodic steady state. In the following figures, mean values of pressure and flow waveforms are computed by averaging over three cardiac cycles. Waveforms in the ascending aorta for the full simulation of the standard Fontan are depicted in the left panel of Figure 7.7. In the right panel, we see a pie chart of the arterial blood flow distribution to different vascular beds, computed as:

$$\text{flow distribution to vascular bed} = 100 \times \frac{\text{mean flow into vascular bed}}{\text{mean aortic flow}}.$$

The left panel of Figure 7.8 demonstrates the effect of increasing mesenteric resistance index (from $\gamma = 1$ to $\gamma = 4$) on the flow waveform in the superior mesenteric artery (SMA), the artery which provides blood to the intestine, in the standard Fontan circulation. The mean flow decreases as γ increases, and in particular there is a substantial reduction of flow during diastole. At the highest resistance index there is

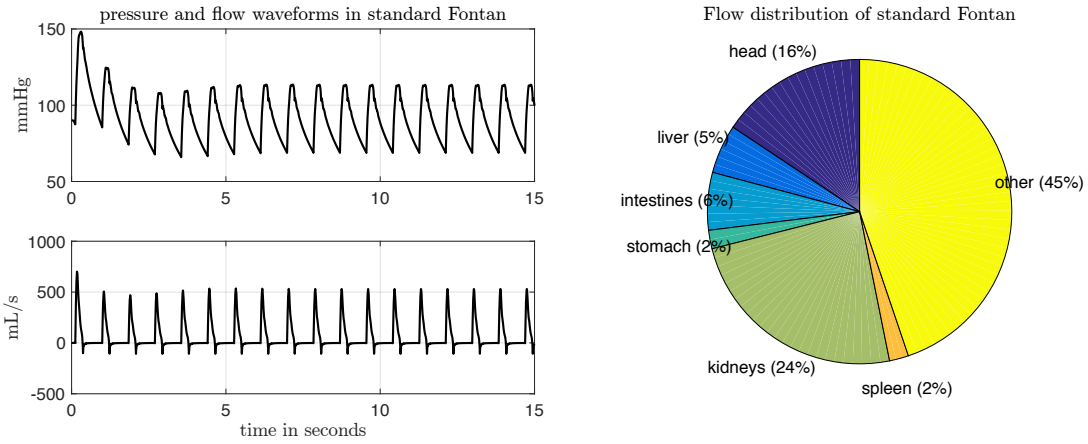

Figure 7.7 : The figure on the left displays pressure and flow in the ascending aorta of the standard Fontan circulation reaching a periodic steady state. The pie chart on the right displays the arterial flow distribution to different vascular beds.

even some backward, or regurgitant, flow. Small values of diastolic flow in Fontan patients with protein losing enteropathy has been clinically observed, see e.g. the right panel of Figure 7.8 [6, 119].

7.6 Results for the fenestration and hepatic vein exclusion

Figure 7.9 presents the changes in the arterial flow distribution as the mesenteric resistance index increases. We highlight in particular the flow to the intestines, which, as expected, decreases as γ increases.

In Figure 7.10 we examine the effect of a fenestration or hepatic vein exclusion on the SMA flow waveform. The hepatic vein exclusion is the most effective modification for increasing flow to the intestine, followed by the 10mm fenestration. Both modifications to the standard Fontan are less effective for high values of mesenteric resistance.

Figure 7.12 depicts hemodynamics variables for each Fontan configuration as the

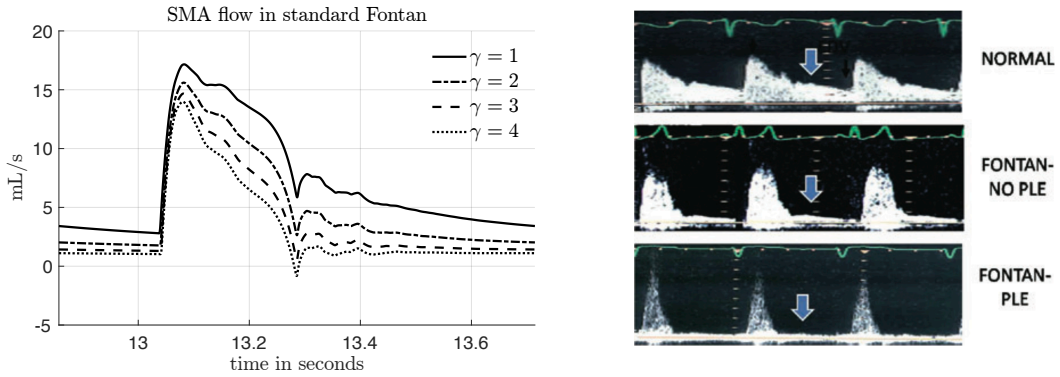

Figure 7.8 : On the left are flow waveforms in the superior mesenteric artery of the standard Fontan circulation, with increasing values of the mesenteric resistance index γ. On the right are experimental measurements of SMA flow adapted from [6] with permission (© 2007, the Author Journal compilation © 2007 *Congenital Heart Disease*, Wiley Publishing, Inc.).

mesenteric resistance index varies. We explore clinical variables computed from pressure and flow waveforms in addition to the cardiac output and ejection fraction, which are extracted from the ventricular pressure–volume loop depicted in Figure 7.11. The *end systolic volume* (ESV), *end diastolic volume* (EDV), and the *stroke volume* (SV) are defined as follows:

$$ESV = \text{minimum ventricular volume},$$

$$EDV = \text{maximum ventricular volume},$$

$$SV = EDV - ESV.$$

Then the *cardiac output* is defined

$$\text{cardiac output} = \text{heart rate} \times SV,$$

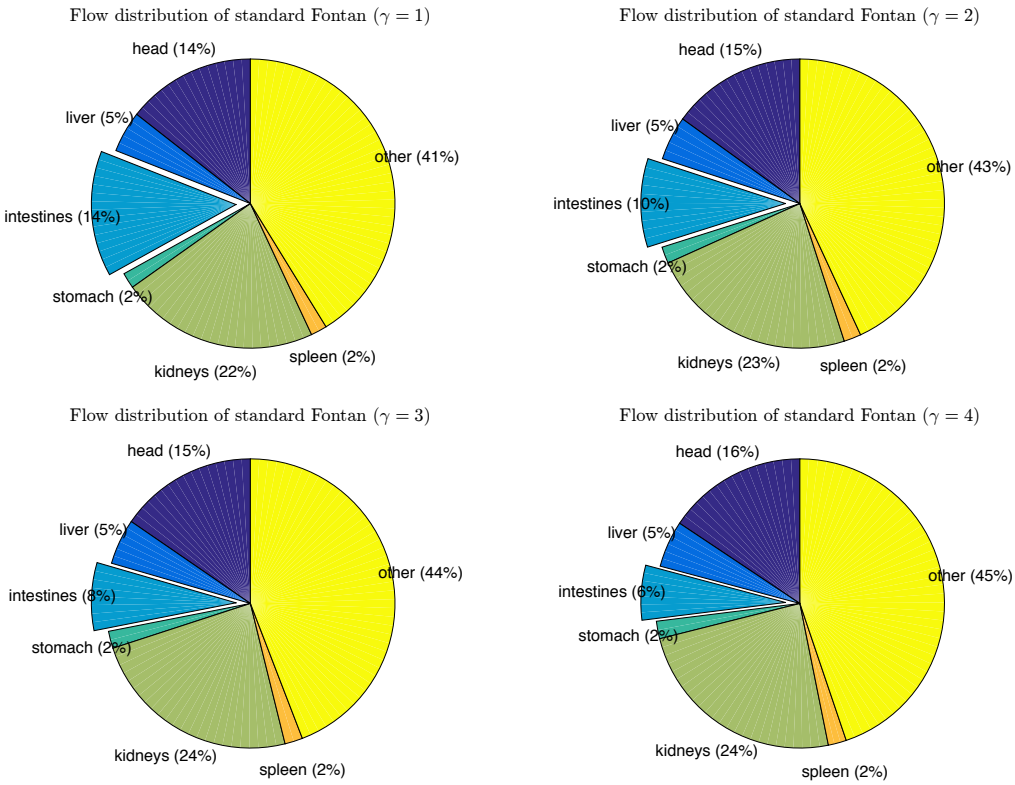

Figure 7.9 : Flow distributions in the standard Fontan for increasing mesenteric vascular resistance index γ.

and the *ejection fraction* is

$$\text{ejection fraction} = \frac{EDV - ESV}{EDV}.$$

Ejection fraction and cardiac output are measures of cardiac performance; low values of these indices indicate diminished heart strength, abnormalities in the peripheral vasculature, and/or other physiological problems.

As expected, in the bottom two panels of Figure 7.12, cardiac output and ejection fraction decrease when γ increases. In the top left panel, we notice the fenestration has almost no effect on the pressure in the portal venous circulation, whereas the hepatic exclusion drastically decreases the portal venous pressure. The top right

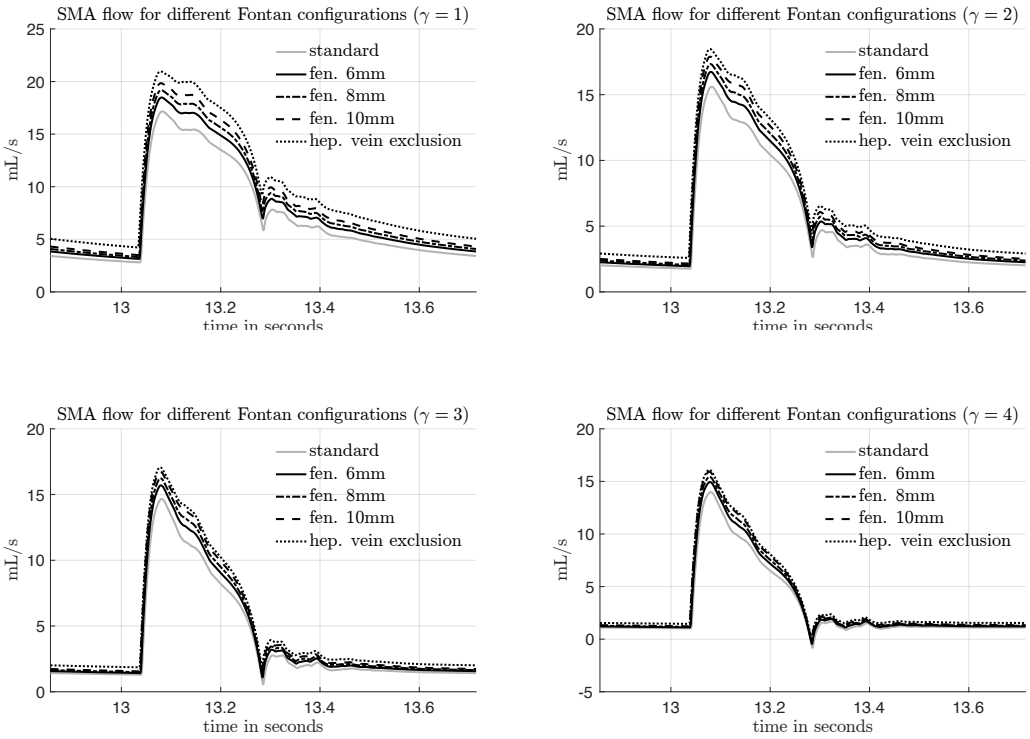

Figure 7.10 : Flow waveforms in superior mesenteric artery.

panel indicates the fenestration leads to a drop in the pulmonary artery pressure, while the hepatic vein exclusion leads to a small increase. These changes in pulmonary artery pressure (and surrounding pressures in the "Fontan pathway") are consistent with results from some surgical reports where measurements are taken pre and post operation [96, 99]. In summary, fenestration relieves pulmonary arterial hypertension while the hepatic exclusion mitigates portal venous hypertension.

In the middle left panel of Figure 7.12, we examine a clinical index used to assess flow distributions in the splanchnic circulation: the ratio of mean SMA flow to mean celiac artery flow. As mesenteric resistance increases, flow is diverted from the

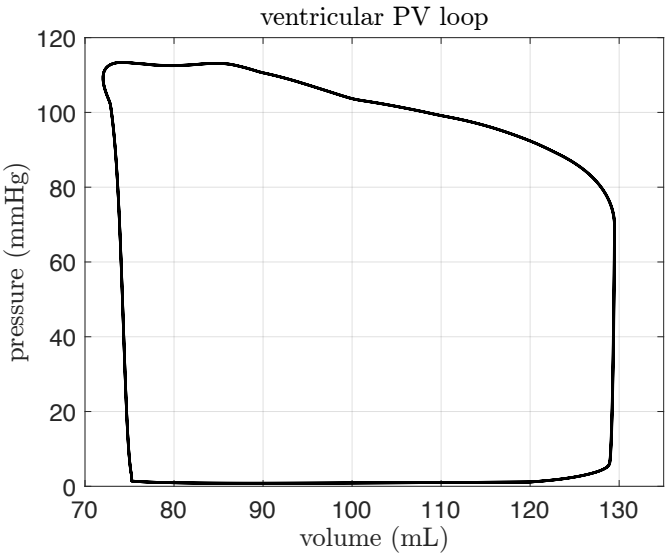

Figure 7.11 : Pressure–volume loop for the ventricle in the standard Fontan circulation with $\gamma = 1$.

intestine to the other parts of the splanchnic circulation via the celiac artery, thereby decreasing this ratio. This index was found to be smaller in Fontan patients with abnormal enteric protein loss (AEPL) as compared to patients without AEPL [118].

Finally, in the middle right panel of Figure 7.12, one notices an increase in the mean SMA flow for both the fenestration and hepatic vein exclusion, with the latter modification providing the largest increase.

Figures 7.13 and 7.14 provide more detail regarding the hemodynamics in the splanchnic and pulmonary circulations. Each bar corresponds to the relative percent change in mean flow or mean pressure in a given vessel, as compared to the standard Fontan model. Figure 7.13 depicts the impact of different fenestration sizes, with a larger fenestration leading to greater relative changes. Further, the fenestrated Fontan has lower pulmonary artery pressure but almost no change in the portal venous pressure. The overall hemodynamic changes from the standard Fontan to the

fenestrated Fontan are relatively mild, with no relative differences in flow or pressure exceeding about 30%.

In contrast, as depicted in Figure 7.14, the hepatic exclusion leads to larger relative changes in the splanchnic circulation, most strikingly in the flow and pressure waveforms of the common hepatic vein and hepatic portal vein. This drop in pressure highlights the effectiveness of this modification in combating venous and portal venous congestion, thought to be factors potentially leading to complications in the Fontan physiology [120, 121, 122].

The decrease in portal venous pressure after the hepatic exclusion leads to a substantial increase in flow through the superior mesenteric artery to the intestines, and through the celiac artery to the liver and the rest of the splanchnic circulation. Physicians have suggested that protein losing enteropathy and other splanchnic problems are correlated with low flow to this part of the circulation, so enhanced profusion may mitigate complications from the Fontan physiology [6]. We remark that the fenestration also increases profusion in this area, as seen in Figure 7.13, despite a small increase in the portal venous pressure. In sum, the success of both fenestrations and hepatic exclusions in resolving protein losing enteropathy may be due to their similar effect on blood flow to the intestines and liver [99, 97].

Lastly, we consider the *arterial elastance*, Ea, and *end–systolic elastance*, Ees, defined as follows [123, 116]:

$$Ea = \frac{\text{maximum ventricular pressure}}{SV}, \quad \text{and} \quad Ees = \frac{\text{mean arterial pressure}}{ESV}.$$

The values defined in this way may be easily computed with patient data, i.e. PV loops and arterial blood pressure measurements, and we remark that this aproach has been validated with an animal model [123]. The arterial elastance provides a rough measurement of the "afterload" experienced by the ventricle, i.e. the effective resis-

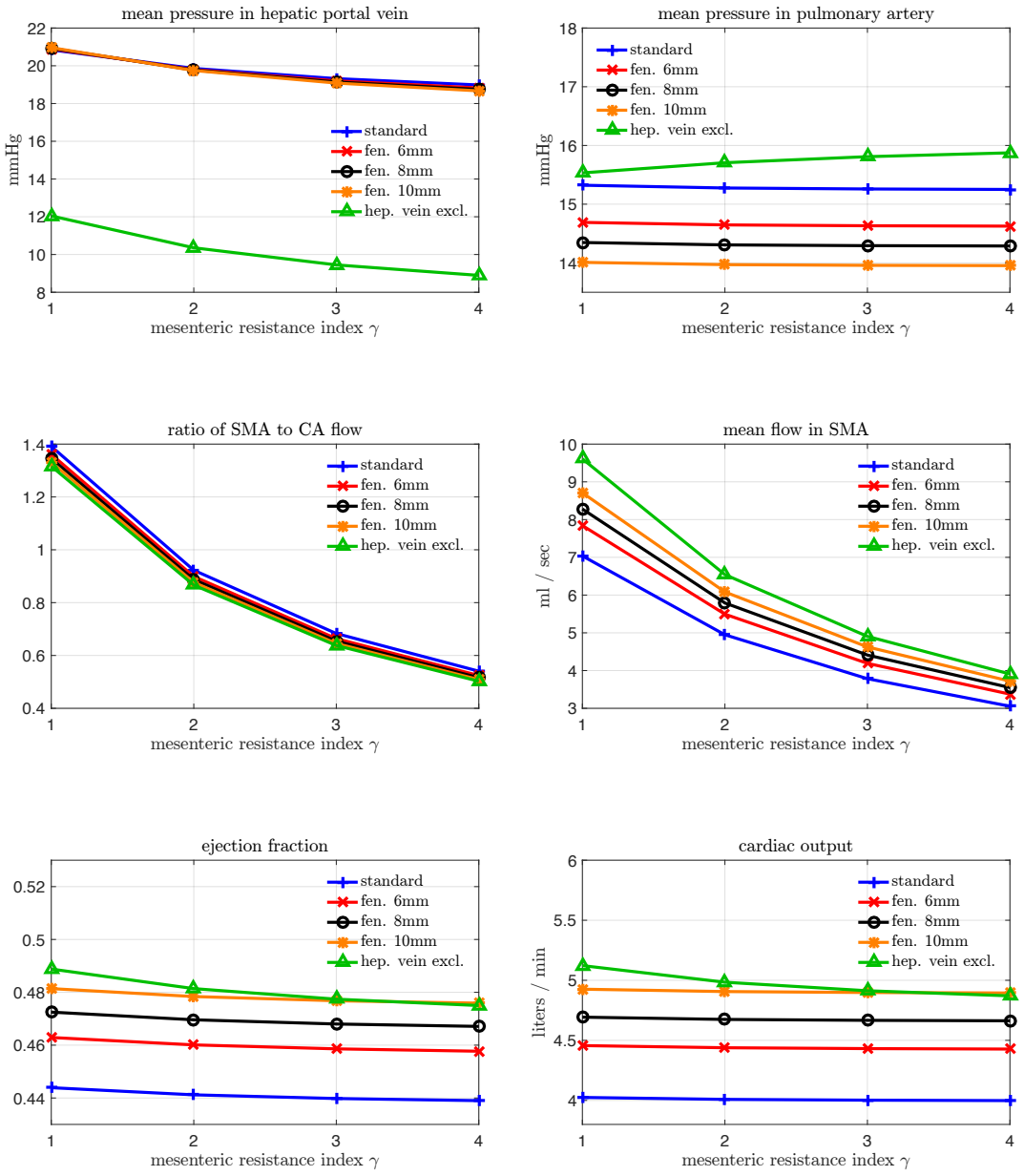

Figure 7.12 : The figures above display several model outputs for the standard Fontan, fenestrated Fontan, and Fontan with hepatic vein exclusion. Each output is plotted as a function of increasing intestinal resistance.

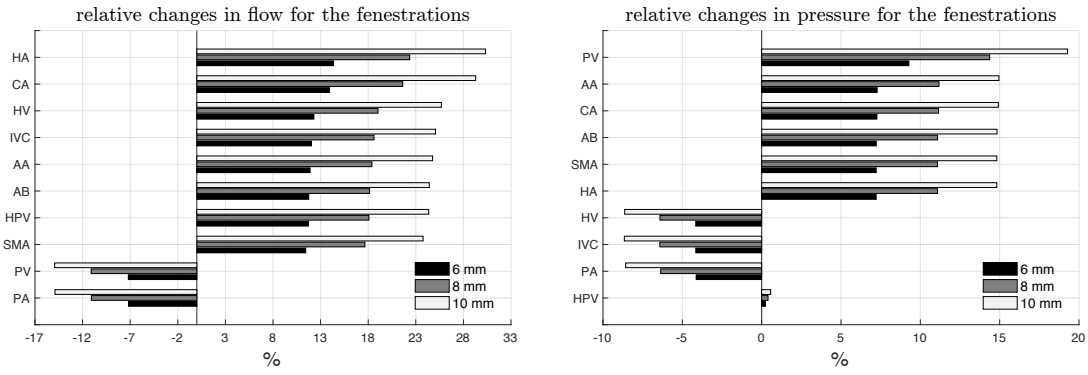

Figure 7.13 : The figures above display percent change of mean flow and mean pressure values for the fenstrated Fontan with $\gamma = 1$. The vessels are the ascending aorta (AA), abdominal aorta (AB), celiac artery (CA), hepatic artery (HA), superior mesenteric artery (SMA), common hepatic vein (HV), inferior vena cava (IVC), hepatic portal vein (HPV), pulmonary artery (PA), and pulmonary vein (PV).

tance of the vessel trees and organ beds combined. This can be seen by assuming the product of effective resistance and compliance remains relatively constant and noting that elastance is the reciprocal of compliance. By construction of the physiology, hearts within a Fontan circuit experience an elevated afterload since the lungs are placed in series with the organ beds.

The end–systolic elastance is an index for contractility, or strength of the ventricle. High values of Ees indicate a firm and muscular contraction, while low values suggest the ventricle is too compliant at the end of systole. A clinically relevant ratio defined to be Ea/Ees is called the *contractility–afterload mismatch*. High values correspond to a weak ventricle experiencing a high afterload while lower values suggest a more "efficient" hemodynamic configuration. We are particularly interested in this ratio since physicians observed larger contractility–afterload mismatch in Fontan patients

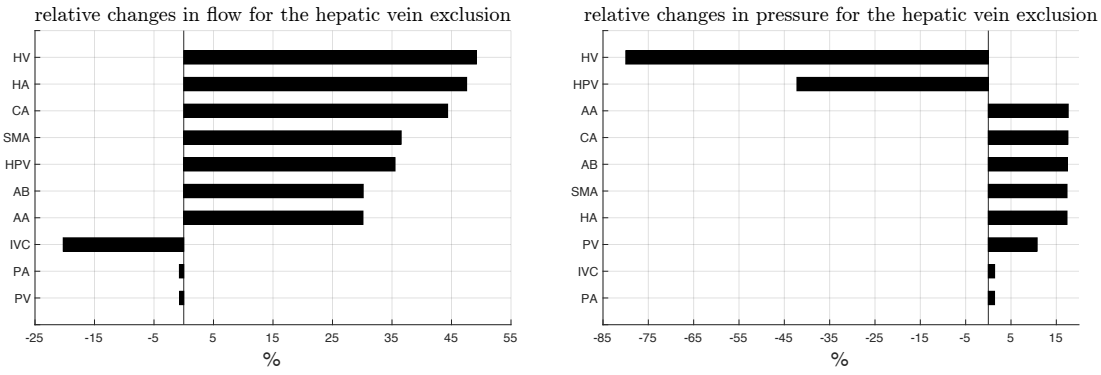

Figure 7.14 : The figures above display percent change of mean flow and mean pressure values for the Fontan with hepatic exclusion with $\gamma = 1$. The vessels are the ascending aorta (AA), abdominal aorta (AB), celiac artery (CA), hepatic artery (HA), superior mesenteric artery (SMA), common hepatic vein (HV), inferior vena cava (IVC), hepatic portal vein (HPV), pulmonary artery (PA), and pulmonary vein (PV).

diagnosed with protein losing enteropathy, compared to patients without this problem [116].

In Figures 7.15 and 7.16, we explore changes in Ea, Ees, and the contractility–afterload mismatch among the different Fontan configurations, as the mesenteric resistance index varies. The left panel of Figure 7.15 depicts an increase in Ea as γ increases; this observation aligns well with clinical data showing an increase in Ea in Fontan patients with protein losing enteropathy [116]. Further, we observe a decrease in Ea and an increase in Ees for the fenestration and hepatic exclusion, when compared to the values for the standard Fontan. This difference indicates both surgical modifications to the standard Fontan decrease afterload and increase contractility, as measured by these clinical indices. Figure 7.16 indicates the hepatic exclusion leads to the most efficient hemodynamic configuration considered, followed by the 10mm fen-

estration. In sum, both the fenestration and hepatic exclusion lead to more optimal cardiovascular physiologies, as measured by the contractility–afterload mismatch.

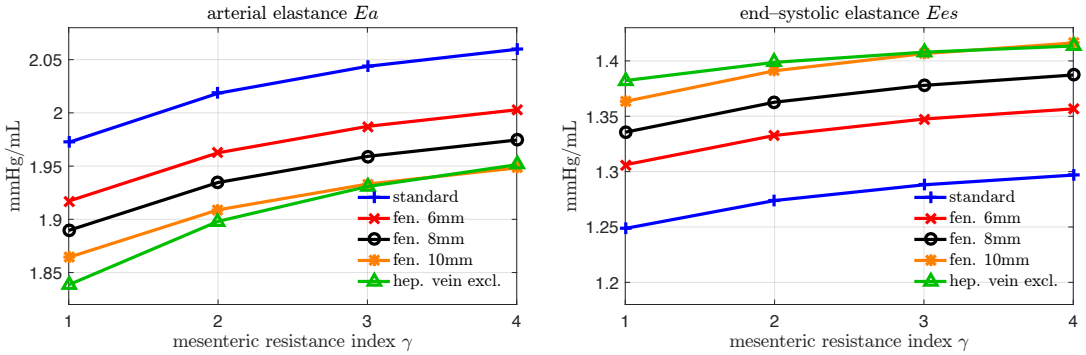

Figure 7.15 : Plots of the arterial elastance and end–systolic elastance for different configurations and values of the mesenteric resistance index γ.

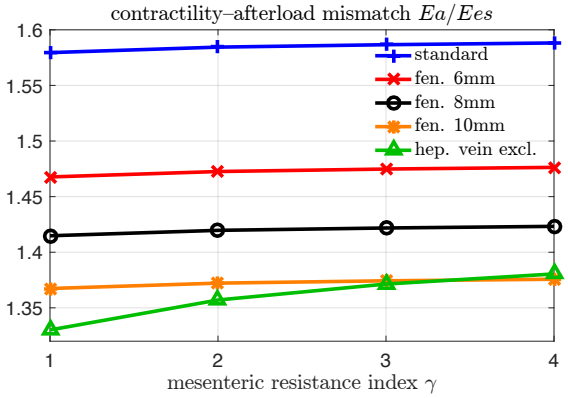

Figure 7.16 : Plots of the contractility–afterload mismatch for different configurations and values of the mesenteric resistance index γ.

7.7 Conclusions

In this chapter, we described models for three variations of the Fontan physiology: (1) the standard extracardiac Fontan, (2) the fenestrated Fontan, and (3) the Fontan with hepatic vein exclusion. Three diameters for the fenestration conduit were considered. The fenestration or hepatic exclusion may result from surgical modification of the standard Fontan physiology in response to complications in the splanchnic circulation.

Our interests were in quantifying cardiovascular changes in the fenestrated Fontan and Fontan with hepatic exclusion, with respect to the hemodynamics of the standard Fontan physiology. We considered clinical variables in addition to mean flow and mean pressure changes in vessels around the intestines and liver.

The hepatic vein exclusion lead to the largest overall changes with respect to standard Fontan hemodynamics, with a notable drop in the mean pressure of the portal vessels; this pressure drop increased flow to the intestines. The fenestration also increased mesenteric flow, but did not decrease the pressure in the portal circulation; instead, our results show a drop in the pulmonary artery pressure. Both the fenestration and hepatic vein exclusion lead to favorable changes in the contractility–afterload mismatch.

Chapter 8

Conclusions

In this thesis, we studied theoretical and computational aspects of reduced models for blood flow, compared different formulations in the context of smooth and discontinuous solutions, and applied these models to characterize the hemodynamics of patients with hypoplastic left heart syndrome.

8.1 Summary

The partial differential equations describing one–dimensional blood flow in an elastic vessel were discretized with two different methods. Discontinuous Galerkin formulations were employed to approximate solutions of the nonlinear hyperbolic system in conservative form, and the numerical method of characteristics was used to compute solutions of the diagonal nonlinear hyperbolic system satisfied by the Riemann invariants. We found that both methods produced very similar results, even in large vessel networks. The numerical method of characteristics is more computationally efficient, since it requires no CFL–type condition for the time–step. The discontinuous Galerkin scheme has better mass–conserving properties and suffers from less numerical diffusion.

Analysis for the numerical method of characteristics and discontinous Galerkin schemes were given. Our results for the numerical method of characteristics established stability and convergence, independent of a time–step restriction. We developed

a priori error estimates for a discontinuous Galerkin scheme in space coupled to an explicit second order Adams–Bashforth method in time, which is very popular in the blood flow modeling literature. This result holds only for scalar nonlinear conservation laws. Our efforts to extend these results to nonlinear hyperbolic systems, like reduced models for blood flow, included the verification of symmetrizability for the (A, Q) and (A, U) systems.

These numerical methods were implemented in a modular C/C^{++} software framework in collaboration with Sebastián Acosta and Craig Rusin. This implementation includes various boundary conditions for one–dimensional vessels, like junctions, organ beds, and hearts, to facilitate the rapid development of one–dimensional/zero–dimensional cardiovascular models.

We presented a numerical comparison of various reduced blood flow models appearing in the literature, namely the (A, Q) and (A, U) systems, which depend on a parameter called the Coriolis coefficient. This parameter takes different values for different choices of the axial velocity profile, and our simulations explored its effect on smooth and discontinuous solutions.

Lastly, we developed closed loop vessel network models of the Fontan circulation. In addition to the standard extracardiac Fontan, we considered the fenestrated Fontan and the Fontan with hepatic vein exclusion. Our computational experiments revealed the impact of a fenestration or hepatic vein exclusion on hemodynamics, with a particular emphasis on the splanchnic circulation and other clinically relevant variables.

8.2 Future work

There are many open computational questions related to this work. First, is it possible to extend error estimates of discontinuous Galerkin schemes for scalar conservation laws to a particular class of nonlinear hyperbolic systems? Some recent work exists for symmetrizable systems, but aspects of this theory are not entirely clear. It would also be important to develop this theory for special numerical fluxes, like the upwinding flux depending on the Riemann invariants, and also numerical schemes for hyperbolic systems with boundary conditions.

In our derivation of the error estimates for the discontinous Galerkin scheme coupled to a multistep method, we needed a CFL condition, since the time discretization is explicit. Von Neumann–type stability analysis for this Adams–Bashforth method suggests a weaker CFL condition; is it possible to derive the same estimates in this case? More broadly, how should one approach analysis for explicit multistep time discretizations coupled to discontinuous Galerkin schemes for hyperbolic conservation laws? There is ample theory for Runge–Kutta discontinuous Galerkin methods, but little work exists for explicit multistep schemes.

The software developed as part of this thesis will enable computational experiments for many cardiovascular problems. A small extension of the Fontan models could include a characterization of the effect of negative intrathoracic pressure on venous return; researchers speculate this negative pressure is important in this population, since their blood flows passively into the lungs. This experiment would amount to varying the reference pressure in vessels above the diaphragm, and could also include a study on the impact of positive pressure ventilation. Some related computational results exist in the literature, but to our knowledge, few of these approaches employ one–dimensional models for the vessels.

A large component of our future work will be the continual development of the software for simulating reduced blood flow models. These will include new models and discretizations for hearts and organ beds, with more anatomical detail or better numerical properties like mass conservation. For example, it would be useful to include electrophysiology in the heart model and incorporate EKG data from Texas Children's Hospital. Another project would entail the numerical approximation for viscoelastic vessels, requiring modifications in both the discontinuous Galerkin and numerical method of characteristics schemes.

Appendix A

Appendix

A.1 Small closed loop circulation parameters

ID	name	type	A_0 (inlet) (cm^2)	A_0 (outlet) (cm^2)	length (cm)	β (dynes/cm^3)	inlet ID	outlet ID
0	systemic_arteries	systemic_artery	6.8	6.8	15	250000	0	1
1	systemic_veins	systemic_vein	5.0	5.0	15	19473	1	2
2	pulmonary_arteries	pulmonary_artery	7.1	7.1	6	49726	2	3
3	pulmonary_veins	pulmonary_vein	8.0	8.0	6	15084	3	0

Table A.1 : Vessel parameters for small circulation network.

	p_0 (dynes/cm^2)
systemic_artery	1.200e+05
systemic_vein	6.600e+03
pulmonary_artery	2.000e+04
pulmonary_vein	9.300e+03

Table A.2 : Reference pressure values for the small circulation network.

node ID	model name
0	left_heart_with_valves_semi_implicit
1	systemic_beds
2	right_heart_with_valves_semi_implicit
3	venous_beds

Table A.3 : Node IDs and model names for the small circulation network.

	V_0 (mL)	$V(t=0)$ (mL)	$E_{\min}$ $\left(\frac{\text{dynes}}{\text{cm}^2}\right)$	$E_{\max}$ $\left(\frac{\text{dynes}}{\text{cm}^2}\right)$	m_1	m_2	τ_1	τ_2	K $\left(\frac{\text{s}}{\text{mL}}\right)$	t_{onset} (s)
L. ventricle	2.000e+01	6.000e+01	1.000e+03	7.000e+04	3.000e+00	2.700e+01	2.690e-01	4.520e-01	5.000e-04	0.000e+00
L. atrium	1.200e+01	3.600e+01	1.000e+03	7.000e+03	3.000e+00	1.300e+01	1.100e-01	1.800e-01	5.000e-04	8.500e-01
R. ventricle	5.000e+01	1.500e+02	1.000e+03	7.000e+04	3.000e+00	2.700e+01	2.690e-01	4.520e-01	5.000e-04	0.000e+00
R. atrium	3.000e+01	9.000e+01	1.000e+03	7.000e+03	3.000e+00	1.300e+01	1.100e-01	1.800e-01	5.000e-04	8.500e-01

Table A.4 : Parameters for the heart in the small circulation circulation.

	B $\left(\frac{\text{dynes}\cdot\text{s}^2}{\text{cm}^5}\right)$	L $\left(\frac{\text{dynes}\cdot\text{s}^2}{\text{cm}^5}\right)$	R $\left(\frac{\text{dynes}\cdot\text{s}}{\text{cm}^5}\right)$	γ $\left(\frac{\text{cm}^2}{\text{dynes}}\right)$
L. interior	3.000e-02	5.000e-03	1.000e-03	5.000e-03
L. exterior	3.000e-02	5.000e-03	1.000e-03	3.000e-03
R. interior	3.000e-02	5.000e-03	1.000e-03	5.000e-03
R. exterior	3.000e-02	5.000e-03	1.000e-03	3.000e-03

Table A.5 : Parameters for the valves in the small circulation circulation.

	C_art $\left(\frac{\text{cm}^5}{\text{dynes}}\right)$	R_cap $\left(\frac{\text{dynes}\cdot\text{s}}{\text{cm}^5}\right)$	C_ven $\left(\frac{\text{cm}^5}{\text{dynes}}\right)$	V_ref (mL)
systemic_beds	7.500e-04	1.200e+03	8.300e-03	2.000e+03
venous_beds	7.500e-03	6.666e+01	1.130e-02	2.000e+03

Table A.6 : Parameters for the organ beds in the small circulation circulation.

A.2 Normal circulation parameters

ID	name	type	A_0 (inlet) (cm^2)	A_0 (outlet) (cm^2)	length (cm)	inlet ID	outlet ID
0	lv_outflow_tract	systemic_artery	6.927919	6.927919	1.000	0	1
1	aortic_root	systemic_artery	6.927919	6.927919	1.000	1	2
2	ascending_aorta	systemic_artery	6.788668	6.788668	4.000	2	3
3	aortic_arch_I	systemic_artery	5.227924	5.227924	2.000	3	11
4	brachiocephalic	systemic_artery	1.539380	1.539380	3.400	3	4
5	subclavian_I_R	systemic_artery	1.130973	1.042305	3.400	4	5
6	carotid_R	systemic_artery	0.502655	0.502655	17.700	4	10
7	vertebral_R	systemic_artery	0.113411	0.111155	14.800	5	75
8	internal_thoracic_R	systemic_artery	0.066052	0.066052	8.000	5	80
9	subclavian_II_R	systemic_artery	0.950332	0.950332	2.500	5	6
10	thyrocervical_R	systemic_artery	0.166190	0.166190	5.000	6	76
11	axiliary_I_R	systemic_artery	0.899202	0.899202	5.000	6	7
12	subscapular_R	systemic_artery	0.113411	0.113411	4.000	7	76
13	axiliary_II_R	systemic_artery	0.817128	0.459635	34.700	7	8
14	radius_R	systemic_artery	0.101788	0.060350	23.500	8	77
15	ulnar_I_R	systemic_artery	0.196350	0.196350	6.700	8	9
16	interosseous_R	systemic_artery	0.025447	0.025447	7.900	9	77
17	ulnar_II_R	systemic_artery	0.125664	0.115812	17.100	9	77
18	internal_carotid_R	systemic_artery	0.331831	0.331831	17.600	10	74
19	external_carotid_R	systemic_artery	0.331831	0.331831	17.700	10	74
20	aortic_arch_II	systemic_artery	4.830513	4.830513	3.900	11	13
21	carotid_L	systemic_artery	0.430084	0.430084	20.800	11	12
22	internal_carotid_L	systemic_artery	0.282743	0.282743	17.600	12	74
23	external_carotid_L	systemic_artery	0.282743	0.282743	17.700	12	74
24	thoracic_aorta_I	systemic_artery	3.801327	3.147879	5.200	13	19
25	subclavian_I_L	systemic_artery	0.950332	0.857674	3.400	13	14

Table A.7 : Vessel parameters for normal circulation network.

ID	name	type	A_0 (inlet) (cm^2)	A_0 (outlet) (cm^2)	length (cm)	inlet ID	outlet ID
26	vertebral_L	systemic_artery	0.125664	0.115812	14.800	14	75
27	internal_thoracic_L	systemic_artery	0.057256	0.057256	8.000	14	80
28	sublclavian_II_L	systemic_artery	0.679291	0.679291	2.500	14	15
29	thyrocervical_L	systemic_artery	0.125664	0.125664	5.000	15	78
30	axiliary_I_L	systemic_artery	0.636173	0.636173	5.000	15	16
31	subscapular_L	systemic_artery	0.080425	0.080425	4.000	16	78
32	axiliary_II_L	systemic_artery	0.515300	0.305521	34.700	16	17
33	radius_L	systemic_artery	0.053093	0.043966	23.500	17	79
34	ulnar_I_L	systemic_artery	0.145220	0.145220	6.700	17	18
35	interosseous_L	systemic_artery	0.025447	0.025447	7.900	18	79
36	ulnar_II_L	systemic_artery	0.125664	0.118237	17.100	18	79
37	intercostals	systemic_artery	0.045239	0.045239	8.000	19	80
38	thoracic_aorta_II	systemic_artery	2.377871	1.598810	10.400	19	20
39	abdominal_aorta_I	systemic_artery	1.168987	1.168987	5.300	20	22
40	celiac	systemic_artery	0.453646	0.453646	2.000	20	21
41	hepatic	systemic_artery	0.180956	0.180956	6.600	21	81
42	splenic	systemic_artery	0.125664	0.125664	6.300	21	82
43	gastric	systemic_artery	0.264208	0.238448	7.100	21	83
44	superior_mesenteric	systemic_artery	0.282743	0.282743	5.900	22	84
45	abdominal_aorta_II	systemic_artery	1.093588	1.093588	1.000	22	23
46	renal_L	systemic_artery	0.212372	0.212372	3.200	23	86
47	abdominal_aorta_III	systemic_artery	1.020703	1.020703	1.000	23	24
48	renal_R	systemic_artery	0.212372	0.212372	3.200	24	85
49	abdominal_aorta_IV	systemic_artery	0.950332	0.875826	10.600	24	25
50	inferior_mesenteric	systemic_artery	0.080425	0.080425	5.000	25	84
51	abdominal_aorta_V	systemic_artery	0.849487	0.782887	1.000	25	26
52	common_iliac_L	systemic_artery	0.430084	0.413053	5.900	26	30
53	common_iliac_R	systemic_artery	0.430084	0.413053	5.800	26	27
54	external_iliac_L	systemic_artery	0.246301	0.236547	14.400	27	28
55	internal_iliac_L	systemic_artery	0.220618	0.220618	5.000	27	88
56	femoral_L	systemic_artery	0.196350	0.148617	44.300	28	29
57	deep_femoral_L	systemic_artery	0.070686	0.058535	12.600	28	89
58	posterior_tibial_L	systemic_artery	0.075477	0.068118	32.100	29	91
59	anterior_tibial_L	systemic_artery	0.053093	0.046913	34.300	29	91
60	external_iliac_R	systemic_artery	0.246301	0.236547	14.500	30	31

Table A.8 : Vessel parameters for normal circulation network (continued).

ID	name	type	A_0 (inlet) (cm^2)	A_0 (outlet) (cm^2)	length (cm)	inlet ID	outlet ID
61	internal_iliac_R	systemic_artery	0.220618	0.220618	5.000	30	88
62	femoral_R	systemic_artery	0.196350	0.148617	44.400	31	32
63	deep_femoral_R	systemic_artery	0.070686	0.058535	12.700	31	87
64	posterior_tibial_R	systemic_artery	0.075477	0.068118	32.200	32	90
65	anterior_tibial_R	systemic_artery	0.053093	0.046913	34.400	32	90
66	vertebral_R	systemic_vein	0.173494	0.187652	14.800	75	56
67	internal_jugular_R	systemic_vein	1.606061	1.737115	17.600	74	56
68	transverse_cervical_R	systemic_vein	0.264208	0.285767	5.000	76	55
69	external_jugular_R	systemic_vein	0.679291	0.734721	17.700	74	55
70	radius_R	systemic_vein	0.096211	0.145558	23.500	77	50
71	ulnar_II_R	systemic_vein	0.180956	0.195722	17.100	77	49
72	interosseus_R	systemic_vein	0.041548	0.041548	7.900	77	49
73	ulnar_I_R	systemic_vein	0.229022	0.229022	6.700	49	50
74	brachial_R	systemic_vein	0.395919	0.395919	20.820	50	53
75	cephalic_I_R	systemic_vein	0.017671	0.017671	11.100	77	52
76	basilic_I_R	systemic_vein	0.125664	0.125664	18.800	77	48
77	median_antebrachial_R	systemic_vein	0.070686	0.070686	18.800	77	48
78	basilic_II_R	systemic_vein	0.166190	0.166190	4.700	48	51
79	median_cubital_R	systemic_vein	0.407150	0.407150	8.850	52	51
80	cephalic_II_R	systemic_vein	0.418539	0.418539	36.610	52	54
81	basilic_III_R	systemic_vein	0.196350	0.196350	20.820	51	53
82	subscapular_R	systemic_vein	0.220618	0.238621	4.000	76	54
83	axiliary_R	systemic_vein	0.528102	0.528102	6.940	53	54
84	subclavian_R	systemic_vein	0.801185	0.801185	5.200	54	55
85	brachiocephalic_I_R	systemic_vein	1.227185	1.227185	3.400	55	56
86	brachiocephalic_II_R	systemic_vein	2.405282	2.910391	4.000	56	66
87	vertebral_L	systemic_vein	0.180956	0.195722	17.100	75	65
88	internal_jugular_L	systemic_vein	1.188229	1.285188	17.600	74	65
89	transverse_cervical_L	systemic_vein	0.196350	0.212372	5.000	78	64
90	external_jugular_L	systemic_vein	0.502655	0.543671	17.100	74	64
91	radius_L	systemic_vein	0.070686	0.083982	10.400	79	59
92	ulnar_II_L	systemic_vein	0.188574	0.200058	17.100	79	57
93	interosseus_L	systemic_vein	0.041548	0.041548	7.900	79	57
94	ulnar_I_L	systemic_vein	0.229022	0.229022	6.700	57	59
95	brachial_L	systemic_vein	0.395919	0.395919	20.820	59	62

Table A.9 : Vessel parameters for normal circulation network (continued).

ID	name	type	A_0 (inlet) (cm^2)	A_0 (outlet) (cm^2)	length (cm)	inlet ID	outlet ID
96	cephalic_I_L	systemic_vein	0.017671	0.017671	11.100	79	60
97	basilic_I_L	systemic_vein	0.125664	0.125664	18.800	79	58
98	median_antebrachial_L	systemic_vein	0.070686	0.070686	18.800	79	58
99	basilic_II_L	systemic_vein	0.166190	0.166190	4.700	58	61
100	median_cubital_L	systemic_vein	0.407150	0.407150	8.850	61	60
101	cephalic_II_L	systemic_vein	0.418539	0.418539	36.610	60	63
102	basilic_III_L	systemic_vein	0.196350	0.196350	20.820	61	62
103	subscapular_L	systemic_vein	0.159043	0.172021	4.000	78	63
104	axiliary_L	systemic_vein	0.528102	0.528102	6.940	62	63
105	subclavian_L	systemic_vein	0.801185	0.801185	5.200	63	64
106	brachiocephalic_I_L	systemic_vein	1.149901	1.149901	3.400	64	65
107	brachiocephalic_II_L	systemic_vein	1.985565	2.402534	6.000	65	66
108	superior_vena_cava_I	systemic_vein	3.801327	4.599606	2.000	66	67
109	azygous	systemic_vein	0.515300	0.623513	15.000	80	67
110	superior_vena_cava_II	systemic_vein	3.986078	4.811055	4.000	67	73
111	posterior_tibial_R	systemic_vein	0.107521	0.118542	32.200	90	33
112	anterior_tibial_R	systemic_vein	0.075477	0.084806	34.400	90	33
113	small_saphenous_R	systemic_vein	0.080425	0.111983	34.400	90	34
114	great_saphenous_R	systemic_vein	0.113411	0.203642	78.800	90	36
115	popliteal_R	systemic_vein	0.125664	0.125664	16.100	33	34
116	femoral_I_R	systemic_vein	0.229022	0.292438	39.960	34	35
117	deep_femoral_R	systemic_vein	0.113411	0.113411	12.700	87	35
118	femoral_II_R	systemic_vein	0.352565	0.352565	4.440	35	36
119	external_iliac_R	systemic_vein	0.373928	0.389035	14.500	36	37
120	internal_iliac_R	systemic_vein	0.384845	0.384845	5.000	88	37
121	common_iliac_R	systemic_vein	0.636173	0.661874	5.900	37	43
122	posterior_tibial_L	systemic_vein	0.107521	0.118542	32.200	91	38
123	anterior_tibial_L	systemic_vein	0.075477	0.084806	34.400	91	38
124	small_saphenous_L	systemic_vein	0.080425	0.111983	34.400	91	39
125	great_saphenous_L	systemic_vein	0.113411	0.203642	78.800	91	41
126	popliteal_L	systemic_vein	0.125664	0.125664	16.100	38	39
127	femoral_I_L	systemic_vein	0.229022	0.292438	44.300	39	40
128	deep_femoral_L	systemic_vein	0.113411	0.113411	12.600	89	40
129	femoral_II_L	systemic_vein	0.352565	0.352565	4.440	40	41
130	external_iliac_L	systemic_vein	0.373928	0.389035	14.400	41	42

Table A.10 : Vessel parameters for normal circulation network (continued).

ID	name	type	A_0 (inlet) (cm^2)	A_0 (outlet) (cm^2)	length (cm)	inlet ID	outlet ID
131	internal_iliac_L	systemic_vein	0.342119	0.342119	5.000	88	42
132	common_iliac_L	systemic_vein	0.636173	0.661874	5.800	42	43
133	inferior_vena_cava_I	systemic_vein	1.474114	1.751395	11.600	43	44
134	renal_R	systemic_vein	0.331831	0.331831	3.200	85	44
135	inferior_vena_cava_II	systemic_vein	1.495712	1.495712	1.000	44	45
136	renal_L	systemic_vein	0.331831	0.331831	3.200	86	45
137	inferior_vena_cava_III	systemic_vein	1.697167	1.697167	2.000	45	46
138	right_hepatic	systemic_vein	0.785398	0.785398	6.600	81	46
139	left_hepatic	systemic_vein	0.580880	0.580880	3.300	81	47
140	middle_hepatic	systemic_vein	0.594468	0.594468	4.800	81	47
141	common_hepatic	systemic_vein	1.452672	1.452672	1.200	47	46
142	inferior_vena_cava_IV	systemic_vein	4.908739	3.976078	7.000	46	73
143	splenic	portal_vein	0.363168	0.363168	6.300	82	68
144	inferior_mesenteric_I	portal_vein	0.125664	0.125664	7.000	84	68
145	inferior_mesenteric_II	portal_vein	0.418539	0.707330	1.000	68	69
146	superior_mesenteric	portal_vein	0.441786	0.441786	5.900	84	69
147	hepatic_portal_I	portal_vein	0.664761	0.664761	2.000	69	70
148	gastric	portal_vein	0.107521	0.107521	1.000	83	70
149	hepatic_portal_II	portal_vein	1.093588	1.093588	3.000	70	81
150	rv_outflow_tract	pulmonary_artery	7.068583	7.068583	1.000	73	71
151	main_pulmonary_artery	pulmonary_artery	7.068583	7.068583	4.300	71	72
152	pulmonary_artery_L	pulmonary_artery	2.986477	2.986477	2.800	72	92
153	pulmonary_artery_R	pulmonary_artery	4.337361	4.337361	4.100	72	93
154	lower_pulmonary_L	pulmonary_vein	1.168987	1.168987	13.000	92	0
155	upper_pulmonary_L	pulmonary_vein	1.246898	1.246898	13.000	92	0
156	lower_pulmonary_R	pulmonary_vein	1.517468	1.517468	13.000	93	0
157	upper_pulmonary_R	pulmonary_vein	1.306981	1.306981	13.000	93	0

Table A.11 : Vessel parameters for normal circulation network (continued).

	k_1 (dynes/cm^2)	k_2	k_3 (dynes/cm^2)	p_0 (dynes/cm^2)
systemic_artery	4.000e+04	-3.000e+00	1.500e+05	1.2000e+05
systemic_vein	3.000e+05	-1.050e+01	2.000e+04	6.6660e+03
pulmonary_artery	5.000e+04	-1.500e+01	5.000e+04	1.4000e+04
pulmonary_vein	5.000e+04	-1.500e+01	5.000e+04	1.3332e+04
portal_vein	3.000e+05	-1.050e+01	1.500e+04	1.3332e+04

Table A.12 : Parameters for each class of vessels in the normal circulation network.

node ID	model name
0	left_heart_with_valves_semi_implicit
73	right_heart_with_valves_semi_implicit
74	head
75	neck
76	R_shoulder
77	R_arm
78	L_shoulder
79	L_arm
80	thorax
81	liver
82	spleen
83	stomach
84	intestines
85	R_kidney
86	L_kidney
87	R_thigh
88	pelvic_region
89	L_thigh
90	R_lower_leg
91	L_lower_leg
92	L_lung
93	R_lung

Table A.13 : Node IDs and model names for the normal circulation network. Nodes with IDs 1–72 are interior nodes.

	V_0 (mL)	$V(t=0)$ (mL)	$E_{\min}$ $\left(\frac{\text{dynes}}{\text{cm}^2}\right)$	$E_{\max}$ $\left(\frac{\text{dynes}}{\text{cm}^2}\right)$	m_1	m_2	τ_1	τ_2	K $\left(\frac{\text{s}}{\text{mL}}\right)$	t_{onset} (s)
L. ventricle	2.400e+01	5.000e+01	1.200e+03	1.200e+05	3.000e+00	2.700e+01	2.700e-01	4.500e-01	5.000e-04	0.000e+00
L. atrium	1.200e+01	2.400e+01	1.200e+03	1.200e+04	3.000e+00	2.700e+01	1.100e-01	1.800e-01	5.000e-04	8.500e-01
R. ventricle	4.600e+01	1.000e+02	1.200e+03	1.200e+05	3.000e+00	2.700e+01	2.700e-01	4.500e-01	5.000e-04	0.000e+00
R. atrium	2.300e+01	5.000e+01	1.200e+03	1.200e+04	3.000e+00	2.700e+01	1.100e-01	1.800e-01	5.000e-04	8.500e-01

Table A.14 : Parameters for the heart in the normal circulation circulation.

	B $\left(\frac{\text{dynes·s}^2}{\text{cm}^8}\right)$	L $\left(\frac{\text{dynes·s}^2}{\text{cm}^5}\right)$	R $\left(\frac{\text{dynes·s}}{\text{cm}^5}\right)$	γ $\left(\frac{\text{cm}^2}{\text{dynes}}\right)$
L. interior	3.000e-02	5.000e-03	1.000e-03	5.000e-03
L. exterior	3.000e-02	5.000e-03	1.000e-03	3.000e-03
R. interior	3.000e-02	5.000e-03	1.000e-03	5.000e-03
R. exterior	3.000e-02	5.000e-03	1.000e-03	3.000e-03

Table A.15 : Parameters for the valves in the normal circulation circulation.

	C_art $\left(\frac{\text{cm}^5}{\text{dynes}}\right)$	R_cap $\left(\frac{\text{dynes·s}}{\text{cm}^5}\right)$	C_ven $\left(\frac{\text{cm}^5}{\text{dynes}}\right)$	V_ref (mL)
head	3.000e-05	4.000e+03	3.000e-04	1.150e+02
neck	4.000e-05	1.000e+04	4.000e-04	8.000e+01
R_shoulder	1.500e-05	2.000e+04	1.500e-04	1.200e+02
R_arm	2.000e-05	1.500e+04	2.000e-04	1.200e+02
L_shoulder	1.500e-05	2.000e+04	1.500e-04	1.200e+02
L_arm	2.000e-05	1.500e+04	2.000e-04	1.200e+02
thorax	1.000e-04	4.000e+03	1.000e-03	8.500e+01
spleen	4.000e-05	5.000e+03	4.000e-04	8.000e+01
stomach	2.000e-05	2.000e+04	2.000e-04	8.000e+01
intestines	1.000e-04	3.000e+03	1.000e-03	2.500e+02
R_kidney	1.000e-04	2.500e+03	1.000e-03	1.300e+02
L_kidney	1.000e-04	2.500e+03	1.000e-03	1.300e+02
R_thigh	3.000e-05	1.500e+04	3.000e-04	1.700e+02
pelvic_region	3.000e-05	1.500e+04	3.000e-04	1.550e+02
L_thigh	3.000e-05	1.500e+04	3.000e-04	1.700e+02
R_lower_leg	5.000e-05	1.000e+04	5.000e-04	8.500e+01
L_lower_leg	5.000e-05	1.000e+04	5.000e-04	8.500e+01
L_lung	1.000e-03	4.500e+01	2.000e-03	7.000e+02
R_lung	1.000e-03	4.000e+01	2.000e-03	7.000e+02

Table A.16 : Parameters for the organ beds in the normal circulation circulation.

R_{int} $\left(\frac{\text{dynes·s}}{\text{cm}^5}\right)$	R_{cap} $\left(\frac{\text{dynes·s}}{\text{cm}^5}\right)$	C_{int} $\left(\frac{\text{cm}^5}{\text{dynes}}\right)$	C_{portal} $\left(\frac{\text{cm}^5}{\text{dynes}}\right)$	C_{ven} $\left(\frac{\text{cm}^5}{\text{dynes}}\right)$	V_{ref} (mL)
5.000e+03	5.000e+02	5.000e-05	5.000e-04	5.000e-04	4.300e+02

Table A.17 : Parameters for the liver in the normal circulation circulation.

A.3 Standard Fontan parameters

ID	name	type	A_0 (inlet) (cm^2)	A_0 (outlet) (cm^2)	length (cm)	inlet ID	outlet ID
0	lv_outflow_tract	systemic_artery	6.927919	6.927919	1.000	0	1
1	aortic_root	systemic_artery	6.927919	6.927919	1.000	1	2
2	ascending_aorta	systemic_artery	6.788668	6.788668	4.000	2	3
3	aortic_arch_I	systemic_artery	5.227924	5.227924	2.000	3	11
4	brachiocephalic	systemic_artery	1.539380	1.539380	3.400	3	4
5	subclavian_I_R	systemic_artery	1.130973	1.042305	3.400	4	5
6	carotid_R	systemic_artery	0.502655	0.502655	17.700	4	10
7	vertebral_R	systemic_artery	0.113411	0.111155	14.800	5	73
8	internal_thoracic_R	systemic_artery	0.066052	0.066052	8.000	5	78
9	subclavian_II_R	systemic_artery	0.950332	0.950332	2.500	5	6
10	thyrocervical_R	systemic_artery	0.166190	0.166190	5.000	6	74
11	axiliary_I_R	systemic_artery	0.899202	0.899202	5.000	6	7
12	subscapular_R	systemic_artery	0.113411	0.113411	4.000	7	74
13	axiliary_II_R	systemic_artery	0.817128	0.459635	34.700	7	8
14	radius_R	systemic_artery	0.101788	0.060350	23.500	8	75
15	ulnar_I_R	systemic_artery	0.196350	0.196350	6.700	8	9
16	interosseous_R	systemic_artery	0.025447	0.025447	7.900	9	75
17	ulnar_II_R	systemic_artery	0.125664	0.115812	17.100	9	75
18	internal_carotid_R	systemic_artery	0.331831	0.331831	17.600	10	72
19	external_carotid_R	systemic_artery	0.331831	0.331831	17.700	10	72
20	aortic_arch_II	systemic_artery	4.830513	4.830513	3.900	11	13
21	carotid_L	systemic_artery	0.430084	0.430084	20.800	11	12
22	internal_carotid_L	systemic_artery	0.282743	0.282743	17.600	12	72
23	external_carotid_L	systemic_artery	0.282743	0.282743	17.700	12	72
24	thoracic_aorta_I	systemic_artery	3.801327	3.147879	5.200	13	19
25	subclavian_I_L	systemic_artery	0.950332	0.857674	3.400	13	14

Table A.18 : Vessel parameters for standard Fontan network.

ID	name	type	A_0 (inlet) (cm^2)	A_0 (outlet) (cm^2)	length (cm)	inlet ID	outlet ID
26	vertebral_L	systemic_artery	0.125664	0.115812	14.800	14	73
27	internal_thoracic_L	systemic_artery	0.057256	0.057256	8.000	14	78
28	sublclavian_II_L	systemic_artery	0.679291	0.679291	2.500	14	15
29	thyrocervical_L	systemic_artery	0.125664	0.125664	5.000	15	76
30	axiliary_I_L	systemic_artery	0.636173	0.636173	5.000	15	16
31	subscapular_L	systemic_artery	0.080425	0.080425	4.000	16	76
32	axiliary_II_L	systemic_artery	0.515300	0.305521	34.700	16	17
33	radius_L	systemic_artery	0.053093	0.043966	23.500	17	77
34	ulnar_I_L	systemic_artery	0.145220	0.145220	6.700	17	18
35	interosseous_L	systemic_artery	0.025447	0.025447	7.900	18	77
36	ulnar_II_L	systemic_artery	0.125664	0.118237	17.100	18	77
37	intercostals	systemic_artery	0.045239	0.045239	8.000	19	78
38	thoracic_aorta_II	systemic_artery	2.377871	1.598810	10.400	19	20
39	abdominal_aorta_I	systemic_artery	1.168987	1.168987	5.300	20	22
40	celiac	systemic_artery	0.453646	0.453646	2.000	20	21
41	hepatic	systemic_artery	0.180956	0.180956	6.600	21	79
42	splenic	systemic_artery	0.125664	0.125664	6.300	21	80
43	gastric	systemic_artery	0.264208	0.238448	7.100	21	81
44	superior_mesenteric	systemic_artery	0.282743	0.282743	5.900	22	82
45	abdominal_aorta_II	systemic_artery	1.093588	1.093588	1.000	22	23
46	renal_L	systemic_artery	0.212372	0.212372	3.200	23	84
47	abdominal_aorta_III	systemic_artery	1.020703	1.020703	1.000	23	24
48	renal_R	systemic_artery	0.212372	0.212372	3.200	24	83
49	abdominal_aorta_IV	systemic_artery	0.950332	0.875826	10.600	24	25
50	inferior_mesenteric	systemic_artery	0.080425	0.080425	5.000	25	82
51	abdominal_aorta_V	systemic_artery	0.849487	0.782887	1.000	25	26
52	common_iliac_L	systemic_artery	0.430084	0.413053	5.900	26	30
53	common_iliac_R	systemic_artery	0.430084	0.413053	5.800	26	27
54	external_iliac_L	systemic_artery	0.246301	0.236547	14.400	27	28
55	internal_iliac_L	systemic_artery	0.220618	0.220618	5.000	27	86
56	femoral_L	systemic_artery	0.196350	0.148617	44.300	28	29
57	deep_femoral_L	systemic_artery	0.070686	0.058535	12.600	28	87
58	posterior_tibial_L	systemic_artery	0.075477	0.068118	32.100	29	89
59	anterior_tibial_L	systemic_artery	0.053093	0.046913	34.300	29	89
60	external_iliac_R	systemic_artery	0.246301	0.236547	14.500	30	31

Table A.19 : Vessel parameters for standard Fontan network (continued).

ID	name	type	A_0 (inlet) (cm^2)	A_0 (outlet) (cm^2)	length (cm)	inlet ID	outlet ID
61	internal_iliac_R	systemic_artery	0.220618	0.220618	5.000	30	86
62	femoral_R	systemic_artery	0.196350	0.148617	44.400	31	32
63	deep_femoral_R	systemic_artery	0.070686	0.058535	12.700	31	85
64	posterior_tibial_R	systemic_artery	0.075477	0.068118	32.200	32	88
65	anterior_tibial_R	systemic_artery	0.053093	0.046913	34.400	32	88
66	vertebral_R	systemic_vein	0.173494	0.187652	14.800	73	56
67	internal_jugular_R	systemic_vein	1.606061	1.737115	17.600	72	56
68	transverse_cervical_R	systemic_vein	0.264208	0.285767	5.000	74	55
69	external_jugular_R	systemic_vein	0.679291	0.734721	17.700	72	55
70	radius_R	systemic_vein	0.096211	0.145558	23.500	75	50
71	ulnar_II_R	systemic_vein	0.180956	0.195722	17.100	75	49
72	interosseus_R	systemic_vein	0.041548	0.041548	7.900	75	49
73	ulnar_I_R	systemic_vein	0.229022	0.229022	6.700	49	50
74	brachial_R	systemic_vein	0.395919	0.395919	20.820	50	53
75	cephalic_I_R	systemic_vein	0.017671	0.017671	11.100	75	52
76	basilic_I_R	systemic_vein	0.125664	0.125664	18.800	75	48
77	median_antebrachial_R	systemic_vein	0.070686	0.070686	18.800	75	48
78	basilic_II_R	systemic_vein	0.166190	0.166190	4.700	48	51
79	median_cubital_R	systemic_vein	0.407150	0.407150	8.850	52	51
80	cephalic_II_R	systemic_vein	0.418539	0.418539	36.610	52	54
81	basilic_III_R	systemic_vein	0.196350	0.196350	20.820	51	53
82	subscapular_R	systemic_vein	0.220618	0.238621	4.000	74	54
83	axiliary_R	systemic_vein	0.528102	0.528102	6.940	53	54
84	subclavian_R	systemic_vein	0.801185	0.801185	5.200	54	55
85	brachiocephalic_I_R	systemic_vein	1.227185	1.227185	3.400	55	56
86	brachiocephalic_II_R	systemic_vein	2.405282	2.910391	4.000	56	66
87	vertebral_L	systemic_vein	0.180956	0.195722	17.100	73	65
88	internal_jugular_L	systemic_vein	1.188229	1.285188	17.600	72	65
89	transverse_cervical_L	systemic_vein	0.196350	0.212372	5.000	76	64
90	external_jugular_L	systemic_vein	0.502655	0.543671	17.100	72	64
91	radius_L	systemic_vein	0.070686	0.083982	10.400	77	59
92	ulnar_II_L	systemic_vein	0.188574	0.200058	17.100	77	57
93	interosseus_L	systemic_vein	0.041548	0.041548	7.900	77	57
94	ulnar_I_L	systemic_vein	0.229022	0.229022	6.700	57	59
95	brachial_L	systemic_vein	0.395919	0.395919	20.820	59	62

Table A.20 : Vessel parameters for standard Fontan network (continued).

ID	name	type	A_0 (inlet) (cm^2)	A_0 (outlet) (cm^2)	length (cm)	inlet ID	outlet ID
96	cephalic_I_L	systemic_vein	0.017671	0.017671	11.100	77	60
97	basilic_I_L	systemic_vein	0.125664	0.125664	18.800	77	58
98	median_antebrachial_L	systemic_vein	0.070686	0.070686	18.800	77	58
99	basilic_II_L	systemic_vein	0.166190	0.166190	4.700	58	61
100	median_cubital_L	systemic_vein	0.407150	0.407150	8.850	61	60
101	cephalic_II_L	systemic_vein	0.418539	0.418539	36.610	60	63
102	basilic_III_L	systemic_vein	0.196350	0.196350	20.820	61	62
103	subscapular_L	systemic_vein	0.159043	0.172021	4.000	76	63
104	axiliary_L	systemic_vein	0.528102	0.528102	6.940	62	63
105	subclavian_L	systemic_vein	0.801185	0.801185	5.200	63	64
106	brachiocephalic_I_L	systemic_vein	1.149901	1.149901	3.400	64	65
107	brachiocephalic_II_L	systemic_vein	1.985565	2.402534	6.000	65	66
108	superior_vena_cava_I	systemic_vein	3.801327	4.599606	2.000	66	67
109	azygous	systemic_vein	0.515300	0.623513	15.000	78	67
110	superior_vena_cava_II	systemic_vein	3.986078	4.811055	4.000	67	71
111	posterior_tibial_R	systemic_vein	0.107521	0.118542	32.200	88	33
112	anterior_tibial_R	systemic_vein	0.075477	0.084806	34.400	88	33
113	small_saphenous_R	systemic_vein	0.080425	0.111983	34.400	88	34
114	great_saphenous_R	systemic_vein	0.113411	0.203642	78.800	88	36
115	popliteal_R	systemic_vein	0.125664	0.125664	16.100	33	34
116	femoral_I_R	systemic_vein	0.229022	0.292438	39.960	34	35
117	deep_femoral_R	systemic_vein	0.113411	0.113411	12.700	85	35
118	femoral_II_R	systemic_vein	0.352565	0.352565	4.440	35	36
119	external_iliac_R	systemic_vein	0.373928	0.389035	14.500	36	37
120	internal_iliac_R	systemic_vein	0.384845	0.384845	5.000	86	37
121	common_iliac_R	systemic_vein	0.636173	0.661874	5.900	37	43
122	posterior_tibial_L	systemic_vein	0.107521	0.118542	32.200	89	38
123	anterior_tibial_L	systemic_vein	0.075477	0.084806	34.400	89	38
124	small_saphenous_L	systemic_vein	0.080425	0.111983	34.400	89	39
125	great_saphenous_L	systemic_vein	0.113411	0.203642	78.800	89	41
126	popliteal_L	systemic_vein	0.125664	0.125664	16.100	38	39
127	femoral_I_L	systemic_vein	0.229022	0.292438	44.300	39	40
128	deep_femoral_L	systemic_vein	0.113411	0.113411	12.600	87	40
129	femoral_II_L	systemic_vein	0.352565	0.352565	4.440	40	41
130	external_iliac_L	systemic_vein	0.373928	0.389035	14.400	41	42

Table A.21 : Vessel parameters for standard Fontan network (continued).

ID	name	type	A_0 (inlet) (cm^2)	A_0 (outlet) (cm^2)	length (cm)	inlet ID	outlet ID
131	internal_iliac_L	systemic_vein	0.342119	0.342119	5.000	86	42
132	common_iliac_L	systemic_vein	0.636173	0.661874	5.800	42	43
133	inferior_vena_cava_I	systemic_vein	1.474114	1.751395	11.600	43	44
134	renal_R	systemic_vein	0.331831	0.331831	3.200	83	44
135	inferior_vena_cava_II	systemic_vein	1.495712	1.495712	1.000	44	45
136	renal_L	systemic_vein	0.331831	0.331831	3.200	84	45
137	inferior_vena_cava_III	systemic_vein	1.697167	1.697167	2.000	45	46
138	right_hepatic	systemic_vein	0.785398	0.785398	6.600	79	46
139	left_hepatic	systemic_vein	0.580880	0.580880	3.300	79	47
140	middle_hepatic	systemic_vein	0.594468	0.594468	4.800	79	47
141	common_hepatic	systemic_vein	1.452672	1.452672	1.200	47	46
142	inferior_vena_cava_IV	systemic_vein	4.908739	3.976078	7.000	46	71
143	splenic	portal_vein	0.363168	0.363168	6.300	80	68
144	inferior_mesenteric_I	portal_vein	0.125664	0.125664	7.000	82	68
145	inferior_mesenteric_II	portal_vein	0.418539	0.707330	1.000	68	69
146	superior_mesenteric	portal_vein	0.441786	0.441786	5.900	82	69
147	hepatic_portal_I	portal_vein	0.664761	0.664761	2.000	69	70
148	gastric	portal_vein	0.107521	0.107521	1.000	81	70
149	hepatic_portal_II	portal_vein	1.093588	1.093588	3.000	70	79
150	pulmonary_artery_L	pulmonary_artery	2.986477	2.986477	2.800	71	90
151	pulmonary_artery_R	pulmonary_artery	4.337361	4.337361	4.100	71	91
152	lower_pulmonary_R	pulmonary_vein	1.517468	1.517468	13.000	91	0
153	upper_pulmonary_R	pulmonary_vein	1.306981	1.306981	13.000	91	0
154	lower_pulmonary_L	pulmonary_vein	1.168987	1.168987	13.000	90	0
155	upper_pulmonary_L	pulmonary_vein	1.246898	1.246898	13.000	90	0

Table A.22 : Vessel parameters for standard Fontan network (continued).

	k_1 (dynes/cm^2)	k_2	k_3 (dynes/cm^2)	p_0 (dynes/cm^2)
systemic_artery	1.000e+05	-2.970e+00	1.500e+05	1.2000e+05
systemic_vein	3.000e+05	-1.188e+01	1.500e+04	1.2000e+04
pulmonary_artery	2.000e+05	-1.485e+01	3.000e+05	1.2000e+04
pulmonary_vein	3.000e+05	-1.485e+01	4.000e+05	9.0000e+03
portal_vein	1.000e+05	-7.425e+00	5.000e+03	1.2000e+04

Table A.23 : Parameters for each class of vessels in the standard Fontan network.

node ID	model name
0	right_heart_with_valves_semi_implicit
72	head
73	neck
74	R_shoulder
75	R_arm
76	L_shoulder
77	L_arm
78	thorax
79	liver
80	spleen
81	stomach
82	intestines
83	R_kidney
84	L_kidney
85	R_thigh
86	pelvic_region
87	L_thigh
88	R_lower_leg
89	L_lower_leg
90	L_lung
91	R_lung

Table A.24 : Node IDs and model names for the standard Fontan network. Nodes with IDs 1–71 are interior nodes.

	V_0 (mL)	$V(t=0)$ (mL)	$E_{\min}$ $\left(\frac{\text{dynes}}{\text{cm}^2}\right)$	$E_{\max}$ $\left(\frac{\text{dynes}}{\text{cm}^2}\right)$	m_1	m_2	τ_1	τ_2	K $\left(\frac{\text{s}}{\text{mL}}\right)$	t_{onset} (s)
ventricle	4.800e+01	1.500e+02	1.000e+03	3.000e+05	3.000e+00	2.700e+01	2.690e-01	4.520e-01	5.000e-04	0.000e+00
atrium	2.500e+01	8.000e+01	1.000e+03	1.500e+04	2.000e+00	1.300e+01	1.100e-01	1.800e-01	1.000e-04	8.500e-01

Table A.25 : Parameters for the right heart in the standard Fontan circulation.

	B $\left(\frac{\text{dynes}\cdot\text{s}^2}{\text{cm}^5}\right)$	L $\left(\frac{\text{dynes}\cdot\text{s}^2}{\text{cm}^5}\right)$	R $\left(\frac{\text{dynes}\cdot\text{s}}{\text{cm}^5}\right)$	γ $\left(\frac{\text{cm}^2}{\text{dynes}}\right)$
interior	1.000e-02	5.000e-03	1.000e-03	5.000e-03
exterior	5.000e-03	5.000e-03	1.000e-03	3.000e-03

Table A.26 : Parameters for the valves in the standard Fontan circulation.

	C_{art} $\left(\frac{\text{cm}^5}{\text{dynes}}\right)$	R_{cap} $\left(\frac{\text{dynes·s}}{\text{cm}^5}\right)$	C_{ven} $\left(\frac{\text{cm}^5}{\text{dynes}}\right)$	V_{ref} (mL)
head	3.000e-05	5.000e+03	3.000e-04	1.200e+02
neck	4.000e-05	1.000e+04	4.000e-04	8.000e+01
R_shoulder	1.500e-05	2.000e+04	1.500e-04	1.200e+02
R_arm	2.000e-05	1.500e+04	2.000e-04	1.200e+02
L_shoulder	1.500e-05	2.000e+04	1.500e-04	1.200e+02
L_arm	2.000e-05	1.500e+04	2.000e-04	1.200e+02
thorax	1.000e-04	4.000e+03	1.000e-03	1.000e+02
spleen	4.000e-05	3.500e+04	4.000e-04	7.000e+01
stomach	2.000e-05	4.000e+04	2.000e-04	7.000e+01
intestines	1.000e-04	3.000e+03	1.000e-03	2.500e+02
R_kidney	1.000e-04	2.500e+03	1.000e-03	1.300e+02
L_kidney	1.000e-04	2.500e+03	1.000e-03	1.300e+02
R_thigh	3.000e-05	1.500e+04	3.000e-04	1.700e+02
pelvic_region	3.000e-05	1.500e+04	3.000e-04	1.600e+02
L_thigh	3.000e-05	1.500e+04	3.000e-04	1.700e+02
R_lower_leg	5.000e-05	1.000e+04	5.000e-04	8.500e+01
L_lower_leg	5.000e-05	1.000e+04	5.000e-04	8.500e+01
L_lung	1.000e-03	4.500e+01	2.000e-03	7.000e+02
R_lung	1.000e-03	4.000e+01	2.000e-03	7.000e+02

Table A.27 : Parameters for the organ beds in the standard Fontan circulation.

R_{int} $\left(\frac{\text{dynes·s}}{\text{cm}^5}\right)$	R_{cap} $\left(\frac{\text{dynes·s}}{\text{cm}^5}\right)$	C_{int} $\left(\frac{\text{cm}^5}{\text{dynes}}\right)$	C_{portal} $\left(\frac{\text{cm}^5}{\text{dynes}}\right)$	C_{ven} $\left(\frac{\text{cm}^5}{\text{dynes}}\right)$	V_{ref} (mL)
2.000e+04	2.000e+02	5.000e-05	5.000e-04	5.000e-04	4.250e+02

Table A.28 : Parameters for the liver in the standard Fontan circulation.

A.4 Fenestrated Fontan parameters

ID	name	type	A_0 (inlet) (cm^2)	A_0 (outlet) (cm^2)	length (cm)	inlet ID	outlet ID
0	lv_outflow_tract	systemic_artery	6.927919	6.927919	1.000	0	1
1	aortic_root	systemic_artery	6.927919	6.927919	1.000	1	2
2	ascending_aorta	systemic_artery	6.788668	6.788668	4.000	2	3
3	aortic_arch_I	systemic_artery	5.227924	5.227924	2.000	3	11
4	brachiocephalic	systemic_artery	1.539380	1.539380	3.400	3	4
5	subclavian_I_R	systemic_artery	1.130973	1.042305	3.400	4	5
6	carotid_R	systemic_artery	0.502655	0.502655	17.700	4	10
7	vertebral_R	systemic_artery	0.113411	0.111155	14.800	5	73
8	internal_thoracic_R	systemic_artery	0.066052	0.066052	8.000	5	78
9	subclavian_II_R	systemic_artery	0.950332	0.950332	2.500	5	6
10	thyrocervical_R	systemic_artery	0.166190	0.166190	5.000	6	74
11	axiliary_I_R	systemic_artery	0.899202	0.899202	5.000	6	7
12	subscapular_R	systemic_artery	0.113411	0.113411	4.000	7	74
13	axiliary_II_R	systemic_artery	0.817128	0.459635	34.700	7	8
14	radius_R	systemic_artery	0.101788	0.060350	23.500	8	75
15	ulnar_I_R	systemic_artery	0.196350	0.196350	6.700	8	9
16	interosseous_R	systemic_artery	0.025447	0.025447	7.900	9	75
17	ulnar_II_R	systemic_artery	0.125664	0.115812	17.100	9	75
18	internal_carotid_R	systemic_artery	0.331831	0.331831	17.600	10	72
19	external_carotid_R	systemic_artery	0.331831	0.331831	17.700	10	72
20	aortic_arch_II	systemic_artery	4.830513	4.830513	3.900	11	13
21	carotid_L	systemic_artery	0.430084	0.430084	20.800	11	12
22	internal_carotid_L	systemic_artery	0.282743	0.282743	17.600	12	72
23	external_carotid_L	systemic_artery	0.282743	0.282743	17.700	12	72
24	thoracic_aorta_I	systemic_artery	3.801327	3.147879	5.200	13	19
25	subclavian_I_L	systemic_artery	0.950332	0.857674	3.400	13	14

Table A.29 : Vessel parameters for fenestrated Fontan network.

ID	name	type	A_0 (inlet) (cm^2)	A_0 (outlet) (cm^2)	length (cm)	inlet ID	outlet ID
26	vertebral_L	systemic_artery	0.125664	0.115812	14.800	14	73
27	internal_thoracic_L	systemic_artery	0.057256	0.057256	8.000	14	78
28	sublclavian_II_L	systemic_artery	0.679291	0.679291	2.500	14	15
29	thyrocervical_L	systemic_artery	0.125664	0.125664	5.000	15	76
30	axiliary_I_L	systemic_artery	0.636173	0.636173	5.000	15	16
31	subscapular_L	systemic_artery	0.080425	0.080425	4.000	16	76
32	axiliary_II_L	systemic_artery	0.515300	0.305521	34.700	16	17
33	radius_L	systemic_artery	0.053093	0.043966	23.500	17	77
34	ulnar_I_L	systemic_artery	0.145220	0.145220	6.700	17	18
35	interosseous_L	systemic_artery	0.025447	0.025447	7.900	18	77
36	ulnar_II_L	systemic_artery	0.125664	0.118237	17.100	18	77
37	intercostals	systemic_artery	0.045239	0.045239	8.000	19	78
38	thoracic_aorta_II	systemic_artery	2.377871	1.598810	10.400	19	20
39	abdominal_aorta_I	systemic_artery	1.168987	1.168987	5.300	20	22
40	celiac	systemic_artery	0.453646	0.453646	2.000	20	21
41	hepatic	systemic_artery	0.180956	0.180956	6.600	21	79
42	splenic	systemic_artery	0.125664	0.125664	6.300	21	80
43	gastric	systemic_artery	0.264208	0.238448	7.100	21	81
44	superior_mesenteric	systemic_artery	0.282743	0.282743	5.900	22	82
45	abdominal_aorta_II	systemic_artery	1.093588	1.093588	1.000	22	23
46	renal_L	systemic_artery	0.212372	0.212372	3.200	23	84
47	abdominal_aorta_III	systemic_artery	1.020703	1.020703	1.000	23	24
48	renal_R	systemic_artery	0.212372	0.212372	3.200	24	83
49	abdominal_aorta_IV	systemic_artery	0.950332	0.875826	10.600	24	25
50	inferior_mesenteric	systemic_artery	0.080425	0.080425	5.000	25	82
51	abdominal_aorta_V	systemic_artery	0.849487	0.782887	1.000	25	26
52	common_iliac_L	systemic_artery	0.430084	0.413053	5.900	26	30
53	common_iliac_R	systemic_artery	0.430084	0.413053	5.800	26	27
54	external_iliac_L	systemic_artery	0.246301	0.236547	14.400	27	28
55	internal_iliac_L	systemic_artery	0.220618	0.220618	5.000	27	86
56	femoral_L	systemic_artery	0.196350	0.148617	44.300	28	29
57	deep_femoral_L	systemic_artery	0.070686	0.058535	12.600	28	87
58	posterior_tibial_L	systemic_artery	0.075477	0.068118	32.100	29	89
59	anterior_tibial_L	systemic_artery	0.053093	0.046913	34.300	29	89
60	external_iliac_R	systemic_artery	0.246301	0.236547	14.500	30	31

Table A.30 : Vessel parameters for fenestrated Fontan network (continued).

ID	name	type	A_0 (inlet) (cm^2)	A_0 (outlet) (cm^2)	length (cm)	inlet ID	outlet ID
61	internal_iliac_R	systemic_artery	0.220618	0.220618	5.000	30	86
62	femoral_R	systemic_artery	0.196350	0.148617	44.400	31	32
63	deep_femoral_R	systemic_artery	0.070686	0.058535	12.700	31	85
64	posterior_tibial_R	systemic_artery	0.075477	0.068118	32.200	32	88
65	anterior_tibial_R	systemic_artery	0.053093	0.046913	34.400	32	88
66	vertebral_R	systemic_vein	0.173494	0.187652	14.800	73	56
67	internal_jugular_R	systemic_vein	1.606061	1.737115	17.600	72	56
68	transverse_cervical_R	systemic_vein	0.264208	0.285767	5.000	74	55
69	external_jugular_R	systemic_vein	0.679291	0.734721	17.700	72	55
70	radius_R	systemic_vein	0.096211	0.145558	23.500	75	50
71	ulnar_II_R	systemic_vein	0.180956	0.195722	17.100	75	49
72	interosseus_R	systemic_vein	0.041548	0.041548	7.900	75	49
73	ulnar_I_R	systemic_vein	0.229022	0.229022	6.700	49	50
74	brachial_R	systemic_vein	0.395919	0.395919	20.820	50	53
75	cephalic_I_R	systemic_vein	0.017671	0.017671	11.100	75	52
76	basilic_I_R	systemic_vein	0.125664	0.125664	18.800	75	48
77	median_antebrachial_R	systemic_vein	0.070686	0.070686	18.800	75	48
78	basilic_II_R	systemic_vein	0.166190	0.166190	4.700	48	51
79	median_cubital_R	systemic_vein	0.407150	0.407150	8.850	52	51
80	cephalic_II_R	systemic_vein	0.418539	0.418539	36.610	52	54
81	basilic_III_R	systemic_vein	0.196350	0.196350	20.820	51	53
82	subscapular_R	systemic_vein	0.220618	0.238621	4.000	74	54
83	axiliary_R	systemic_vein	0.528102	0.528102	6.940	53	54
84	subclavian_R	systemic_vein	0.801185	0.801185	5.200	54	55
85	brachiocephalic_I_R	systemic_vein	1.227185	1.227185	3.400	55	56
86	brachiocephalic_II_R	systemic_vein	2.405282	2.910391	4.000	56	66
87	vertebral_L	systemic_vein	0.180956	0.195722	17.100	73	65
88	internal_jugular_L	systemic_vein	1.188229	1.285188	17.600	72	65
89	transverse_cervical_L	systemic_vein	0.196350	0.212372	5.000	76	64
90	external_jugular_L	systemic_vein	0.502655	0.543671	17.100	72	64
91	radius_L	systemic_vein	0.070686	0.083982	10.400	77	59
92	ulnar_II_L	systemic_vein	0.188574	0.200058	17.100	77	57
93	interosseus_L	systemic_vein	0.041548	0.041548	7.900	77	57
94	ulnar_I_L	systemic_vein	0.229022	0.229022	6.700	57	59
95	brachial_L	systemic_vein	0.395919	0.395919	20.820	59	62

Table A.31 : Vessel parameters for fenestrated Fontan network (continued).

ID	name	type	A_0 (inlet) (cm^2)	A_0 (outlet) (cm^2)	length (cm)	inlet ID	outlet ID
96	cephalic_I_L	systemic_vein	0.017671	0.017671	11.100	77	60
97	basilic_I_L	systemic_vein	0.125664	0.125664	18.800	77	58
98	median_antebrachial_L	systemic_vein	0.070686	0.070686	18.800	77	58
99	basilic_II_L	systemic_vein	0.166190	0.166190	4.700	58	61
100	median_cubital_L	systemic_vein	0.407150	0.407150	8.850	61	60
101	cephalic_II_L	systemic_vein	0.418539	0.418539	36.610	60	63
102	basilic_III_L	systemic_vein	0.196350	0.196350	20.820	61	62
103	subscapular_L	systemic_vein	0.159043	0.172021	4.000	76	63
104	axiliary_L	systemic_vein	0.528102	0.528102	6.940	62	63
105	subclavian_L	systemic_vein	0.801185	0.801185	5.200	63	64
106	brachiocephalic_I_L	systemic_vein	1.149901	1.149901	3.400	64	65
107	brachiocephalic_II_L	systemic_vein	1.985565	2.402534	6.000	65	66
108	superior_vena_cava_I	systemic_vein	3.801327	4.599606	2.000	66	67
109	azygous	systemic_vein	0.515300	0.623513	15.000	78	67
110	superior_vena_cava_II	systemic_vein	3.986078	4.811055	4.000	67	71
111	posterior_tibial_R	systemic_vein	0.107521	0.118542	32.200	88	33
112	anterior_tibial_R	systemic_vein	0.075477	0.084806	34.400	88	33
113	small_saphenous_R	systemic_vein	0.080425	0.111983	34.400	88	34
114	great_saphenous_R	systemic_vein	0.113411	0.203642	78.800	88	36
115	popliteal_R	systemic_vein	0.125664	0.125664	16.100	33	34
116	femoral_I_R	systemic_vein	0.229022	0.292438	39.960	34	35
117	deep_femoral_R	systemic_vein	0.113411	0.113411	12.700	85	35
118	femoral_II_R	systemic_vein	0.352565	0.352565	4.440	35	36
119	external_iliac_R	systemic_vein	0.373928	0.389035	14.500	36	37
120	internal_iliac_R	systemic_vein	0.384845	0.384845	5.000	86	37
121	common_iliac_R	systemic_vein	0.636173	0.661874	5.900	37	43
122	posterior_tibial_L	systemic_vein	0.107521	0.118542	32.200	89	38
123	anterior_tibial_L	systemic_vein	0.075477	0.084806	34.400	89	38
124	small_saphenous_L	systemic_vein	0.080425	0.111983	34.400	89	39
125	great_saphenous_L	systemic_vein	0.113411	0.203642	78.800	89	41
126	popliteal_L	systemic_vein	0.125664	0.125664	16.100	38	39
127	femoral_I_L	systemic_vein	0.229022	0.292438	44.300	39	40
128	deep_femoral_L	systemic_vein	0.113411	0.113411	12.600	87	40
129	femoral_II_L	systemic_vein	0.352565	0.352565	4.440	40	41
130	external_iliac_L	systemic_vein	0.373928	0.389035	14.400	41	42

Table A.32 : Vessel parameters for fenestrated Fontan network (continued).

ID	name	type	A_0 (inlet) (cm^2)	A_0 (outlet) (cm^2)	length (cm)	inlet ID	outlet ID
131	internal_iliac_L	systemic_vein	0.342119	0.342119	5.000	86	42
132	common_iliac_L	systemic_vein	0.636173	0.661874	5.800	42	43
133	inferior_vena_cava_I	systemic_vein	1.474114	1.751395	11.600	43	44
134	renal_R	systemic_vein	0.331831	0.331831	3.200	83	44
135	inferior_vena_cava_II	systemic_vein	1.495712	1.495712	1.000	44	45
136	renal_L	systemic_vein	0.331831	0.331831	3.200	84	45
137	inferior_vena_cava_III	systemic_vein	1.697167	1.697167	2.000	45	46
138	right_hepatic	systemic_vein	0.785398	0.785398	6.600	79	46
139	left_hepatic	systemic_vein	0.580880	0.580880	3.300	79	47
140	middle_hepatic	systemic_vein	0.594468	0.594468	4.800	79	47
141	common_hepatic	systemic_vein	1.452672	1.452672	1.200	47	46
142	inferior_vena_cava_IV	systemic_vein	4.908739	4.500000	3.500	46	92
143	splenic	portal_vein	0.363168	0.363168	6.300	80	68
144	inferior_mesenteric_I	portal_vein	0.125664	0.125664	7.000	82	68
145	inferior_mesenteric_II	portal_vein	0.418539	0.707330	1.000	68	69
146	superior_mesenteric	portal_vein	0.441786	0.441786	5.900	82	69
147	hepatic_portal_I	portal_vein	0.664761	0.664761	2.000	69	70
148	gastric	portal_vein	0.107521	0.107521	1.000	81	70
149	hepatic_portal_II	portal_vein	1.093588	1.093588	3.000	70	79
150	pulmonary_artery_L	pulmonary_artery	2.986477	2.986477	2.800	71	90
151	pulmonary_artery_R	pulmonary_artery	4.337361	4.337361	4.100	71	91
152	lower_pulmonary_R	pulmonary_vein	1.517468	1.517468	13.000	91	0
153	upper_pulmonary_R	pulmonary_vein	1.306981	1.306981	13.000	91	0
154	lower_pulmonary_L	pulmonary_vein	1.168987	1.168987	13.000	90	0
155	upper_pulmonary_L	pulmonary_vein	1.246898	1.246898	13.000	90	0
156	inferior_vena_cava_V	systemic_vein	4.500000	3.976078	3.500	92	71
157	fenestration_tube_I	systemic_vein	0.502700	0.502700	0.500	92	93
158	fenestration_tube_II	pulmonary_vein	0.502700	0.502700	0.500	93	0

Table A.33 : Vessel parameters for fenestrated Fontan network (continued).

	k_1 (dynes/cm^2)	k_2	k_3 (dynes/cm^2)	p_0 (dynes/cm^2)
systemic_artery	1.000e+05	-2.970e+00	1.500e+05	1.2000e+05
systemic_vein	3.000e+05	-1.188e+01	1.500e+04	1.2000e+04
pulmonary_artery	2.000e+05	-1.485e+01	3.000e+05	1.2000e+04
pulmonary_vein	3.000e+05	-1.485e+01	4.000e+05	9.0000e+03
portal_vein	1.000e+05	-7.425e+00	5.000e+03	1.2000e+04

Table A.34 : Parameters for each class of vessels in the fenestrated Fontan network.

node ID	model name
0	right_heart_with_valves_semi_implicit
72	head
73	neck
74	R_shoulder
75	R_arm
76	L_shoulder
77	L_arm
78	thorax
79	liver
80	spleen
81	stomach
82	intestines
83	R_kidney
84	L_kidney
85	R_thigh
86	pelvic_region
87	L_thigh
88	R_lower_leg
89	L_lower_leg
90	L_lung
91	R_lung
93	fenestration_bed

Table A.35 : Node IDs and model names for the fenestrated Fontan network. Nodes with IDs 1–71 and 92 are interior nodes.

	V_0 (mL)	$V(t=0)$ (mL)	$E_{\min}$ $\left(\frac{\text{dynes}}{\text{cm}^2}\right)$	$E_{\max}$ $\left(\frac{\text{dynes}}{\text{cm}^2}\right)$	m_1	m_2	τ_1	τ_2	K $\left(\frac{\text{s}}{\text{mL}}\right)$	t_{onset} (s)
ventricle	4.800e+01	1.500e+02	1.000e+03	3.000e+05	3.000e+00	2.700e+01	2.690e-01	4.520e-01	5.000e-04	0.000e+00
atrium	2.500e+01	8.000e+01	1.000e+03	1.500e+04	2.000e+00	1.300e+01	1.100e-01	1.800e-01	1.000e-04	8.500e-01

Table A.36 : Parameters for the right heart in the fenestrated Fontan circulation.

	B $\left(\frac{\text{dynes}\cdot\text{s}^2}{\text{cm}^5}\right)$	L $\left(\frac{\text{dynes}\cdot\text{s}^2}{\text{cm}^5}\right)$	R $\left(\frac{\text{dynes}\cdot\text{s}}{\text{cm}^5}\right)$	γ $\left(\frac{\text{cm}^2}{\text{dynes}}\right)$
interior	1.000e-02	5.000e-03	1.000e-03	5.000e-03
exterior	5.000e-03	5.000e-03	1.000e-03	3.000e-03

Table A.37 : Parameters for the valves in the fenestrated Fontan circulation.

	C_{art} $\left(\frac{\text{cm}^5}{\text{dynes}}\right)$	R_{cap} $\left(\frac{\text{dynes·s}}{\text{cm}^5}\right)$	C_{ven} $\left(\frac{\text{cm}^5}{\text{dynes}}\right)$	V_{ref} (mL)
head	3.000e-05	5.000e+03	3.000e-04	1.200e+02
neck	4.000e-05	1.000e+04	4.000e-04	8.000e+01
R_shoulder	1.500e-05	2.000e+04	1.500e-04	1.200e+02
R_arm	2.000e-05	1.500e+04	2.000e-04	1.200e+02
L_shoulder	1.500e-05	2.000e+04	1.500e-04	1.200e+02
L_arm	2.000e-05	1.500e+04	2.000e-04	1.200e+02
thorax	1.000e-04	4.000e+03	1.000e-03	1.000e+02
spleen	4.000e-05	3.500e+04	4.000e-04	7.000e+01
stomach	2.000e-05	4.000e+04	2.000e-04	7.000e+01
intestines	1.000e-04	3.000e+03	1.000e-03	2.500e+02
R_kidney	1.000e-04	2.500e+03	1.000e-03	1.300e+02
L_kidney	1.000e-04	2.500e+03	1.000e-03	1.300e+02
R_thigh	3.000e-05	1.500e+04	3.000e-04	1.700e+02
pelvic_region	3.000e-05	1.500e+04	3.000e-04	1.600e+02
L_thigh	3.000e-05	1.500e+04	3.000e-04	1.700e+02
R_lower_leg	5.000e-05	1.000e+04	5.000e-04	8.500e+01
L_lower_leg	5.000e-05	1.000e+04	5.000e-04	8.500e+01
L_lung	1.000e-03	4.500e+01	2.000e-03	7.000e+02
R_lung	1.000e-03	4.000e+01	2.000e-03	7.000e+02
fenestration_bed	0.000e+00	1.000e+01	0.000e+00	5.000e+00

Table A.38 : Parameters for the organ beds in the fenestrated Fontan circulation.

R_{int} $\left(\frac{\text{dynes·s}}{\text{cm}^5}\right)$	R_{cap} $\left(\frac{\text{dynes·s}}{\text{cm}^5}\right)$	C_{int} $\left(\frac{\text{cm}^5}{\text{dynes}}\right)$	C_{portal} $\left(\frac{\text{cm}^5}{\text{dynes}}\right)$	C_{ven} $\left(\frac{\text{cm}^5}{\text{dynes}}\right)$	V_{ref} (mL)
2.000e+04	2.000e+02	5.000e-05	5.000e-04	5.000e-04	4.250e+02

Table A.39 : Parameters for the liver in the fenestrated Fontan circulation.

A.5 Fontan with hepatic exclusion parameters

ID	name	type	A_0 (inlet) (cm^2)	A_0 (outlet) (cm^2)	length (cm)	inlet ID	outlet ID
0	lv_outflow_tract	systemic_artery	6.927919	6.927919	1.000	0	1
1	aortic_root	systemic_artery	6.927919	6.927919	1.000	1	2
2	ascending_aorta	systemic_artery	6.788668	6.788668	4.000	2	3
3	aortic_arch_I	systemic_artery	5.227924	5.227924	2.000	3	11
4	brachiocephalic	systemic_artery	1.539380	1.539380	3.400	3	4
5	subclavian_I_R	systemic_artery	1.130973	1.042305	3.400	4	5
6	carotid_R	systemic_artery	0.502655	0.502655	17.700	4	10
7	vertebral_R	systemic_artery	0.113411	0.111155	14.800	5	73
8	internal_thoracic_R	systemic_artery	0.066052	0.066052	8.000	5	78
9	subclavian_II_R	systemic_artery	0.950332	0.950332	2.500	5	6
10	thyrocervical_R	systemic_artery	0.166190	0.166190	5.000	6	74
11	axiliary_I_R	systemic_artery	0.899202	0.899202	5.000	6	7
12	subscapular_R	systemic_artery	0.113411	0.113411	4.000	7	74
13	axiliary_II_R	systemic_artery	0.817128	0.459635	34.700	7	8
14	radius_R	systemic_artery	0.101788	0.060350	23.500	8	75
15	ulnar_I_R	systemic_artery	0.196350	0.196350	6.700	8	9
16	interosseous_R	systemic_artery	0.025447	0.025447	7.900	9	75
17	ulnar_II_R	systemic_artery	0.125664	0.115812	17.100	9	75
18	internal_carotid_R	systemic_artery	0.331831	0.331831	17.600	10	72
19	external_carotid_R	systemic_artery	0.331831	0.331831	17.700	10	72
20	aortic_arch_II	systemic_artery	4.830513	4.830513	3.900	11	13
21	carotid_L	systemic_artery	0.430084	0.430084	20.800	11	12
22	internal_carotid_L	systemic_artery	0.282743	0.282743	17.600	12	72
23	external_carotid_L	systemic_artery	0.282743	0.282743	17.700	12	72
24	thoracic_aorta_I	systemic_artery	3.801327	3.147879	5.200	13	19
25	subclavian_I_L	systemic_artery	0.950332	0.857674	3.400	13	14

Table A.40 : Vessel parameters for Fontan with hepatic exclusion network.

ID	name	type	A_0 (inlet) (cm^2)	A_0 (outlet) (cm^2)	length (cm)	inlet ID	outlet ID
26	vertebral_L	systemic_artery	0.125664	0.115812	14.800	14	73
27	internal_thoracic_L	systemic_artery	0.057256	0.057256	8.000	14	78
28	sublclavian_II_L	systemic_artery	0.679291	0.679291	2.500	14	15
29	thyrocervical_L	systemic_artery	0.125664	0.125664	5.000	15	76
30	axiliary_I_L	systemic_artery	0.636173	0.636173	5.000	15	16
31	subscapular_L	systemic_artery	0.080425	0.080425	4.000	16	76
32	axiliary_II_L	systemic_artery	0.515300	0.305521	34.700	16	17
33	radius_L	systemic_artery	0.053093	0.043966	23.500	17	77
34	ulnar_I_L	systemic_artery	0.145220	0.145220	6.700	17	18
35	interosseous_L	systemic_artery	0.025447	0.025447	7.900	18	77
36	ulnar_II_L	systemic_artery	0.125664	0.118237	17.100	18	77
37	intercostals	systemic_artery	0.045239	0.045239	8.000	19	78
38	thoracic_aorta_II	systemic_artery	2.377871	1.598810	10.400	19	20
39	abdominal_aorta_I	systemic_artery	1.168987	1.168987	5.300	20	22
40	celiac	systemic_artery	0.453646	0.453646	2.000	20	21
41	hepatic	systemic_artery	0.180956	0.180956	6.600	21	79
42	splenic	systemic_artery	0.125664	0.125664	6.300	21	80
43	gastric	systemic_artery	0.264208	0.238448	7.100	21	81
44	superior_mesenteric	systemic_artery	0.282743	0.282743	5.900	22	82
45	abdominal_aorta_II	systemic_artery	1.093588	1.093588	1.000	22	23
46	renal_L	systemic_artery	0.212372	0.212372	3.200	23	84
47	abdominal_aorta_III	systemic_artery	1.020703	1.020703	1.000	23	24
48	renal_R	systemic_artery	0.212372	0.212372	3.200	24	83
49	abdominal_aorta_IV	systemic_artery	0.950332	0.875826	10.600	24	25
50	inferior_mesenteric	systemic_artery	0.080425	0.080425	5.000	25	82
51	abdominal_aorta_V	systemic_artery	0.849487	0.782887	1.000	25	26
52	common_iliac_L	systemic_artery	0.430084	0.413053	5.900	26	30
53	common_iliac_R	systemic_artery	0.430084	0.413053	5.800	26	27
54	external_iliac_L	systemic_artery	0.246301	0.236547	14.400	27	28
55	internal_iliac_L	systemic_artery	0.220618	0.220618	5.000	27	86
56	femoral_L	systemic_artery	0.196350	0.148617	44.300	28	29
57	deep_femoral_L	systemic_artery	0.070686	0.058535	12.600	28	87
58	posterior_tibial_L	systemic_artery	0.075477	0.068118	32.100	29	89
59	anterior_tibial_L	systemic_artery	0.053093	0.046913	34.300	29	89
60	external_iliac_R	systemic_artery	0.246301	0.236547	14.500	30	31

Table A.41 : Vessel parameters for Fontan with hepatic exclusion network (continued).

ID	name	type	A_0 (inlet) (cm^2)	A_0 (outlet) (cm^2)	length (cm)	inlet ID	outlet ID
61	internal_iliac_R	systemic_artery	0.220618	0.220618	5.000	30	86
62	femoral_R	systemic_artery	0.196350	0.148617	44.400	31	32
63	deep_femoral_R	systemic_artery	0.070686	0.058535	12.700	31	85
64	posterior_tibial_R	systemic_artery	0.075477	0.068118	32.200	32	88
65	anterior_tibial_R	systemic_artery	0.053093	0.046913	34.400	32	88
66	vertebral_R	systemic_vein	0.173494	0.187652	14.800	73	56
67	internal_jugular_R	systemic_vein	1.606061	1.737115	17.600	72	56
68	transverse_cervical_R	systemic_vein	0.264208	0.285767	5.000	74	55
69	external_jugular_R	systemic_vein	0.679291	0.734721	17.700	72	55
70	radius_R	systemic_vein	0.096211	0.145558	23.500	75	50
71	ulnar_II_R	systemic_vein	0.180956	0.195722	17.100	75	49
72	interosseus_R	systemic_vein	0.041548	0.041548	7.900	75	49
73	ulnar_I_R	systemic_vein	0.229022	0.229022	6.700	49	50
74	brachial_R	systemic_vein	0.395919	0.395919	20.820	50	53
75	cephalic_I_R	systemic_vein	0.017671	0.017671	11.100	75	52
76	basilic_I_R	systemic_vein	0.125664	0.125664	18.800	75	48
77	median_antebrachial_R	systemic_vein	0.070686	0.070686	18.800	75	48
78	basilic_II_R	systemic_vein	0.166190	0.166190	4.700	48	51
79	median_cubital_R	systemic_vein	0.407150	0.407150	8.850	52	51
80	cephalic_II_R	systemic_vein	0.418539	0.418539	36.610	52	54
81	basilic_III_R	systemic_vein	0.196350	0.196350	20.820	51	53
82	subscapular_R	systemic_vein	0.220618	0.238621	4.000	74	54
83	axiliary_R	systemic_vein	0.528102	0.528102	6.940	53	54
84	subclavian_R	systemic_vein	0.801185	0.801185	5.200	54	55
85	brachiocephalic_I_R	systemic_vein	1.227185	1.227185	3.400	55	56
86	brachiocephalic_II_R	systemic_vein	2.405282	2.910391	4.000	56	66
87	vertebral_L	systemic_vein	0.180956	0.195722	17.100	73	65
88	internal_jugular_L	systemic_vein	1.188229	1.285188	17.600	72	65
89	transverse_cervical_L	systemic_vein	0.196350	0.212372	5.000	76	64
90	external_jugular_L	systemic_vein	0.502655	0.543671	17.100	72	64
91	radius_L	systemic_vein	0.070686	0.083982	10.400	77	59
92	ulnar_II_L	systemic_vein	0.188574	0.200058	17.100	77	57
93	interosseus_L	systemic_vein	0.041548	0.041548	7.900	77	57
94	ulnar_I_L	systemic_vein	0.229022	0.229022	6.700	57	59
95	brachial_L	systemic_vein	0.395919	0.395919	20.820	59	62

Table A.42 : Vessel parameters for Fontan with hepatic exclusion network (continued).

ID	name	type	A_0 (inlet) (cm^2)	A_0 (outlet) (cm^2)	length (cm)	inlet ID	outlet ID
96	cephalic_I_L	systemic_vein	0.017671	0.017671	11.100	77	60
97	basilic_I_L	systemic_vein	0.125664	0.125664	18.800	77	58
98	median_antebrachial_L	systemic_vein	0.070686	0.070686	18.800	77	58
99	basilic_II_L	systemic_vein	0.166190	0.166190	4.700	58	61
100	median_cubital_L	systemic_vein	0.407150	0.407150	8.850	61	60
101	cephalic_II_L	systemic_vein	0.418539	0.418539	36.610	60	63
102	basilic_III_L	systemic_vein	0.196350	0.196350	20.820	61	62
103	subscapular_L	systemic_vein	0.159043	0.172021	4.000	76	63
104	axiliary_L	systemic_vein	0.528102	0.528102	6.940	62	63
105	subclavian_L	systemic_vein	0.801185	0.801185	5.200	63	64
106	brachiocephalic_I_L	systemic_vein	1.149901	1.149901	3.400	64	65
107	brachiocephalic_II_L	systemic_vein	1.985565	2.402534	6.000	65	66
108	superior_vena_cava_I	systemic_vein	3.801327	4.599606	2.000	66	67
109	azygous	systemic_vein	0.515300	0.623513	15.000	78	67
110	superior_vena_cava_II	systemic_vein	3.986078	4.811055	4.000	67	71
111	posterior_tibial_R	systemic_vein	0.107521	0.118542	32.200	88	33
112	anterior_tibial_R	systemic_vein	0.075477	0.084806	34.400	88	33
113	small_saphenous_R	systemic_vein	0.080425	0.111983	34.400	88	34
114	great_saphenous_R	systemic_vein	0.113411	0.203642	78.800	88	36
115	popliteal_R	systemic_vein	0.125664	0.125664	16.100	33	34
116	femoral_I_R	systemic_vein	0.229022	0.292438	39.960	34	35
117	deep_femoral_R	systemic_vein	0.113411	0.113411	12.700	85	35
118	femoral_II_R	systemic_vein	0.352565	0.352565	4.440	35	36
119	external_iliac_R	systemic_vein	0.373928	0.389035	14.500	36	37
120	internal_iliac_R	systemic_vein	0.384845	0.384845	5.000	86	37
121	common_iliac_R	systemic_vein	0.636173	0.661874	5.900	37	43
122	posterior_tibial_L	systemic_vein	0.107521	0.118542	32.200	89	38
123	anterior_tibial_L	systemic_vein	0.075477	0.084806	34.400	89	38
124	small_saphenous_L	systemic_vein	0.080425	0.111983	34.400	89	39
125	great_saphenous_L	systemic_vein	0.113411	0.203642	78.800	89	41
126	popliteal_L	systemic_vein	0.125664	0.125664	16.100	38	39
127	femoral_I_L	systemic_vein	0.229022	0.292438	44.300	39	40
128	deep_femoral_L	systemic_vein	0.113411	0.113411	12.600	87	40
129	femoral_II_L	systemic_vein	0.352565	0.352565	4.440	40	41
130	external_iliac_L	systemic_vein	0.373928	0.389035	14.400	41	42

Table A.43 : Vessel parameters for Fontan with hepatic exclusion network (continued).

ID	name	type	A_0 (inlet) (cm^2)	A_0 (outlet) (cm^2)	length (cm)	inlet ID	outlet ID
131	internal_iliac_L	systemic_vein	0.342119	0.342119	5.000	86	42
132	common_iliac_L	systemic_vein	0.636173	0.661874	5.800	42	43
133	inferior_vena_cava_I	systemic_vein	1.474114	1.751395	11.600	43	44
134	renal_R	systemic_vein	0.331831	0.331831	3.200	83	44
135	inferior_vena_cava_II	systemic_vein	1.495712	1.495712	1.000	44	45
136	renal_L	systemic_vein	0.331831	0.331831	3.200	84	45
137	inferior_vena_cava_III	systemic_vein	1.697167	1.697167	2.000	45	46
138	right_hepatic	systemic_vein	0.785398	0.785398	6.600	79	0
139	left_hepatic	systemic_vein	0.580880	0.580880	3.300	79	47
140	middle_hepatic	systemic_vein	0.594468	0.594468	4.800	79	47
141	common_hepatic	systemic_vein	1.452672	1.452672	1.200	47	0
142	inferior_vena_cava_IV	systemic_vein	4.908739	3.976078	7.000	46	71
143	splenic	portal_vein	0.363168	0.363168	6.300	80	68
144	inferior_mesenteric_I	portal_vein	0.125664	0.125664	7.000	82	68
145	inferior_mesenteric_II	portal_vein	0.418539	0.707330	1.000	68	69
146	superior_mesenteric	portal_vein	0.441786	0.441786	5.900	82	69
147	hepatic_portal_I	portal_vein	0.664761	0.664761	2.000	69	70
148	gastric	portal_vein	0.107521	0.107521	1.000	81	70
149	hepatic_portal_II	portal_vein	1.093588	1.093588	3.000	70	79
150	pulmonary_artery_L	pulmonary_artery	2.986477	2.986477	2.800	71	90
151	pulmonary_artery_R	pulmonary_artery	4.337361	4.337361	4.100	71	91
152	lower_pulmonary_R	pulmonary_vein	1.517468	1.517468	13.000	91	0
153	upper_pulmonary_R	pulmonary_vein	1.306981	1.306981	13.000	91	0
154	lower_pulmonary_L	pulmonary_vein	1.168987	1.168987	13.000	90	0
155	upper_pulmonary_L	pulmonary_vein	1.246898	1.246898	13.000	90	0

Table A.44 : Vessel parameters for Fontan with hepatic exclusion network (continued).

	k_1 (dynes/cm^2)	k_2	k_3 (dynes/cm^2)	p_0 (dynes/cm^2)
systemic_artery	1.000e+05	-2.970e+00	1.500e+05	1.2000e+05
systemic_vein	3.000e+05	-1.188e+01	1.500e+04	1.2000e+04
pulmonary_artery	2.000e+05	-1.485e+01	3.000e+05	1.2000e+04
pulmonary_vein	3.000e+05	-1.485e+01	4.000e+05	9.0000e+03
portal_vein	1.000e+05	-7.425e+00	5.000e+03	1.2000e+04

Table A.45 : Parameters for each class of vessels in the Fontan with hepatic exclusion network.

node ID	model name
0	right_heart_with_valves_semi_implicit
72	head
73	neck
74	R_shoulder
75	R_arm
76	L_shoulder
77	L_arm
78	thorax
79	liver
80	spleen
81	stomach
82	intestines
83	R_kidney
84	L_kidney
85	R_thigh
86	pelvic_region
87	L_thigh
88	R_lower_leg
89	L_lower_leg
90	L_lung
91	R_lung

Table A.46 : Node IDs and model names for the Fontan with hepatic exclusion network. Nodes with IDs 1–71 are interior nodes.

	V_0 (mL)	$V(t=0)$ (mL)	$E_{\min}$ $\left(\frac{\text{dynes}}{\text{cm}^2}\right)$	$E_{\max}$ $\left(\frac{\text{dynes}}{\text{cm}^2}\right)$	m_1	m_2	τ_1	τ_2	K $\left(\frac{\text{s}}{\text{mL}}\right)$	t_{onset} (s)
ventricle	4.800e+01	1.500e+02	1.000e+03	3.000e+05	3.000e+00	2.700e+01	2.690e-01	4.520e-01	5.000e-04	0.000e+00
atrium	2.500e+01	8.000e+01	1.000e+03	1.500e+04	2.000e+00	1.300e+01	1.100e-01	1.800e-01	1.000e-04	8.500e-01

Table A.47 : Parameters for the right heart in the Fontan with hepatic exclusion circulation.

	B $\left(\frac{\text{dynes}\cdot\text{s}^2}{\text{cm}^5}\right)$	L $\left(\frac{\text{dynes}\cdot\text{s}^2}{\text{cm}^5}\right)$	R $\left(\frac{\text{dynes}\cdot\text{s}}{\text{cm}^5}\right)$	γ $\left(\frac{\text{cm}^2}{\text{dynes}}\right)$
interior	1.000e-02	5.000e-03	1.000e-03	5.000e-03
exterior	5.000e-03	5.000e-03	1.000e-03	3.000e-03

Table A.48 : Parameters for the valves in the Fontan with hepatic exclusion circulation.

	C_{art} $\left(\frac{\text{cm}^5}{\text{dynes}}\right)$	R_{cap} $\left(\frac{\text{dynes·s}}{\text{cm}^5}\right)$	C_{ven} $\left(\frac{\text{cm}^5}{\text{dynes}}\right)$	V_{ref} (mL)
head	3.000e-05	5.000e+03	3.000e-04	1.200e+02
neck	4.000e-05	1.000e+04	4.000e-04	8.000e+01
R_shoulder	1.500e-05	2.000e+04	1.500e-04	1.200e+02
R_arm	2.000e-05	1.500e+04	2.000e-04	1.200e+02
L_shoulder	1.500e-05	2.000e+04	1.500e-04	1.200e+02
L_arm	2.000e-05	1.500e+04	2.000e-04	1.200e+02
thorax	1.000e-04	4.000e+03	1.000e-03	1.000e+02
spleen	4.000e-05	3.500e+04	4.000e-04	7.000e+01
stomach	2.000e-05	4.000e+04	2.000e-04	7.000e+01
intestines	1.000e-04	3.000e+03	1.000e-03	2.500e+02
R_kidney	1.000e-04	2.500e+03	1.000e-03	1.300e+02
L_kidney	1.000e-04	2.500e+03	1.000e-03	1.300e+02
R_thigh	3.000e-05	1.500e+04	3.000e-04	1.700e+02
pelvic_region	3.000e-05	1.500e+04	3.000e-04	1.600e+02
L_thigh	3.000e-05	1.500e+04	3.000e-04	1.700e+02
R_lower_leg	5.000e-05	1.000e+04	5.000e-04	8.500e+01
L_lower_leg	5.000e-05	1.000e+04	5.000e-04	8.500e+01
L_lung	1.000e-03	4.500e+01	2.000e-03	7.000e+02
R_lung	1.000e-03	4.000e+01	2.000e-03	7.000e+02

Table A.49 : Parameters for the organ beds in the Fontan with hepatic exclusion circulation.

R_{int} $\left(\frac{\text{dynes·s}}{\text{cm}^5}\right)$	R_{cap} $\left(\frac{\text{dynes·s}}{\text{cm}^5}\right)$	C_{int} $\left(\frac{\text{cm}^5}{\text{dynes}}\right)$	C_{portal} $\left(\frac{\text{cm}^5}{\text{dynes}}\right)$	C_{ven} $\left(\frac{\text{cm}^5}{\text{dynes}}\right)$	V_{ref} (mL)
2.000e+04	2.000e+02	5.000e-05	5.000e-04	5.000e-04	4.250e+02

Table A.50 : Parameters for the liver in the Fontan with hepatic exclusion circulation.

Bibliography

[1] A. Marshall, "Hypoplastic left heart syndrome," *uptodate.com*, 2015.

[2] J. Mynard, M. Davidson, D. Penny, and J. Smolich, "A simple, versatile valve model for use in lumped parameter and one-dimensional cardiovascular models," *International Journal for Numerical Methods in Biomedical Engineering*, vol. 28, no. 6-7, pp. 626–641, 2012.

[3] J. P. Mynard, *Computer modelling and wave intensity analysis of perinatal cardiovascular function and dysfunction*. PhD thesis, University of Melbourne and Murdoch Childrens Research Institute, 2011.

[4] S. Sherwin, L. Formaggia, J. Peiro, and V. Franke, "Computational modelling of 1D blood flow with variable mechanical properties and its application to the simulation of wave propagation in the human arterial system," *International Journal for Numerical Methods in Fluids*, vol. 43, no. 6-7, pp. 673–700, 2003.

[5] J. W. Remington and E. H. Wood, "Formation of peripheral pulse contour in man," *Journal of Applied Physiology*, vol. 9, no. 3, pp. 433–442, 1956.

[6] J. Rychik, "Protein-losing enteropathy after Fontan operation," *Congenital Heart Disease*, vol. 2, no. 5, pp. 288–300, 2007.

[7] T. J. Hughes, *A Study of the One-Dimensional Theory of Arterial Pulse Propagation*. PhD thesis, University of California, Berkeley, 1974.

[8] S. Čanić and E. H. Kim, "Mathematical analysis of the quasilinear effects in a hyperbolic model blood flow through compliant axi-symmetric vessels," *Mathematical Methods in the Applied Sciences*, vol. 26, no. 14, pp. 1161–1186, 2003.

[9] L. Formaggia, J.-F. Gerbeau, F. Nobile, and A. Quarteroni, "On the coupling of 3D and 1D Navier–Stokes equations for flow problems in compliant vessels," *Computer Methods in Applied Mechanics and Engineering*, vol. 191, no. 6, pp. 561–582, 2001.

[10] M. Á. Fernández, V. Milisic, and A. Quarteroni, "Analysis of a geometrical multiscale blood flow model based on the coupling of ODEs and hyperbolic PDEs," *Multiscale Modeling & Simulation*, vol. 4, no. 1, pp. 215–236, 2005.

[11] M. S. Olufsen, C. S. Peskin, W. Y. Kim, E. M. Pedersen, A. Nadim, and J. Larsen, "Numerical simulation and experimental validation of blood flow in arteries with structured-tree outflow conditions," *Annals of Biomedical Engineering*, vol. 28, no. 11, pp. 1281–1299, 2000.

[12] J. Mynard and P. Nithiarasu, "A 1D arterial blood flow model incorporating ventricular pressure, aortic valve and regional coronary flow using the locally conservative Galerkin (LCG) method," *Communications in Numerical Methods in Engineering*, vol. 24, no. 5, pp. 367–417, 2008.

[13] J. P. Mynard and J. J. Smolich, "One-dimensional haemodynamic modeling and wave dynamics in the entire adult circulation," *Annals of Biomedical Engineering*, vol. 43, no. 6, pp. 1443–1460, 2015.

[14] A. L. Marsden, I. E. Vignon-Clementel, F. P. Chan, J. A. Feinstein, and C. A. Taylor, "Effects of exercise and respiration on hemodynamic efficiency in CFD

simulations of the total cavopulmonary connection," *Annals of Biomedical Engineering*, vol. 35, no. 2, pp. 250–263, 2007.

[15] I. E. Vignon-Clementel, C. A. Figueroa, K. E. Jansen, and C. A. Taylor, "Outflow boundary conditions for three-dimensional finite element modeling of blood flow and pressure in arteries," *Computer Methods in Applied Mechanics and Engineering*, vol. 195, no. 29, pp. 3776–3796, 2006.

[16] J. Lambert, *Fluid Flow in a Nonrigid Tube.* PhD thesis, Purdue University, 1956.

[17] L. Formaggia, F. Nobile, and A. Quarteroni, "A one dimensional model for blood flow: application to vascular prosthesis," in *Mathematical Modeling and Numerical Simulation in Continuum Mechanics*, pp. 137–153, Springer, 2002.

[18] L. Formaggia, D. Lamponi, and A. Quarteroni, "One-dimensional models for blood flow in arteries," *Journal of Engineering Mathematics*, vol. 47, no. 3-4, pp. 251–276, 2003.

[19] A. Quarteroni and A. Veneziani, "Analysis of a geometrical multiscale model based on the coupling of ODE and PDE for blood flow simulations," *Multiscale Modeling & Simulation*, vol. 1, no. 2, pp. 173–195, 2003.

[20] B. Cockburn, S.-Y. Lin, and C.-W. Shu, "TVB Runge-Kutta local projection discontinuous Galerkin finite element method for conservation laws III: one-dimensional systems," *Journal of Computational Physics*, vol. 84, no. 1, pp. 90–113, 1989.

[21] P. Blanco and R. Feijóo, "A dimensionally-heterogeneous closed-loop model for

the cardiovascular system and its applications," *Medical Engineering & Physics*, vol. 35, no. 5, pp. 652–667, 2013.

[22] P. Lax and B. Wendroff, "Systems of conservation laws," *Communications on Pure and Applied Mathematics*, vol. 13, pp. 217–237, 1960.

[23] P. Reymond, F. Merenda, F. Perren, D. Rüfenacht, and N. Stergiopulos, "Validation of a one-dimensional model of the systemic arterial tree," *American Journal of Physiology-Heart and Circulatory Physiology*, vol. 297, no. 1, pp. H208–H222, 2009.

[24] N. Westerhof, F. Bosman, C. J. De Vries, and A. Noordergraaf, "Analog studies of the human systemic arterial tree," *Journal of Biomechanics*, vol. 2, no. 2, pp. 121–143, 1969.

[25] N. Stergiopulos, D. Young, and T. Rogge, "Computer simulation of arterial flow with applications to arterial and aortic stenoses," *Journal of Biomechanics*, vol. 25, no. 12, pp. 1477–1488, 1992.

[26] C. Thomas and P. Nithiarasu, "An element-wise, locally conservative Galerkin (LCG) method for solving diffusion and convection–diffusion problems," *International Journal for Numerical Methods in Engineering*, vol. 73, no. 5, pp. 642–664, 2008.

[27] X. Wang, J.-M. Fullana, and P.-Y. Lagrée, "Verification and comparison of four numerical schemes for a 1D viscoelastic blood flow model," *Computer Methods in Biomechanics and Biomedical Engineering*, vol. 18, no. 15, pp. 1704–1725, 2015.

[28] E. Boileau, P. Nithiarasu, P. J. Blanco, L. O. Müller, F. E. Fossan, L. R. Hellevik, W. P. Donders, W. Huberts, M. Willemet, and J. Alastruey, "A benchmark study of numerical schemes for one-dimensional arterial blood flow modelling," *International Journal for Numerical Methods in Biomedical Engineering*, vol. 31, no. 10, 2015.

[29] B. Cockburn and C.-W. Shu, "TVB Runge-Kutta local projection discontinuous Galerkin finite element method for conservation laws. II. general framework," *Mathematics of Computation*, vol. 52, no. 186, pp. 411–435, 1989.

[30] B. Cockburn, S. Hou, and C.-W. Shu, "The Runge-Kutta local projection discontinuous Galerkin finite element method for conservation laws. IV. The multidimensional case," *Mathematics of Computation*, vol. 54, no. 190, pp. 545–581, 1990.

[31] B. Cockburn and C.-W. Shu, "The Runge–Kutta discontinuous Galerkin method for conservation laws V: multidimensional systems," *Journal of Computational Physics*, vol. 141, no. 2, pp. 199–224, 1998.

[32] Q. Zhang and C.-W. Shu, "Error estimates to smooth solutions of Runge–Kutta discontinuous Galerkin methods for scalar conservation laws," *SIAM Journal on Numerical Analysis*, vol. 42, no. 2, pp. 641–666, 2004.

[33] Q. Zhang and C.-W. Shu, "Error estimates to smooth solutions of Runge-Kutta discontinuous Galerkin method for symmetrizable systems of conservation laws," *SIAM Journal on Numerical Analysis*, vol. 44, no. 4, pp. 1703–1720, 2006.

[34] J. Luo, C.-W. Shu, and Q. Zhang, "A priori error estimates to smooth solutions of the third order Runge–Kutta discontinuous Galerkin method for symmetrizable systems of conservation laws," *ESAIM: Mathematical Modelling and Numerical Analysis*, vol. 49, no. 4, pp. 991–1018, 2015.

[35] O. Barnea, E. H. Austin, B. Richman, and W. P. Santamore, "Balancing the circulation: theoretic optimization of pulmonary/systemic flow ratio in hypoplastic left heart syndrome," *Journal of the American College of Cardiology*, vol. 24, no. 5, pp. 1376–1381, 1994.

[36] O. Barnea, W. P. Santamore, A. Rossi, E. Salloum, S. Chien, and E. H. Austin, "Estimation of oxygen delivery in newborns with a univentricular circulation," *Circulation*, vol. 98, no. 14, pp. 1407–1413, 1998.

[37] H.-H. Sievers, A. Gerdes, J. Kunze, and G. Pfister, "Superior hydrodynamics of a modified cavopulmonary connection for the Norwood operation," *The Annals of Thoracic Surgery*, vol. 65, no. 6, pp. 1741–1745, 1998.

[38] F. Migliavacca, R. Balossino, G. Pennati, G. Dubini, T.-Y. Hsia, M. R. de Leval, and E. L. Bove, "Multiscale modelling in biofluidynamics: application to reconstructive paediatric cardiac surgery," *Journal of Biomechanics*, vol. 39, no. 6, pp. 1010–1020, 2006.

[39] Y. Qian, J. Liu, K. Itatani, K. Miyaji, and M. Umezu, "Computational hemodynamic analysis in congenital heart disease: simulation of the Norwood procedure," *Annals of Biomedical Engineering*, vol. 38, no. 7, pp. 2302–2313, 2010.

[40] C. Corsini, D. Cosentino, G. Pennati, G. Dubini, T.-Y. Hsia, and F. Migliavacca, "Multiscale models of the hybrid palliation for hypoplastic left heart syndrome,"

Journal of Biomechanics, vol. 44, no. 4, pp. 767–770, 2011.

[41] T.-Y. Hsia, D. Cosentino, C. Corsini, G. Pennati, G. Dubini, F. Migliavacca, *et al.*, "Use of mathematical modeling to compare and predict hemodynamic effects between hybrid and surgical Norwood palliations for hypoplastic left heart syndrome," *Circulation*, vol. 124, no. 11 suppl 1, pp. S204–S210, 2011.

[42] A. Ceballos, E. Divo, R. Argueta-Morales, C. Calderone, A. Kassab, and W. DeCampli, "A multi-scale CFD analysis of the hybrid Norwood palliative treatment for hypoplastic left heart syndrome: Effect of reverse Blalock-Taussing shunt diameter," in *ASME 2013 International Mechanical Engineering Congress and Exposition*, pp. V03BT03A045–V03BT03A045, American Society of Mechanical Engineers, 2013.

[43] M. E. Moghadam, F. Migliavacca, I. E. Vignon-Clementel, T.-Y. Hsia, and A. L. Marsden, "Optimization of shunt placement for the norwood surgery using multi-domain modeling," *Journal of Biomechanical Engineering*, vol. 134, no. 5, p. 051002, 2012.

[44] K. K. Whitehead, K. Pekkan, H. D. Kitajima, S. M. Paridon, A. P. Yoganathan, and M. A. Fogel, "Nonlinear power loss during exercise in single-ventricle patients after the Fontan: Insights from computational fluid dynamics," *Circulation*, vol. 116, no. 11 suppl, pp. I–165–I–171, 2007.

[45] J. Liu, Y. Qian, Q. Sun, J. Liu, and M. Umezu, "Use of computational fluid dynamics to estimate hemodynamic effects of respiration on hypoplastic left heart syndrome surgery: total cavopulmonary connection treatments," *The Scientific World Journal*, vol. 2013, 2013.

[46] E. Kung, G. Pennati, F. Migliavacca, T.-Y. Hsia, R. Figliola, A. Marsden, and A. Giardini, "A simulation protocol for exercise physiology in Fontan patients using a closed loop lumped-parameter model," *Journal of Biomechanical Engineering*, vol. 136, no. 8, 2014.

[47] S. Acosta, C. Puelz, B. Rivière, D. J. Penny, and C. G. Rusin, "Numerical method of characteristics for one-dimensional blood flow," *Journal of Computational Physics*, vol. 294, pp. 96–109, 2015.

[48] C. Puelz, B. Rivière, S. Čanić, and C. Rusin, "Comparison of reduced blood flow models using Runge–Kutta discontinuous Galerkin methods," *Applied Numerical Mathematics*, vol. 115, pp. 114–141, 2017.

[49] L. Formaggia, A. Quarteroni, and A. Veneziani, *Cardiovascular Mathematics: Modeling and simulation of the circulatory system*, vol. 1. Springer Science & Business Media, 2010.

[50] A. Harten, "On the symmetric form of systems of conservation laws with entropy," *Journal of Computational Physics*, vol. 49, no. 1, pp. 151–164, 1983.

[51] C. Puelz and B. Rivière, "A priori error estimates of Adams-Bashforth discontinuous Galerkin methods for scalar nonlinear conservation laws," *submitted*, 2017.

[52] M. Zakerzadeh and G. May, "On the convergence of a shock capturing discontinuous Galerkin method for nonlinear hyperbolic systems of conservation laws," *SIAM Journal on Numerical Analysis*, vol. 54, no. 2, pp. 874–898, 2016.

[53] C. Dafermos, *Hyperbolic conservation laws in continuum physics, volume 325*

of Grundlehren der Mathematischen Wissenschaften [Fundamental Principles of Mathematical Sciences]. Springer-Verlag, Berlin, 2010.

[54] D. Di Pietro and A. Ern, *Mathematical Aspects of Discontinuous Galerkin Methods*, vol. 69. Springer Science & Business Media, 2011.

[55] S. Sherwin, V. Franke, J. Peiró, and K. Parker, "One-dimensional modelling of a vascular network in space-time variables," *Journal of Engineering Mathematics*, vol. 47, no. 3-4, pp. 217–250, 2003.

[56] J. Alastruey, S. Moore, K. Parker, T. David, J. Peiró, and S. Sherwin, "Reduced modelling of blood flow in the cerebral circulation: coupling 1-D, 0-D and cerebral auto-regulation models," *International Journal for Numerical Methods in Fluids*, vol. 56, no. 8, pp. 1061–1067, 2008.

[57] L. Dumas, T. El Bouti, and D. Lucor, "A robust and subject-specific hemodynamic model of the lower limb based on noninvasive arterial measurements," *Journal of Biomechanical Engineering*, vol. 139, no. 1, p. 011002, 2017.

[58] K. Matthys, J. Alastruey, J. Peiró, A. Khir, P. Segers, P. Verdonck, K. Parker, and S. Sherwin, "Pulse wave propagation in a model human arterial network: assessment of 1-D numerical simulations against in vitro measurements," *Journal of Biomechanics*, vol. 40, no. 15, pp. 3476–3486, 2007.

[59] E. Bollache, N. Kachenoura, A. Redheuil, F. Frouin, E. Mousseaux, P. Recho, and D. Lucor, "Descending aorta subject-specific one-dimensional model validated against in vivo data," *Journal of Biomechanics*, vol. 47, no. 2, pp. 424–431, 2014.

[60] R. Cascaval, C. D'Apice, M. D'Arienzo, and R. Manzo, "Boundary control for an arterial system," *Journal of Fluid Flow*, vol. 3, 2016.

[61] B. Cockburn and C. Shu, "The Runge-Kutta local projection P^1 discontinuous-Galerkin finite element method for scalar conservation laws," *RAIRO-Modélisation Mathématique et Analyse Numérique*, vol. 25, no. 3, pp. 337–361, 1991.

[62] Q. Zhang and C. Shu, "Stability analysis and a priori error estimates of the third order explicit Runge-Kutta discontinuous Galerkin method for scalar conservation laws," *SIAM Journal on Numerical Analysis*, vol. 48, no. 3, pp. 1038–1063, 2010.

[63] H. Wang, C. Shu, and Q. Zhang, "Stability analysis and error estimates of local discontinuous Galerkin methods with implicit–explicit time-marching for nonlinear convection–diffusion problems," *Applied Mathematics and Computation*, vol. 272, pp. 237–258, 2016.

[64] E. Deriaz, "Stability conditions for the numerical solution of convection-dominated problems with skew-symmetric discretizations," *SIAM Journal on Numerical Analysis*, vol. 50, no. 3, pp. 1058–1085, 2012.

[65] A. Mikelic, G. Guidoboni, and S. Čanić, "Fluid-structure interaction in a pre-stressed tube with thick elastic walls I: the stationary Stokes problem," *Networks and Heterogeneous Media*, vol. 2, no. 3, p. 397, 2007.

[66] L. C. Evans, *Partial Differential Equations*. Providence, Rhode Land: American Mathematical Society, second ed., 2010.

[67] S. Acosta, C. Puelz, B. Rivière, D. Penny, K. Brady, and C. Rusin, "Cardiovascular mechanics in the early stages of pulmonary hypertension: a computational study," *submitted*, 2017.

[68] N. Westerhof, J.-W. Lankhaar, and B. E. Westerhof, "The arterial windkessel," *Medical & Biological Engineering & Computing*, vol. 47, no. 2, pp. 131–141, 2009.

[69] J. Alastruey, K. H. Parker, and S. J. Sherwin, "Arterial pulse wave haemodynamics," in *11th International Conference on Pressure Surges*, pp. 401–442, Virtual PiE Led t/a BHR Group: Lisbon, Portugal, 2012.

[70] S. Acosta, D. Penny, and C. Rusin, "An effective model of blood flow in capillary beds," *Microvascular Research*, vol. 100, pp. 40–47, 2015.

[71] M. S. Olufsen, "Structured tree outflow condition for blood flow in larger systemic arteries," *American Journal of Physiology-Heart and Circulatory Physiology*, vol. 276, no. 1, pp. H257–H268, 1999.

[72] M. T. Politi, A. Ghigo, J. M. Fernández, I. Khelifa, J. Gaudric, J. M. Fullana, and P.-Y. Lagrée, "The dicrotic notch analyzed by a numerical model," *Computers in Biology and Medicine*, vol. 72, pp. 54–64, 2016.

[73] N. Xiao, J. Alastruey, and C. Alberto Figueroa, "A systematic comparison between 1-D and 3-D hemodynamics in compliant arterial models," *International Journal for Numerical Methods in Biomedical Engineering*, vol. 30, no. 2, pp. 204–231, 2014.

[74] P. J. Blanco, M. Pivello, S. Urquiza, and R. Feijóo, "On the potentialities of 3D–1D coupled models in hemodynamics simulations," *Journal of Biomechanics*,

vol. 42, no. 7, pp. 919–930, 2009.

[75] L. Grinberg, T. Anor, J. Madsen, A. Yakhot, and G. Karniadakis, "Large–scale simulation of the human arterial tree," *Clinical and Experimental Pharmacology and Physiology*, vol. 36, no. 2, pp. 194–205, 2009.

[76] A. Quarteroni, A. Veneziani, and C. Vergara, "Geometric multiscale modeling of the cardiovascular system, between theory and practice," *Computer Methods in Applied Mechanics and Engineering*, vol. 302, pp. 193–252, 2016.

[77] T. J. Hughes and J. Lubliner, "On the one-dimensional theory of blood flow in the larger vessels," *Mathematical Biosciences*, vol. 18, no. 1, pp. 161–170, 1973.

[78] D. Bessems, M. Rutten, and F. Van De Vosse, "A wave propagation model of blood flow in large vessels using an approximate velocity profile function," *Journal of Fluid Mechanics*, vol. 580, pp. 145–168, 2007.

[79] K. Azer and C. S. Peskin, "A one-dimensional model of blood flow in arteries with friction and convection based on the Womersley velocity profile," *Cardiovascular Engineering*, vol. 7, no. 2, pp. 51–73, 2007.

[80] A. Coccarelli, E. Boileau, D. Parthimos, and P. Nithiarasu, "An advanced computational bioheat transfer model for a human body with an embedded systemic circulation," *Biomechanics and Modeling in Mechanobiology*, vol. 15, no. 5, pp. 1173–1190, 2016.

[81] C. Sheng, S. Sarwal, K. Watts, and A. Marble, "Computational simulation of blood flow in human systemic circulation incorporating an external force field," *Medical and Biological Engineering and Computing*, vol. 33, no. 1, pp. 8–17, 1995.

[82] E. Marchandise, M. Willemet, and V. Lacroix, "A numerical hemodynamic tool for predictive vascular surgery," *Medical Engineering and Physics*, vol. 31, no. 1, pp. 131–144, 2009.

[83] L. O. Müller, P. J. Blanco, S. M. Watanabe, and R. A. Feijóo, "A high-order local time stepping finite volume solver for one-dimensional blood flow simulations: application to the ADAN model," *International Journal for Numerical Methods in Biomedical Engineering*, vol. 32, no. 10, 2016.

[84] H. Zhang, N. Fujiwara, M. Kobayashi, S. Yamada, F. Liang, S. Takagi, and M. Oshima, "Development of a numerical method for patient-specific cerebral circulation using 1D–0D simulation of the entire cardiovascular system with SPECT data," *Annals of Biomedical Engineering*, vol. 44, no. 8, pp. 2351–2363, 2016.

[85] O. Delestre and P.-Y. Lagrée, "A "well–balanced" finite volume scheme for blood flow simulation," *International Journal for Numerical Methods in Fluids*, vol. 72, no. 2, pp. 177–205, 2013.

[86] M. Anliker, R. L. Rockwell, and E. Ogden, "Nonlinear analysis of flow pulses and shock waves in arteries," *Zeitschrift für angewandte Mathematik und Physik ZAMP*, vol. 22, no. 2, pp. 217–246, 1971.

[87] J. P. Keener and J. Sneyd, *Mathematical Physiology*, vol. 1. Springer, 1998.

[88] J. P. Murgo, N. Westerhof, J. P. Giolma, and S. A. Altobelli, "Aortic input impedance in normal man: relationship to pressure wave forms," *Circulation*, vol. 62, no. 1, pp. 105–116, 1980.

[89] R. L. Lange and H. H. Hecht, "Genesis of pistol-shot and Korotkoff sounds," *Circulation*, vol. 18, no. 5, pp. 975–978, 1958.

[90] F. Fontan and E. Baudet, "Surgical repair of tricuspid atresia," *Thorax*, vol. 26, no. 3, pp. 240–248, 1971.

[91] A. A. Ghaferi and G. M. Hutchins, "Progression of liver pathology in patients undergoing the Fontan procedure: chronic passive congestion, cardiac cirrhosis, hepatic adenoma, and hepatocellular carcinoma," *The Journal of Thoracic and Cardiovascular Surgery*, vol. 129, no. 6, pp. 1348–1352, 2005.

[92] S. Camposilvan, O. Milanesi, G. Stellin, A. Pettenazzo, L. Zancan, and L. D'Antiga, "Liver and cardiac function in the long term after Fontan operation," *The Annals of Thoracic Surgery*, vol. 86, no. 1, pp. 177–182, 2008.

[93] M. R. De Leval and J. E. Deanfield, "Four decades of Fontan palliation," *Nature Reviews Cardiology*, vol. 7, no. 9, pp. 520–527, 2010.

[94] R. W. Elder, N. M. McCabe, C. Hebson, E. Veledar, R. Romero, R. M. Ford, W. T. Mahle, B. E. Kogon, A. Sahu, M. Jokhadar, *et al.*, "Features of portal hypertension are associated with major adverse events in Fontan patients: the VAST study," *International Journal of Cardiology*, vol. 168, no. 4, pp. 3764–3769, 2013.

[95] J. Rychik, D. Goldberg, and K. Dodds, "Long-term results and consequences of single ventricle palliation," *Progress in Pediatric Cardiology*, vol. 29, no. 1, pp. 19–23, 2010.

[96] B. Kogon, M. McConnell, and W. Book, "Fontan conversion with hepatic vein

exclusion: a means for hepatic preservation in single ventricle heart disease," *Cardiology in the Young*, vol. 26, no. 3, pp. 582–585, 2016.

[97] C. P. Brizard, G. K. Lane, G. Alex, and M. M. Cheung, "Original surgical procedure for the treatment of protein-losing enteropathy in Fontan patients," *Circulation*, vol. 134, no. 8, pp. 625–627, 2016.

[98] J. Rychik, J. J. Rome, and M. L. Jacobs, "Late surgical fenestration for complications after the Fontan operation," *Circulation*, vol. 96, no. 1, pp. 33–36, 1997.

[99] A. K. Singhi and S. Kothandum, "Unusual method of creation of a transcatheter fenestration in an extracardiac conduit Fontan circulation," *Annals of Pediatric Cardiology*, vol. 9, no. 3, p. 258, 2016.

[100] S. P. Kumar, C. S. Rubinstein, J. M. Simsic, A. B. Taylor, J. P. Saul, and S. M. Bradley, "Lateral tunnel versus extracardiac conduit Fontan procedure: a concurrent comparison," *The Annals of Thoracic Surgery*, vol. 76, no. 5, pp. 1389–1397, 2003.

[101] B. R. Imielski, R. K. Woods, K. A. Mussatto, Y. Cao, P. M. Simpson, and J. S. Tweddell, "Fontan fenestration closure and event-free survival," *The Journal of Thoracic and Cardiovascular Surgery*, vol. 145, no. 1, pp. 183–187, 2013.

[102] F. Migliavacca, G. Pennati, G. Dubini, R. Fumero, R. Pietrabissa, G. Urcelay, E. L. Bove, T.-Y. Hsia, and M. R. de Leval, "Modeling of the Norwood circulation: effects of shunt size, vascular resistances, and heart rate," *American Journal of Physiology–Heart and Circulatory Physiology*, vol. 280, no. 5, pp. H2076–H2086, 2001.

[103] C. Vallecilla, R. H. Khiabani, N. Sandoval, M. Fogel, J. C. Briceño, and A. P. Yoganathan, "Effect of high altitude exposure on the hemodynamics of the bidirectional Glenn physiology: Modeling incremented pulmonary vascular resistance and heart rate," *Journal of Biomechanics*, vol. 47, no. 8, pp. 1846–1852, 2014.

[104] C. Vallecilla, R. H. Khiabani, P. Trusty, N. Sandoval, M. Fogel, J. C. Briceño, and A. P. Yoganathan, "Exercise capacity in the Bidirectional Glenn physiology: Coupling cardiac index, ventricular function and oxygen extraction ratio," *Journal of Biomechanics*, vol. 48, no. 10, pp. 1997–2004, 2015.

[105] A. Jalali, G. F. Jones, D. J. Licht, and C. Nataraj, "Application of mathematical modeling for simulation and analysis of hypoplastic left heart syndrome (HLHS) in pre- and postsurgery conditions," *BioMed Research International*, vol. 2015, 2015.

[106] A. J. Chin and R. L. Watrous, "Model-based comparison of the normal and Fontan circulatory systems: part II: major differences in performance characteristics," *World Journal for Pediatric and Congenital Heart Surgery*, vol. 6, no. 3, pp. 360–373, 2015.

[107] R. L. Watrous and A. J. Chin, "Model-based comparison of the normal and Fontan circulatory systems: part I: development of a general purpose, interactive cardiovascular model," *World Journal for Pediatric and Congenital Heart Surgery*, vol. 5, no. 3, pp. 372–384, 2014.

[108] A. Di Molfetta, A. Amodeo, M. G. Gagliardi, M. G. Trivella, L. Fresiello, S. Filippelli, A. Toscano, and G. Ferrari, "Hemodynamic effects of ventricular assist

device implantation on Norwood, Glenn, and Fontan circulation: A simulation study," *Artificial Organs*, vol. 40, no. 1, pp. 34–42, 2016.

[109] M. E. Moghadam, I. E. Vignon-Clementel, R. Figliola, A. L. Marsden, M. of Congenital Hearts Alliance (MOCHA) Investigators, *et al.*, "A modular numerical method for implicit 0D/3D coupling in cardiovascular finite element simulations," *Journal of Computational Physics*, vol. 244, pp. 63–79, 2013.

[110] G. Dubini, M. De Leval, R. Pietrabissa, F. Montevecchi, and R. Fumero, "A numerical fluid mechanical study of repaired congenital heart defects. application to the total cavopulmonary connection," *Journal of Biomechanics*, vol. 29, no. 1, pp. 111–121, 1996.

[111] M. De Leval, G. Dubini, F. Migliavacca, H. Jalali, G. Camporini, A. Redington, and R. Pietrabissa, "Use of computational fluid dynamics in the design of surgical procedures: application to the study of competitive flows in cavopulmonary connections," *The Journal of Thoracic and Cardiovascular Surgery*, vol. 111, no. 3, pp. 502–513, 1996.

[112] F. Migliavacca, M. R. de Leval, G. Dubini, R. Pietrabissa, and R. Fumero, "Computational fluid dynamic simulations of cavopulmonary connections with an extracardiac lateral conduit," *Medical Engineering & Physics*, vol. 21, no. 3, pp. 187–193, 1999.

[113] T.-Y. Hsia, F. Migliavacca, S. Pittaccio, A. Radaelli, G. Dubini, G. Pennati, and M. de Leval, "Computational fluid dynamic study of flow optimization in realistic models of the total cavopulmonary connections," *Journal of Surgical Research*, vol. 116, no. 2, pp. 305–313, 2004.

[114] D. A. de Zélicourt, K. Pekkan, L. Wills, K. Kanter, J. Forbess, S. Sharma, M. Fogel, and A. P. Yoganathan, "In vitro flow analysis of a patient-specific intraatrial total cavopulmonary connection," *The Annals of Thoracic Surgery*, vol. 79, no. 6, pp. 2094–2102, 2005.

[115] A. L. Marsden, A. J. Bernstein, V. M. Reddy, S. C. Shadden, R. L. Spilker, F. P. Chan, C. A. Taylor, and J. A. Feinstein, "Evaluation of a novel Y-shaped extracardiac Fontan baffle using computational fluid dynamics," *The Journal of Thoracic and Cardiovascular Surgery*, vol. 137, no. 2, pp. 394–403, 2009.

[116] H. Ozawa, T. Ueno, S. Iwai, H. Kawata, K. Nishigaki, H. Kishimoto, and Y. Sawa, "Contractility–afterload mismatch in patients with protein-losing enteropathy after the Fontan operation," *Pediatric Cardiology*, vol. 35, no. 7, pp. 1225–1231, 2014.

[117] J. Rychik and S. Gui-Yang, "Relation of mesenteric vascular resistance after Fontan operation and protein-losing enteropathy," *The American Journal of Cardiology*, vol. 90, no. 6, pp. 672–674, 2002.

[118] A. M. Ostrow, H. Freeze, and J. Rychik, "Protein-losing enteropathy after Fontan operation: investigations into possible pathophysiologic mechanisms," *The Annals of Thoracic Surgery*, vol. 82, no. 2, pp. 695–700, 2006.

[119] O. Uzun, J. K. Wong, V. Bhole, and O. Stumper, "Resolution of protein-losing enteropathy and normalization of mesenteric Doppler flow with sildenafil after Fontan," *The Annals of Thoracic Surgery*, vol. 82, no. 6, pp. e39–e40, 2006.

[120] G. Agnoletti, G. Ferraro, R. Bordese, D. Marini, S. Gala, L. Bergamasco, F. Ferroni, P. L. Calvo, C. Barletti, F. Cisarò, *et al.*, "Fontan circulation causes early,

severe liver damage. should we offer patients a tailored strategy?," *International Journal of Cardiology*, vol. 209, pp. 60–65, 2016.

[121] L. Deorsola, E. Aidala, M. T. Cascarano, A. Valori, G. Agnoletti, and C. P. Napoleone, "Liver stiffness modifications shortly after total cavopulmonary connection," *Interactive CardioVascular and Thoracic Surgery*, vol. 23, no. 4, pp. 513–518, 2016.

[122] D. Wolff, J. P. van Melle, H. Dijkstra, B. Bartelds, T. P. Willems, H. Hillege, A. P. van den Berg, T. Ebels, P. E. Sijens, and R. M. Berger, "The Fontan circulation and the liver: A magnetic resonance diffusion-weighted imaging study," *International Journal of Cardiology*, vol. 202, pp. 595–600, 2016.

[123] Y. Tanoue, A. Sese, Y. Ueno, K. Joh, and T. Hijii, "Bidirectional Glenn procedure improves the mechanical efficiency of a total cavopulmonary connection in high-risk Fontan candidates," *Circulation*, vol. 103, no. 17, pp. 2176–2180, 2001.